Study of positive electrode materials for lithium-ion batteries by experimental and theoretical soft and hard X-ray photoemission spectroscopy

Roberto Fantin

▶ To cite this version:

Roberto Fantin. Study of positive electrode materials for lithium-ion batteries by experimental and theoretical soft and hard X-ray photoemission spectroscopy. Materials Science [cond-mat.mtrl-sci]. Université Grenoble Alpes [2020-..], 2024. English. NNT : 2024GRALI027 . tel-04659960

HAL Id: tel-04659960
https://theses.hal.science/tel-04659960

Submitted on 23 Jul 2024

THÈSE

Pour obtenir le grade de

DOCTEUR DE L'UNIVERSITÉ GRENOBLE ALPES

École doctorale : I-MEP2 - Ingénierie - Matériaux, Mécanique, Environnement, Energétique, Procédés, Production
Spécialité : 2MGE - Matériaux, Mécanique, Génie civil, Electrochimie
Unité de recherche : CEA Grenoble / LITEN

Etude des matériaux d'électrode positive pour accumulateurs lithium-ions par spectroscopie de photoémission à rayonnement X mous et durs expérimentale et théorique

Study of positive electrode materials for lithium-ion batteries by experimental and theoretical soft and hard X-ray photoemission spectroscopy

Présentée par :

Roberto FANTIN

Direction de thèse :

Anass BENAYAD Directeur de recherche, CEA Grenoble	Directeur de thèse
Ambroise VAN ROEKEGHEM Ingénieur chercheur, CEA Grenoble	Co-encadrant de thèse

Rapporteurs :

Rémi DEDRYVERE
Professeur, Université de Pau et des Pays de l'Adour
Philipp HANSMANN
Professeur, Friedrich-Alexander-University Erlangen-Nürnberg

Thèse soutenue publiquement le **10 avril 2024**, devant le jury composé de :

Anass BENAYAD Directeur de recherche, CEA Grenoble	Directeur de thèse
Rémi DEDRYVERE Professeur, Université de Pau et des Pays de l'Adour	Rapporteur
Philipp HANSMANN Professeur, Friedrich-Alexander-University Erlangen-Nürnberg	Rapporteur
Renaud BOUCHET Professeur, Université Grenoble Alpes	Président du jury
Maria HAHLIN Professeure, Uppsala University	Examinatrice

Invités :

Ambroise VAN ROEKEGHEM
Ingénieur chercheur, CEA Grenoble
Jean-Pascal RUEFF
Directeur de recherche, Synchrotron Soleil

Study of positive electrode materials for lithium-ion batteries by experimental and theoretical soft and hard X-ray photoemission spectroscopy

Étude des matériaux d'électrode positive pour accumulateurs lithium-ions par spectroscopie de photoémission à rayonnement X mous et durs expérimentale et théorique

Roberto Fantin

2024

Abstract for the general public

Lithium-ion batteries play a crucial role in the current energy transition, supporting electric mobility and renewable energy storage. To this end, the storable energy and efficiency of batteries must be improved. Among other factors, the performance is limited by the ability of positive electrode materials to reversibly exchange lithium ions and electrons. In this joint experimental and theoretical study, we aim to understand electron transfer on an atomic scale. The research has been carried out using $LiNiO_2$, Li_2MnO_3, and $LiCoO_2$ as model systems in the context of positive electrode materials for next-generation Li-ion batteries. By distinguishing between degraded surface layers and bulk material, we uncover a local electronic mechanism during delithiation that highlights the central role of oxygen ions in charge compensation. These results challenge conventional theories and offer promising directions for improving battery performance.

Résumé grand public

Les batteries lithium-ion sont actuellement limitées par la faculté des matériaux d'électrode positive à échanger réversiblement les ions lithium et les électrons. Cette étude vise à comprendre les transferts d'électrons à l'échelle atomique dans les oxydes lamellaires de métaux de transition pour mieux appréhender le comportement en cyclage des futures générations d’électrodes. Grâce à une approche nouvelle basée sur la spectroscopie de photoémission à rayonnement X et calculs théoriques, nous avons dressé une cartographie détaillée des variations de la structure chimique et électronique depuis l’extrême surface jusqu’au volume des électrodes à chaque stade de la désinsertion des ions lithium. Nous avons ainsi mis en évidence le rôle majeur des atomes d’oxygène dans les mécanismes redox de ces matériaux d’électrode. Ces résultats apportent un regard nouveau sur le rôle des anions en tant que centre redox offrant des pistes prometteuses pour améliorer les performances des batteries.

Riassunto per il pubblico generale

Le batterie agli ioni di litio sono attualmente limitate dalla capacità dei materiali usati come elettrodi positivi di scambiare reversibilmente ioni litio ed elettroni. In questa tesi, si è studiato il trasferimento degli elettroni negli ossidi lamellari di metalli di transizione per comprendere meglio il loro comportamento durante il processo di carica e scarica delle batterie. Grazie ad un nuovo approccio basato sulla spettroscopia di fotoelettroni a raggi X e calcoli teorici, abbiamo caratterizzato le variazioni della struttura chimica ed elettronica in funzione della profondità (fino ai primi 30 nanometri) e della de-intercalazione degli ioni di litio. In tal modo, è stato possibile evidenziare il ruolo degli atomi di ossigeno nel compensare la rimozione degli ioni litio attraverso la distribuzione della carica in eccesso con un meccanismo detto di ‶auto-regolazione". Sulla base di questi risultati, si evidenziano alcune direzioni promettenti per migliorare le prestazioni delle batterie.

Abstract

This thesis has the objective to understand the redox compensation mechanism of positive electrode materials sustaining lithium-ion battery (dis-)charge processes. The study is conducted for $LiNiO_2$, Li_2MnO_3, and $LiCoO_2$, archetype materials for the state-of-art high-energy positive electrode materials $Li[Ni_xMn_yCo_z]O_2$. Despite these materials having been studied for decades, the link between electronic correlations and redox mechanism during (de-)lithiation is not well understood. In particular, the role of transition metals and oxygen ions in the redox process is yet to be clarified and resolved in-depth from the surface towards the bulk.

To this goal, we establish a novel methodology based on laboratory- and synchrotron-based soft and hard X-ray photoemission spectroscopy (XPS, HAXPES) to probe qualitatively and quantitatively the electronic structure from the extreme surface down to ~20-30 nm. This allows us to follow the evolution of positive solid electrode-electrolyte interphase, surface electrode material degradation, and bulk electronic structure upon cycling. Notably, the thickness and chemical structure of the surface degradation layer depends on the increase of oxygen valence, related to its interaction with the transition metal. Subsequently, we investigate the evolution of the bulk electronic structure upon cycling by analyzing the transition metal 2p core-level HAXPES spectra with electronic structure simulations based on density functional (DFT) and cluster model (CMT) theories. We evaluate the role of transition metals and oxygen in the redox process by quantifying the 3d-3d Coulomb repulsion and oxygen ligand-metal 2p-3d charge transfer (Δ). The spectra analysis for $LiCoO_2$ and $LiNiO_2$ highlights a decrease of Δ towards the negative charge transfer regime indicating a leading role of the oxygen ions in the charge compensation mechanism. The delithiation process is therefore controlled by the local electron transfer from oxygen 2p orbitals to limit charge accumulation in the metal 3d orbitals.

Résumé

Le succès des oxydes de métaux de transition lamellaires ($LiMO_2$, M : Ni, Co, Mn) en tant que matériaux d'électrode positive est dû à leurs capacités à intercaler de manière réversible les ions lithium en préservant l'intégrité cristalline de l'électrode. Bien que les $LiMO_2$, soit largement étudiés et utilisés, les mécanismes en jeu à l'échelle électronique lors de la désinsertion/insertion du lithium ne sont toujours pas clarifiés. Cette thèse a pour objectif d'appréhender les mécanismes de compensation de charge dans les matériaux d'électrode positive $LiMO_2$ pendant leur cyclage. En particulier, le rôle des métaux de transition et des ions d'oxygène dans le processus d'oxydoréduction reste à élucider en différenciant les processus de surface de ceux du bulk du matériau.

Pour ce faire, grâce à une approche qualitative et quantitative basée sur la spectroscopie de photoémission de rayons X de laboratoire et synchrotron, mous et durs (XPS, HAXPES), nous avons résolu la structure électronique et chimique des électrodes Li_xMO_2 depuis l'extrême surface jusqu'à ~20-30 nm. Nous avons mis en évidence des points communs et des différences sur la nature chimique et l'épaisseur de la couche de passivation de surface « *solide electrolyte interphase- SEI* », la structure électronique à proximité de la SEI et dans le volume des électrodes en fonction de la nature du métal de transition. Le couplage entre HAXPES et simulation à base de model de cluster (CMT) et de théorie de la fonctionnelle de densité (DFT) a permis de réinterpréter le rôle de l'oxygène dans les processus de transfert de charge. Ainsi, nous avons identifié, à chaque étape de la désinsertion du lithium dans Li_xMO_2, la contribution de la répulsion Coulombique « 3d-3d » et le transfert de charge « 2p-3d » entre l'oxygène et le métal (Δ). L'analyse expérimentale et théorique des spectres des niveaux de cœur des composés $LiCoO_2$ et $LiNiO_2$ à différents stades de la delithiation a mis évidence la présence d'un régime de transfert de charge négatif indiquant le rôle prépondérant des ions oxygène dans le mécanisme de compensation de charge.

Table of contents

Annex

Context and outline of the thesis

The global environmental situation needs no introduction. It is well known that reducing greenhouse gas emissions to slow global warming is the most urgent challenge facing our society. Achieving this goal requires a radical change in our economic models, particularly in the energy sector, driven by long-term and large-scale policies identified in the United Nations "Sustainable Development Goals" [1]. Indeed, the European Union has set the legislative goal of reducing emissions by 55 % by 2030 and achieving a climate-neutral society by 2050 in the "Fit for 55" package [2].

Battery development has a key role to play in supporting this transition to a sustainable energy model. The European research initiative "Battery 2030+" has been established to address this need [3]. In its "Battery Manifesto", lithium-ion battery technology is identified as the main driving force in the current energy storage landscape [4]. This leading role is driven by the current accelerated transition to electric mobility. In the "Battery 2030+" roadmap updated in 2023, the long-term research directions have been identified and distinguished into three main themes [4,5]. One of these general themes consists of the fundamental understanding and development of battery interfaces and materials through a combined experimental and computational approach.

The FOCUS "Multiscale battery simulation applied to electrode materials" project of the French Alternative Energies and Atomic Energy Commission (CEA) launched in 2020 fits into this context [6]. The goal of the project is to study battery materials from atomic to device scale through the coordinated deployment of 15 theses and post-docs to develop predictive theoretical models. In this context, a primary focus is given to the coupling of physical modeling and experimental characterization.

This thesis is part of the FOCUS Battery project and was carried out at the Innovation Laboratory for New Energy Technologies and Nanomaterials (LITEN) research institute of the CEA in Grenoble, France. The thesis focuses on two fundamental aspects concerning the positive electrode materials of lithium-ion batteries: resolving the bulk electronic structure and the electrode-electrolyte interface evolution upon cycling. These elements are fundamental to the operation of lithium-ion batteries, making their understanding a vital resource for directing the development of better materials. At the same time, these aspects are known to be among the least understood in the lithium-ion battery field [7,8].

This is largely caused by the lack of combined experimental and theoretical methods with an adequate surface resolution for interfaces and sensitivity to electronic structure, the need for which has recently been emphasized by the scientific community [8,9]. This thesis aims to address that need through the development of an integrated experimental and theoretical approach based on soft and hard X-ray photoelectron spectroscopy (XPS, HAXPES), specifically. The experimental characterizations were carried out with a novel laboratory spectrometer of the Nanocharacterization Platform (PFNC) that allows probing on an equal footing the nanoscale interfaces and buried bulk electronic structures of the electrode materials. The interdisciplinary nature of the project was concretized in the execution of the thesis across two CEA laboratories: the Laboratory of Advanced Characterization for Energy (LCAE) for the experimental study and the Laboratory for Multiphysics Modelling and Simulation (LMPS) for the theoretical one.

The manuscript is organized as follows:

Chapter 1 reviews the current understanding and open research directions regarding the electronic structure and surface chemistry of layered transition metal oxides, introducing the main questions that motivated this thesis.

Chapter 2 describes the overall experimental and theoretical methodology, highlighting the combination of XPS and HAXPES to discriminate surface and bulk electronic states and the application of density functional and cluster model theories (DFT, CMT) for interpreting the latter.

Chapter 3 introduces the experimental framework through a detailed core-level spectra analysis for the pristine electrode materials Li_2MnO_3, $LiCoO_2$, and $LiNiO_2$.

Chapter 4 discusses the surface chemical composition changes of the electrode materials due to Li+ deintercalation as a result of XPS and HAXPES qualitative and quantitative analysis.

Chapter 5 builds on the above analysis to study the core-level HAXPES spectra changes upon delithiation using CMT simulations to understand the bulk charge compensation mechanism in layered lithium transition metal oxides.

Chapter 1

Charge compensation and degradation mechanisms of layered transition metal oxides

The current knowledge on the layered transition metal oxides used as positive electrode active materials is reviewed, highlighting the role of their electronic structure and surface chemistry in Li-ion batteries. The chemical and physical perspectives on their electronic structure are presented, followed by a review of approximately four decades of research aiming to understand the redox process mechanism. The major instability issues are then introduced, presenting what is known about the degradation mechanisms associated with redox processes from the extreme surface toward the bulk.

1.1 Fundamentals of Li-ion batteries

A lithium-ion battery is an electrochemical cell based on the reversible transfer of lithium ions between two electrodes through an electrolyte and electrons through the external circuit. When using a conventional liquid electrolyte, a porous electrolyte-permeable separator is added to avoid physical contact between the electrodes and define the electrolyte layer thickness. While Li^+ ions move through the electrolyte, electrons are forced to move through an external circuit that is electronically connected to the electrodes via metallic current collectors.

The scheme of the device is shown in **Figure 1.1.1**. The movement of lithium ions through the electrolyte is coupled with an electric current flow through an external circuit that is fed into the device during battery charging process and can be used for external work when the battery is discharging. Depending on the direction of this process, both electrodes can act as anode (oxidation) and cathode (reduction), whose redox reactions are indicated below, assuming electrodes based on graphite (C) and layered metal oxides ($LiMO_2$), respectively [10]:

$$Li_xMO_2 + (1-x)Li^+ + (1-x)e^- \rightleftarrows LiMO_2$$ **Equation 1.1.1**

$$Li_xC \rightleftarrows C + x\,e^- + x\,Li^+$$ **Equation 1.1.2**

Conventionally, electrodes are often named with respect to their role during the discharge process [11], i.e. from left to right in the equations above. A more accurate definition is based on the relative potential of the two electrodes: the electrodes with higher and lower potential are defined as positive electrode (conventionally, cathode) and negative electrode (anode), respectively. In this thesis, we will adopt the latter nomenclature.

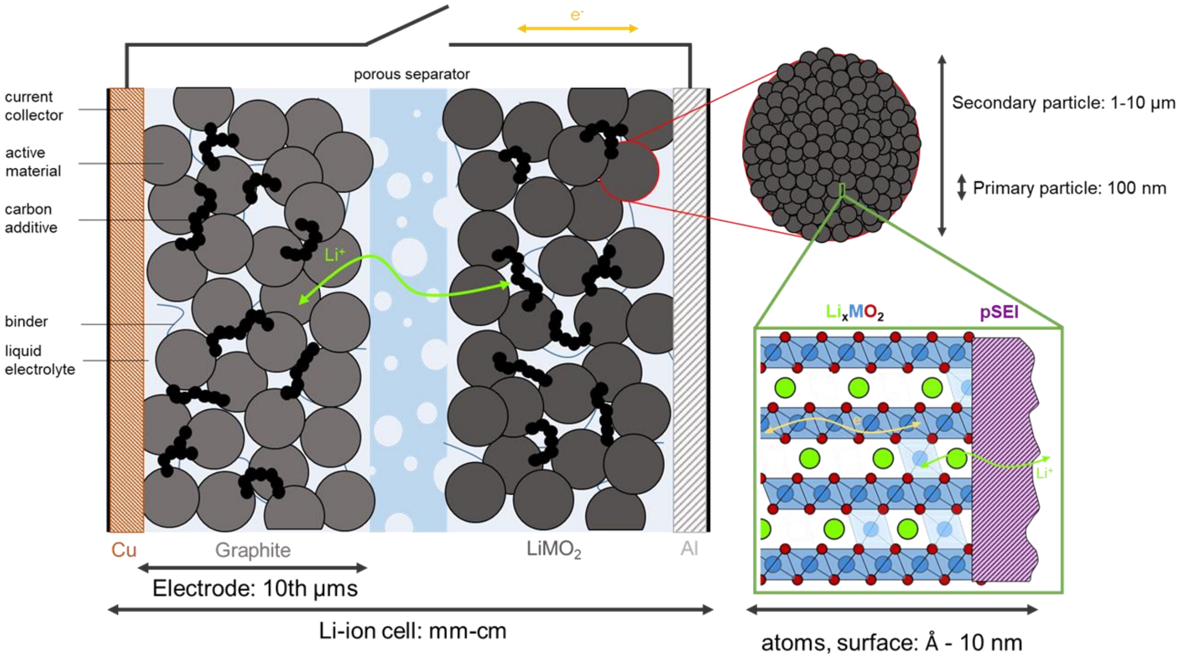

Figure 1.1.1 Schematic illustration of a Li-ion cell, indicating electrode components and Li^+ and electrons (e^-) pathways. The length scales ranging from full cell to fundamental charge transfer processes are shown. Adapted from ref. [10,12,13].

A lithium-ion battery is a system spanning a wide range of length scales. While the complete device is in the order of mm-cm, each electrode is a heterogeneous system comprising active material, binders and additives which form sub-millimeter microstructures [9,12,13]. The active materials typically consist of particles from a few micrometers to some tens; however, the single crystalline grains are smaller (~100 nm). Finally, the atomic dimension (Å-nm) is the one in which the fundamental redox processes underlying the operation of the entire device take place, to which is added a further dimension, the depth, since these mechanisms involve the surface and bulk layers in a different way (Figure 1.1.1).

The interplay of the processes happening at each scale makes the theoretical and experimental study of lithium-ion batteries very interdisciplinary and requires the combination of different scientific areas for a complete understanding. In this thesis, we focus on the atomic scale. The intrinsic properties of the active materials in the two electrodes define fundamental aspects for battery performance, including the energy that can be stored in the battery [10,14]. Moreover, the nature of the interfaces between the various components plays a fundamental role in the reversibility of the cycling process and long-term stability of the battery [10,14,15].

1.1.1 Electrochemical basics

The energy storable E in a Li-ion battery depends on the cell voltage V and the total exchanged charge with the system, named battery capacity Q [10]. In particular, E is given by the integral of the de-intercalation curve $V(q)$ with respect to the capacity q [10]:

$$E = \int_0^Q V(q)\,dq \qquad \textbf{Equation 1.1.3}$$

In practice, the volumetric and gravimetric energy densities -- the energy normalized to cell volume and weight, respectively -- are typically used to compare the batteries performance, which therefore depends also on the molecular weight and specific volume of the materials [14,16,17]. However, both V and Q are strictly related to the cell chemistry [14].

At the thermodynamic equilibrium, the open-circuit cell potential V_{OC} depends on the difference between the electrochemical potential of negative and positive electrodes (μ_n and μ_p, respectively) following the Nerst equation [10,18]:

$$V_{OC} = \frac{\mu_n - \mu_p}{e} \qquad \textbf{Equation 1.1.4}$$

with e the electron charge. To avoid electrolyte involvement in redox reactions, V_{OC} should be within the electrochemical stability window of the electrolyte used (E_W), defined by its highest occupied and lowest unoccupied molecular orbital (HOMO and LUMO, respectively) [19]. However, this does not happen in real devices: the LUMO level has a potential higher than μ_n while the HOMO has a lower potential than μ_p, inducing reduction and oxidation of the electrolyte, respectively [**Figure 1.1.2(a)**] [19]. The formation of electrically insulating solid electrode-electrolyte interphases (SEI) kinetically hinder these degradative processes until suppressing them when a sufficient thickness is reached [20]. This is typically in the order of a few nanometers for the positive electrode and in the range between 1 -100 nm for the negative one [9].

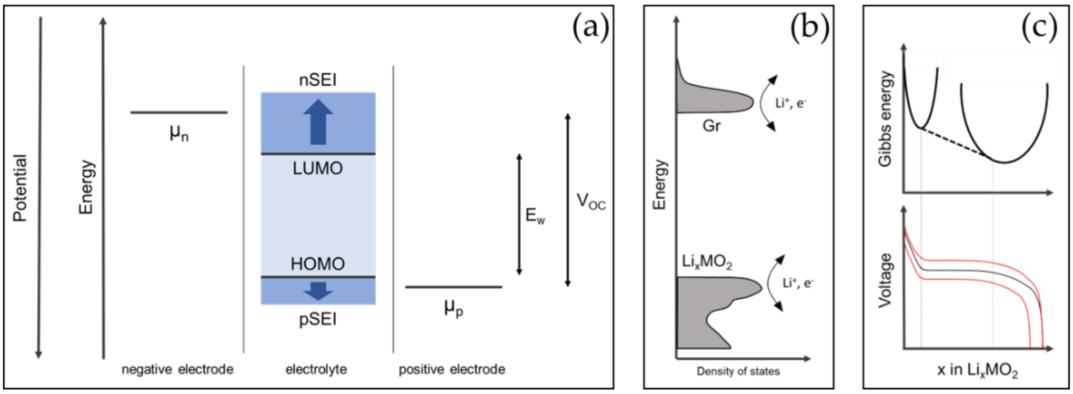

Figure 1.1.2 (a) Energy level diagram for the electrodes and electrolyte, highlighting the formation of passivation layers i.e. the positive and negative solid electrolyte interphases (SEI). Adapted from ref. [19]. (b) Qualitative valence band plots for the electrodes. (c) Relation between the cell voltage (bottom) and thermodynamic phase transitions (top) for a general Li_xMO_2 material. Red lines indicate the measured voltage due to charge and discharge overpotentials. Adapted from ref. [8].

Note that μ_n, μ_p, and therefore V_{OC} are intrinsic characteristics of the electronic structure of the electrode materials [**Figure 1.1.2(b)**] [10,18]. In fact, the electrons participating in the redox reactions of **Equation 1.1.1** arise from the electronic valence states closest to their Fermi level. **Understanding the impact of this process on the electronic structure and its relationship with the deintercalation process is the first major objective of this thesis.**

Since the electrochemical potentials are defined by the derivative of the Gibbs free energy, the shape of the (de)intercalation curve provides information on internal structural and/or phase transformations taking place during these processes [18]. Assuming a constant potential for the negative electrode (e.g. experimentally obtained by using lithium metal), a constant potential V(x) indicates a two-phase region while a linear increase/decrease show a solid solution for the positive electrode material [**Figure 1.1.2(c)**]. Moreover, the presence of internal resistances upon charge and discharge defines overpotentials that modify the cell voltage as schematized in **Figure 1.1.2(c)**. Kinetic processes such as diffusion of lithium ions into the electrodes and electrolyte and charge exchange at the interfaces contribute to the internal resistance.

The theoretical capacity a material can offer Q_{theo} can be estimated by the Faraday law as $Q_{theo} = \frac{zF}{M}$, with M the molar weight, z the number of electrons exchanged by formula unit, and F the Faraday constant. Thus, the quantity of lithium ions exchanged by the material x can be estimated from the measured capacity Q as $x = \frac{Q}{Q_{theo}}$, allowing to deduce the average stoichiometry of the electrode materials (**Equation 1.1.1**). The reversibility of the (de)intercalation process is expressed by the charge/discharge capacity ratio, called coulombic efficiency (CE = Q_{ch}/Q_{dis}) [10]. Although it cannot be exactly 100% due to the second law of thermodynamics, state-of-the-art materials and devices make it possible to achieve high reversibility. However, degradation processes of materials and interfaces cause a progressive decrease of both capacities. To indicate the stability of a battery, the capacity is conventionally indicated after a certain number of cycles with respect to that in the first cycle [10].

1.1.2 Families of positive electrode materials

Although in this thesis we will focus on layered transition metal lamellar oxides ($LiMO_2$), it is insightful to compare them with the others technologically relevant families of positive electrode materials such as spinel structure oxides (LiM_2O_4), and polyoxides with an olivine structure ($LiMXO_4$) [16,21]. All three classes of materials are commercialized for various applications spanning from electric vehicles to portable electronics. Another sub-class of layered oxides, in which the Li concentration is higher than the transition metal (Li-rich oxides, LRO), is also distinguished by its promised electrochemical performance. Despite the Li-rich category is instead still at research level, its fundamental properties are highly relevant in the context of layered oxides, as will be discussed in **Section 1.4.5**.

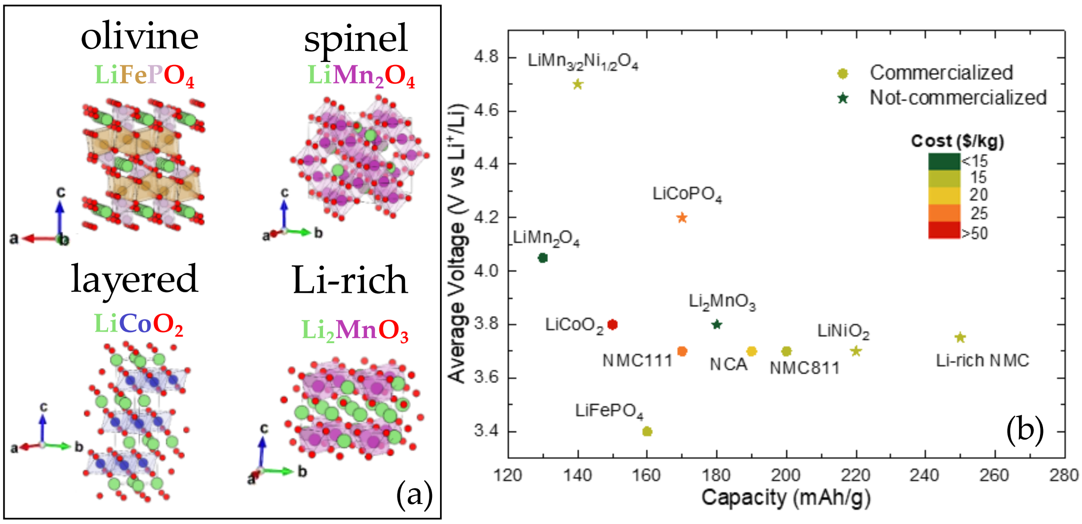

Figure 1.1.3 (a) Crystal structures of representative materials for the main classes of positive electrode materials. (b) Average voltage vs capacity for different families of positive electrode materials. The data shown was taken from ref. [22–24].

The crystalline structures of the reference materials for each category are illustrated in **Figure 1.1.3(a)**. The structural and electronic characteristics of the three families of materials induce different capacities and voltages behaviors, as shown in **Figure 1.1.3(b)** [16], leading to different energy densities and stabilities. Layered transition metal oxides are considered the best candidates for developing batteries that can store more energy [18,22,25]. However, better stability and lower cost of raw materials make the other two categories equally interesting for applications with lower requirements by means of energy density [17,21].

1.2 Crystallography of layered lithium transition metal oxides

The crystal structure of layered transition metal oxides with stoichiometry Li_xMO_2 ($0<x<1$) consists of a face centered cubic (fcc) close-packed oxygen framework in which Li and M ions are encaged in edge-sharing octahedral sites LiO_6/MO_6 and fill alternating layers [18]. Delmas and coworkers introduced a nomenclature for this class of materials based on the coordination site for the intercalant ion (O=octahedral, T=tetrahedral, P=prismatic) followed by the number of MO_2 layers to describe the repeating units [26].

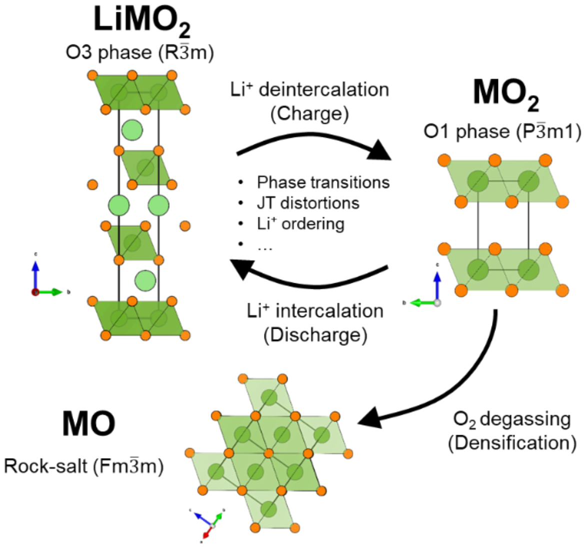

Figure 1.2.1 Schematic of the general structural changes involved during Li^+ (de)intercalation in a layered transition metal oxide.

In the most technologically relevant cases (M = Co, Ni, Mn), fully intercalated $LiMO_2$ and de-intercalated MO_2 typically have the O3 and O1 structures with rhombohedral symmetry (space group R-3m) as shown in **Figure 1.2.1** [18]. First (two-phase) or second (continuous) order phase transitions can be observed depending on the host exact composition. However, the O1 structure is rarely obtained upon electrochemical deintercalation [27]. In fact, the O3 structure tends to persist even upon phase transitions that occur during (de)lithiation.

Phase transitions reversibility is crucial for the stability of the material upon cycling and the kinetics of the (de)intercalation process [18]. While in some cases lithium (de)intercalation is performed with minimal changes for the host structure, large volume changes and/or structural distortions can occur. The latter can lower the symmetry from rhombohedral to monoclinic, as indicated with an apostrophe in Delmas' notation (e.g. O'3).

Beyond the deintercalation line, phase degradation to spinel (LiM_2O_4) and rocksalt ($Li_xM_{1-x}O$) structures can occur by rearrangement of the Li and M ions in the fcc oxygen structure [18,28]. In particular, the layered-to-rocksalt transformation is a critical issue in these compounds as it involves a disordering of Li and M occupations, with typically a larger concentration of the latter followed by oxygen release (densification) [18].

It is possible to synthesize Li-excess oxide with $Li_{1+x}M_{1-x}O_2$ formula, where the additional Li ions substitute the transition metal in its layers and tend to arrange in honeycomb structures [29]. The forehead of these materials is Li_2MnO_3, with an excess of x=1/3. Two structural models were proposed in the literature: $Li_{1+x}M_{1-x}O_2$ was described as either a single solid solution with uniform Li/M mixing or as a heterogeneous solid system consisting of Li_2MO_3 and $LiMO_2$ nano-domains [29]. In any case, two M and four Li ions coordinate oxygen ions involved in the honeycomb arrangements [30,31]. This local coordination has been proposed to explain the redox compensation mechanism for Li-rich oxides.

1.3 Electronic structure of layered transition metal oxides: a dual perspective

The electronic structure of layered transition metal oxides plays a crucial role in the charge and discharge processes of lithium-ion batteries [14,19,32,33]. As Li^+ (de)intercalation can affect the crystal structure of the host layered oxide, the same can happen with the removal and addition of electrons in the electronic structure. Of course, both aspects are intrinsically coupled.

Since the birth of the lithium-ion battery, the redox process during deintercalation has been explained based on well-known concepts of solid-state electrochemistry [10,21,34,35]. These interpretative models are still used to understand the fundamental mechanisms of positive electrode materials including next-generation candidates, which present “unusual” large capacities that cannot be accounted for by classic models that assumes a cation-centered redox process [36]. This called for improvement of the models, that eventually are becoming closer and closer to models developed in the solid-state physics field.

Indeed, the study of the electronic structure of transition metal oxides has been and still is of great importance in solid-state physics [37,38]. Single-electron theoretical models typically fails to describe the electronic structure of these materials, indicating the importance of electron-electron interaction (correlation) effects in these systems, which need to be deal with other approaches, namely many-body methods [38,38–41]. In this framework, a crucial role of oxygen anions was recognized early on [42,43].

Both perspectives are presented below, showing the need for a unification to further advance the fundamental understanding of redox processes in batteries.

1.3.1 The solid-state (electro-)chemistry perspective: from cationic redox potentials to anionic redox processes

The valence band of 3d transition metal oxides is constituted by the O 2p and M 3d bands, whose relative energy position rules the redox compensation mechanism in lithium-ion batteries [10,32,33,44]. The transition metals are coordinated by six oxygen ligands in slightly distorted octahedra. The crystal field of such coordination induces a splitting of degenerate the 3d states into a lower-energy three-fold manifold and a higher-energy two-fold one [18,44]. These bands are referred to by means of their symmetry within the group theory as t_{2g}, comprising the d_{xy}, d_{xz}, and d_{yz} orbitals, and e_g, having d_{3r-z2} and d_{x2-y2} symmetries. Their difference in energy is explained by looking at the local orientation as shown in **Figure 1.3.1(a)**: while the t_{2g} orbitals point towards the space in between the oxygen ligands, the e_g ones are aligned to the M-O bonds and therefore feel larger Coulomb repulsion of the O 2p orbitals.

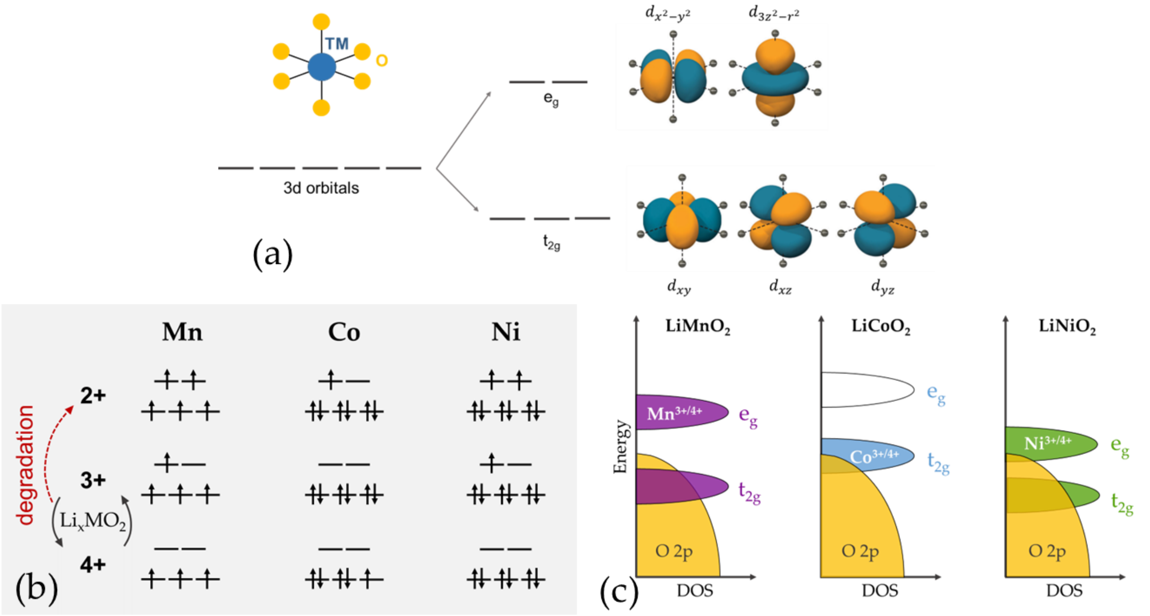

Figure 1.3.1 First insight on the electronic structure of 3d transition metal oxides. (a) Crystal field splitting of the 3d orbitals for a transition metal ion in octahedral coordination. Reprinted from [45]. (b) Electronic configurations for Mn, Co, and Ni at different oxidation states following Hund's rule and crystal field splitting. (c) Qualitative energy diagrams of $LiMO_2$ commonly adopted in the literature. Adapted from ref. [46].

Crystal field and atomic Hund's rule of maximum multiplicity are the first two ingredients for filling the 3d orbitals. High- or low-spin configurations are obtained whether the crystal field splitting (historically defined as 10Dq) is smaller or larger than the electron spin pairing energy [18,44]. **Figure 1.3.1(b)** shows the ionic configurations for Mn, Co, and Ni with 2+, 3+, 4+ oxidation state, which are the most common cases in lithium transition metal oxides for lithium-ion batteries. For late, high valence 3d transition metal oxides (Co and Ni), the octahedral splitting is typically large leading to low spin configuration. Earlier 3d transition metal oxides (Mn) can instead show high-spin local structures since the crystal field splitting is smaller.

Octahedral distortions such as in the R-3m space group (local D_{3d} symmetry) or partial filling of the t_{2g} or e_g bands lead to lower symmetry local coordination. When the e_g states are only partially filled, the energy of the filled orbital is typically lowered with respect to the unoccupied one, breaking the octahedral symmetry. This effect, known as Jahn-Teller distortion, is typically verified in molecular systems as well as early 3d solids such as Mn-based oxides, but is not observed in some relevant cases of solids for Li-ion battery application (e.g. $LiNiO_2$), suggesting a dominant role of other physical effects [28,47,48]. Concerning the D_{3d} symmetry, this induces an additional splitting of the t_{2g} band into a two-fold degenerate band with e_g symmetry and one orbital having a_{1g} symmetry [47]. However, this splitting is smaller than the one related to octahedral coordination.

The energy of the M 3d bands depend on the metal and its oxidation state (i.e. its configuration as shown above) as well as the local environment [21,25]. Qualitatively, anion electronegativity, ligand-metal covalency and the Madelung potential give altogether a so-called inductive-effect that shifts the position of the transition metal redox-active band with respect to the O 2p one [10,19,21,49]. Accordingly, the voltage of the cationic redox couple increases for less covalent M-L bonds (L=ligand) [49,50]. Historically, this was the reason for moving from layered sulfides ($LiTiS_2$) to oxides ($LiCoO_2$), which could deliver higher voltages because of the more ionic character of the host material [35]. In principle, this could lead to the assumption that covalency might play a secondary role in the electronic structure of $LiMO_2$. However, as discussed in the next section, this proved to be wrong for late 3d transition metal oxides.

Based on the above considerations, qualitative diagrams were realized to describe the redox process of conventional materials such as $LiNiO_2$, $LiMnO_2$ and $LiCoO_2$ [**Figure 1.3.1(c)**] [46]. In this picture, the highest occupied band is the one involved in the one-electron redox process associated with delithiation (**Equation 1.1.1**) and is referred to as the $M^{3+/4+}$ cationic redox couple [18,19,46,50]. Upon oxidation, its position decreases in energy (increasing voltage) and can eventually reach the top of the ligand band. According to Goodenough and co-workers, this presents an intrinsic voltage limit, due to a Fermi level pinning to the ligand band: further oxidation affects more and more the oxygen states, leading to structural degradation [10]. This is the case of Li_xCoO_2, whose intrinsic voltage limit is expected at x~0.5, corresponding to a voltage of ~4.2 V vs Li^+/Li [10]. Nevertheless, material optimization by surface engineering and bulk doping are breaking this limit, showing stable cycling up to 4.5-4.6 V vs Li^+/Li at the laboratory level [51–55].

The above concepts can be formalized within molecular orbital theory (MOT), where the overlap of M 3d and (unoccupied) 4sp and O 2p ligands in octahedral configuration leads to the diagram shown in **Figure 1.3.2(a)** [44,56]. In this framework, bonding molecular orbitals have a strong O 2p character while non-bonding ones have stronger M 3d character; the t_{2g} states, due to low overlap with O 2p ligands, are classified as non-bonding states.

Note that, within this theory, the ligand band is assumed to play a spectator role since it simply tunes the redox potential of the metal centers and set its intrinsic limit. However, the study of Li_2MnO_3 and Li-rich derived compounds put this understanding into question. Indeed, the large capacity observed could not be described solely by cationic oxidation: in Li_2MnO_3, for example, Mn is already in its expected highest oxidation state possible (4+) [36,57,58]. MOT diagrams turned useful in rationalizing this aspect: because of the different local coordination, a non-bonding O 2p state is formed [**Figure 1.3.2(b)**] [30,31,56]. Its presence and energy position relative to the M t_{2g} and e_g bands is proposed to explain the redox mechanism of these compounds: whenever it is the first state available for the redox reaction, a so-called anionic redox would take place [57,59]. Although appealing, this explanation is not sufficient to explain all experimental observations related to anionic redox-active systems and the various mechanisms are under discussion in literature [36].

Nevertheless, a clear distinction between "conventional" and "Li-excess" transition metal oxides, based on cationic and anionic redox mechanisms, emerged. In the most recent years, however, the line dividing these systems is progressively vanishing as more and more experimental and theoretical findings are revealing a rather different picture for the electronic structure of "classical" layered oxides, in which the role of oxygen remained hidden beneath the qualitative definitions given above.

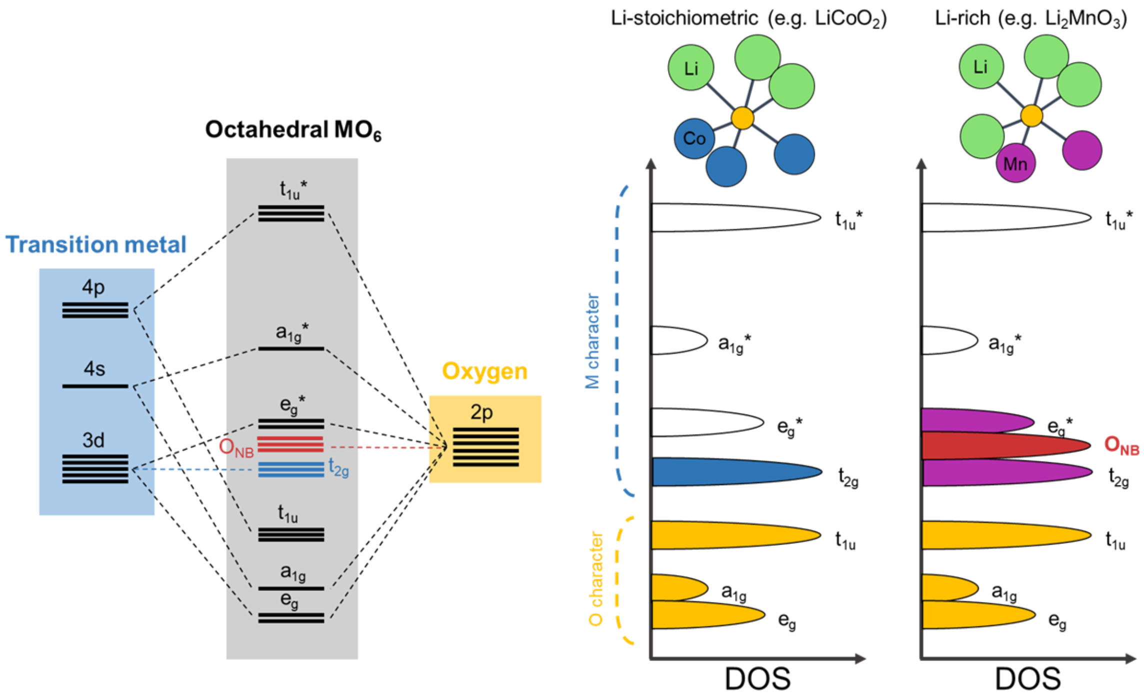

(a) (b)

Figure 1.3.2 Electronic structure of lithium transition metal oxides from molecular orbital theory perspective. (a) Molecular orbital diagram for a MO$_2$ complex in octahedral environment including non-bonding metal t_{2g} and O 2p states. The latter appear only in case of Li-rich stoichiometries. (b) Qualitative density of states derived from the diagram in (a) for LiCoO$_2$ and Li2MnO$_3$. Adapted from ref. [30,44,56,57].

1.3.2 The solid-state physics perspective: electronic correlations and ligand-metal charge transfer

One key aspects regarding the electronic structure of 3d transition metal oxides and implicitly shown in Figure 1.3.1(c) is that the 3d bandwidth is typically very narrow, resembling that of an isolated atomic electronic structure [38,40]. Indeed, the low-energy electronic structure of these compounds can show atomic-like, localized character that is better understood in atom-based rather than electron-based theories [38,40]. Because of the 3d electrons localization, their reciprocal interaction becomes not negligible and cannot be taken into account in single-electron pictures. Such electron-electron interaction is called electronic correlation, and the materials presenting it, among which are the 3d transition metal oxides, are defined as strongly correlated [60].

The impact of electronic correlation becomes clear when considering that a partial occupation of the valence transition metal 3d bands does not necessarily lead to a metallic conductivity, as expected in conventional single-electron theories. This was first observed for NiO: despite the valence band presents a $3d^8$ electronic configuration, a low electron conductivity and a band gap of ~4 eV were instead measured [61,62]. The opening of such gap was explained by the coulomb repulsion between the 3d electrons, which localizes them within each atom in the solid, as described by the many-body Hubbard model Hamiltonian, written below in second quantization formalism and whose physics is sketched in **Figure 1.3.3(a)** [39,60,61,63]:

$$H = t \sum_{(i,j)\sigma} \left(c_{i,\sigma}^{\dagger} c_{j,\sigma} + c_{j,\sigma}^{\dagger} c_{i,\sigma} \right) + U \sum_{i} c_{i,\uparrow}^{\dagger} c_{i,\uparrow} \, c_{i,\downarrow}^{\dagger} c_{i,\downarrow} \qquad \textbf{Equation 1.3.1}$$

Where t is the hopping energy from one site to a neighbor one, U is the Coulomb repulsion, conventionally called Hubbard U, $c^{\dagger}$ and c are creation and annihilation operators, i and j electron indexes, and $\sigma = \uparrow, \downarrow$ the spin index. Note that t is related to the bandwidth D (for example, $t = D/4$ in a semicircular density of state).

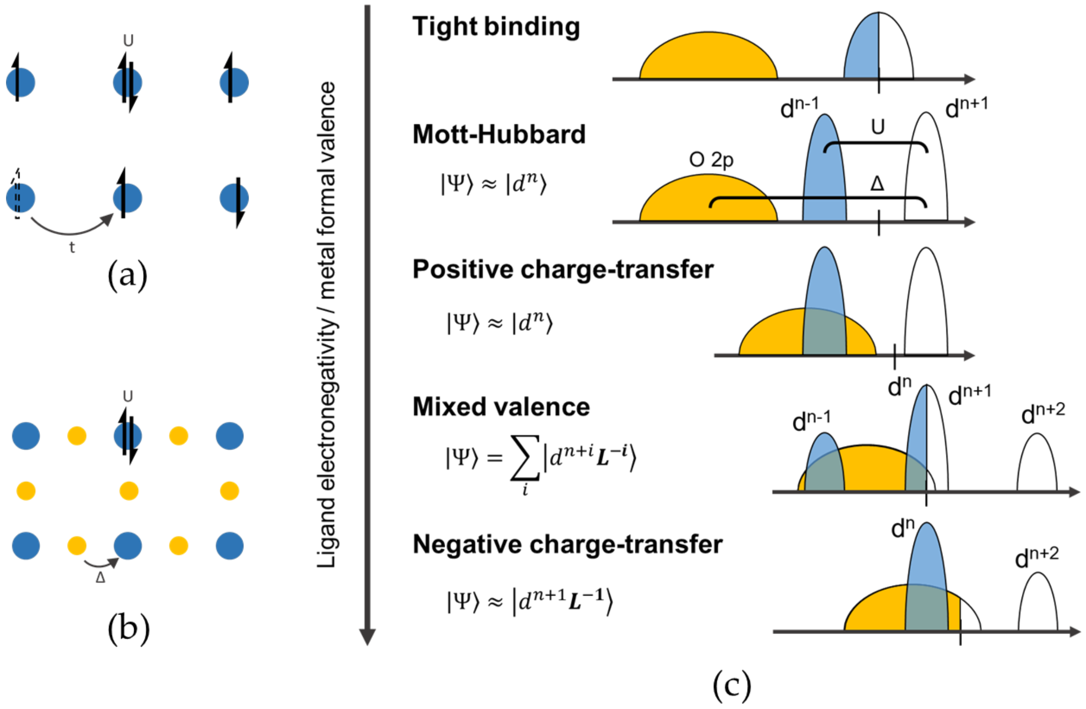

Figure 1.3.3 Schematic picture for (a) the Mott-Hubbard and (b) Anderson models assuming a two-dimensional square lattice. Blue and yellow circles represent metal and ligand atoms, respectively. (c) Low energy electron removal and addition spectra for a generic 3d transition metal compound. No significant metal-ligand covalency is assumed in this approximation. Starting from the upper model, in which 3d electrons are not interacting hence a partial filling leads to band metal, turning on the 3d electronic correlations splits the 3d band into upper and bottom Hubbard bands, whose position with respect to the O 2p band depends on the Δ/U ratio. Adapted from ref. [42].

In the Mott-Hubbard model, materials properties are defined by the competition between itineracy and localization of the 3d electrons i.e. kinetic and coulombic energy: the system behaves as a metal for U/D<<1 but becomes an insulator for U/D>>1 [63]. In the former case, the Hamiltonian can eventually simplify in a tight-binding model where electrons are completely itinerant. In the second case, the materials are called Mott-Hubbard insulators to differentiate with classic band insulators. The resulting bands are referred to as upper and lower Hubbard bands.

Further spectroscopic investigations of transition metal oxides called for the inclusion of the O 2p band in the picture given the Mott-Hubbard physics, leading to the Anderson model Hamiltonian as schematized in **Figure 1.3.3(b)** [42,60]:

$$H = \sum_{i\sigma} \varepsilon_{i\sigma}^{d} d_{i\sigma}^{\dagger} d_{i\sigma} + \sum_{i\sigma} \varepsilon_{i\sigma}^{p} p_{i\sigma}^{\dagger} p_{i\sigma} + \\ \sum_{(ij)\sigma} V_{ij} \left(d_{i,\sigma}^{\dagger} p_{j,\sigma} + d_{i,\sigma}^{\dagger} p_{j,\sigma} \right) + U \sum_{ijkl} d_{i,\uparrow}^{\dagger} d_{j,\uparrow} d_{k,\downarrow}^{\dagger} d_{l,\downarrow} \qquad \textbf{Equation 1.3.2}$$

Where d and p indicate M 3d and O 2p orbitals and V is the hybridization strength between the two sets of orbitals. While the Hubbard U is the energy cost for an electron transfer between two metal sites $d_i^n d_j^n \longrightarrow d_i^{n+1} d_j^{n-1}$, a charge transfer energy Δ is associated with charge fluctuations of type $d_i^n \longrightarrow d_i^{n+1}\boldsymbol{L}$, with $\boldsymbol{L}$ a ligand hole [42,43]. Accordingly, the competition between U and Δ describes different regimes (and band gap characters) for the transition metal oxides, as described by the Zaanen-Sawatzky-Allen (ZSA) theory [43].

In the ZSA theory, the properties of the solid are studied by considering an ionic cluster model where covalency, electronic correlations, and charge transfer are taken into account within a configuration interaction approach [43,64,65]. The many-body wavefunction of the system is defined as linear combination of different configurations [42,43,64–66]:

$$\Psi = \left| d^n \right\rangle + \left| d^{n+1} \boldsymbol{L}^{-1} \right\rangle + \left| d^{n+2} \boldsymbol{L}^{-2} \right\rangle + \cdots \qquad \textbf{Equation 1.3.3}$$

The as-defined model Hamiltonian can then be solved by exact diagonalization methods (see **Section 2.2.2** for more details).

Within the ZSA theory, four different regimes for the transition metal oxides are found depending on the Δ/U ratio [**Figure 1.3.3(c)**] [42]. The first two regimes, namely the Mott-Hubbard insulator (U<Δ), the charge transfer insulator (U>Δ) have been studied since the nineties for many compounds. With decreasing Δ, however, two other regimes were recognized later on. The valence mixed or intermediate state corresponds to the case in which the upper Hubbard band crossed the O 2p band, leading to large covalency between p-d and a non-trivial electronic structure, with large fluctuation between different electronic configurations. Finally, in the negative charge transfer region ($\Delta < 0$), the O 2p is self-doped and the transition metal ions do not take the formal oxidation state. Since this will be a recurrent concept in this thesis, the formal oxidation state will be indicated by roman notation (e.g. III) to make a distinction between this concept and the actual ionic charge (e.g. 3+).

Small and/or negative charge transfer are typical for late high-valence 3d transition metal ions because of their larger electronegativity [42]. This includes Co and Ni in their highest oxidation states and therefore can potentially apply to battery-related materials. Nevertheless, the electronic structures shown in [**Figure 1.3.3(c)**] do not correspond to those presented in the previous section [**Figure 1.3.1(c)**] and traditionally used to interpret the redox compensation mechanism in the Li-ion battery field. As will be discussed in the next section, this disagreement reflects the two different scientific pathways that can be distinguished in the last decades of research aimed to clarify the electronic structure of layered transition metal oxides in the framework of Li-ion batteries.

1.4 The charge compensation mechanism: retrospective and outlook

In this section, the buildup of knowledge on the charge compensation mechanism in layered transition metal oxides within the past four decades will be summarized. A schematized perspective of it is proposed in **Figure 1.4.1**, distinguishing the most relevant materials (or groups): $LiCoO_2$, $LiNiO_2$, NMC, and Li-rich NMCs.

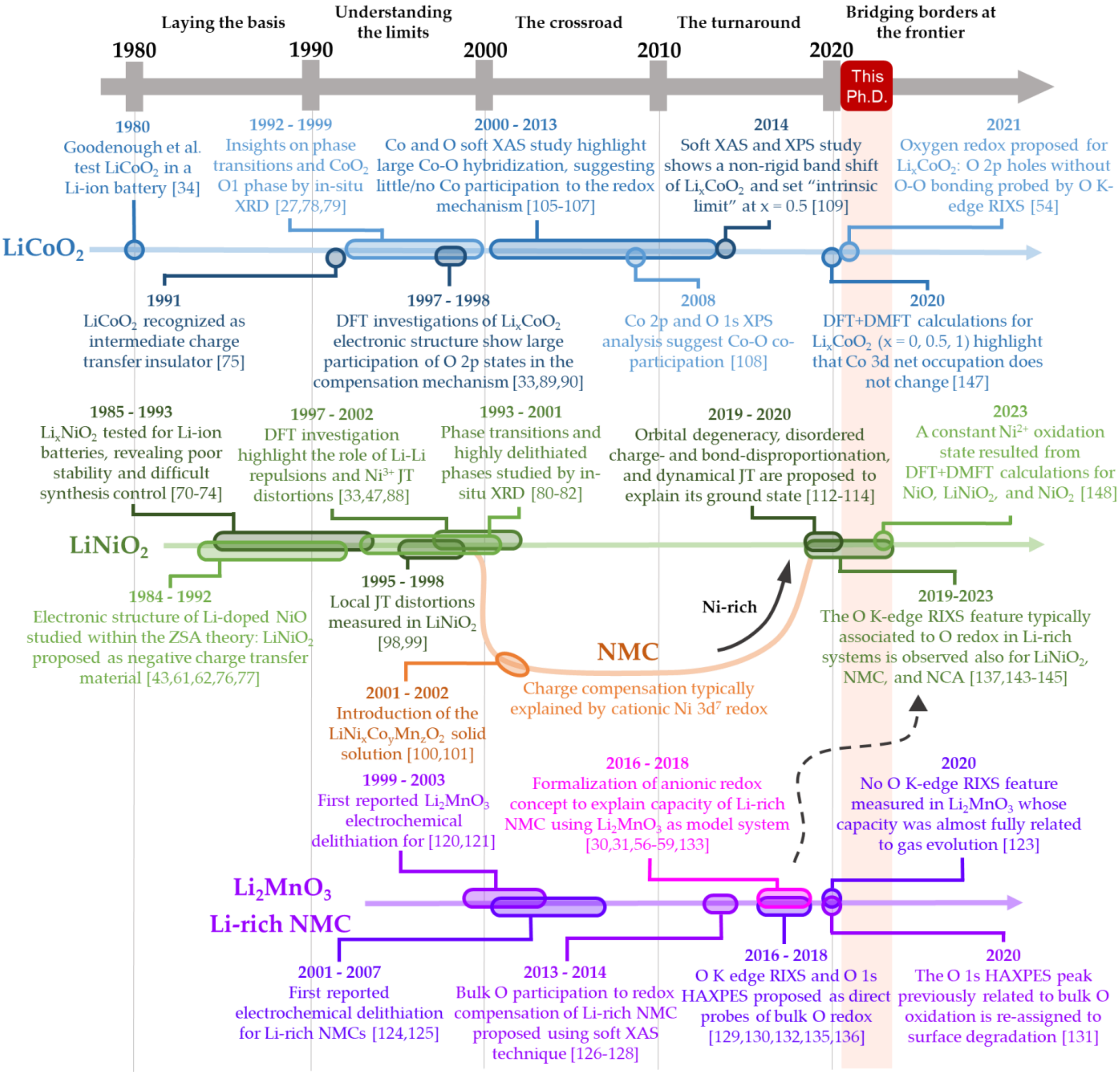

1980
Goodenough et al. test $LiCoO_2$ in a Li-ion battery [34]

1992 - 1999
Insights on phase transitions and CoO_2 O1 phase by in-situ XRD [27,78,79]

2000 - 2013
Co and O soft XAS study highlight large Co-O hybridization, suggesting little/no Co participation to the redox mechanism [105-107]

2014
Soft XAS and XPS study shows a non-rigid band shift of Li_xCoO_2 and set "intrinsic limit" at $x = 0.5$ [109]

2021
Oxygen redox proposed for Li_xCoO_2: O 2p holes without O-O bonding probed by O K-edge RIXS [54]

1991
$LiCoO_2$ recognized as intermediate charge transfer insulator [75]

1997 - 1998
DFT investigations of Li_xCoO_2 electronic structure show large participation of O 2p states in the compensation mechanism [33,89,90]

2008
Co 2p and O 1s XPS analysis suggest Co-O co-participation [108]

2020
DFT+DMFT calculations for Li_xCoO_2 ($x = 0, 0.5, 1$) highlight that Co 3d net occupation does not change [147]

1985 - 1993
Li_xNiO_2 tested for Li-ion batteries, revealing poor stability and difficult synthesis control [70-74]

1997 - 2002
DFT investigation highlight the role of Li-Li repulsions and Ni^{3+} JT distortions [33,47,88]

1993 - 2001
Phase transitions and highly delithiated phases studied by in-situ XRD [80-82]

2019 - 2020
Orbital degeneracy, disordered charge- and bond-disproportionation, and dynamical JT are proposed to explain its ground state [112-114]

2023
A constant Ni^{2+} oxidation state resulted from DFT+DMFT calculations for NiO, $LiNiO_2$, and NiO_2 [148]

1984 - 1992
Electronic structure of Li-doped NiO studied within the ZSA theory: $LiNiO_2$ proposed as negative charge transfer material [43,61,62,76,77]

1995 - 1998
Local JT distortions measured in $LiNiO_2$ [98,99]

2019-2023
The O K-edge RIXS feature typically associated to O redox in Li-rich systems is observed also for $LiNiO_2$, NMC, and NCA [137,143-145]

2001 - 2002
Introduction of the $LiNi_xCo_yMn_zO_2$ solid solution [100,101]

Charge compensation typically explained by cationic Ni $3d^7$ redox

1999 - 2003
First reported Li_2MnO_3 electrochemical delithiation for [120,121]

2016 - 2018
Formalization of anionic redox concept to explain capacity of Li-rich NMC using Li_2MnO_3 as model system [30,31,56-59,133]

2020
No O K-edge RIXS feature measured in Li_2MnO_3 whose capacity was almost fully related to gas evolution [123]

2001 - 2007
First reported electrochemical delithiation for Li-rich NMCs [124,125]

2013 - 2014
Bulk O participation to redox compensation of Li-rich NMC proposed using soft XAS technique [126-128]

2016 - 2018
O K edge RIXS and O 1s HAXPES proposed as direct probes of bulk O redox [129,130,132,135,136]

2020
The O 1s HAXPES peak previously related to bulk O oxidation is re-assigned to surface degradation [131]

Figure 1.4.1 Investigation of the charge compensation process of layered transition metal oxides in the past decades.

1.4.1 “Laying the basis”: first applications of $LiCoO_2$ and $LiNiO_2$ in Li-ion cells and insights from the ZSA theory (1980-1990)

From a background of fundamental research on the magnetic properties of 3d transition metal oxides, Goodenough and coworkers initiated the study of layered 3d transition metal oxides for Li-ion battery applications in 1980, when he reported the first cycling data of Li_xCoO_2 [34]. The voltage of this compound was nearly double of its forehead Li_xTiS_2, whose intercalation chemistry was studied by Whittingham et al. [67]. This improvement led to the commercialization of the first Li-ion battery in 1991, after the crucial substitution of Li metal with graphite as carbon-based negative electrode active material by Yoshino et al., who fabricated the first commercial-type Li-ion cell [68]. For their key contributions to the development of this technology and its relevance in nowadays-human society, the three researchers were awarded the Nobel Prize in 2019 [69].

Soon after the discovery of Li_xCoO_2, other parent compounds were tested for their electrochemical performance. In particular, Li_xNiO_2 was highlighted as possible candidate, although Li/Ni inter-site disordering during both synthesis and electrochemical deintercalation, leading to low stability upon cycling, prevented the commercialization of $LiNiO_2$-based batteries [70–74]. Conventionally, the redox compensation mechanism was related to the redox activity of low-spin $Co^{III/IV}$ and $Ni^{III/IV}$ redox couples based on crystallography and magnetic properties of these compounds [73].

These pioneering studies were concomitant with the development of the ZSA theory and the finding of NiO as a charge transfer insulator [43,62]. Soon after, Sawatzky’s group studied the electronic properties of Li-doped CoO and NiO [75–77]. Their interest on Li substitution was not due to Li-ion battery application but on its hole-doping effect as criteria to classify the material in the ZSA diagram. By combining X-ray Absorption spectroscopy (XAS), Bremsstrahlung isochromatic spectroscopy (BIS) and XPS with cluster model theory calculations, they found that $Li_xCo_{1-x}O$ and $Li_xNi_{1-x}O$ ($0<x<0.5$) behave as charge transfer insulators [75–77]. Note that $x=0.5$ gives the layered rhombohedral structure used in Li-ion battery, as confirmed by X-ray diffraction (XRD) characterization [75,76].

More specifically, a large *p-d* covalency was deduced by studying the O K-edge XAS pre-peak region of $Li_xNi_{1-x}O$ [**Figure 1.4.2(a)**]. The peak at 532 eV, related to Ni 3d hybridized with O 2p states, sharply decreased upon Li substitution, while a lower-energy peak appeared at 528.5 eV, suggesting that the hole compensating Li substitution had oxygen character [76,77]. The stabilization of the localized oxygen role was explained by O 2p antiferromagnetic exchange interaction, argued to be stronger than Ni-Ni super-exchange [77]. This would imply that $LiNiO_2$ lies in the negative charge transfer regime where the $|d^8\boldsymbol{L}\rangle$ state has a lower energy than the nominal $|d^7\rangle$ [**Figure 1.4.2(b)**]. A chemical perspective of this was given by Goodenough, who discussed this behavior as a shift of the Ni^{3+}-O^{2-} = Ni^{2+}-O^{-} equilibrium to the right side [48]. However, no direct comparison between experiment and theoretical calculations was brought to support the latter conclusion.

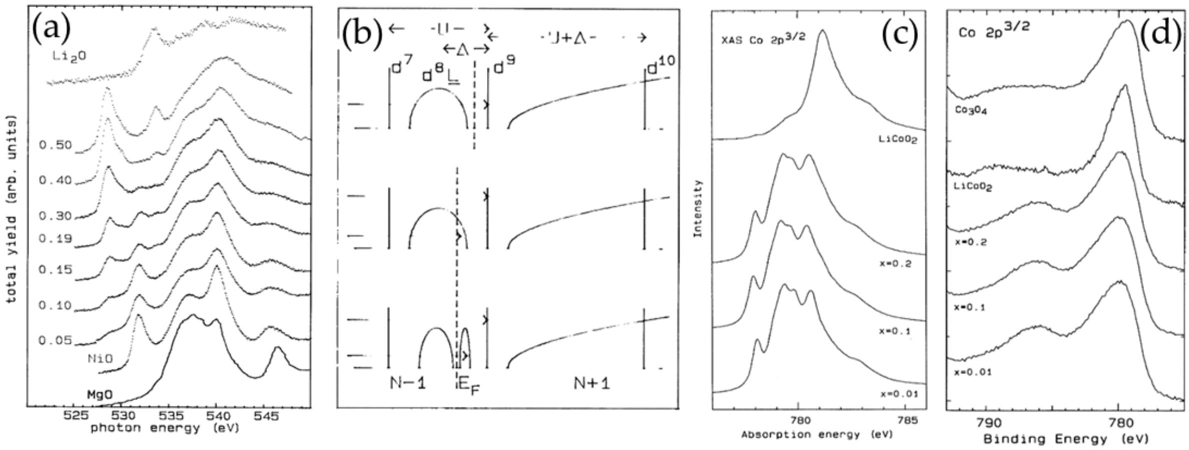

Figure 1.4.2 (a) O K-edge spectra for a series of $Li_xNi_{1-x}O$ samples, where x is indicated on the left side. For comparison, the spectra for reference MgO, NiO, and Li_2O samples are also shown. Reprinted from ref. [77] (b) Qualitative electron addition and removal spectra for (top) a charge transfer insulator e.g. NiO, modified by Li doping assuming either (middle) a rigid-band model or (bottom) hole localization on the O 2p states around lithium. Reprinted from ref. [77]. (c) Co L-edge XAS and (d) Co 2p XPS spectra for $Li_xCo_{1-x}O$ doped samples and $LiCoO_2$. Reprinted from ref. [75].

With an analogous methodology, CoO was classified as intermediate between Mott-Hubbard and charge transfer insulator [75]. With low Li^+ doping (x<0.2), the local electronic structure of Co did not change significantly as measured by Co L edge XAS and Co 2p XPS, indicating hole-doping of the O 2p band as in the case of the parent nickelate compounds. However, larger lithium substitution up to $LiCoO_2$ does oxidize high-spin Co^{II} ($|t_{2g}^5 e_g^2\rangle$, S=3/2) to low-spin Co^{III} ($|t_{2g}^6 e_g^0\rangle$, S=0), as deduced by the changes in the core-level spectra [**Figure 1.4.2(c,d)**]. Eventually, $LiCoO_2$ also falls in the intermediate region and is characterized by both large p-d hybridization (O K edge XAS) and 3d electronic correlations as deduced by the valence band satellite structure [75].

These results draw a different perspective of the electronic structure of the lithiated compounds than that assumed in the contemporary electrochemical studies. The relevant hole doping in the O 2p band of $LiCoO_2$ and $LiNiO_2$ sets a different starting point for the charge compensation upon Li deintercalation. However, delithiated compounds were not studied by Sawatzky and coauthors, and the strongly parameter-dependent model calculations left space for improvements on the theoretical side. Moreover, due to the well-known tendency to Li/Ni disorder in $Li_xNi_{1-x}O$ [71], the spectroscopy characterization needed further investigation.

1.4.2 "Understanding the limits": insights on end-member structures phases by XRD and DFT (1990-2000)

In the nineties, the development of the *in-situ* XRD technique allowed characterizing the crystal structure changes of $LiCoO_2$, $LiNiO_2$, and $LiCo_zNi_{1-z}O_2$ inside electrochemical cells. These studies clarified the nature of some phase transitions, showing the impact of monoclinic distortions and Li ordering as observed for example for $Li_{0.5}CoO_2$ [78]. A particular attention was given to the deeply delithiated phases of Li_xCoO_2 and Li_xNiO_2 ($x<0.5$ and 0.2, respectively). A strong shrinking of the MO_2 interlayer distance and a tendence of transition metal displacement filling the empty Li sites were observed for these phases [**Figure 1.4.3(a,b)**] [27,79–82]. Such behavior was related to the low cycle stability of the highly delithiated layered oxides.

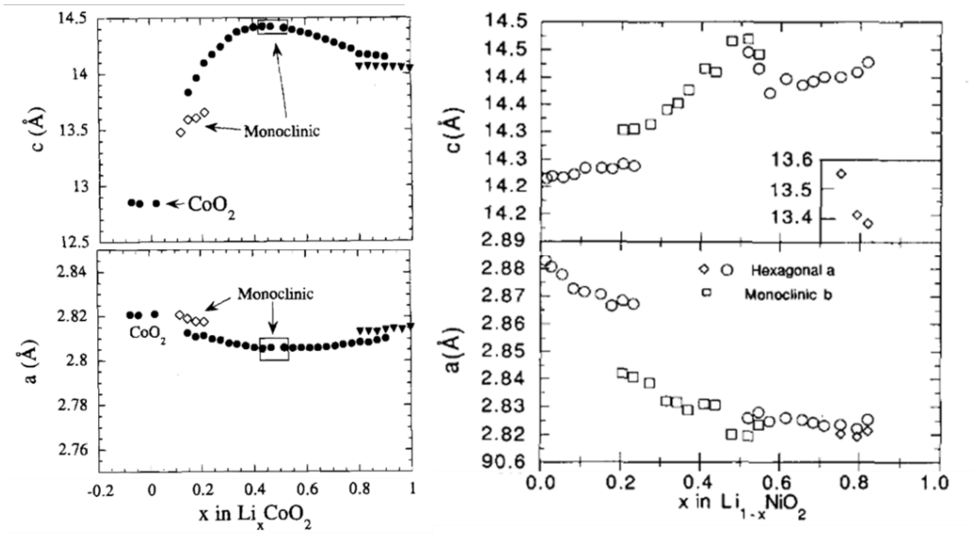

(a) (b)

Figure 1.4.3 Evolution of the cell parameters as function of Li stoichiometry in (a) Li_xCoO_2 and (b) Li_xNiO_2 materials as resulted by *in-situ* XRD. Reprinted from ref. [79,82]. The data find good agreement with more recent publications [83–86].

The end-member $Ni_{1-x}Co_xO_2$ metastable O1 phases were prepared and characterized by Tarascon's group by *in-situ* XRD, highlighting a shrinking of the O-O distance [27]. This was explained by assuming a partial role of oxygen in the deintercalation process. Notably, this behavior was not interpreted in the framework of the ZSA theory but by recalling J. Rouxel's studies on the redox chemistry of transition metal chalcogenides [87].

These insights were supported by *ab initio* Density Function Theory (DFT) studies for both Li_xCoO_2 and Li_xNiO_2 by Ceder et al. [33,88,89]. By combining DFT calculations with thermodynamic considerations for the Li-ion cell system and cluster expansion methods to deal with Li ion disordered in partially delithiated structures, the authors presented a systematic approach to predict average voltages, deintercalation curves, and phase diagrams for the layered systems. The MOT interpretation of the electronic structure (**Section 1.3.1**) found fair agreement with the band structures presented for Li_xCoO_2 [33]. However, the analysis of the contribution of metal 3d and ligand 2p orbitals to the average voltage revealed an increasing role in the charge compensation by oxygen going from Sc to Zn along the row of 3d transition metals [**Figure 1.4.4(a)**] [33].

This was highlighted for the Li_xCoO_2 system by observing the differential electron density maps between decreasingly delithiated structures, which showed larger differences located around oxygen [89]. Wolverton and Zunger gave a similar result, shown in **Figure 1.4.4(b)**. They observed that the Co 3d occupation almost did not change from $LiCoO_2$ to CoO_2 [90]. Such behavior was explained by a "self-regulating response" of the system driven by charge imbalance minimization, similar to what observed in previous studies on transition metal impurities embedded in semiconductor matrixes [90]. This tendency of Co 3d to maintain a constant local charge regardless of the external conditions was later generalized to the transition metal family, disputing the conventional idea that oxidation states are directly linked to ionic charges [91,92]. However, such generalization was not widely accepted and the debate about this issue continues [93–97]. Despite the above great advancements, DFT-based calculations based on local density approximation (LDA) could not account completely for the electronic correlations effect. In particular, the metal-insulator transition observed for 0.75<x<0.94 for Li_xCoO_2 by Delmas et al. could not be predicted by Ceder's studies [89].

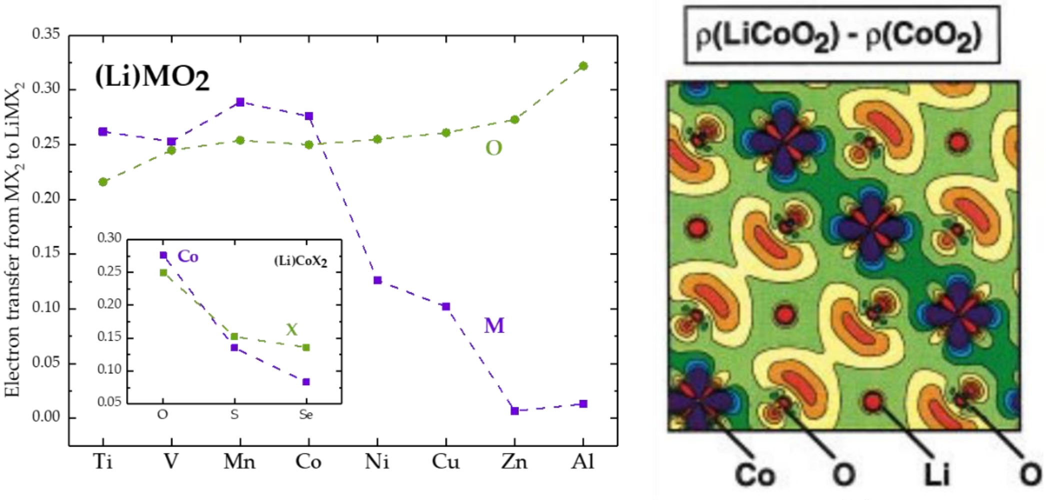

(a) (b)

Figure 1.4.4 Insights on the charge compensation mechanism by LDA calculations. (a) Electron transfer of metal M and ligand X from MX_2 to $LiMX_2$ as a function of the 3d transition metal. The inset shows the trend by increasing ligand electronegativity with constant Co ion. Data taken from ref. [33]. (b) Differential electron density plot from $LiCoO_2$ to CoO_2 calculated by Wolverton and Zunger in ref. [90]. Red and blue regions show regions with electron depletion and increase, respectively.

The Li_xNiO_2 system was harder to study within DFT methods. In principle, $LiNiO_2$ is a Jahn-Teller active system due to the Ni^{III} formal electronic structure ($t_{2g}^6e_g^1$). However, the long-range order measured by XRD matched with the rhombohedral O3 structure of $LiCoO_2$, although local distortions were confirmed by Extended X-ray Absorption Fine Structure (EXAFS) and neutron diffraction investigations [47,98,99]. Besides, standard LDA calculations for $LiNiO_2$ lead to a metallic ground state in contrast to the experimentally verified semiconductor's gap [33]. Moreover, the $LiNiO_2$ system was known to be easily affected by Li-off stoichiometry and Li/Ni intermixing defects, which can easily alter the characterized material's properties depending on z in $Li_{1-z}Ni_{1+z}O_2$. Therefore, proper and reproducible comparisons between experiment and theory were hard to obtain. Because of this, the findings on Li_xCoO_2 charge compensation mechanism were not directly transferred to Li_xNiO_2. Jahn-Teller distortions led by Li^+ inter- and intra-layer repulsion and consequent $Ni^{III/IV}$ charge ordering, were instead considered to dominate in the electronic structure of this system [88].

1.4.3 "The crossroads": seeking better electrochemical performance with NMC while carrying on fundamental investigations for $LiCoO_2$ (2000-2010)

The low structural stability of $LiNiO_2$ was overcame by bulk doping the structure with other 3d transition metals, leading to $LiNi_xMn_yCo_zO_2$ (NMC) solid solution with x+y+z=1, introduced by Dahn's group in 2001 [100,101]. The superior electrochemical performance of substituted oxides supported the spreading of this technology, essential to power portable electronics first and electric vehicles afterwards, and led the intense research in the Li-ion battery field that continues nowadays [25]. In fact, the synergy between each ion was found to result in materials with properties that are overall better than the simple sum of each [18].

Along this research direction, the charge compensation mechanism was kept being attributed to the cation redox couple as initially proposed, formalizing the concepts presented in Section 1.3.1 in numerous review articles [10,18,19,49,50]. In this framework, although the role of each transition metal in NMC was not understood from a fundamental point of view, systematic studies clarified their impact on the electrochemical performance [18]. Al and Mn are conventionally assumed to be redox-inactive upon Li^+ (de)intercalation [18]. A stabilizing role was however related to these ions, since larger concentrations of Mn or Al in the NMC or NCA structures typically improve cycle life and thermal stability. Manganese in particular is often considered to reduce Ni from III to II because of the largest oxidation potential of the $Mn^{III/IV}$ couple to the $Ni^{II/III}$ and $Ni^{III/IV}$ ones [18,50]. Therefore, it is believed that the Ni^{II}/Ni^{III} ratio could depend on the Mn concentration in NMC [50]. Ni and Co are typically considered redox active. Due to different redox potentials, a larger Ni concentration leads to an increase in battery specific capacity (with constant upper cut-off voltage), while larger concentrations of Co allows to increase the average voltage [18,50,102]. Since the electrolyte stability is improved at lower voltages and because of the high cost and humanitarian concerns of Co extraction, its reduction is overall favored from socio-economic point of views [102]. Some authors even questioned the actual need of cobalt in modern positive electrode materials, although at the moment small concentrations are still widely used in the state-of-art Ni-rich NMC materials (Ni concentration > 80 %) [55,103,104].

Meanwhile, the seminal works by Ceder and Sawatzky inspired several experimental investigations to understand the predicted fundamental oxygen-driven charge compensation mechanism. Note that most studies focused on $LiCoO_2$, probably because it was the most stable and best-known system that perfectly fitted the role of model system for the whole family of layered 3d transition metal oxides.

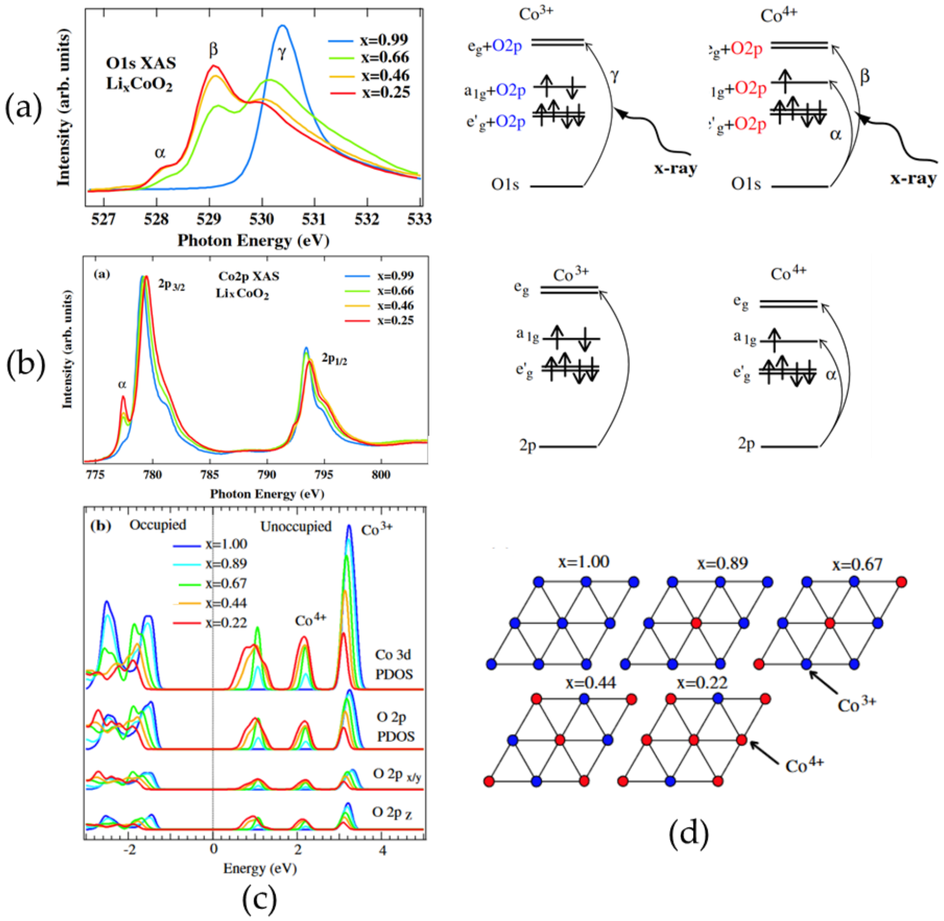

Figure 1.4.5 Insights on the charge compensation mechanism by soft XAS analysis. (a) O K-edge and (b) Co L-edge XAS spectra for a series of Li_xCoO_2. The diagrams on the right side show proposed transition explaining the main features of the spectra. (c) Hartree-Fock calculation for the total and partial density of states using a 2D triangular lattice model in which the Co^{3+}/Co^{4+} ratio was varied to mimic the deintercalation. The corresponding models are shown in figure (d). Reprinted from. [105].

In agreement with the above theoretical findings, O K-edge XAS revealed a significant evolution of the O local electronic structure, in contrast with minor changes observed by Co L-edge XAS [**Figure 1.4.5(a,b)**] [105–107]. Mizokawa et al. rationalized XAS spectral features using Hartree-Fock simulations for mixtures of Co^{III}/Co^{IV} ions in the triangular CoO$_2$ lattice (i.e. within the D$_{3d}$ crystal field), highlighting a larger concentration of O 2p holes around Co^{4+}, assumed in its formal $e'^{4}_{g}a_{1g}^{2}e_{g}^{0}$ configuration [**Figure 1.4.5(c,d)**] [105]. Note the charge-separated Co^{III}/Co^{IV} model used by Mizokawa et al. does not agree with the previous DFT studies (e.g. the "self-regulating response" mechanism) in which Co local charge would not change so drastically upon deintercalation.

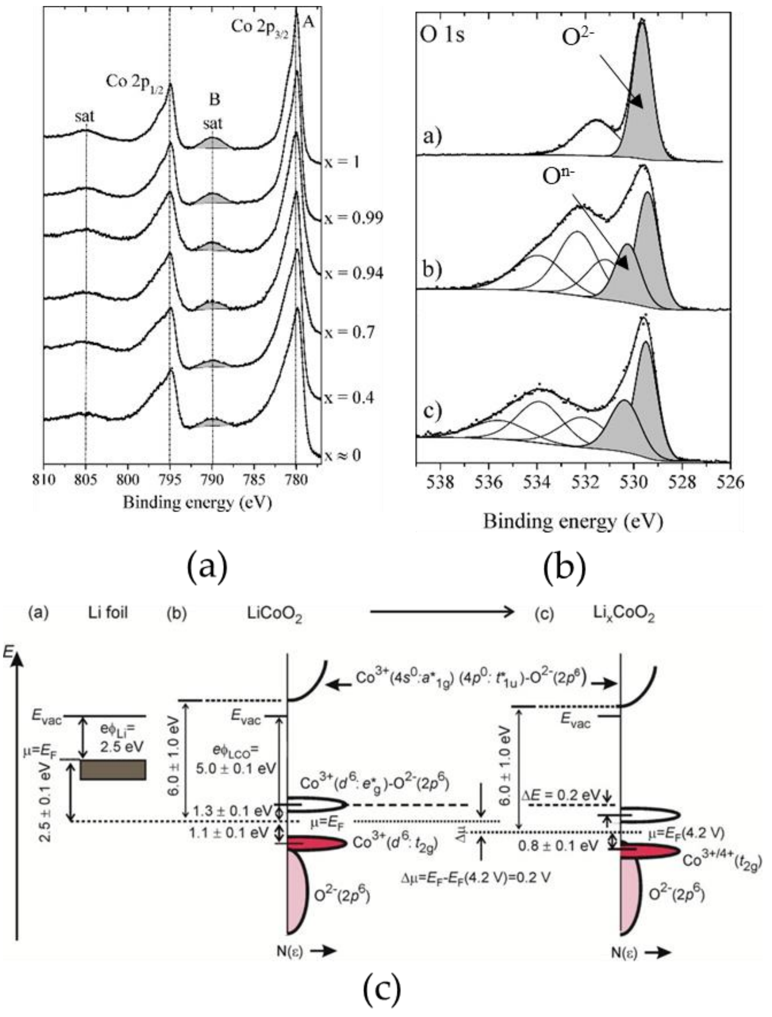

Figure 1.4.6 Insights on the charge compensation mechanism by soft XPS analysis. (a) Co 2p XPS spectra for progressively de-lithiated Li$_x$CoO$_2$ samples. (b) O 1s XPS spectra for pristine LiCoO$_2$, CoO$_2$, and the same CoO$_2$ samples but with exaggerated charge neutralization to shift the surface insulating components indicated by empty peaks. The grey peaks were related to oxygen ions in the Li$_x$CoO$_2$ lattice at two different oxidation states. Reprinted from ref. [108]. (c) Energy diagram obtained by combining soft XAS and XPS in-situ analysis on LiCoO$_2$ and Li$_{0.5}$CoO$_2$ thin films, showing the non-rigid band shift effect upon de-lithiation. Reprinted from ref. [109].

Dahéron et al. gave a different perspective by using core-level XPS [108]. The authors interpreted the decrease of the charge-transfer satellite peak of Co 2p and Co 3p XPS spectra as signature of partial oxidation of Co^{III}, although no characteristic feature could be referred to Co^{IV} [**Figure 1.4.6(a)**]. A similar result was obtained by Ikedo et al., whose Hartree-Fock simulations for the Co 2p peaks of $LiCoO_2$ confirmed the charge transfer and strongly covalent nature of the Li_xCoO_2 system [110]. However, Dahéron et al. observed also an intensity increase in the O 1s XPS spectra at higher-binding energies to the peak related to lattice anions, which was referred to partial oxygen oxidation process [**Figure 1.4.6(b)**] [108]. Therefore, they concluded that the electron transfer mechanism of Li_xCoO_2 is due to a co-participation of both Co and O.

A combination of *in-situ* UPS, XPS and XAS for a Li_xCoO_2 thin film by Jaegermann et al. pushed forward this interpretation [109]. By deriving the energy diagram models via experimental study, they proposed that cations (Co^{3+}/Co^{4+}) and anions (O^{2-}/O^{-}) contribute at two different stages of delithiation [**Figure 1.4.6(c)**]. The transition point was identified in x~0.5, where the Co 3d band would be pinned to the O 2p one, imposing an intrinsic voltage limit for the electrochemical stability of Li_xCoO_2. This interpretation is in good agreement with that proposed by Goodenough [10], although it does not account for the actual stability of $LiCoO_2$, that can be cycled up to 4.5-4.6 V [51–53,55,111]. However, the proposed energy diagrams did not account for electronic correlations or *p-d* hybridization, and the interpretation of core level Co 2p XPS was still based on cluster model assumptions, without supporting theoretical XPS simulation carried out for delithiated Li_xCoO_2 compounds. Finally, as for the XPS study by Dahéron et al., the limited depth probed by soft XPS was not considered, although it was recognized that surface degradation may play a major role upon delithiation.

In summary, while oxygen participation to the redox compensation mechanism in Li_xCoO_2 could be confirmed by several experiments, the nature of the co-participating cobalt and the differences between surface and bulk electronic structures (hence the actual mechanism) is still unclear. For this reason, this system continues to intrigue both theoreticians and experimentalists.

1.4.4 “The turnaround”: reignited interest for $LiNiO_2$ (2010-2020)

Since the discovery of NMC and NCA, the Li_xNiO_2 system was less investigated by fundamental point of view in contrast to the constant advancement for the Li_xCoO_2 system [28]. However, the need of Li-ion batteries with larger energy densities led to development of Ni-rich NMC and NCA materials that eventually put again Li_xNiO_2 on the hotspot as the end-member for these solid solutions [28,102]. Clarifying its microscopic properties is considered a crucial fundamental challenge to control and improve the electrochemical performance of Ni-rich materials.

In 2019, three breakthrough studies on $LiNiO_2$ ground state were published [112–114]. Based on previous findings on rare-earth Ni $3d^7$ nickelates studied in the high-temperature superconductivity field [115], Sawatzky's group proposed that self-doped oxygen holes in $LiNiO_2$ are disordered in a glassy electronic structure [112]. The random distribution of holes in the O 2p ligands would be favored to the Jahn-Teller distortion by an entropy gain due to the large number of nearly degenerate states found by DFT calculations, some of which including bond and charge disproportionation. While long-range neutron diffraction data could be fit even with undistorted rhombohedral structure, the inclusion of bond disproportionation significantly improved the description of short-range structural data [**Figure 1.4.7(a,b)**]. The authors proposed that electronic disorder would arise considering the many ground state structural models found at similar energy at DFT+U level [**Figure 1.4.7(c,d)**]. Therefore, the $LiNiO_2$ structure was described as random arrangement of a few NiO_6 building blocks, characterized by different number of O holes, cluster size, and (when active) Jahn-Teller distortion orientations [**Figure 1.4.7(e-g)**].

Sicolo et al. gave a different explanation: in their *ab-initio* molecular dynamics (AIMD) study, the JT distortions were observed to dynamically change orientation without a cooperative effect that order them in the long range [**Figure 1.4.7(h)**]. In this study, the authors did find Ni ions in the conventional trivalent state with no oxygen holes. However, a recent AIMD investigation[1] for the same system but based on different DFT approximation for the exchange-correlation functional suggests a radically different conclusion, where it is the bond- and charge-disproportionation to be dynamically changing [116].

In general, it seems that DFT+U investigations of $LiNiO_2$ electronic structure are significantly sensitive to the approximation employed for treating the electronic correlations. To overcome this issue, Korotin et al. studied the dynamical nature of $LiNiO_2$ electronic structure by DFT plus dynamical mean field theory (DFT+DMFT), the state-of-art many-body technique for studying weakly and strongly correlated systems [113]. With this method, a paraorbital ground state was obtained i.e. even when in $3d^7$ electronic configurations, the d_{z2} and d_{x2-y2} orbitals are equally filled, lifting off the JT distortion. In agreement with the early-proposed negative charge transfer picture, the occupancy of $|d^7\rangle$ and $|d^8\boldsymbol{L}^{-1}\rangle$ $3d^8$ were found to be nearly equal.

---

[1] Not proofed at the time this paragraph is written.

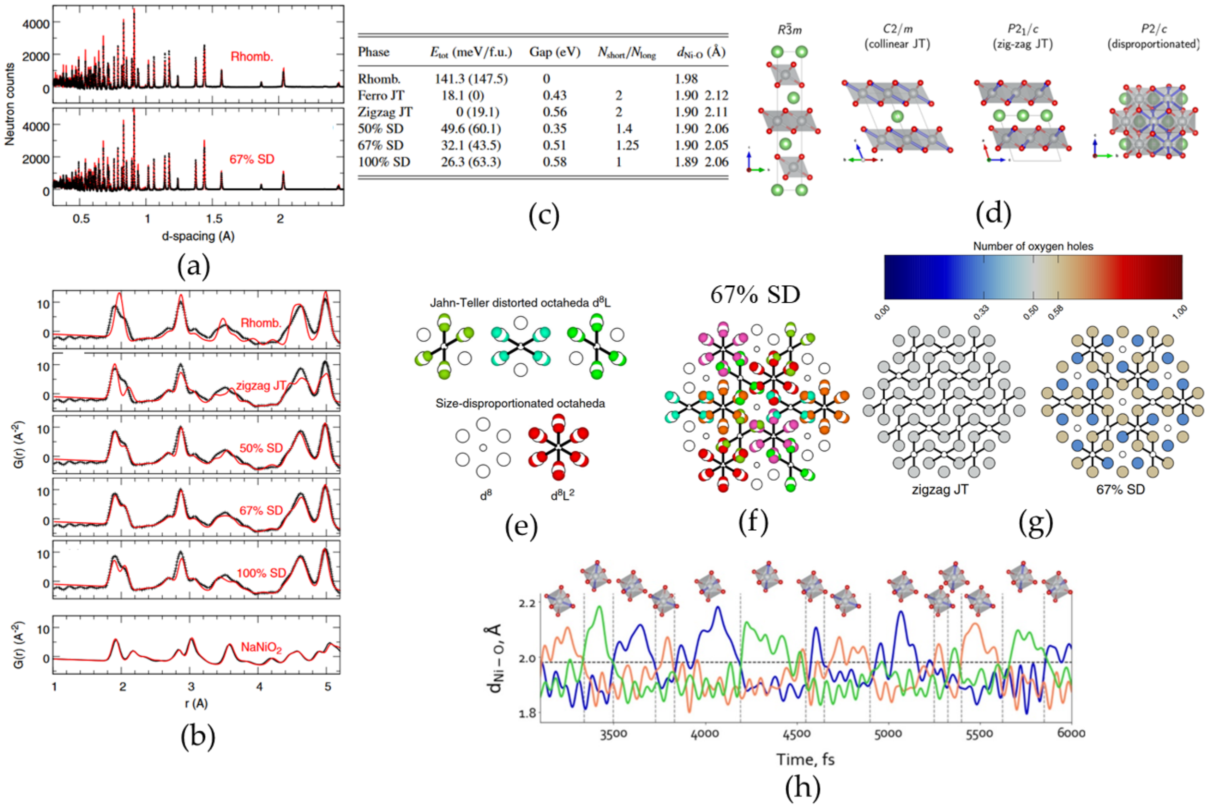

Phase	E_{tot} (meV/f.u.)	Gap (eV)	N_{short}/N_{long}	$d_{Ni\text{-}O}$ (Å)
Rhomb.	141.3 (147.5)	0		1.98
Ferro JT	18.1 (0)	0.43	2	1.90 2.12
Zigzag JT	0 (19.1)	0.56	2	1.90 2.11
50% SD	49.6 (60.1)	0.35	1.4	1.90 2.06
67% SD	32.1 (43.5)	0.51	1.25	1.90 2.05
100% SD	26.3 (63.3)	0.58	1	1.89 2.06

Figure 1.4.7 Proposed models for the ground state electronic structure of LiNiO₂. While the long-range structure measured by neutron diffraction is well described by both classic rhombohedral structure and bond-size disproportionation model in (a), the latter significantly improves the description for short-range order as shown in the fits for the neutron pair distribution function in (b). (c) Total energy and (d) crystal structures for LiNiO₂ assuming different structural models (JT = Jahn Teller, SD = Size disproportionation). The values in parenthesis are for NaNiO₂. (e) The five building blocks describing the disordered SD model. The density of oxygen holes with e_g symmetry is shown as isosurface colored plot. (f,g) schematic illustrations for the O 2p hole density in the 67% SD phase compared to the zigzag JT phase, typical for NaNiO₂. (h) Variation of the Ni-O bond lengths over time calculated by AIMD. Reprinted from ref. [112,114].

Overall, the presence of oxygen holes in the ground state of $LiNiO_2$ starts to be accepted by the community nowadays, although there is no consensus yet on the details beneath its electronic structure. Still, moving beyond a classic interpretation that assigns a static trivalent oxidation state to Ni local configurations requires to reinterpret the conventional cationic-centered redox compensation mechanism assumed until now. This work has been approached by a few studies published by the time this Ph.D. thesis was carried out.

1.4.5 "One step back to jump ahead": probing oxygen electronic structure in Li-rich positive electrode materials (2000-2020)

Before presenting the latest advancements on the understanding of $LiMO_2$ electronic structures, it is insightful to consider the Li-rich $Li_{1+x}M_{1-x}O_2$ (LRO) systems. These materials have attracted intense research due to their large energy densities exceeding that of Ni-rich NMCs. However, large first-cycle capacity loss, voltage hysteresis and fade as well as other stability issues pose a great challenge for their commercialization [57]. As for Ni-rich systems, understanding the redox mechanism underneath all these issues is considered the key to develop successful strategies to achieve stable cycling of LROs and would represent a major advancement in battery technology [36].

In the literature, the large capacity of LROs has been referred to as "anomalous", because it exceeds what could be compensated by the transition metal redox only as expressed by the Faraday law [36,117]. Therefore, a separate oxygen redox is proposed to compensate the remaining Li^+ (de-)intercalation. From this basic understanding, intense research has been devoted to understand and control the so-called anionic redox mechanism. Moreover, a conceptual division between $LiMO_2$ and LRO materials is assumed in most theories for the latter, that assign a standard cationic redox mechanism to $LiMO_2$ and a different anionic/cationic co-participation to the former [30,31,56,118,119].

The forehead of this class of materials is Li_2MnO_3, whose electrochemical activity was first investigated by various authors around 2000 [120–122]. Robertson and Bruce proposed that O^{2-} oxidation upon delithiation was responsible for electrolyte degradation, whose acidic byproduct would intercalate H^+ in exchange of Li^+ [121]. The first charge curve rapidly evolved towards the typical shape of spinel $LiMn_2O_4$, indicating bulk degradation [121]. O_2 and CO_2 gas evolution measured by Yu et al corroborated these hypothesis [122]. Eventually, gas evolution was related to most of the electrochemical capacity of Li_2MnO_3 by a combination of titration and mass spectroscopy techniques, while no changes in Mn and O bulk electronic structures were observed by X-ray spectroscopy techniques [123].

Although Li_2MnO_3 is nowadays considered overall inactive to anionic redox and has bad cycle stability, the derivation of substituted compounds had a different electrochemical behavior and better performance [57]. Dahn's group showed that partially Ni-substituted Li_2MnO_3 with formal $Li[Ni_xLi_{(1/3-2x/3)}Mn_{(2/3-x/3)}]O_2$ could deliver more than 200 mAh/g after several cycles, although the same issue of a first irreversible capacity loss associated to a high voltage plateau was also observed [124]. Further substitution with Co led to various Li-rich and M-rich oxides formulations similar to

$Li[Li_{0.2}Ni_{0.13}Mn_{0.54}Co_{0.13}]O_2$, whose structural complexity has been mentioned in **Section 1.1** [125]. As for Li_2MnO_3, cationic redox was not sufficient to explain the large capacity of LROs, characterized by a two-steps first-cycle charge profile followed by an "S-sloped" discharge curve [**Figure 1.4.8(a)**]. These features were at first attributed to large O_2 loss leading to material densification [117,124]. However, Delmas's group showed that large deoxygenation could not explain the cation average oxidation states at the end of discharge measured by soft and hard XAS, redox titration and magnetic measurements [126–128]. The authors proposed a distinct mechanism for oxygen redox in the bulk and on the surface of the particles, concluding that only surface O redox led to irreversible oxygen loss [128].

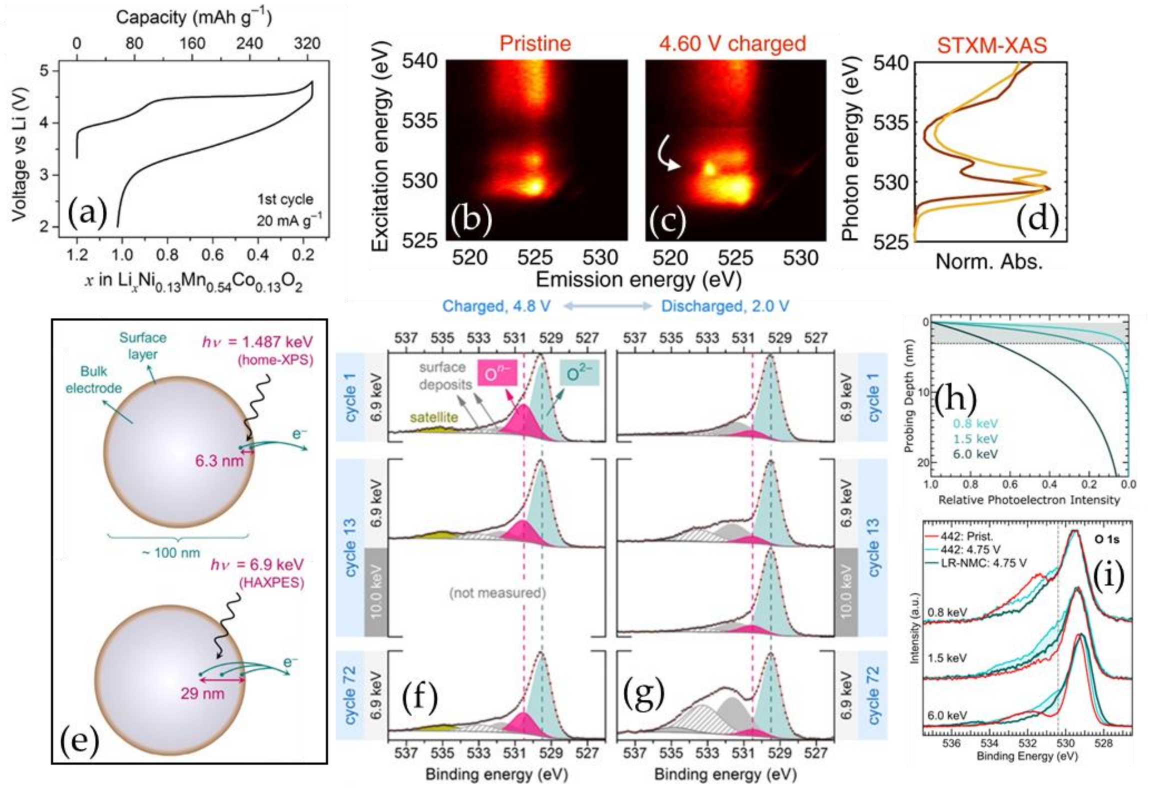

Figure 1.4.8 Experimental insight on the charge compensation mechanism of Li-rich NMC materials. (a) Typical first-cycle charge and discharge curve. Reprinted from [129]. O K-edge RIXS maps for (b) pristine and (c) charged Li-rich NMC material, highlighting the feature commonly related to bulk anionic redox. (d) Bulk-sensitive XAS spectra corresponding to the RIXS maps. Reprinted from [130]. (e) Sketch for the comparison between conventional in-lab XPS and synchrotron HAXPES. O 1s HAXPES spectra for Li-rich NMC at (f) charged and (g) discharge state at different cycles, highlighting the periodical increase/decrease of the O^{n-} peak related to anionic redox in the paper. Reprinted from [129]. (h) Calculated intensity decay with increasing depth for three different photon energies, showing that the sensitivity to first nanometers is still significant. (i) Comparison of O 1s XPS and HAXPES spectra for NMC442 at pristine and charged state as well as Li-rich NMC at charged state, showing a larger intensity in the 530 eV region expected for the bulk oxidized oxygen component for NMC442, in which no anionic redox was expected. Reprinted from [131].

While distinguished from classic $LiMO_2$, the charge compensation of LROs has been related to $Li_2Ru_xSn_{1-x}O_3$, designed as model systems by the Tarascon's group [31,132–

134]. The authors proposed a "metal-driven reductive coupling mechanism" [31]: O^{2-} to O^{-} oxidation would be followed by metal reduction (e.g. Ru^{6+} to Ru^{5+}) and condensation of the O^{-} ligand forming peroxo-like $(O_2)^{2-}$ species with shorter O-O bonds that stabilize bulk oxygen holes. The formation of O^{-} was explained by means of molecular orbital theory applied to the specific local coordination of the O 2p orbitals, as discussed in **Section 1.3.1**. Noteworthy, the reductive mechanism drawn by Saubanère et al. in ref. [59] would be referred to as ligand-to-metal charge transfer in a different context.

To understand the redox mechanism of these compounds, experimental techniques sensitive to local oxygen oxidation state in the bulk material were necessary. In fact, two spectroscopic tools emerged as direct probes of O bulk oxidation: O K-edge resonant inelastic X-ray spectroscopy (RIXS) [119,130] and O 1s hard X-ray photoelectron spectroscopy (HAXPES) [129,135]. A detailed explanation for the techniques can be found in ref. [136] for RIXS and in **Section 2.1.1** for HAXPES. Below, we only discuss their application to the context of studying anionic redox in Li-rich NMCs.

The idea behind application of RIXS to study O redox is to overcome the large influence of p-d hybridization in the O K-edge XAS spectra [130]. The technique explores XAS features with the subsequent X-ray emission decay in an overall "photon-in photon-out" process, which allows to distinguish the states involved in the excitations (e.g. vibronic, magnetic, and electronic) as well as their localized or itinerant nature [36,136]. Since the observable is the emitted X-ray, the technique is typically classified as bulk sensitive [36]. In case of the O K-edge for LROs, two major changes were commonly observed for all systems upon charging [**Figure 1.4.8(b-d)**]: a sharp feature at excitation and emission energies of 531 eV and 523.5 eV, respectively, in the range typical for O_2 and peroxides, and vibronic modes with fundamental energy separation of 0.19 eV, comparable to O_2 [36,118,119,130,136]. The appearance of these features at the end of the first voltage plateau (referred to cationic redox) and the similarities with oxidized O species led to consider RIXS as the major probe for investigating O-redox behavior in battery materials [136,137]. However, a theoretical investigation of these features is still missing.

Core level O 1s HAXPES was identified as experimental tool for characterizing bulk anionic redox following the initial observation of the appearance of a peak at 530.5 eV upon charging [132] for $LiRu_{0.5}Sn_{0.5}O_2$. However, its origin was unclear, since its position is typical for both peroxides and transition metal surface under-coordinated oxides [138] and the study was carried out by conventional lab-based soft XPS, with a limited probing depth. Based on these preliminary findings, HAXPES investigations of Li-rich NMCs were carried out, confirming that an analogous O 1s peak could be measured also with larger the depth sensitivity[**Figure 1.4.8(e)**] [129,135,139]. This led the Tarascon's group to address this technique as a "direct probe" of anionic redox

[**Figure 1.4.8(f,g)**] [129,135]. However, the experiments typically reported a comparable or even larger peak intensity close to the surface [129,135,139,140]. Notably, a similar observation by lab-based XPS for deeply charged Li_xCoO_2 was also related to oxygen participation in the redox process [108].

Eventually, the above interpretation was called into question by a comparison of conventional and Li-rich charged NMCs, which showed analogous increase if the ~530.5 eV peak, even more intense for conventional non-anionic redox-active materials [**Figure 1.4.8(h,i)**] [131]. In parallel, investigation of surface transition metal oxidation state by L-edge XAS suggested partial reduction of Ni and Mn in the same region. Therefore, it was concluded that this feature was related to surface degradation i.e. metal reduction and/or O under-coordination. Nevertheless, this opinion is not widely accepted and O 1s HAXPES is still employed to study the redox mechanism of LROs by following the evolution of the 530.5 eV peak [141,142].

1.4.6 “Bridging borders at the frontier”: linking theoretical understanding with experimental observations (2020-now)

Following the experimental and theoretical assessment of the anionic redox process, several studies were carried out for conventional model system. In contrast to the expected behavior for non-Li rich oxides, whose capacity could be in principle explained by cationic redox, $LiCoO_2$ [53,54], $LiNiO_2$ [137,143], NMC [144], and NCA [145] all showed the RIXS feature at high voltages that was previously related to anionic redox in LROs. Therefore, these studies questioned the fundamental understanding of the redox compensation mechanism for layered transition metal oxides, suggesting a prime role of oxygen going beyond the simple tuning of the cation redox couple (inductive effect) or a partial involvement by hybridization with the transition metal 3d states.

Motivated by the increase of the uppercut off voltage to 4.6 V vs Li^+/Li towards high-energy density applications, the redox compensation of $LiCoO_2$ at high voltage continues to intrigue the battery community. In fact, thanks to bulk and/or surface modifications, Li_xCoO_2 shows stable cyclability beyond the classic limit of 4.2 V up to 4.5 - 4.6 V [51,146]. While oxygen holes upon delithiation were measured by O K edge XAS, this was mostly related to Co 3d - O 2p hybridization [105,106]. However, the finding of the O K-edge RIXS peak suggested a more complex interplay between Co and O, as discussed by E. Hu et al [54]. In fact, the authors questioned previous criteria for anionic redox identified in the DFT+U study by Saubanére et al. [31], namely the presence of local Li-O-Li configurations and O-O dimer formations, both absent in highly delithiated Li_xCoO_2. Therefore, they proposed that O redox was promoted instead by the enhanced hybridization itself, although the mechanism remains unclear [54].

A possible reason for this disagreement can stand in the DFT+U approximation, as suggested by Isaacs and Marianetti, who compared it with DFT+DMFT calculations for Li_xCoO_2 (x=1, 0.5, 0) and highlighted the failure of the static DFT+U approach to predict metallic phases for CoO_2 and $Li_{0.5}CoO_2$, as observed experimentally [147]. In their calculations, the number of Co 3d electrons did not change significantly with decreasing x [**Figure 1.4.9(a)**]. This result recalls the "self-regulation mechanism" proposed early on by Wolverton and Zunger [**Figure 1.4.4(b)**] [90]. With an average occupation constantly around seven electrons, only a spread of atomic state probabilities with different spin and number of electrons resulted from the DFT+DMFT calculation [147]. However, no direct link of this theoretical study with spectroscopic observation could confirm these findings.

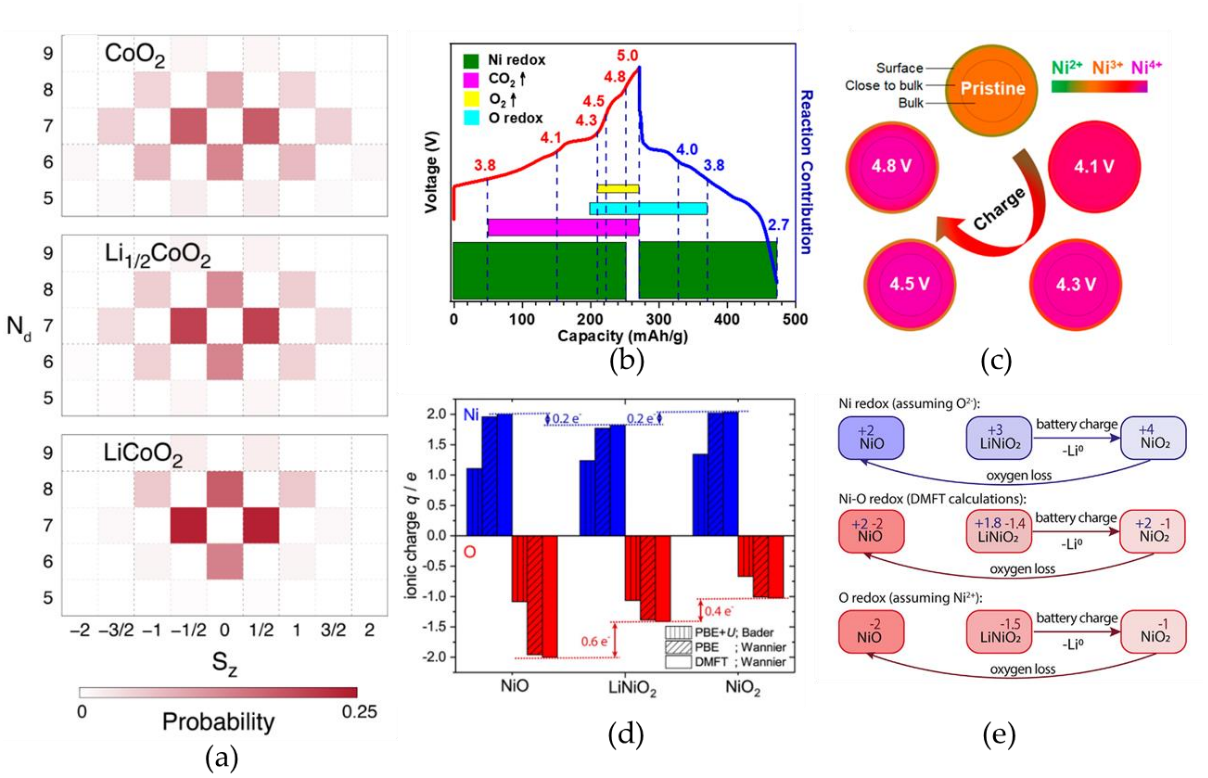

Figure 1.4.9 (a) DFT+DMFT prediction of Co atomic states by means of Co 3d occupation and local spin state for $LiCoO_2$, $Li_{1/2}CoO_2$, and CoO_2. Reprinted from [147]. (b,c) Proposed charge compensation mechanism for LixNiO2 based on Ni L-edge and K-edge XAS, O K-edge RIXS, and gas evolution analysis [143]. (d) Ni and O oxidation states calculated by DFT and DFT+DMFT for NiO, LiNiO2, and NiO2, highlighting the larger electron transfer for O 2p states. (e) Revisited charge compensation mechanism for Li_xNiO_2: the redox center is shifted from Ni to O. Reprinted from [148].

The first explanation of the O K-edge RIXS peak appearing in Li_xNiO_2 near full delithiation was given by Li et al. based on the ionic picture indicated in **Figure**

1.3.1(c). Accordingly, oxidation of low-spin Ni^{III} to Ni^{IV} would leave unaffected the O 2p band until near complete electron withdrawal from the e$_g$ states [**Figure 1.4.9(b,c)**]. Surface and bulk sensitive XAS as well as operando differential electrochemical mass spectrometry (DEMS) completed this picture by highlighting surface densification due to O_2 release and Ni reduction [143]. However, this interpretation overlooks most previous studies on $LiNiO_2$ ground state and does not explain the origin for O redox mechanism in a Li-stoichiometric oxide.

Other studies on NMC and NCA materials refer to the analogous RIXS feature as a consequence of increased hybridization [144,145]. This conclusion agrees with the RIXS study of Li_xCoO_2 [54] but goes in contrast with the basic premise about RIXS being able to distinguish hybridization and O redox due to non-bonding O states [130]. Interestingly, this structural requisite for anionic redox in the Li-rich systems has been formalized using Li_2MnO_3 as model system [30,31], despite no characteristic RIXS features were observed for this compound [123]. This highlights the relevance of Ni and/or Co interaction with the O 2p states to unlock this spectroscopic response.

Menon et al. re-investigated this issue by measuring high-resolution O K-edge RIXS spectra for 2 at% W-doped $LiNiO_2$, which not only confirmed the appearance of the feature observed by Li et al but also revealed the vibronic modes similar to O_2 [137]. Because of the absence of lone pairs as in LROs, they propose that a different common origin could be the cause of O redox behavior in both stoichiometric and Li-rich oxides [137]. In a subsequent DFT+DMFT study, the same group highlighted the significant O 2p hole doping going from NiO to $LiNiO_2$ and even further towards NiO_2 [148]. Indeed, the average Ni 3d occupation would stay close to 8 in all cases, while the O 2p oxidation state moves from -2 (NiO) to -1.5 ($LiNiO_2$) to -1 (NiO_2) [**Figure 1.4.9(d,e)**]. O and Ni K-edge XAS simulations matching well the experiment within this anion-centered redox compensation mechanism corroborated this finding. In agreement with this study, Ni L-edge XAS simulations based on cluster model theory gave $\left|d^8\boldsymbol{L}^{-1}\right\rangle$ and $\left|d^8\boldsymbol{L}^{-2}\right\rangle$ as the most relevant states for $LiNiO_2$ and NiO_2, respectively [149].

In summary, the once-diverging pathways of Li-rich and Li-stoichiometric oxides are now colliding due to similar spectroscopic observations that suggest common physics involved in the charge compensation mechanism. The most recent studies on $LiCoO_2$ and $LiNiO_2$ systems (mostly published during the time this thesis was carried out) highlighted a tendency of transition metal cations to preserve the local net charge by depleting the surrounding O 2p orbitals. Investigating this behavior by core-level HAXPES in combination with electronic structure simulations is one main target of this thesis.

As evident in the above paragraphs, the most recent studies are based on XAS and/or RIXS characterization. As further detailed in the next chapter, photoelectron spectroscopy is characterized by a large sensitivity to interatomic interaction being based on an ionization process that enhance core-hole screening effects. Therefore, it can bring valuable insights on the complex metal-oxygen interplay outlined by XAS and RIXS studies. **However, HAXPES characterizations are indeed less frequently conducted due to the ambiguities on bulk sensitivity, O 1s interpretation, and non-trivial transition metal line-shapes. Addressing these methodological and theoretical challenges constitutes the second major objective of this thesis.** For the third one, we refer to the next section.

1.5 Degradation of layered transition metal oxides in Li-ion batteries

Whatever charge compensation mechanism allows layered transition metal oxides to (de-)intercalate Li^+, the process is not fully reversible and the material tends to degrade upon cycling in Li-ion batteries. This is related to several instability issues, distinguished according to their physical origin into thermal, mechanical, and (electro)chemical (**Figure 1.5.1**). The aim of this section is to introduce them giving emphasis to the latter since it is the typical subject of XPS studies for battery materials.

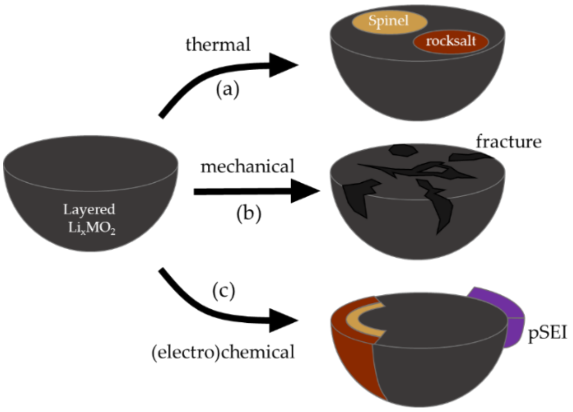

Figure 1.5.1 Schematic representation of the three types of degradation mechanisms in lithium layered oxides. Adapted from [18].

1.5.1 Thermal instability

As early recognized by first principle calculations, partially deintercalated layered oxides are metastable phases with respect to related transition metal spinel and rocksalt oxides [150,151]. As shown below, the decomposition reactions produce O_2 gas species [152].

$$Li_xMO_2 \rightarrow \frac{x+1}{3} Li_{3-\frac{3}{x+1}} M_{\frac{3}{x+1}} O_4 + \frac{1-2x}{3} O_2$$

Equation 1.5.1

Equation 1.5.2

$$Li_xMO_2 \rightarrow (x+1) Li_{1-\frac{1}{x+1}} M_{\frac{1}{x+1}} O + \frac{1-x}{2} O_2$$

The fact that the material does not spontaneously decompose releasing oxygen was explained by the kinetic hindrance of this process in the bulk structure, where the O_2 molecules could hardly diffuse outward [153]. Nevertheless, as will be discussed below in **Section 1.5.3**, this spontaneous process is observed to occur on particle surfaces.

The phase degradation kinetics depends on the energetic cost for transition metal migration to the Li^+ sites left empty upon deintercalation. This depends on the transition metal ion size and its stability in octahedral (O_h) environment with respect to tetrahedral (T_d) coordination, since the least energetic migration path involves a passage through a nearest neighbor tetrahedral site ($O_h \rightarrow T_d \rightarrow O_h$) [150]. Accordingly, the tendency of trivalent ions to migrate in NMC materials sees the following order: Mn^{III} > Ni^{III} > Co^{III} [50]. Concerning Ni-rich NMC and $LiNiO_2$, the Ni/Li interlayer mixing is generally explained by the facility for Ni^{II} to occupy the Li octahedral site due to their similar cation sizes (Ni^{III}: 0.56 Å, Ni^{II}: 0.69 Å, Li^+: 0.76 Å. [28]. However, the recent findings on the latter electronic structure presented in **Section 1.4.4** imply that taking tabulated values for Ni cationic size could overlook other fundamental mechanisms.

While the layered phases are metastable at room temperature, heating at >200 °C favors the reactions expressed in **Equation 1.5.1** and **Equation 1.5.2** in a two-step process, as resulted by thermogravimetric analysis with coupled mass spectrometry (TGA-MS) studies [154,155]. Moreover, systematic investigations clarified that the onset of decomposition is lowered by increasing Ni content [154]. This represents a critical issue for Li-ion battery safety since the reactions are exothermic and the produced O_2 can react with the electrolyte. Therefore, decomposition of the bulk layered phase can start the so-called thermal runaway i.e. chain reactions that can eventually lead to battery explosion [25].

1.5.2 Mechanical instability

The progressive deintercalation of $LiMO_2$ modifies the transition metal interlayer spacing, with a first mild increase and a subsequent abrupt shrinking, typically related to a phase transition towards the end of deintercalation (**Figure 1.4.3**). The electronic origin of this behavior is typically explained on a qualitative level as follows [156]. The Li^+ deintercalation progressively lowers the electrostatic screening effect of the Li^+ layer to the reciprocal repulsion between adjacent MO_2 layers, causing a slight increase in the interlayer distance. Further oxidation is proposed to induce a re-hybridization process that lowers the effective charge on the O atoms and therefore the interlayer repulsion, leading to the collapse along the c-axis of the rhombohedral structure. Noteworthy, while this charge transfer process is widely accepted to explain this crystallographic behavior, its impact on the electronic structure is less clear.

The shrinking of the interlayer distance causes an anisotropic lattice strain on the crystals, released by fractures that break the grain borders in the secondary particles starting from the first charge step [157]. Secondary particle cracking can be observed by SEM technique, as in the example given in **Figure 1.5.2** where the measurements were performed *in-situ* for a single particle [158]. As a margin note, it is interesting to point out that particle cracking could be studied also by their acoustic emission [159].

Particle cracking has two major effects: (1) exposing new surface to the electrolyte and (2) reducing the electric connectivity between active material and current collector, making part of the material effectively inactive. The increase of effective surface area may have initial beneficial effect in conventional Li-ion cells since it allows electrolyte infiltration within the cracked particles, improving the (de)intercalation kinetics [160,161]. However, exposure of virgin surface induces further material degradation through the mechanisms shown in the next section, making such continuous interplay between cracking and surface degradation one of the main causes for the capacity fade of layered oxides [162].

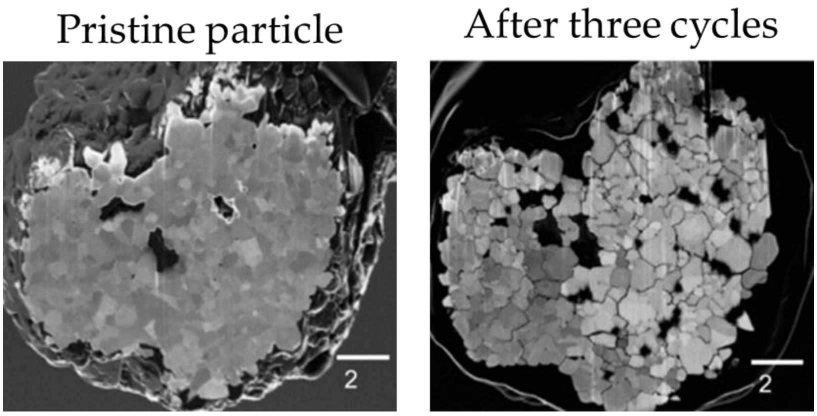

Figure 1.5.2 ***in-situ*** **SEM imaging of a secondary NCA particle before and after three charge-discharge cycles. Reproduced from [158].**

1.5.3 Surface electrochemical instability

The surface chemistry of Li_xMO_2 plays a major role in the electrochemical deintercalation process. Although the mechanism is not completely understood, a qualitative model for the structure, composition, and morphology of a general Li_xMO_2 surface structure can be outlined, as shown in **Figure 1.5.3**. As introduced in **Section 1.1**, electrochemical decomposition of the electrolyte due to either a misalignment of electrode and electrolyte respective energy levels and/or chemical reactions form a deposit layer on the electrode particle surface called solid-electrolyte interphase (SEI).

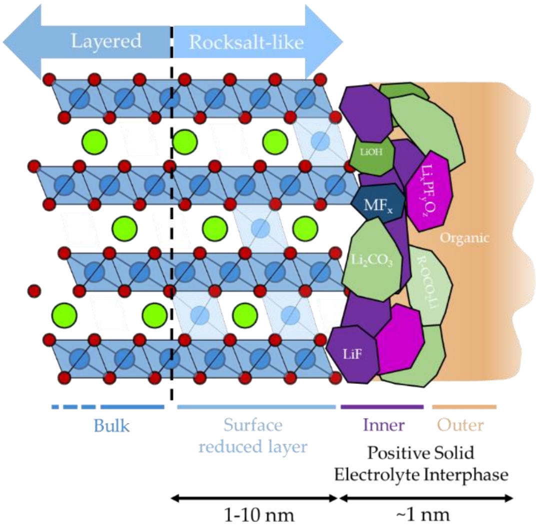

Figure 1.5.3 Schematic model for the surface layers developing due to surface electrochemical degradation mechanisms occurring in layered lithium transition metal oxides. The model was inspired by ref. [20,163,164].

In the case of the positive electrode, this is often referred to as cathode electrolyte interphase (CEI) in the literature, although herein we define it as positive SEI (pSEI) for consistency with the adopted nomenclature. Typically, the pSEI is distinguished from the surface degradation of the layered structure beneath it (herein the surface reduced layer SRL), which is an intrinsic property of layered oxides as explained in **Section 1.5.1**. While both layers are strictly interlinked and could be regarded as a single multilayer interphase, it is more convenient to discuss them separately. Moreover, it is insightful to look at the surface of pristine materials, whose chemical composition can determine the performance in the Li-ion cell.

1.5.3.1 Surface chemistry of pristine $LiMO_2$

Nowadays, battery-grade positive electrode materials are commonly stored and handled in air-free environment. The impact of air moisture on battery performance was observed early on by Dahn et al. while attempting to cycle $LiCoO_2$ in the high voltage regime (4.5-4.6 V) [111]. Starting with a material stored in ambient atmosphere, exposing fresh surface by grinding or heating significantly improved the capacity retention [**Figure 1.5.4(a)**]. The effect of ambient storage is even more critical for NMC [165]. Gauthier et al. explained this tendency by the increase of O anions nucleophilicity when bound with Ni [**Figure 1.5.4(b)**]: the O 2p states tend to donate electrons more easily for late transition metal oxides [20].

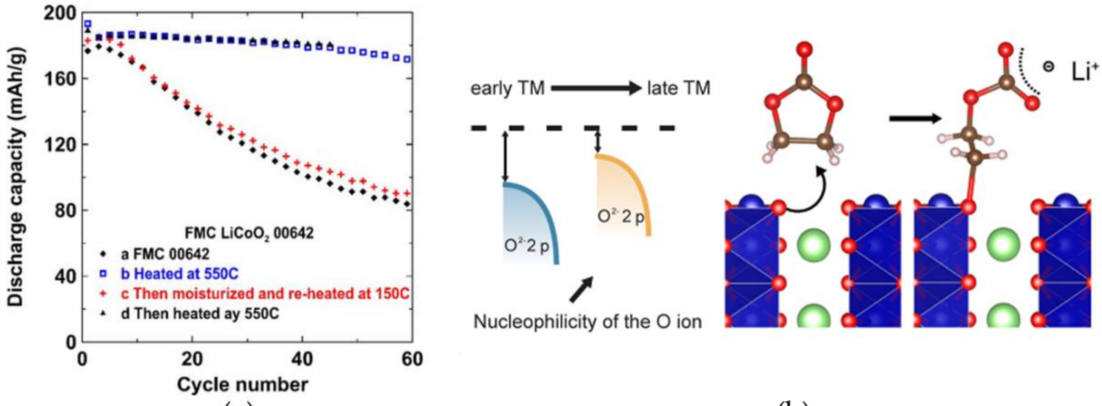

(a) (b)

Figure 1.5.4 (a) Discharge capacity retention for $LiCoO_2$ charged up to 4.5 V, showing the beneficial effect of surface cleaning via heating. Reprinted from [111]. (b) Schematic illustration of the nucleophilic attack mechanism proposed by Gauthier et al. to explain the stronger reactivity of Ni-based compared to Co-based materials [20].

Air instability was explained by the reactivity of $LiMO_2$ surface layers with H_2O and CO_2 forming lithium-containing surface impurities such as Li_2O, LiOH, Li_2CO_3, and transition metal carbonates and (oxy-)hydroxides [165–167]. Such species are commonly observed at the surface of $LiCoO_2$, $LiNiO_2$, and NMC by XPS [108,166,168,169]. These lithiated surface species are generally electronic insulators and decompose at high voltage releasing O_2 and CO_2. Therefore, their presence is commonly referred to as detrimental for battery performance and stability [147,151].

1.5.3.2 The pSEI: formation, properties, and characterization

Despite the pSEI has been deeply investigated and reviewed during the last decades, it is commonly recognized that the fundamental mechanisms behind its formation and evolution as well as its properties are still poorly understood [7,20]. This can be explained by the challenge of characterizing a highly-sensitive, few-nanometer thick interphase with dynamic nature evolving inside a Li-ion cell during operation, when a multitude of interlinked processes happen at the positive electrode surface [9]. Moreover, the number of studies on this interphase falls short with respect to those dedicated to its anodic counterpart (the nSEI) [7,20]. Nevertheless, some general understanding can be outlined.

The thermodynamic and kinetic aspects about the formation of an interphase between electrode and electrolyte have been presented in **Section 1.1**. In general, pSEI formation is driven by electrolyte decomposition, which can occur via either chemical redox or electrochemical (faraidic) redox, or even by acid-base reactions [7]. However, the energy difference between the HOMO level of the electrolyte and the PE chemical potential is typically quite small. This is why chemical decomposition pathways are expected to dominate the formation of the pSEI over electrochemical decomposition, which is instead predominant in the formation of the nSEI [20]. Despite the different origin, similar chemical species due to solvent and salt decomposition are typically found in both n- and pSEI, although the latter is significantly thinner [7,20].

Various pSEI models have been proposed in the literature (see for example figure 6 of ref. [20]), with a general buildup of understanding leading to the model shown in **Figure 1.5.3**, adapted from more recent studies [163,164]. Nowadays, the pSEI is typically distinguished into inner and outer region: the former mainly consists of inorganic salts resulted by $LiPF_6$ degradation [163,170], often represented in a mosaic-like arrangement following the pioneering work by Peled et al. for the nSEI [171] while the outer region contains organic deposits such as polycarbonates, due to solvent degradation [164].

Based on on-line electrochemical mass spectrometry (OEMS) gas analysis, Jung et al. proposed the mechanisms shown in **Figure 1.5.5** for the chemical and electrochemical oxidation pathways, with emphasis on reactions at high voltage and deintercalation levels [152]. In the electrochemical pathway, solvent molecules are oxidized by reducing the PE surface. To compensate this process, Li^+ ions are re-intercalated in the host material causing voltage drops in the cell. While the rate of this pathway is expected to increase upon charge, the onset of surface decomposition leads to a faster chemical decomposition of the electrolyte by reacting with the release of singlet $^1O_2$ molecules. Therefore, the evolution of the pSEI is intrinsically linked to the PE surface degradation.

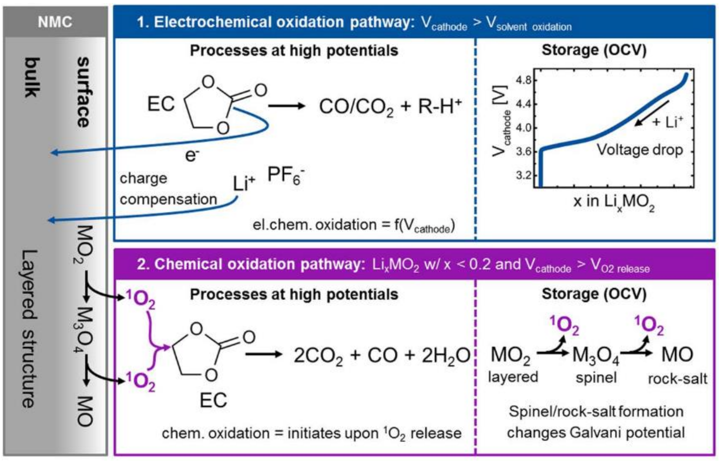

Figure 1.5.5 Comparison of electrochemical and chemical oxidation mechanism proposed by Jung et al. in ref [152].

As mentioned above, the lack of more detailed information on SEI formation and evolution is due to its challenging characterization even by current state-of-art methodologies. Ideally, a multi-technique approach that combines chemical sensitivity, spatial (both lateral and in-depth) and temporal resolution (i.e. in-situ and in-operando measurements) would be required [15,172]. However, the current understanding mostly relies on separate *ex-situ* characterization. Among the various techniques, the most frequently used ones are those with the highest surface chemical sensitivity, namely XPS, TEM, and TOF-SIMS.

XPS is widely employed to characterize surfaces and interphases of battery materials [108,163,166,170,173–183]. A representative example of *ex-situ* characterization is shown in **Figure 1.5.6(a)** (top), showing the O 1s and F 1s core levels spectra measured for a series of $LiCoO_2$ electrodes [170]. The chemical sensitivity of XPS allows to distinguish different chemical species in the pSEI. In this specific case, the authors studied the dynamic nature of the pSEI, which is observed to reversibly form and decompose upon cycling [170]. Such behavior was related to a cross-talking mechanism with the opposite nSEI by dedicated protocols. Beyond the identification of the chemical species of the pSEI, XPS quantitative analysis can give the relative atomic surface concentration. As shown in **Figure 1.5.6(a)** (bottom), the results of quantitative analysis indicate a “breathing” behavior of the pSEI to form during discharge and decompose upon charging.

Often used in combination with XPS, TOF-SIMS has the advantage of higher in-depth and lateral resolution [184–188]. The technique allows measuring the concentration of specific secondary ions sputtered by the primary beam, which can be used to understand the in-depth distribution of chemical species in the pSEI. When combined with a sufficiently focused primary ion beam, i.e. including a lateral resolution mapping, 3D images such as those shown in **Figure 1.5.6(b)**. In this example, Sheng et al. studied the impact of an amorphous lithium carbonate coating layer on the pSEI composition and electrochemical performance for a Ni-rich NMC material [189]: as evident in the 3D reconstructed images, a thinner and more homogeneous pSEI is obtained by this surface treatment.

An important aspect of the pSEI is its morphology, typically probed by TEM imaging technique. However, as pointed out by Zhang et al., this technique is particularly sensitive on material preparation and acquisition settings, that can easily alter the reactive surface layers [190]. By making use of cryogenic TEM and with a specific sample preparation protocol, the authors showed that even a fast short circuit, easily happening during cell disassembling, can significantly alter the pSEI morphology [**Figure 1.5.6(c)**]. In absence of this process, a systematic investigation of particle surfaces highlight that no uniform pSEI coating is present, implying that the pSEI has a rather heterogeneous morphology [190].

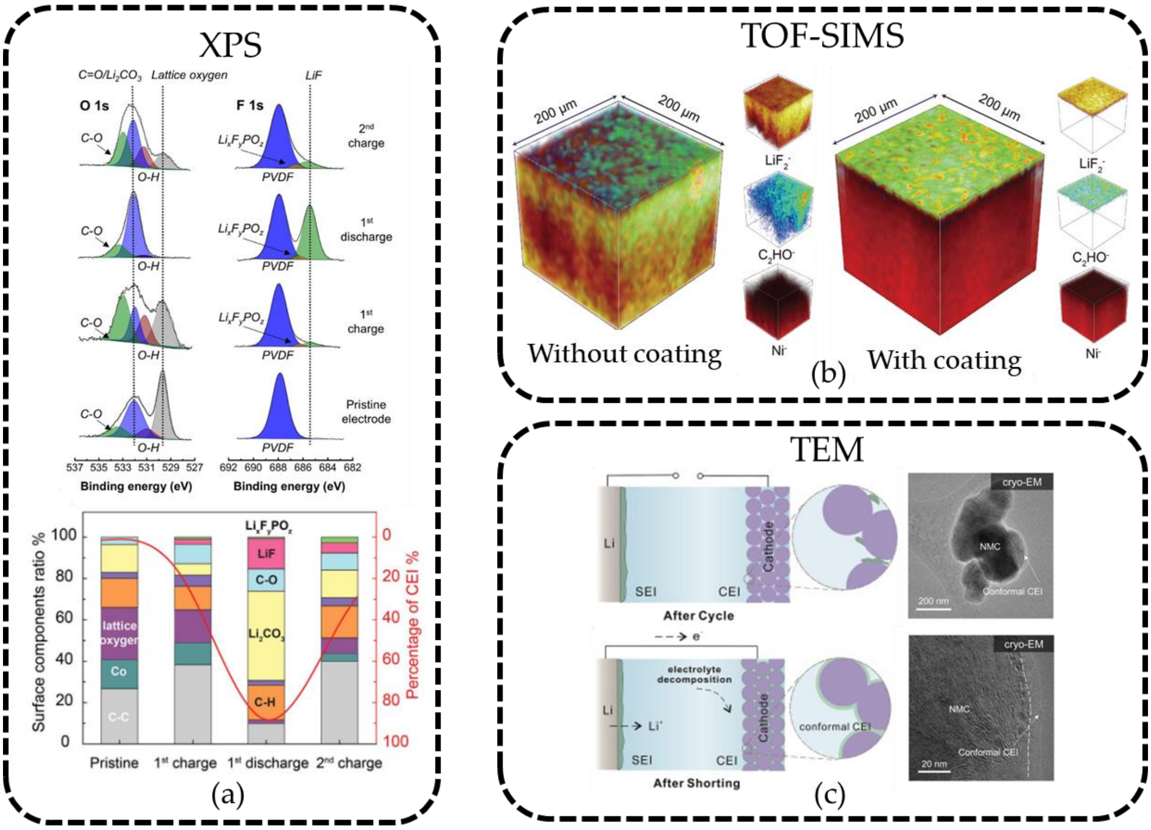

Figure 1.5.6 Main characterization techniques for the pSEI. (a) O 1s and F 1s XPS spectra for a series of Li_xCoO_2 samples at different cycled conditions. Peak fitting allows to distinguish different surface components of the pSEI. In the panel below, quantitative analysis was carried out considering the rest of high-resolution spectra. Reproduced from [170]. (b) 3D TOF-SIMS images of secondary-ion fragments for coated and uncoated NMC samples. Reproduced from [189]. (c) Left: schematics for pSEI formation in normal conditions or after controlled short-circuiting. Right: Cryo-TEM images for the pSEI deposited on a NMC particle after short-circuiting. Reproduced from [190].

1.5.3.3 The SRL: formation, properties, and characterization

Beyond the pSEI growth, related to oxidative decomposition of the electrolyte, surface degradation of positive electrode material has a large impact on material stability. Although a growing number of reports highlight the importance of the herein called surface reduced layer (SRL) in the operation of lamellar oxides in Li-ion batteries, the characterization of this interface is just as complex as for pSEI [149,191–195]. Because of the challenging characterization of SRL composition, structure, and morphology, the mechanisms behind its formation and evolution remain overall unclear. As for the pSEI, however, some general understanding has buildup during the last decades.

Following the discussion of Section 1.5.1, the surface of partially de-lithiated layered oxides spontaneously tends to reconstruct into cubic phases releasing oxygen (see eq. 2.5.1 and 2.5.2). Since the evidences of the SRL mostly come for Ni-rich NMC materials, this layer is often referred to NiO-like rock-salt layer [28]. Indeed, as for the other instability issues, a larger Ni concentration enhances the destabilization of the surface structure [20,28]. This has been explained by the small Ni^{2+} cation radii, similar to Li^{+}, as well as to a lower stability of oxygen anions, which tends to oxidize forming O_2 at the surface [28,153,196].

Generally, the SRL tends to be considered inert material with a passivating function: after falling into the Li ion layer at reduced II state, the activity of transition metal ions is considered to be irreversible loss [18,20]. Moreover, the densification of the SRL hinders Li^{+} diffusion, increasing the cell impedance [152,162,192]. However, it should be noted that some recent insight propose a dynamic nature as for the pSEI [191].

The characterization of the SRL consists of studying its main properties related to the surface degradation mechanism, constituted by surface reconstruction (I), surface reduction of transition metal ions (II), and O_2 release (III) as sketched in **Figure 1.5.7(a)**.

The use of atomic resolved imaging technique such as scanning transmission electron microscopy (STEM) allows to directly visualize the surface reconstruction into rocksalt/spinel structures of sufficiently small single particles [192,194,197–201]. An example of this technique is shown in **Figure 1.5.7(b)**, showing the SRL of a $LiNi_{0.4}Mn_{0.4}Co_{0.18}Ti_{0.02}O_2$ particle after one 2.5-4.7 V cycle in a liquid Li-ion cell [192]. Beyond imaging, structural analysis can be performed by the Fourier transform of selected areas of the image, as shown in the panels on the right side for the rocksalt (top) and layered (bottom) structure.

Electron energy loss spectroscopy (EELS) [192,193,195,202,203] and soft XAS [130,136,143,145,195] are the most widely employed techniques for studying the surface transition metal reduction, as they both combine a high surface sensitivity couple with capability to probe local electronic structure. The physical process at the basis of both EELS and XAS is the core-to-valence excitation by an electron or an X-ray beam, respectively. Therefore, the spectra are qualitatively comparable, as shown in **Figure 1.5.7(c,d)** where Ni L-edge EELS and XAS spectra were acquired for the same $LiNi_{0.4}Mn_{0.4}Co_{0.18}Ti_{0.02}O_2$ material [195]. However, while EELS provides better in-depth resolution, the energy resolution and signal-noise ratio of XAS spectra, typically performed in synchrotron facilities, is significantly better. Soft XAS allows to perform depth profile by changing detection mode from Auger electron yield (AEY, 1–2 nm) to total electron yield (TEY, 2–5 nm), to fluorescence yield (FY, ~50 nm) [195].

Generally, the interpretation of TM L- and K-edge EELS and XAS spectra is non-trivial as it depends on local symmetry, intra-atomic and interatomic interactions, which can be only fully understood by coupling with dedicated theoretical investigations. However, many studies tend to approximate specific spectral shapes to unique oxidation states, often leading to misleading interpretation related to cationic/anionic redox.

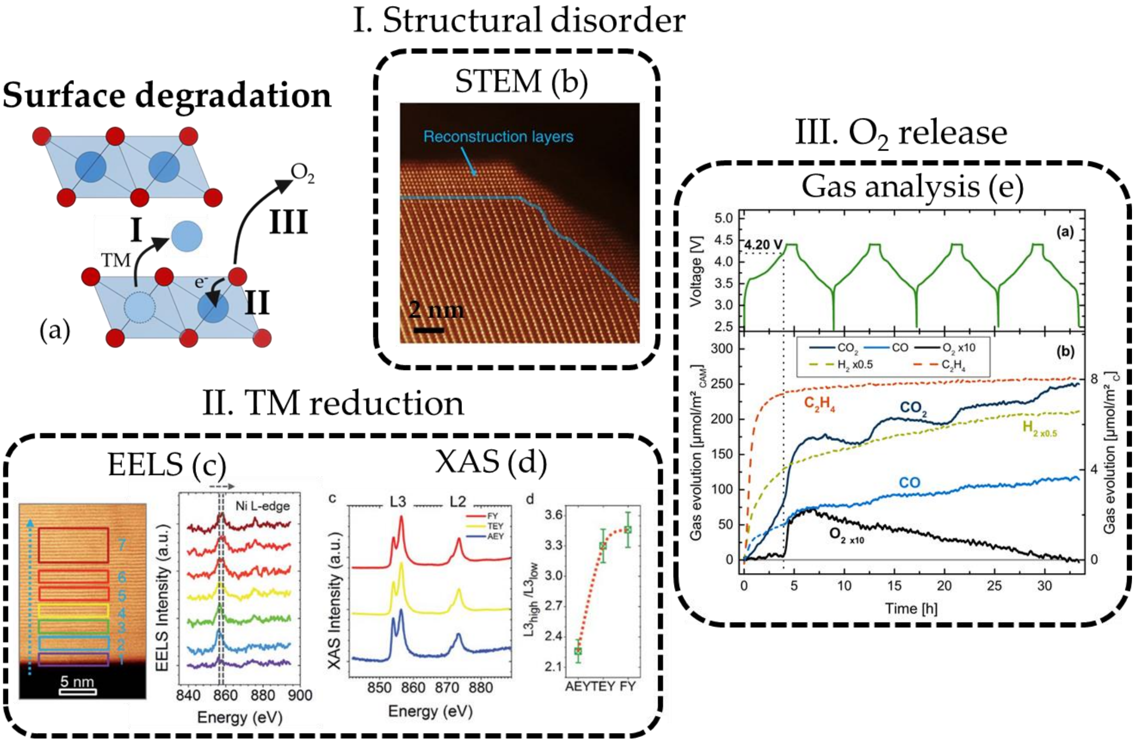

Figure 1.5.7 Characterization approaches for the SRL. (a) Sketch showing the effects of the layered-to-rocksalt surface degradation: (I) structural disorder, (II) TM reduction, and (III) O_2 release. (b) Atomic-resolution STEM image showing the surface structural degradation of a $LiNi_{0.4}Mn_{0.4}Co_{0.18}Ti_{0.02}O_2$ particle exposed to Li-ion electrolyte for ~30 h. The "Reconstruction layers" have a disordered rocksalt structure opposite to the bulk layered structure. The surface reduction of transition metal ions on the same material was studied by performing Ni L-edge (c) spatially resolved EELS and (d) XAS at different acquisition modes. For both techniques, the decrease of the lower-energy L_3 peak to the higher-energy one [e.g. the $L3_{high}/L3_{low}$ ratio in (d)] was related to partial surface Ni reduction. The EELS spectra shown in (c) were measured in the zone indicated by the STEM image on the left-hand side. Reprinted from [195]. (e) Gas evolution measured by OEMS for NMC811 upon cycling. Reprinted from ref [204].

Noteworthy, such complexity is also at the basis of XPS and HAXPES analysis of M core level line shapes. However, the interatomic screening effects become more relevant in photoemission spectroscopy, forcing it to leave apart the fully ionic picture. This and the fact that lab-based XPS equipment does not typically have the required bulk sensitivity to study the buried SRL hindered the application of XPS to this issue. In fact, while complementary to XAS analysis, XPS is rarely used to study the SRL in the literature. Nevertheless, XPS can give some advantages: (1) study the whole interphase i.e. SRL and pSEI (2) study qualitatively and quantitatively both M and O spectra (3) get more insight into the M-O interplay, often hidden in XAS analysis. **These perspectives open to the third main objective of the thesis: combining soft and hard X-ray photoelectron spectroscopy for performing qualitative and**

quantitative depth analysis across the complex multilayer interphase of layered transition metal oxides.

Finally, *in-situ* and *operando* gas analysis gives a unique perspective on the formation of the SRL layer, as it allows to quantify the release of O_2, CO_2 etc. and follow their voltage dependence [143,152,204–206]. An example by the Gasteiger's group is shown in **Figure 1.5.7(e)** [204].

1.5.4 Impact of degradation mechanisms on battery performance

As mentioned above, mechanical, thermal, and surface instabilities are strictly interconnected to each other. The interplay of several mechanisms is even broader at the cell level, as degradation mechanisms at each component of the battery can be linked to each other. Therefore, studying battery degradation is an extremely complex and broad topic as it requires to account for all mechanisms and their interdependence on a multiscale level [11,207]. Herein, we limit the discussion to the effects of the above-said degradation mechanism affecting the positive electrode material, to the cell capacity fade.

A significant first-cycle capacity loss, absent in subsequent cycling, is observed for all $LiMO_2$ materials [208,209]. Indeed, it is very common that the Coulomb efficiency of the first cycle is ~80-90% in contrast to the following cycles, where it approached 99% [208,209]. Most of this capacity loss seems to be associated with kinetic hindrance for Li^+ diffusion inside the re-lithiating particles. This can be recovered by both improving particle connectivity via calendaring and with a constant potential discharge step, as shown in **Figure 1.5.8(a)** for NMC811 electrodes. Nevertheless, some capacity loss is effectively irreversible: this was attributed to surface degradation i.e. either the loss of active material related to the SRL formation or loss of Li^+ in the nSEI and pSEI formation [208,209].

Beyond the first cycle, the same kinetic hindrance effect continues to limit the amount of Li^+ that can be re-intercalated on discharge, which in turn controls the amount of deintercalated Li^+ on charge. Moreover, impedance increase due to formation of the SRL and pSEI surface layers lowers the effective state-of-charge range i.e. the range of x in Li_xNiO_2, as shown in the bottom panel of **Figure 1.5.8(b)** [162,210]. For Ni-rich systems, the decrease of the charge capacity seems to be related to suppression of the high-voltage H2-H3 transition, related to the abrupt shrinking of the interlayer spacing. Indeed, while *in-situ* and *operando* structural investigations revealed no significant bulk degradation in terms of increasing Li/Ni intermixing upon cycling [162,194,211], the appearance of a secondary so-called fatigued phase was reported by Xu and coworkers [194]. Its origin was related to a pinning of the interlayer spacing coming from the surface rocksalt layer, as sketched in **Figure 1.5.8(c)**: indeed, the fatigued phase had stoichiometry and structure resembling that of the H2 phase.

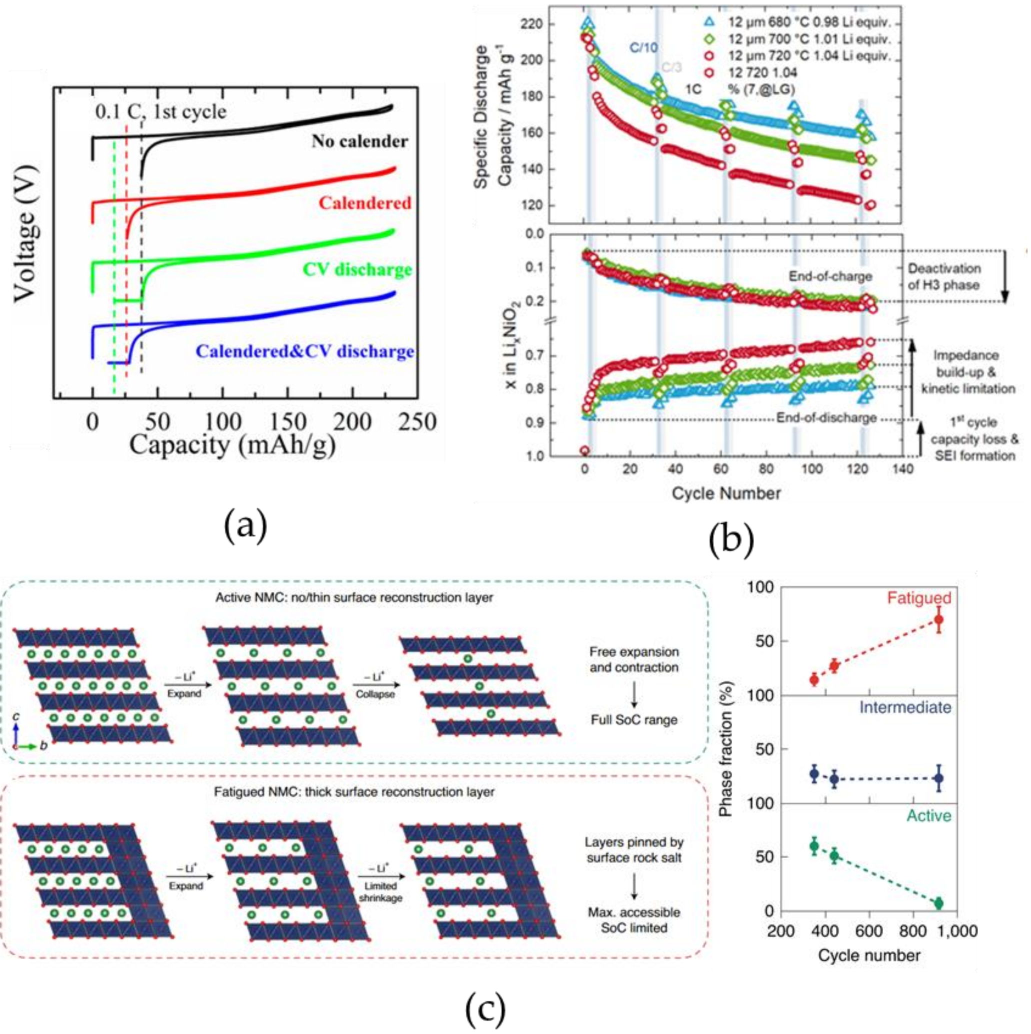

Figure 1.5.8 Impact of positive electrode material degradation on the capacity retention in Li-ion cells. (a) First-cycle capacity loss for a NMC811 sample with or without protocols to reduce the loss due to kinetic hindrance due to low Li+ diffusion at the end of discharge. Reprinted from [209]. (b) Discharge capacity as a function of cycle for different batches of $LiNiO_2$ (prepared with different amounts of precursors). In the panel below, the average Li stoichiometry at the end of charge and discharge is shown, indicating a shrinking of the range of composition achievable upon cycling. Reprinted from ref [210]. (c) Left: mechanism for the growth of bulk fatigued phase due to surface structure pinning by the rocksalt-like densified layer. Right: phase fraction estimated by operando XRD analysis for NMC811 after long cycling tests. Reprinted from [194].

1.6 Chapter conclusions and outlook

This chapter introduced the main concepts and theories to describe the electronic structure of $LiMO_2$ materials and its impact on electrode bulk and surface stability. The vast literature on charge compensation and degradation mechanisms associated with (de-)lithiation was summarized, identifying cornerstones and current research directions. Nowadays, although more and more attention is given to materials with lithium-rich stoichiometries from an application point of view, the actual mechanism of conventional materials, identified in $LiCoO_2$ and $LiNiO_2$ model systems, is still not entirely clear. **Questions to be clarified are: what is the role of oxygen in the charge compensation mechanism of layered metal oxide electrodes? What changes by replacing Co with Ni? What is the electronic structure of $LiNiO_2$?**

The fact that these issues are still open is testified by the many studies published while this thesis was being conducted on this topic. Herein, the coupling of core-level spectroscopy with electronic structure simulations emerged as the most effective methodology for addressing these questions. In this thesis, we will follow this state-of-the-art approach, which will be based on X-ray photoelectron spectroscopy. In this way, the interaction between metal and oxygen and the electronic correlation phenomena will be emphasized, allowing us to look at the charge compensation mechanism from a different point of view than that of absorption spectroscopy. To this end, it was necessary to develop step-by-step an experimental and theoretical method of analyzing the core spectra of transition metals and oxygen.

Chapter 2

Methodology

2.1 Soft and hard X-ray photoelectron spectroscopy of lithium transition metal oxides

The combination of conventional laboratory XPS with HAXPES characterization and its application to the specific case of layered lithium transition metal oxides are discussed below. A review of the basic principles of XPS is given in **Annex A**. The link between experimental and computational methods is also established.

2.1.1 Lab-based HAXPES for Li-ion battery applications

In the last few decades, HAXPES [2] applications had a large expansion worldwide due to the development of dedicated beamlines and, more recently, the availability of this technique even at lab-scale [212]. This thesis represents one of the first applications of an in-lab HAXPES equipment to investigate battery-related materials.

The main interest in performing HAXPES over XPS characterization is the increased information depth that can be achieved with increasing X-rays energies, opening to new experimental and analytical methodologies [212,213]. This is shown in **Figure 2.1.1**: by increasing the photoelectron kinetic energy (hence increasing the exciting photon energy), the inelastic mean free path can exceed the practical sampling depth limit of 10 nm that can be achieved by conventional Al Kα (1.486 keV) and Mg Kα (1.253 keV) X-ray sources.

---

[2] Conventionally, XPS experiments employing hard X-rays are addressed to as HAXPES (hard X-ray photoelectron spectroscopy). The historical reason for this distinction stands in the type of monochromator used for soft and hard X-rays (grating and single crystals, respectively).

However, the use of X-ray tubes equipped with anodes emitting at higher energies comes with two drawbacks: (1) the photoionization cross-section decrease that requires compensation by high flux and (2) the intrinsic linewidth of practical hard X-ray sources is higher than the classical ones, leading to overall lower energy resolutions. Such constraints were first solved by employing synchrotron radiation. Nowadays, more than 20 beamlines are available for HAXPES experiments worldwide [212].

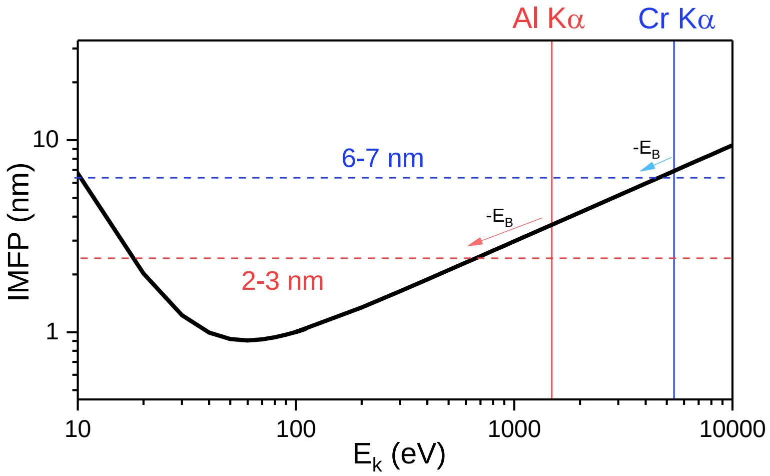

Figure 2.1.1 Universal curve for the inelastic mean free path calculated with the Seah-Dench equation $\lambda = \frac{A}{E_k} + B\sqrt{E_k}$ (where A = 641, B = 0.096 for inorganic compounds). The dotted lines indicate the expected IMFP for Ni 2p photoelectrons (E_B = 850 eV) excited by Al K*α* (1486 eV) and Cr K*α* (5419 eV) X-rays.

Despite the benefits of performing synchrotron HAXPES, laboratory-scale equipment is still required for more accessible and lower-cost analysis of buried interphases and multilayer structures. Beyond economical and practical aspects, these can also present advantages to synchrotron studies, favoring a complementary lab-based and synchrotron HAXPES approach. In fact, the high flux of synchrotron radiation can irreversibly change the sample surface (beam damage effect), which can be overcome by using less intense laboratory sources. Moreover, most synchrotron HAXPES analysis remains at a qualitative level due to the lack of experimental relative sensitivity factors (RSFs) necessary for quantification.

These motivations triggered the development of various lab-based HAXPES that make use of Ag L*α* (2.984 keV), Cr K*α* (5.415 keV), or Ga K*α* (9.252 keV) X-ray sources. For some equipment, including the one used in this thesis, a list of experimental RSFs is now available, enabling HAXPES quantification. However, their actual application to various research fields is still in its infancy: in the field of lithium-ion batteries, for example, no publications outside those related to this thesis have been found at the time of writing this paragraph (September 2023). Further details on the differences between each apparatus, in comparison with synchrotron HAXPES, can be found in ref. [212].

2.1.1.1 Non-destructive depth profile analysis

In typical XPS equipment, depth profiles can be obtained by Ar-ion or Gas Cluster Ion Beam sputtering. However, these are destructive methods and can easily alter the sample surface chemistry by preferential sputtering, as will be shown in **Section 3.3.1**. Nondestructive methods to perform depth-dependent analysis consist of varying either the take-off angle, the core-level of analysis, or finally the incident photon energy. However, the former two approaches remain within the threshold of 10 nm when using Al Kα radiation.

By coupling soft and hard X-ray photoemission spectroscopy, nondestructive depth profiles beyond 10 nm can be achieved (**Figure 2.1.2**). Note that the schematics consider ideal interphases, taking average thicknesses as estimated for various samples in literature by different methods, and overlooks the practical challenges of HAXPES acquisitions in terms of energy resolution and, more critically, signal intensity.

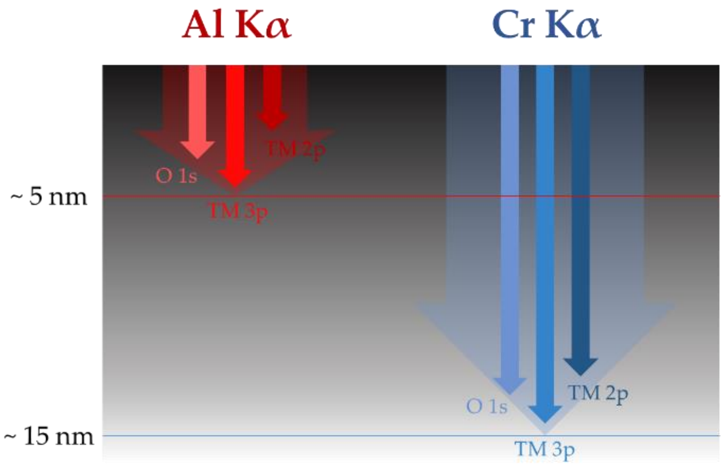

Figure 2.1.2 Schematics of the typical depth sensitivities for the main core levels of transition metal oxides probed by lab-scaled XPS and HAXPES.

In principle, this approach would enable to analyze on equal footing all components of the complex multilayer interphase developed on the positive electrode material upon cycling. Although a few HAXPES studies have been performed for positive electrode materials (**Section 1.4.5**), the aim of those studies was not necessarily to characterize the whole interphase or investigate in-depth the surface-to-bulk evolution of the electronic structure. Therefore, highlighting and discussing the actual limitations of this approach is a central theme of this thesis.

2.1.1.2 Overcoming the superposing Auger electron emission issue

Beyond an increase of the information depth, the use of HAXPES has another important benefit: removing overlapping Auger signals from the core level photoemission spectra. In fact, in an XPS experiment, the detector collects not only electrons ejected by direct photoemission process, but also the second ionization process known as Auger electrons. The energy diagram in Figure 2.1.3(a) illustrates the typical Auger process observed in the XPS spectra of 3d transition metals.

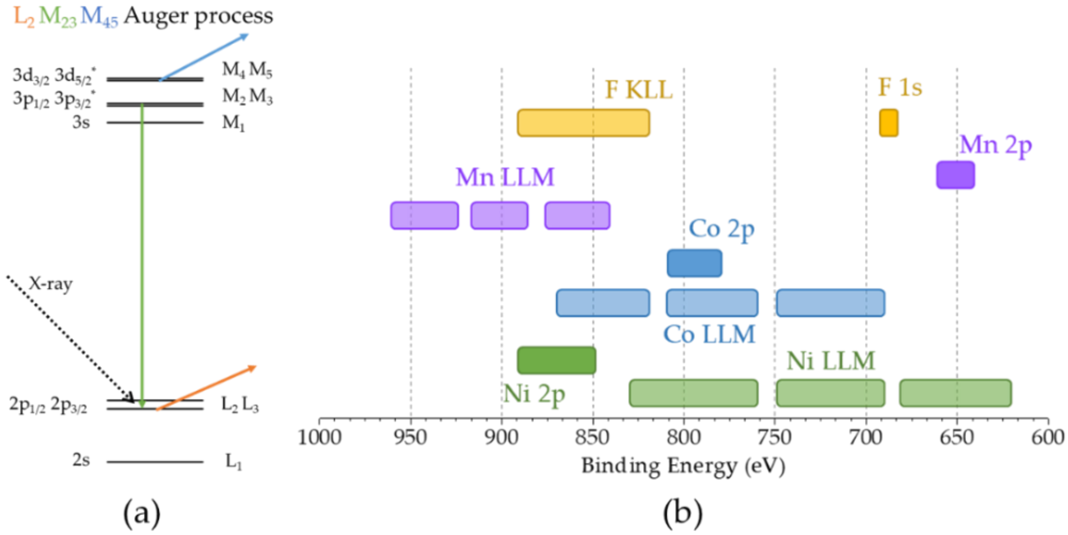

Figure 2.1.3 (a) Energy diagram of an LMM Auger process. The energy levels are labeled using both orbital (left) and X-ray nomenclatures (right). After core-hole creation at the core level C_1, an electron from the level C_2 can fill the hole by releasing some energy. This in turn allows a second electron at the level C_3 to be released. The kinetic energy of the transition is $E_{K,Auger} = E_{L_2} - E_{M_{2,3}} - E_{M_{4,5}}$ and does not depend on the photon energy. (b) Expected overlaps between Auger and photo-electrons for the most common core levels of a transition metal oxide electrodes as probed by the Al Kα X-ray source.

On the one hand, the analysis of Auger peaks can be extremely insightful for chemical analysis: in fact, Auger Electron Spectroscopy (AES) is a well-known technique in surface science. On the other hand, XPS and AES peaks tend to overlap with each other, complicating the analysis. Figure 2.1.3(b) schematically shows the binding energy position of Mn, Co, and Ni, O, and F core-level and Auger peaks when measured with Al Kα source. As evident in the figure, many overlaps are obtained. This has been a long-standing issue for XPS analysis of NMC materials [214–216]. However, Auger electrons have a fixed kinetic energy which depends only on the involved core levels. By using hard X-rays, the "apparent" binding energy shown in an XPS experiment can be shifted to higher binding energies, allowing to measure the core level spectra without Auger contributions.

2.1.2 Study of transition metal oxides by photoemission spectroscopy

The details of XPS spectral shape can inform on the electronic structure of the material. This is exploited specifically for strongly correlated systems such as 3d transition metal oxides. In fact, for these systems, more than one peak related to the same chemical species typically appear in the measured spectra. Therefore, the common peak fitting approach (as summarized in **Annex A**) is not sufficient to qualify and quantify the different chemical and electronic states of transition metal ions in a sample.

2.1.2.1 Satellite peaks

The transition metal core-level spectra are composed by various lines which in principle correspond to different final states. Conventionally, the most intense line is called main line while all others are referred to as satellites peaks [3]. The analysis of transition metals core-level photoemission spectra is based on measuring and interpreting satellites energy position and intensity with respect to the main line. This approach, developed since the ’60 and presented in different textbooks [213,217,218], brought and still brings significant contributions to the understanding of the electronic structure of transition metal oxides. For example, the theory presented in **Section 1.3.2** was built upon experimental and theoretical X-ray spectroscopy insights. The study of layered lithium transition metal oxides presented in this thesis is based on this general framework.

2.1.2.2 Unraveling the photoemission screening effects

The electronic correlations leading to different final states in the XPS spectra can be distinguished into intra-atomic and inter-atomic effects. Because these effects act as a response of the system to the positive core-hole potential, they are typically referred to as screening processes. Various levels of theory were developed, progressively increasing the number of screening channels to be taken into account to fully describe

---

[3] More precisely, these are named intrinsic satellites, since they originate from the photoexcitation step, while electron energy losses happening during its travel towards the surface are called extrinsic satellites. In this chapter, the latter case will be neglected so the distinction between intrinsic and extrinsic satellite drops out.

the photoemission spectra. Such theoretical buildup is schematized in **Figure 2.1.4** (4). The main aspects of the different screening processes are reviewed in **Annex A**.

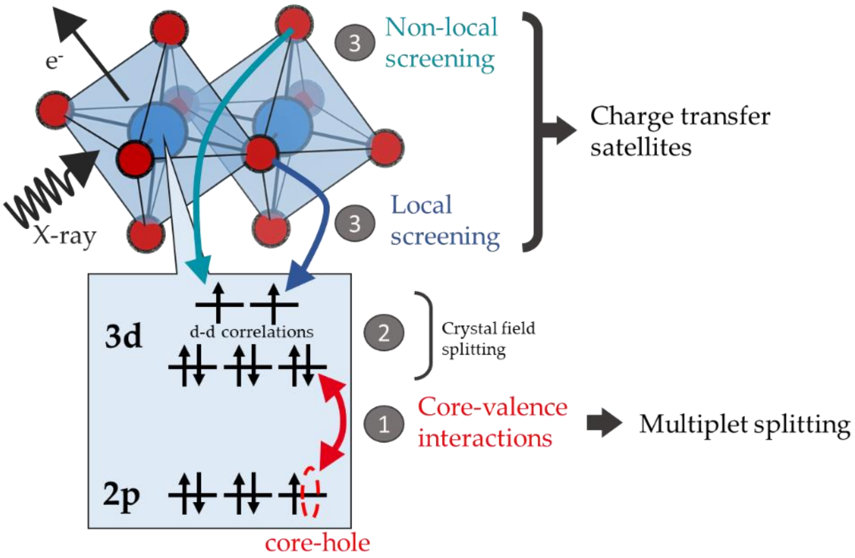

Figure 2.1.4 Schematics for the main interactions involved in an X-ray photoemission process in d^8 metal oxide based material.

Due to the high complexity and case-to-case character of the study of transition metal core-level photoemission spectra, coupling with computational methods is the most robust pathway. This not only supports the experimental analysis but establishes the connection between the photoemission experiment and the corresponding excited electronic structure. Therefore, for a complete analysis of the core-level spectra, it would be necessary to consider in the simulation all the effects that take place once the core-hole is created. However, empirical analysis based on the photoemission theory is also a suitable approach, especially for studying surface effects, which are hard to describe by simulations.

In practice, some screening processes can predominate in the overall spectra depending on the case of study, which can simplify the analysis and direct the choice of the theory to be used. For late-transition metal oxides, in particular, it is well known that inter-atomic charge transfer is far more important than intra-atomic multiplet splitting effects [217,218]. Therefore, both the empirical peak fitting approaches detailed in **Section 3.3.2** and computational methods presented below were adapted towards the interpretation of satellite peaks as charge transfer satellites.

---

[4] Note than in the literature there is no standard nomenclature about the names of such levels of theories, leading to ambiguities (for example, the ligand field theory presented in ref. [218] would be called crystal field theory in ref. [219]).

2.2 Theoretical spectroscopy: from electronic structure calculation to photoemission spectra simulation

The main aim of the computational methods used in this thesis was to complement and gain further insight on the experimental spectroscopy. Simulating the XPS spectra within a given specific theoretical method allows us to resolve the complex spectra of transition metal core levels and gain insights on the electronic structure that gives the experimental response. However, with respect to classic electronic structure calculations, two aspects need to be included: the core-hole potential and electron-electron interactions. The electronic structure calculations performed in this thesis are mostly based on two theories: the density functional theory (DFT) for a first insight of the ground state electronic structure properties, and cluster model theory (CMT) to simulate photoemission spectra and bridge between theory and experiment.

2.2.1 On density functional theory calculations

DFT is a state of art method for calculation of ground state electronic structures without need of experimental parameters. The basic principles of the theory and the computational details for calculations performed in this thesis are given in **Annex B**.

2.2.1.1 Electronic correlations within the density functional theory

The complexity of the analysis of core-level photoemission spectra as outlined above lies on the many-body nature of the photoemission process as it involves local electron-electron interactions. This poses a problem for methods such as DFT, whose accuracy relies on the approximation chosen to describe the system. In the case of 3d transition metal oxides, this translates into the choice of how electronic correlations are treated.

In the literature, DFT+U is the most common method to deal with the strong electronic correlations in layered transition metal oxides used as positive electrode materials. In the DFT+U method a local potential correction, the Hubbard U, is added to the exchange-correlation functional of DFT [220–222]. The Hubbard U is either treated as a parameter and fitted to a certain experimental parameter such as the voltage or the band gap (for example in [32,223,224]) or obtained via *ab initio* techniques [225–228]. In any case, the DFT+U approach has been criticized in the literature to overestimate the correlations for 3d transition metal oxides that present soft correlations and/or metallic character, such as in the Li_xCoO_2 system [147,222,224,228,229].

Leaving apart the discussion about which functional better describes these kinds of compounds, which is a highly debated topic in the literature, it is important to note that none can fully describe the photoemission experiments. In fact, within the single-electron DFT or DFT+U theories, no many-body effects such as the XPS satellites can be theoretically investigated. From this perspective, moving from DFT to DFT+U can be seen as focusing on the main line or on the Hubbard band solely, while the experimental spectral function is a distribution of both.

For this reason, we did not explore the large number of exchange-correlation functionals present in the literature but limited to the GGA in the form given by Perdew-Burke-Ernzerhof (PBE), taken as a starting point for the subsequent cluster model calculations. In fact, a linking between DFT and photoemission experiments was outlined during the thesis. Meanwhile, DFT was also used in some cases to directly calculate the XPS binding energies, as discussed below.

2.2.1.2 *ab initio* binding energy calculation

Although DFT is built upon theorems acting on the ground state, part of its success is based on the capability to capture with significant accuracy properties of excited states. Exploiting the all-electron characteristic of the Wien2k code, it is possible to evaluate the core-level eigenvalues that are calculated within the self-consistent field convergence scheme [230]. In the literature, most studies employing binding energy calculations focused on the surface core-level binding energy shifts (SCLS) i.e. the shift in binding energy of an atom at the extreme surface with respect to the bulk material [231–238]. In the Li-ion battery field, this method is still rarely explored: to our knowledge, only two publications reported binding energy calculations by DFT for battery materials [140,239].

For an accurate prediction of the binding energy, the core-hole potential must be appropriately included in the calculation. Different schemes were proposed in the literature [230,240–242], among them, the Janak-Slater method was chosen for this thesis. The basic idea is to calculate the binding energy from the core-level eigenvalue for the electronic structure of the target material in which half a core-electron was removed. The basic theory and practical details of the method are given in **Annex B**. However, this method allows only to consider the partial screening of the core-hole potential. It does not allow to describe the many-body effects responsible for satellite peaks. Therefore, its application was limited to the study of O 1s peaks. For the transition metal core-level spectra, the CMT was used instead.

2.2.2 Cluster model theory calculations

The CMT is based on the *ansatz* that the investigated electronic properties of the material can be sufficiently well described considering not the whole solid but a local structure [43]. In fact, the Hamiltonian is defined for an atomic cluster (typically a central metal surrounded by ligand atoms), in contrast with the periodical boundary conditions of DFT.

The cluster model Hamiltonian is classically described by parameters for (1) hopping and onsite energies for the single electron interactions, (2) the electron-electron Coulomb interactions, and (3) the charge-transfer process. By including explicitly all electron-electron interactions for the correlated shell, the CMT is a many-body theory in contrast to single electron approaches such as DFT. This makes the CMT more appropriate for studying XPS satellites peaks, at the price of losing the *ab initio* character of DFT. In fact, the parameters entering in the calculation typically need to be tailored to the experiment. However, some methods were proposed in the literature for importing such parameters directly from *ab initio* calculations. In particular, a modified version of the method described by Haverkort et al [219] was adopted in this thesis. An extended description of the theory and all computational details are given in the **Annex E**. The general workflow is summarized below.

2.2.2.1 Building the Hamiltonian supported by *ab initio* methods

First, the converged electronic structure obtained by the GGA calculation was used to build the non-interacting part of the cluster Hamiltonian. To make this conversion, the periodical Kohn-Sham wave-functions were transformed to a localized basis set of maximally localized Wannier functions (MLWFs, detailed in **Annex C**). With the as-obtained MLWFs, a tight binding model Hamiltonian with band dispersion equivalent to the initial one of GGA is constructed. Its hopping and on-site energy terms were then extracted to describe the appropriate cluster model symmetry.

Second, for the electronic correlations and charge transfer energy, two approaches were used. The first is the more conventional one, in which the Hubbard U and charge transfer energy Δ were fitted to the experimental spectra. This method has been widely used in the literature and is considered a robust method for finding these parameters giving access to the microscopic properties of material [64,65,243,244]. Indeed, U and Δ describe important aspects of the physics of 3d transition metal compounds, as explained in **Section 1.3.2**.

Nevertheless, the dependence on empirical parameters can be an issue when the experimental data is affected by surface effects, as typical for battery materials. For this reason, an alternative method based on defining the model parameters from an *ab initio* technique was also explored. Starting from the wannierization mentioned above, the local Coulomb interactions were calculated by the constrained random phase approximation (cRPA) method. The basic principles of this method and computational details can be found in the **Annex D**. Eventually, the use of cRPA supported and overcame the initial methodology based on semi-empirical parameters derived by fitting the photoemission spectra.

2.2.2.2 Accessing ground state properties and spectra simulation

The cluster model Hamiltonian described above was solved via exact diagonalization, leading to the ground state many-body wave function for the target cluster system. Its properties were investigated by computing observables such as the average electron occupation for specific shells and their spin state, or the partial weight of each electronic configuration to the total wave function as $\Psi_{GS} = \alpha\left|d^n\right\rangle + \beta\left|d^{n+1}\boldsymbol{L}^{-1}\right\rangle + \gamma\left|d^{n+2}\boldsymbol{L}^{-2}\right\rangle$ ..., with n the formal occupation.

Furthermore, the excitations of the ground state were studied via the Green's function formalism. By setting up the appropriate excitation and final state Hamiltonian, both valence band and core-level photoemission spectra were simulated. Moreover, the spectral distribution of each configuration contributing to the total spectra was evaluated. In this way, a theoretical support to peak fitting analysis of transition metal core-level spectra could be established.

2.3 Chapter summary

In this chapter, the experimental and computational methods were described, highlighting the strong synergy between the two. The success of this combined approach lies on the nature of photoemission spectroscopy, for which a well-known background theoretical knowledge exists in the literature. **Figure 2.3.1** summarizes the general workflow adopted in this thesis. The use of XPS and HAXPES to perform non-destructive depth analysis is a central part of this method, as it allowed us to discriminate surface and bulk electronic states. However, the simulation of surface effects is a great challenge, which was not approached in this thesis. Instead, the study of surface-to-bulk changes were carried out with peak fitting methodologies. The analysis was supported by the interpretation of bulk-sensitive HAXPES spectra using a combination of computational techniques leading towards *ab initio* photoemission spectra simulations.

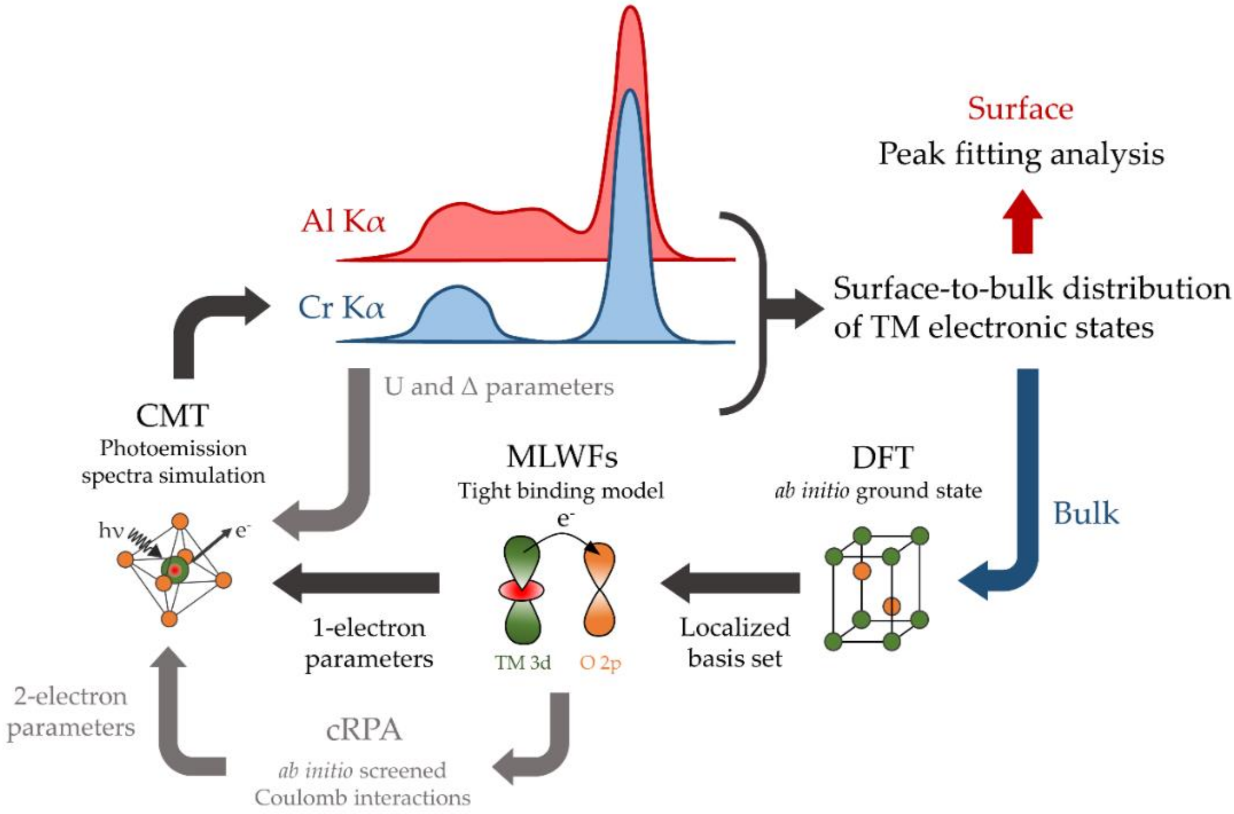

Figure 2.3.1 General methodology that combines experimental and theoretical photoemission spectroscopy as presented in this chapter.

Chapter 3

Surface and bulk signatures of pristine model electrode materials

In this chapter, we present an XPS and HAXPES study of pristine $LiCoO_2$, $LiNiO_2$, and Li_2MnO_3. The complementarity between Al Kα and Cr Kα X-ray sources and the use of quantification to disentangle the surface and bulk contributions are highlighted. The results outlined in this chapter will thus form the basis for the investigations dedicated to cycled materials. Since no chromium-based HAXPES characterization of these materials is present in the literature, the quantification results presented in this chapter are detailed to constitute a reference for upcoming studies. Finally, the analysis of transition metal 2p core level spectra will be discussed concerning the empirical peak fitting methods.

3.1 Choice of model systems

As discussed in **Section 1.4.3**, the role of each transition metal in $Li(Ni,Co,Mn)O_2$ lacks fundamental understanding, in particular concerning the electronic properties. A first step towards filling this gap consists of understanding the behavior of each transition metal independently. This motivates the choice of the three materials studied in this thesis: $LiCoO_2$, $LiNiO_2$, and Li_2MnO_3.

For the study of cobalt- and nickel-based redox compensation mechanism, the most natural choice was to take the related single transition metal layered oxide system, i.e. $LiCoO_2$ and $LiNiO_2$. The charge compensation mechanism of both cobalt- and nickel-based layered oxides is still under discussion in the literature, motivating the use of combined experimental and theoretical study to clarify the role of metal and oxygen (**Section 1.4.6**). Moreover, XPS data for the $LiNiO_2$ system is relatively scarce in the literature, in contrast to $LiCoO_2$. Because of the larger literature background for $LiCoO_2$, this system was the first to be investigated in this thesis and was used also to establish the experimental (and consequently, theoretical) protocols for the other two systems.

While the choice of $LiNiO_2$ and $LiCoO_2$ was quite straightforward, some comments are necessary for Li_2MnO_3. From a general point of view, manganese is considered inert in its IV oxidation state upon (de-)intercalation in NMC: its use is practically motivated by a stabilization of the crystal framework [18]. Since the objective of this thesis is to study the redox compensation mechanism in layered oxides, the study of a manganese–based system was limited to complement the results obtained for $LiNiO_2$ and $LiCoO_2$. However, manganese-pure layered oxides with $LiMnO_2$ stoichiometry are poorly stable and therefore their synthesis is quite challenging [245–247]. Thus, the choice for the manganese model system fell on the parent Li-rich system Li_2MnO_3. Beyond practical reasons, the choice of Li_2MnO_3 has two advantages:

1. It allows to study the MnO_6 cluster in an environment close to NMC materials, where Mn is in nominal IV (and not III) oxidation state (**Section 1.4.3**).
2. It is the forefather for the class of Li-rich oxides (**Section 1.4.5**), which are potential candidates for next-generation cathode materials and whose redox mechanism is proposed to involve oxygen.

Finally, the experimental study of $LiCoO_2$ as a model system was further simplified using binder-free thin films. Due to the unavailability of thin films for $LiNiO_2$ and Li_2MnO_3, powder samples were utilized instead. However, the use of binder and carbon additives in the composite electrodes required special precautions with respect to binder-free $LiCoO_2$ thin films. The structural characterization of all pristine electrode materials is reported in **Annex F**. See **Annex A** for general experimental details on XPS and HAXPES analysis.

3.2 Lab-based XPS and HAXPES characterization of pristine materials

3.2.1 Comparison of XPS and HAXPES survey spectra

Figure 3.2.1 shows the XPS and HAXPES survey spectra of pristine (a) $LiCoO_2$ thin films and (b) $LiNiO_2$ and (c) Li_2MnO_3 powders. All core-levels can be measured with the co-focalized dual source, allowing to investigate the electronic properties of the photo emitting ions at different depths, except for the transition metal 1s deep core levels. However, their binding energy are in the 8 keV range and therefore cannot be measured with the Cr Kα source.

Compared to the XPS survey spectra, two major features are missing in the HAXPES spectra: (1) the C 1s peak, due to both the surface localization of carbonaceous species and the low C 1s photoelectron cross-section and (2) the Auger peaks, because their kinetic energy is photon-energy independent and are thus shifted to larger binding energies in the HAXPES experiments (> 4000 eV). The large broadening and low intensity of the Auger peaks measured with the Cr Kα source impeded to use them as charge-correction reference as proposed in the literature [248].

Note that a scaling of 50 was applied to HAXPES spectra in **Figure 3.2.1**Figure 3.2.. Despite the high power used for Cr Kα photon extraction (50 W versus the 25 W used for Al Kα), the HAXPES signal intensity is about two orders of magnitude lower than that of XPS. In fact, while acquisition of XPS survey spectra typically required about 5 minutes, the noisier HAXPES spectra shown in **Figure 3.2.1** required at least one hour, hence taking significant part of beam time in each experiment. Therefore, HAXPES survey spectra were rarely measured throughout the thesis, in contrast to the common practice for XPS experiments, as they do not typically give much more information than the XPS survey spectra.

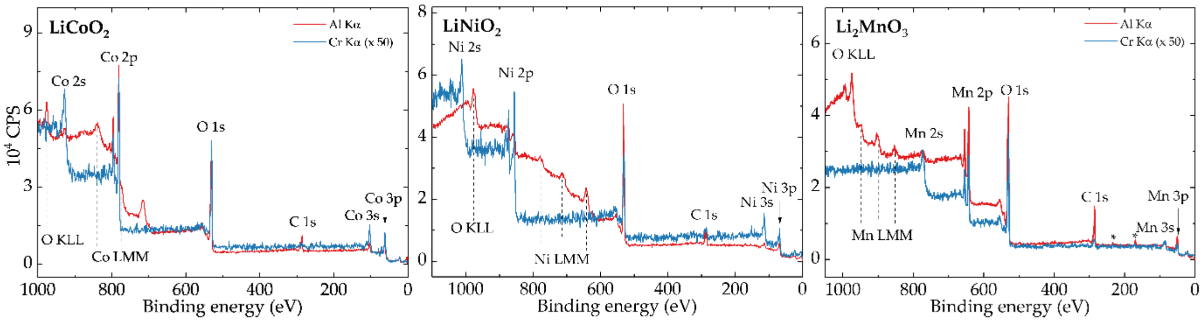

Figure 3.2.1 XPS (red line) and HAXPES (blue line) survey spectra for $LiCoO_2$ thin film (left-hand panel), $LiNiO_2$ powder (middle panel) and Li_2MnO_3 powder (right-hand panel).

3.2.2 $LiCoO_2$

The XPS and HAXPES core-level high-resolution spectra for $LiCoO_2$ thin films are shown in **Figure 3.2.2** and **Figure 3.2.3**, respectively. For comparison, bare $LiCoO_2$ and Co_3O_4 powders were also analyzed. The experimental data is shown as empty black dots while peak fit components and convolution are shown as black and red curves, respectively (when performed). A grey line is used for the background curve. In general, Shirley background was employed except for those cases in which it surpasses the experimental lineshape in the high-energy range (e.g. Co 2p XPS of $LiCoO_2$). For Co 3p and Co 2p core levels, a black curve is also used for better readability. The XPS and HAXPES quantification and peak assignment are shown in **Table 3.2.1** and **Table 3.2.2**, respectively.

The analysis below was based not only on reference materials but also on the large number of XPS studies for this material [75,108,109,163,166,249–256]. However, quantification aspects and (non-destructive) depth profiling are rarely discussed in the literature, making this analysis valuable to answer some discrepancies found in the literature even for this well-known material.

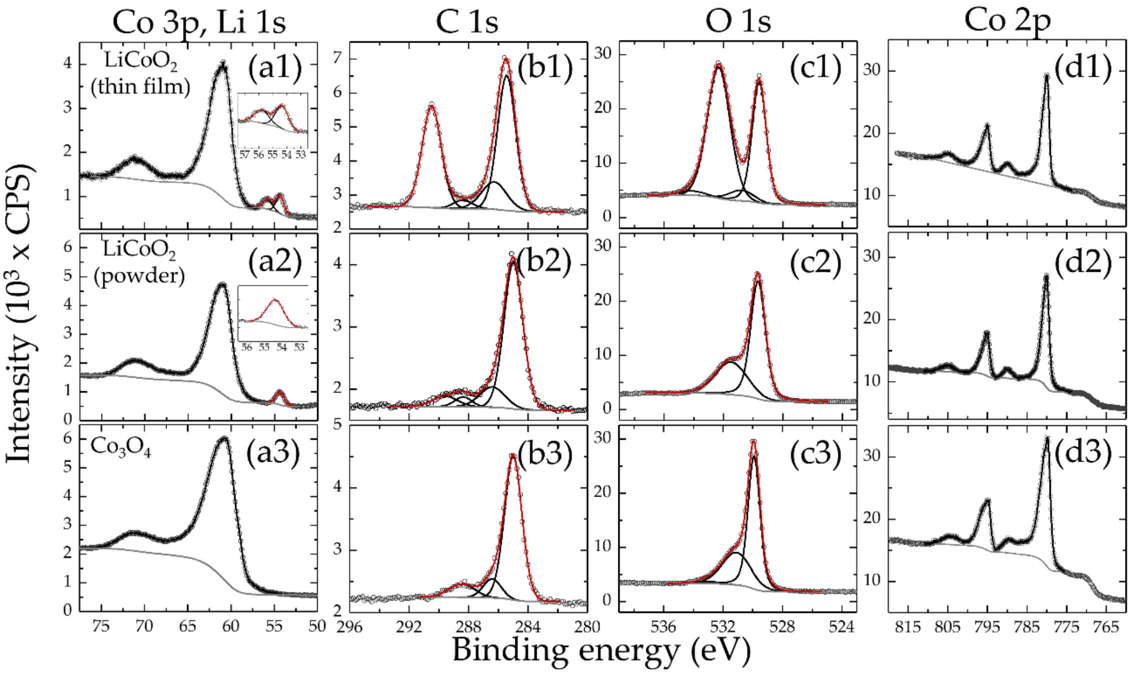

Figure 3.2.2 Core-level XPS spectra for LiCoO$_2$ thin film (first row from the top), LiCoO$_2$ powder (second row), Co$_3$O$_4$ powder (third row).

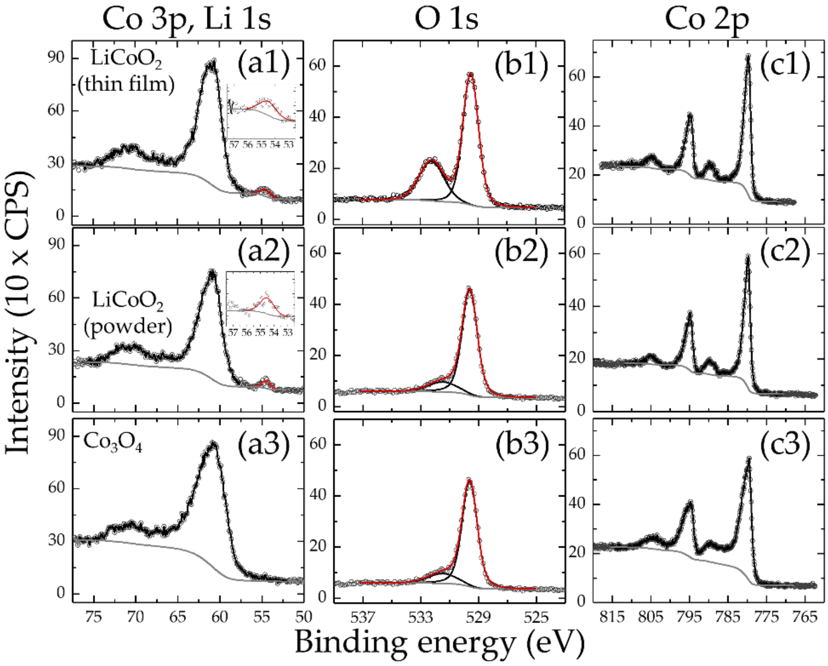

Figure 3.2.3 Core-level HAXPES spectra for LiCoO$_2$ thin film (first row from the top), LiCoO$_2$ powder (second row), and Co$_3$O$_4$ powder (third row).

Orbital	Assignment	$LiCoO_2$ (thin film)			$LiCoO_2$ (powder)			Co_3O_4		
		BE	FWHM	at %	BE	FWHM	at %	BE	FWHM	at %
Li 1s	$LiCoO_2$	54.3	1.1	9.4	54.4	1.1	13.3			
	Li_2CO_3	55.8	1.2	6.0						
Co 2p	$LiCoO_2$ (Co_3O_4)	780.0		9.2	780.1		12.4	60.5		32.4
Co 3p	$LiCoO_2$ (Co_3O_4)	60.9		10.1	61.0		20.8	779.9		19.9
O 1s	lattice	529.6	1.1	16.6	529.7	1.2	27.5	529.9	1.0	24.5
	surface	530.8	1.9	2.9	531.5	2.5	15.0	531.1	2.3	13.2
	CO_3^{2-}	532.3	1.8	25.8						
	C-O, C=O	533.5	2.1	2.0				533.1	1.9	0.7
C 1s	C - C	285.4	1.4	8.5	285.0	1.5	8.2	285.0	1.4	7.3
	C-O	286.3	2.0	2.4	286.4	2.0	1.5	286.4	2.0	1.0
	C=O	288.4	1.5	0.6	288.4	1.4	0.5	288.5	1.4	1.0
	CO_3^{2-}	290.5	1.5	6.7	289.6	2.0	0.8			

Table 3.2.1 Results of the XPS quantitative analysis for the series of cobalt oxide samples. Binding energies (BE) and full width at half maximum (FWHM) are reported in eV.

Orbital	Assignment	$LiCoO_2$ (thin film)			$LiCoO_2$ (powder)			Co_3O_4		
		BE	FWHM	at %	BE	FWHM	at %	BE	FWHM	at %
Li 1s	$LiCoO_2$	54.5	1.5	8.7	54.5	1.2	7.8			
Co 2p	$LiCoO_2$ (Co_3O_4)	779.7		18.9	779.8		14.7	779.5		20.1
Co 3p	$LiCoO_2$ (Co_3O_4)	60.6		18.2	60.8		14.8	60.5		17.4
O 1s	lattice	529.5	1.3	37.2	529.6	1.3	28.6	529.9	1.1	20.0
	CO_3^{2-}				531.5	2.3	4.7	531.1	2.3	4.0
	C-O, C=O	532.2	2.0	16.9				533.0	2.4	0.9
Co 2s	$LiCoO_2$ (Co_3O_4)				926.3		14.8	926.8		18.2
Co 3s	$LiCoO_2$ (Co_3O_4)				102.7		14.5	102.3		19.6

Table 3.2.2 Results of the HAXPES quantitative analysis for the series of cobaltite samples. Binding energies (BE) and full width at half maximum (FWHM) are reported in eV.

3.2.2.1 Co 3p and Co 2p core levels

The Co 3p and Co 2p spectra give a perfect example of the theory presented in Section 2.1.2 as they both show a charge transfer satellite at about 10 eV with respect to the main line. For the Co 2p core level, the spin-orbit coupling separates the $2p_{3/2}$ and $2p_{1/2}$ by about 15 eV. We note that the satellite structure of $LiCoO_2$ and Co_3O_4 is slightly different, reflecting the different electronic structure of cobalt ions in the two systems. While a single peak is observed in $LiCoO_2$, a broader structure is measured for Co_3O_4, suggesting the presence of at least a second peak between the main line and the high-energy satellite (~785 eV) that can be related to the Co^{II} ions. This is corroborated by the spectra for CoO, for which the large satellite peak is found at the same position [257,258].

Indeed, while $LiCoO_2$ formally consists of Co^{III} ions only, a 2:1 mixture of Co^{III} and Co^{II} ions is expected for Co_3O_4. However, it is difficult to move beyond this qualitative interpretation and relate a specific Co 2p spectral shape to a certain Co^{III}/Co^{II} ratio. This is due to the strong influence from the specific electronic environment of the emitting cobalt ion, making difficult to distinguish different electronic states in the experimental spectra.

The comparison between XPS and HAXPES spectra and quantification shows the influence of Auger lines in Co 2p spectra at 770 eV and different surface sensitivity between the shallow Co 3p and deep Co 2p core levels. While a Shirley background function was employed in most cases for defining the quantification region, this was not possible for the XPS spectrum measured for the pristine $LiCoO_2$ thin film, as it would appear above the experimental curve.

Moreover, the overlap with Auger lines can influence the quantification obtained from this core level for all samples. However, this cannot solely account for the differences between the Co at% obtained for Co 3p and Co 2p core levels (**Table 3.2.1**). Note indeed that, for the powder samples, the difference exceeds the expected error for XPS quantification of few at%. Instead, the HAXPES results in **Table 3.2.2** show minimal changes between the quantification results for all core-levels (even including the Co 3s and Co 2s peaks).

It is concluded that the main responsible for the mismatch in the Co 3p and 2p XPS quantification is the different depth probed by the two measures. In fact, the probing depth estimated for the XPS experiments is 3.2 and 5.5 nm for Co 2p and Co 3p, respectively, while it is 14.2 and 16.2 nm for the HAXPES. This implies that there is a relative difference of about 40 % in the depths probed with the Al Kα source when measuring the two core levels. However, the difference narrows to about 10 % with the Cr Kα source. This suggests that the Co at% is not constant within the XPS probing depth of about 5 nm.

3.2.2.2 Li 1s core level

The Li 1s spectra are found at the low binding energy side to the Co 3p core level. From the comparison with the Li-free Co_3O_4 sample, the low-binding energy tail of the Co 3p main line overlaps with the Li 1s. This poses a question for the definition of the background region. The most accurate method would be to define one unique region for both core levels. However, this requires separating the contribution of the Co 3p tail from the Li 1s fit model, which is no trivial. Here, the approach was to simply separate the Li 1s and Co 3p regions by two subsequent Shirley background curves. Therefore, a slight Li at % underestimation may be expected.

In the $LiCoO_2$ powder, the single symmetric peak at 54.4 eV (54.5 eV with HAXPES) was assigned to the Li ions in the layered structure. A second peak at 55.8 eV was measured for the thin film. This additional contribution is only present in the XPS spectrum, suggesting that the species giving this additional contribution are located at the extreme surface. Indeed, it was assigned to Li_2CO_3, a common surface impurity in battery materials (**Annex F**). This interpretation matches well with quantification results and is consistent with the absence of related C 1s and O 1s contributions for the powder sample. Nevertheless, the binding energy of 55.8 eV is larger than the typically reported value in the literature (about 55 eV [166,249]) and to the value of 55.4 eV measured for the bare Li_2CO_3 powder (**Annex F**). This is an example of the unreliability of absolute values for the surface species present on battery materials as discussed in **Annex A**. In fact, despite the binding energy shift of about 0.4 eV, the separation between the Li 1s, C 1s, and O 1s peaks assigned to Li_2CO_3 is consistent with that measured for the reference Li_2CO_3 sample.

A second aspect is observed in the Li 1s HAXPES spectra. The peak related to $LiCoO_2$ appears broader and is slightly shifted by 0.1-0.2 eV to the higher binding energy side. These effects are characteristic for the recoil effect in HAXPES experiment [213]: the momentum of the incident photon is transferred into the ion that ejects a photoelectron with momentum $p_e = \sqrt{2m_eE_{kin}}$. With harder X-rays and larger E_{kin}, the difference between initial and final momentum of the emitting ion becomes significant. Adopting a simple model of a gaseous atoms M, the binding energy shift is estimated as $\Delta E_B = \frac{m}{M}\langle E_{kin}\rangle$ [213]. By substituting into the equation above M = 6.941 u for the Li atoms and the kinetic energy of the Li 1s photoelectron excited by Al Kα and Cr Kα photons (1486.6 and 5414.8 eV, respectively), we obtain ΔE_B = 0.11 and 0.42, respectively. This leads to a shift of about 0.3 eV, slightly larger than the experimental one but within the experimental resolution.

Both the surface-bulk differential charging and the recoil effect have an important practical consequence for the data analysis and interpretation, which can be generalized to any core-level analysis: one cannot expect the binding energy position of a chemical species measured by XPS and HAXPES to be the same. This important aspect is linked to the binding energy correction for insulating samples, which is commonly performed to the C 1s spectra in the Li-ion battery community.

3.2.2.3 C 1s core level

The C 1s XPS spectra were fitted with four components related to different bonding states for the carbonaceous surface species. The peaks are assigned to C-C bond of adventitious carbon at ~285 eV, C-O environments at ~286.5 eV, C=O at ~288 eV, and finally O-C=O or CO_3^{2-} at about 289-290 eV. It is common practice in the Li-ion battery community to refer the binding energy scale of insulating samples to the peak at 285 eV (although for historical reasons, some refer it to 284.6 or 284.8 eV). However, this procedure might induce misinterpretation of the spectra due to differential charging effect [259,260].

Being already questionable for the XPS spectra, this method becomes impracticable for HAXPES analysis. In fact, the C 1s signal intensity was generally very low because of the low photoelectron cross-section and the surface localization of carbon-containing species. Even after relatively long acquisition time (1-2 hours) and by increasing the pass energy, the signal intensity was too low for reliable analysis. Therefore, as for the survey HAXPES data, the routine experiments did not involve measuring the C 1s HAXPES spectra. Moreover, due to the different electronic state between the extreme surface and the layers beneath probed by HAXPES, referencing the HAXPES data to the C-C XPS peak was not considered as first choice. Note in fact that, for cycled samples retrieved at different state of charge, binding energy shifts of both the layered oxide and the surface species can be present. Other strategies were adopted to be able to distinguish the binding energy shifts of the bulk layers, depending on the electrode material.

For the $LiCoO_2$ thin films, the binding energy was referred to the Fermi level of the platinum layer. This approach assumes that the Fermi level of the bottom $LiCoO_2$ layer is well aligned to the metal substrate and does not change significantly over the 20 μm of thickness. For $LiCoO_2$, which is a semiconductor with a room temperature conductivity of 10^{-4} - 10^{-6} S/cm (depending on the Li/Co stoichiometry [261,262]), the approximation is reasonable. Indeed, the binding energies of the core levels peaks assigned to $LiCoO_2$ agree well with the literature overall. Yet, a shift of 0.5 eV was obtained for the C-C peak and observed to slightly change within this range for other $LiCoO_2$ thin film samples. For the reference powders, in absence of metallic contact, the typical approach was instead to first set the C 1s XPS peak at 285 eV. Then, the HAXPES data were shifted to the O 1s position of the low binding energy peak measured in the charge corrected XPS spectra. Eventually, this led to differences between $LiCoO_2$ powder and thin film of ~0.1 eV i.e. within the experimental resolution.

3.2.2.4 O 1s core level

In all samples, the high-energy components of the O 1s spectrum decrease by probing deeper with the Cr Kα X-rays, indicating they are all surface-related components, while the bulk signal (i.e. oxygen in the layered lattice) is mostly related to the peak at 529.7 eV[5]. In fact, for both $LiCoO_2$ samples, an O/Co stoichiometry of 2:1 is obtained when considering the ratio between this component and any Co core level with HAXPES. On the contrary, the same calculation for XPS results suggests oxygen deficiency in the first nanometers.

For the thin film, the intensity of the peak at 532.3 eV is attributed to Li_2CO_3 contamination layer, in agreement with Li 1s and C 1s XPS analysis. The interpretation holds for both XPS and HAXPES spectra considering the lower photoelectron cross section for Li 1s and C 1s photoemission with our HAXPES instrument. This highlights the importance of considering both the larger depth sensitivity and different photoelectron cross-sections for HAXPES analysis.

The higher-energy peaks for the $LiCoO_2$ powder and thin film are not the same. For the powder sample, a single peak at 531.5 eV and relatively high intensity in the XPS spectrum cannot be explained by surface adsorbed species such as Li_2CO_3, due to the absence of the related Li 1s and C 1s components. Note that, in contrast to $LiCoO_2$ thin films which were stored and prepared in protected environment, the $LiCoO_2$ and Co_3O_4 powders were handled in ambient conditions. Therefore, the high-energy peak observed for the two powder samples is probably related to hydroxyls groups of adsorbed water [263].

However, a model for the O 1s XPS spectra for the pristine thin film with only two peaks resulted in bad fit of the experimental curve, especially for the valley at about 530 eV. Therefore, the final model includes a peak at 533.5 eV, related to carbon-oxygen bonds (in agreement with the C 1s analysis) and a peak at 530.8 eV. Note that the assignation of this peak is non-unique in the literature (**Table 3.2.3**): it was attributed to cobalt hydroxide groups, lithium alkylates, and finally oxidized oxygen in delithiated samples. Indeed, this peak will be at the center of the discussion in the next chapter. The hypothesis of surface hydroxide groups or more generally surface defects is the most consistent with our work, including both the cycling data and the study of $LiNiO_2$ and Li_2MnO_3, as discussed below.

---

[5] For the lineshape of the O_{latt} peak, a numerical approximation of Voigt function [LF(1,1,70,450) in CasaXPS] was employed instead of the generally used pseudo-Voigt product function [GL(30)]. We found this model improved the fitting of the low binding energy-tail of the O_{latt} peak without significantly affecting the rest of the fit model, as shown in the example given in **Annex F**. This approach was maintained along this thesis for the analysis of all transition metal oxides.

Ref.	Sample	Peak #1		Peak #2			Peak #3		
		BE	Assignation	BE	ΔBE	Assignation	BE	ΔBE	Assignation
Dupin et al	powder	529.5	lattice	531.5	2	subsurface			
Dahéron et al	pellet	529.7	lattice	530.3	0.6	oxidation(1)	531.6	1.9	subsurface
Schulz et al	thin film	529.8	lattice	530.8	1	hydroxide(2)	531.5	1.7	subsurface
Gauthier et al	thin film	529.7	lattice	530.9	1.2	ROLi	531.9	2.2	Surf/CO_3^{2-}

Table 3.2.3 Comparison of O 1s peak fit models in the literature. For better comparison, all binding energy positions were shifted to match the 285 eV calibration. ΔBE is the binding energy difference between the second or third peak to the first one. (1) Measured for cycled samples. (2) Measured for air-exposed samples.

3.2.2.5 Surface stoichiometry

The cobalt atomic concentrations obtained from Co 3p and 2p core levels were averaged to account for the significant difference in IMFPs for an XPS experiment and approach that of O 1s, which lies in between. In fact, the IMFPs calculated for Co 3p, O 1s and Co 2p photoelectrons excited by the Al Kα source and moving through LiCoO2 are 2.6 nm, 1.9 nm, and 1.5 nm, respectively. Based on this averaged value, the relative concentrations of Li and O were calculated based on the Li 1s and O 1s peaks assigned to the ions in the crystal lattice. Finally, these Li/Co and O/Co ratios were normalized by setting the relative Co concentration to the nominal stoichiometry value. The results are shown in Table 3.2.4.

	XPS	HAXPES
$LiCoO_2$ powder	$Li_{0.8}CoO_{1.7}$	$Li_{0.5}CoO_{1.9}$
$LiCoO_2$ thin film	$Li_{1.0}CoO_{1.7}$	$Li_{0.5}CoO_{2.0}$
Co_3O_4	$Co_3O_{2.8}$	$Co_3O_{3.2}$

Table 3.2.4 Surface stoichiometry of cobalt oxide samples estimated by XPS and HAXPES quantification.

Taking the nominal composition as a reference, the results from XPS and HAXPES analysis go in opposite directions regarding the Li/Co and O/Co ratios. In the latter case, the O/Co generally increased, approaching the formal stoichiometry for the $LiCoO_2$ samples. Instead, the Li/Co decreased. However, a lower Li concentration when probing deeper into the material is suspicious. This unexpected result can be explained instead by the expected underestimation of Li with the peak fitting model used here. Due to large difference in the Li 1s RSFs for XPS and HAXPES, a larger underestimation is to be expected in the latter case.

3.2.3 $LiNiO_2$

The XPS data for pure $LiNiO_2$ is limited in the literature: to our knowledge, very few papers resolved simultaneously Li 1s, O 1s, and Ni core levels and none performed quantitative analysis [167,169,264–267]. As pointed out by some authors, the soft X-rays could not probe throughout the relatively thick surface layers developing on pristine $LiNiO_2$ surface [268,269]. Due to chemical affinity, the published XPS studies on Ni-rich NMC was also considered. These mostly focused on one specific aspect, such as studying the surface contamination layer [162,165,270] or quantifying the $Ni^{II/III}$ ratio [215,267,271–274]. Recent articles discussed the methodology challenges of XPS characterization of Ni-based layered oxides with the Al Kα source. They highlighted the overlap between the F KLL and Ni 2p lines that is sometimes disregarded in the literature [214,215] and the importance of quantification to characterize such a reactive material [168]. Therefore, the present XPS and HAXPES study of high-quality $LiNiO_2$ powder and pristine electrode samples can offer an important reference for the community. To prepare the electrochemically delithiated Li_xNiO_2 materials, commercial-grade electrodes consisting of mixture of PVDF binder, carbon black additive and $LiNiO_2$ active material powder were used. The presence of binder and carbon black was considered by optimizing the sample preparation and measurement conditions, as detailed in **Annex F**.

The data analysis was carried out with support of three other reference nickel compounds: NiO, $Ni(OH)_2$, and $NaNiO_2$. Their core-level XPS and HAXPES spectra are shown in **Figure 3.2.4** and **Figure 3.2.5**. XPS and HAXPES quantification results are shown in **Table 3.2.5** and **Table 3.2.6**. NiO and $Ni(OH)_2$ were compared to $LiNiO_2$ to get further insights on its surface stability and distinguish the XPS signal of nickel ions in different (but structurally close) local environments.

In both $LiNiO_2$ and $NaNiO_2$, Ni is formally in III oxidation state with a Jahn-Teller active $t_{2g}^6e_g^1$ electronic structure. However, the long-range distortion is observed only for $NaNiO_2$, whereas only local, non-cooperative distortions were measured for $LiNiO_2$ (**Section 1.4.2**). This difference led to several theoretical studies, aimed to understand the nature of $LiNiO_2$ ground state (**Section 1.4.4**). Instead, experimental insight on the local electronic structure is missing overall. To our knowledge, only an ArXiv preprint is available on this topic, based on XAS data [275]. Moreover, the XPS literature on $NaNiO_2$ is very limited: only one publication has been found, showing just the Ni $2p_{3/2}$ spectra for $LiNiO_2$ and $NaNiO_2$ [264]. For this reason, the $NaNiO_2$ powders were synthesized within internal CEA collaboration for this XPS and HAXPES study.

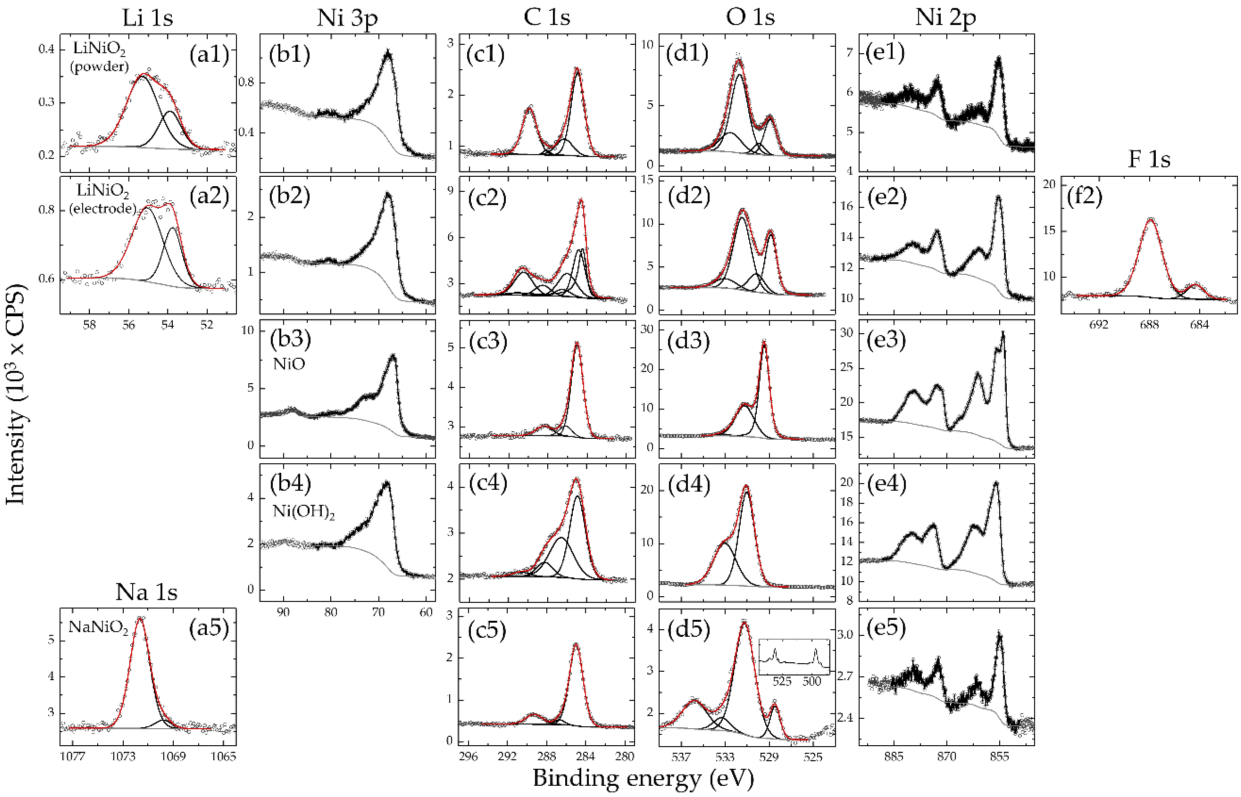

Figure 3.2.4 Core-level XPS spectra for LiNiO$_2$ powder (first row from the top), LiNiO$_2$ electrode (second row), NiO (third row), Ni(OH)$_2$ (fourth row), and NaNiO$_2$ (fifth row).

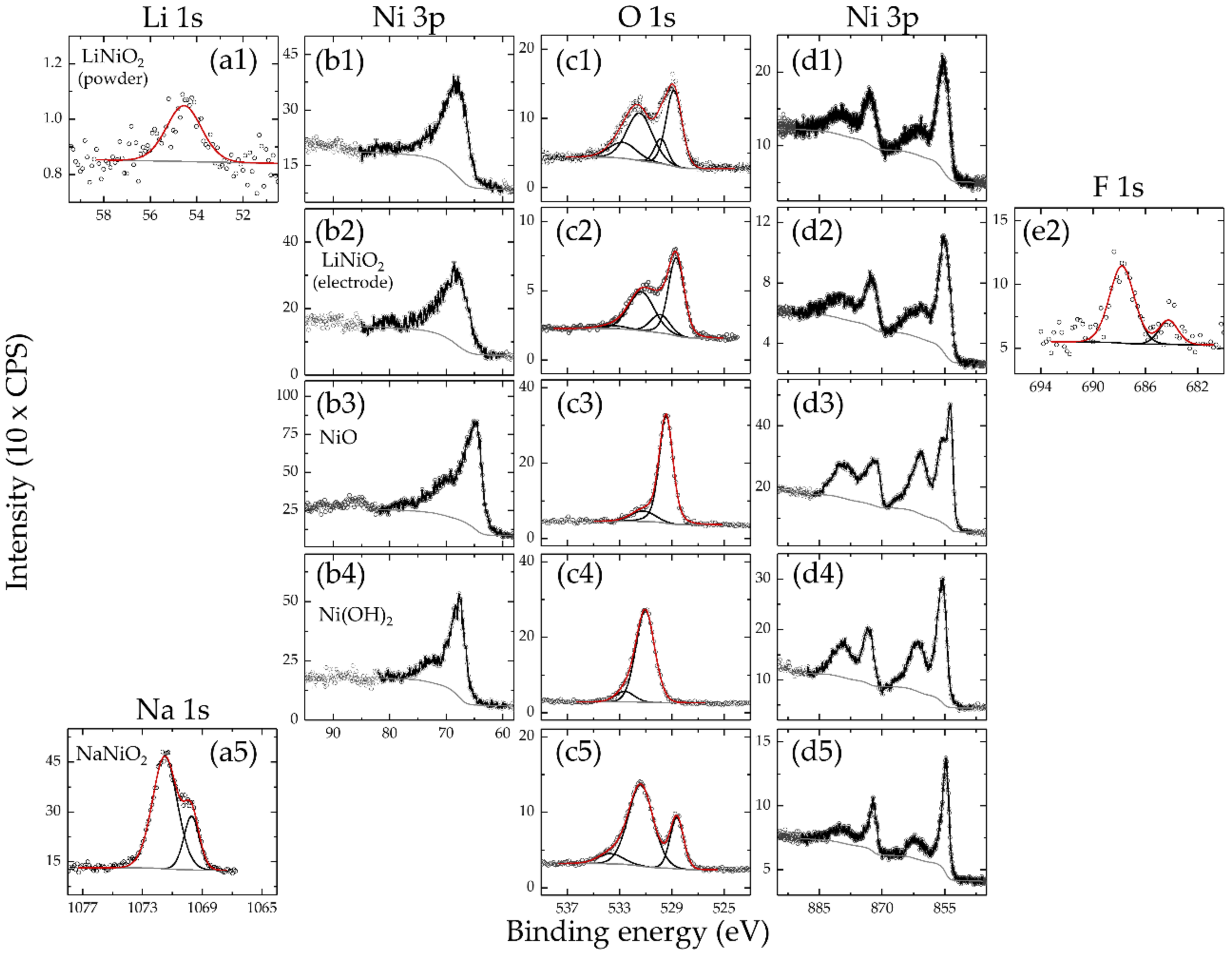

Figure 3.2.5 Core-level HAXPES spectra for LiNiO$_2$ powder (first row from the top), LiNiO$_2$ electrode (second row), NiO (third row), Ni(OH)$_2$ (fourth row), and NaNiO$_2$ (fifth row).

Orbital	Assignation	$LiNiO_2$ powder			$LiNiO_2$ electrode			NiO			$Ni(OH)_2$			$NaNiO_2$		
		BE	FWHM	at %	BE	FWHM	at %	BE	FWHM	at %	BE	FWHM	at %	BE	FWHM	at %
Li 1s	**$LiNiO_2$**	53.9	1.3	4.7	54.1	1.7	4.7									
	Li_2CO_3, LiOH, LiF	55.3	1.9	12.7	55.5	2.0	6.0									
Na 1s	**$NaNiO_2$**													1069.8	1.5	1.1
	Na_2CO_3, NaOH													1071.7	1.8	16.9
Ni 3p	**$LiNiO_2$**	68.2		6.5	68.1		5.5	66.8		19.7	68.1		14.3			
Ni 3s	**$LiNiO_2$**	112.8		10.6				111.9		33.2	113.1		24.8			
Ni 2p	**$LiNiO_2$**	855.2		4.5	855.3		6.8	854.1		16.3	856.1		13.3	855.3		3.1
O 1s	**lattice**	528.9	1.4	7.7	528.8	1.2	4.6	529.5	1.1	15.6	531.0	1.7	21.9	528.5	1.1	3.8
	surface	529.9	1.2	2.1	529.9	1.7	2.8	531.3	2.0	9.1	533.0	2.4	14.0			
	CO_3^{2-}, O=C-O, Ni-OH	531.7	1.8	22.7	531.5	1.9	12.1	533.3	1.5	0.4				531.2	2.2	25.4
	C-O, C=O	532.5	2.3	7.1	533.1	2.5	5.1							533.3	1.8	2.4
	Na KLL Auger													535.8	2.6	7.8
C 1s	**C=C (carbon black)**				284.5	1.0	5.6									
	C-C	284.9	1.6	11.3	284.8	1.6	9.2	285.0	1.4	4.5	284.9	1.9	6.0	285.0	1.6	33.0
	CH_2 (pvdf)				286.3	2.3	8.5									
	C-O	286.3	2.0	2.8	286.4	1.8	2.8	286.2	1.5	0.5	286.6	2.9	4.4	286.7	1.2	1.4
	C=O	288.1	0.8	0.3	288.5	1.9	2.0	288.4	2.0	0.7	288.3	1.9	1.1			
	CO_3^{2-}	289.9	1.8	7.0	290.5	1.0	0.4				290.7	2.0	0.3	289.3	2.0	5.0
	CF_2 (pvdf)				290.8	2.3	8.5									
F 1s	**CF_2 (pvdf)**				688.0	2.3	14.7									
	LiF				684.6	1.4	0									

Table 3.2.5 XPS quantification results for the series of nickelate samples. Binding energies (BE) and full width at half maximum (FWHM) are reported in eV.

Orbital	Assignation	$LiNiO_2$ powder			$LiNiO_2$ electrode			NiO			$Ni(OH)_2$			$NaNiO_2$		
		BE	FWHM	at %	BE	FWHM	at %	BE	FWHM	at %	BE	FWHM	at %	BE	FWHM	at %
Li 1s	$LiNiO_2$	54.6	1.8	10.1												
	Li_2CO_3, LiOH, LiF															
Na 1s	$NaNiO_2$													1069.7	1.2	8.3
	Na_2CO_3, NaOH													1071.5	2.0	27.9
Ni 3p	$LiNiO_2$	67.9		13.3	68.6		10.8	64.5		22.9	67.8		17.4			
Ni 3s	$LiNiO_2$	112.7		13.3	112.5		11.1	109.4		24.0	113.0		17.8			
Ni 2p	$LiNiO_2$	855.7		13.1	855.3		10.9	851.6		25.6	855.4		21.1	854.8		7.9
Ni 2s	$LiNiO_2$	1011.1		9.2												
O 1s	lattice	528.8	1.4	15.6	528.8	1.4	12.0	527.4	1.2	23.7	531.0	1.7	39.3	528.6	1.2	13.0
	surface	529.8	1.2	4.1	530.0	1.5	5.0	529.2	2.2	3.8	532.6	1.7	4.5			
	CO_3^{2-}, O=C-O, Ni-OH	531.5	2.3	15.6	531.5	2.0	10.7							531.4	2.2	38.0
	C-O, C=O	532.8	2.5	5.7	533.1	2.5	4.0							533.7	2.3	4.8
C 1s	*				285.1		28.9									
F 1s	CF_2 (pvdf)				687.9	2.4	6.0									
	LiF				684.5	1.3	0.4									

Table 3.2.6 HAXPES quantification results for the series of nickelate samples. Binding energies (BE) and full width at half maximum (FWHM) are reported in eV.

3.2.3.1 Ni 3p and 2p core levels

In general, we found that the Ni $2p_{3/2}$ core peak was the most sensitive among Ni core levels to changes in electronic structure. For the Ni $2p_{1/2}$ and Ni 3p core levels, this was explained by the shorter core-hole lifetime due to Coster-Kronig and Auger processes. These core-hole relaxation processes increase the intrinsic contribution to the FWHM of the photoelectron peak. Instead, the Ni $2p_{3/2}$ core level spectra are highly sensitive to the local electronic state of Ni ions in each system. All materials are characterized by core level spectra constituted by a main line at 855 eV and a satellite structure at 5-6 eV higher in binding energy. However, inspection of the spectra reveals characteristic details for each compound. As observed for other transition metal (hydr-)oxides, the relative intensity of the satellite peak decreases with higher oxidation state. Moreover, the main line is different between NiO and $Ni(OH)_2$, both formally at Ni^{II} oxidation state. The doublet in NiO has been explained by the non-local screening process (see **Annex A** for details).

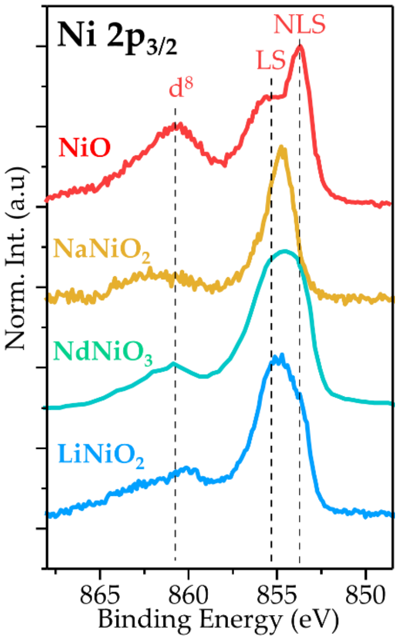

Figure 3.2.6 Ni $2p_{3/2}$ HAXPES spectra of NiO, $NaNiO_2$, $NdNiO_3$, and $LiNiO_2$. The data for $NdNiO_3$ was taken from ref. [276], the synchrotron HAXPES spectra acquired at 9.5 keV was used for $LiNiO_2$ (see Section 3.3.2.3 for details), and lab-based HAXPES spectra are shown for NiO and $NaNiO_2$. The dotted lines are referred to the main final states for NiO (LS: local screening, NLS: non-local screening).

The subtle differences between $LiNiO_2$ and $NaNiO_2$ are highlighted in **Figure 3.2.6**. An asymmetry at low binding energies is observed for $LiNiO_2$, and the satellite peak of $NaNiO_2$ is narrower and centered at higher binding energies. In the figure, the Ni $2p_{3/2}$ spectra for $NdNiO_3$ was also added (digitalized from ref. [276]), showing its similarity to that of $LiNiO_2$. A recent study proposed $NdNiO_3$ to be a negative charge-transfer system, i.e. the electronic structure is overall described as $3d^8\mathbf{L}$ [115]. Noting that the same has been proposed for $LiNiO_2$ (see **Section 1.4.4**), the comparison shown in **Figure 3.2.6** supports this theory. Eventually, our theoretical study presented in **Chapter 5** will corroborate this qualitative conclusion. This can explain why the satellite peak of $LiNiO_2$, $NdNiO_3$, NiO, and $Ni(OH)_2$ are all found at almost the same position.

With respect to $LiCoO_2$, the Ni 3p and Ni 2p peak quantification did not suffer significantly from the overlapping lines except for the F KLL peak in the electrode sample. The mechanical scratching procedure effectively reduced this contribution, which is treated as negligible by comparison with the reference spectra for pure PVDF sample (**Annex F**).

3.2.3.2 Li 1s and Na 1s core levels

The overall structure of Li 1s and Na 1s for the $LiNiO_2$ and $NaNiO_2$ samples is the same and resembles that measured for the $LiCoO_2$ thin film. The spectra were fitted with two peaks, related to alkali ion in the host oxide and to surface species. From the C 1s and O 1s analysis, these mostly consisted of carbonates (see **Annex F** for $NaCoO_3$ reference spectra and quantification). However, the F 1s spectra for the electrode sample revealed a small fraction of LiF. In the literature, Li_2CO_3 and LiF were distinguished by a ~1 eV binding energy difference. However, in this thesis we adopted the simpler two-peaks model and accounted for these contributions by a single peak due to the low sensitivity for the Li 1s spectra. Any attempt of measuring the Li 1s signal for $LiNiO_2$ electrode by HAXPES failed, due to the decreased sensitivity by the presence of matrix elements in the sample.

3.2.3.3 C 1s and F 1s core levels

The same model used for the $LiCoO_2$ was adopted for the C 1s peak of all powder samples. It is noteworthy that, with respect to $LiCoO_2$, a larger concentration of carbonates was found for $LiNiO_2$. Extracting information on $LiNiO_2$ surface species from the C 1s spectrum of $LiNiO_2$ electrode is more challenging, due to the significant contributions from PVDF and carbon black. The two materials were characterized individually to extract the characteristic spectral signatures (**Annex F**). The C 1s of carbon black consists of an asymmetric peak at ~284.5 eV and a weak satellite at 291 eV. The convolution of the experimental spectra was used as spectral lineshape of this component in the composite electrode. For the PVDF, the CF_2 and CH_2 groups were fitted with two peaks separated by 4.5 eV and for which the intensity and FWHM were constrained to be the same. The F 1s spectra of the electrode sample shows a large peak at 688 eV, related to CF_2 groups in PVDF, and a lower binding energy peak at 684 eV, related to LiF. The presence of this component already before cycling can be explained by the acid-base reaction between the PVDF and the basic $LiNiO_2$ or Li_2CO_3. The results of C 1s and F 1s quantification were checked for consistency with regards to the PVDF quantification. Despite such precautions, the complexity of the C 1s fit makes it overall unreliable for quantitative analysis. For this reason, investigation of carbonaceous surface species for the electrode samples was not carried out, focusing instead on the $LiNiO_2$ surface and bulk material instead.

3.2.3.4 O 1s core level

The O 1s XPS and HAXPES spectra were generally fitted with the same model as for the $LiCoO_2$ thin film. The four components were assigned to analogous contributions. Note that the O 1s peak at ~530 eV assigned to surface contributions is in this case very close to the peak measured for NiO. However, it is noteworthy that its relative intensity to the main peak at 528.8 eV is larger than that measured for the $LiCoO_2$ thin film.

3.2.3.5 Surface stoichiometry

The quantitative analysis of $LiNiO_2$ powder and electrode indicate a large deviation from the ideal stoichiometry for both XPS and HAXPES quantification. **Table 3.2.7** summarizes the surface stoichiometries calculated for $LiNiO_2$. The O/Ni stoichiometries obtained for the reference NiO and $Ni(OH)_2$ compounds match well the attended values with both sources. For $NaNiO_2$, instead, the results are similar (but better) than $LiNiO_2$: the stoichiometry is closer to the nominal bulk value with increasing depth sensitivity. However, note that the quantification from the XPS spectrum of $NaNiO_2$ is influenced by the Na KLL Auger lines, overlapping the O 1s peak. Therefore, the analysis highlights that the surface of $LiNiO_2$ particles suffered severe deoxygenation, to the point that the O 1s peak at 530 eV has to be included in the quantification. However, this requires separating Ni surface and bulk contributions, as will be described in **Section 3.3.2.3**.

	XPS	**HAXPES**
$LiNiO_2$ Powder	$Li_{0.9}NiO_{1.4}$	$Li_{0.8}NiO_{1.2}$
$LiNiO_2$ Electrode	$Li_{0.8}NiO_{0.7}$	$Li_{x.x}NiO_{1.1}$
NiO Powder	$NiO_{0.9}$	$NiO_{1.0}$
$Ni(OH)_2$ Powder	$Ni(OH)_{1.6}$	$Ni(OH)_{2.1}$
$NaNiO_2$ Powder	$Na_{0.4}NiO_{1.2}$	$Na_{1.8}NiO_{1.6}$

Table 3.2.7 Surface stoichiometry of nickel oxide samples estimated by XPS and HAXPES quantification.

3.2.4 Li_2MnO_3

In contrast to the previous materials, a few HAXPES characterizations were carried out for Li_2MnO_3 in the literature. As for other Li-rich systems (see **Section 1.4.5**), the O 1s HAXPES spectra of pristine and charged materials were analyzed to infer on the lattice oxygen oxidation [277–279]. However, as pointed out in Ref. [131], the contribution of surface degradation should be accounted for correct interpretation. All HAXPES characterization of Li_2MnO_3 were synchrotron-based and did not include quantification. Lab-based XPS quantitative analysis with conventional Al Kα source was carried out by Quesne-Turin et al. [280]. In line with our results for $LiCoO_2$ and $LiNiO_2$, they highlighted a large difference from ideal stoichiometry at extreme surface and the different results obtained with Mn 2p and Mn 3p core levels. The XPS and HAXPES core levels for Li_2MnO_3 bare powder, pristine electrode and reference MnO_2 powder are shown in **Figure 3.2.7** and **Figure 3.2.8**. The results of quantitative analysis are reported in **Table 3.2.8** and **Table 3.2.9**.

3.2.4.1 Mn 2p, Mn 3p, and Mn 3s core levels

The Mn $2p_{3/2}$ (642.3 eV) and Mn $2p_{1/2}$ (653.8 eV) are separated by a spin-orbit splitting of ~11.5 eV. A third peak at 665.7 is also visible in both XPS and HAXPES spectra for all materials. Cluster model simulations by Morita et al. indicate that this peak is a weak charge-transfer satellite for the Mn $2p_{1/2}$ [279]. An analogous satellite for the Mn $2p_{1/2}$ peak should be also present at about the same position of the Mn $2p_{1/2}$ peak. The Mn $2p_{3/2}$ main line present a doublet [279,280] undetectable with the present energy resolution of ~0.7 eV (with XPS). Another possible explanation is the partial reduction of Mn^{IV} to Mn^{III}, as in MnO(OH) [281], but the low binding energy tail should be shifted to lower binding energies (about 640 eV) [131,281], which is not observed here.

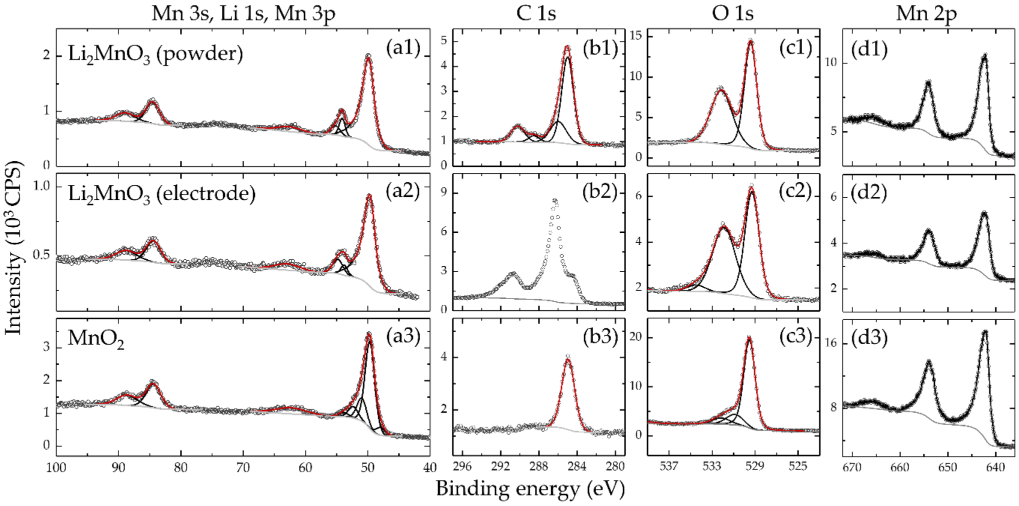

Figure 3.2.7 Core level Mn 3s, Li 1s, Mn 3p, C 1s, O 1s, and Mn 2p XPS spectra of Li_2MnO_3 powder (top row), Li_2MnO_3 electrode (middle row) and reference MnO_2 powder (bottom row).

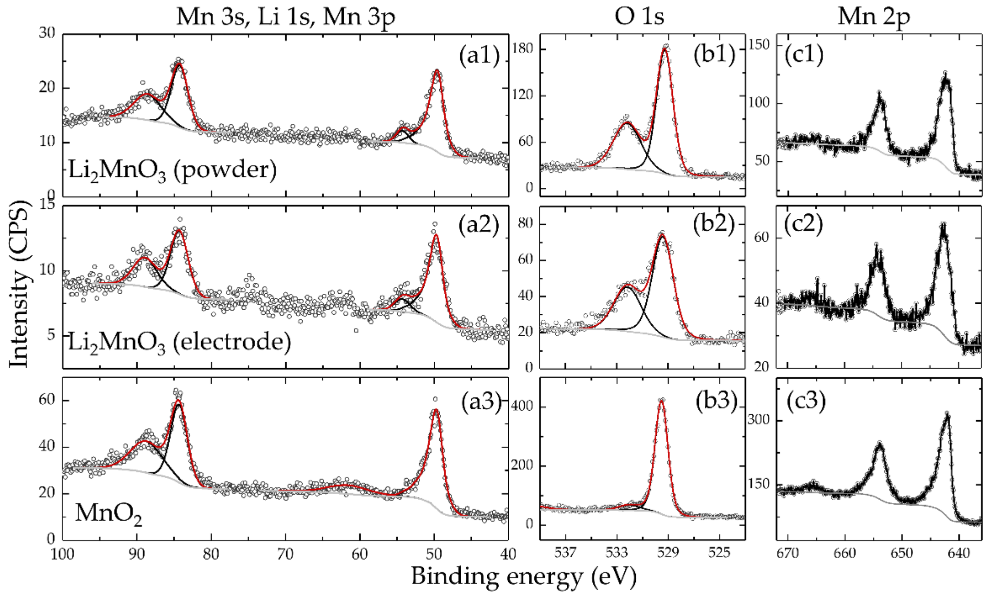

Figure 3.2.8 Core level Mn 3s, Li 1s, Mn 3p, O 1s, and Mn 2p HAXPES spectra of Li_2MnO_3 powder (top row), Li_2MnO_3 electrode (middle row) and reference MnO_2 powder (bottom row).

Orbital	**Assignation**	**Li_2MnO_3 (powder)**			**Li_2MnO_3 (electrode)**			**MnO_2**		
		BE	**FWHM**	**at%**	**BE**	**FWHM**	**at%**	**BE**	**FWHM**	**at%**
Li 1s	**Total**			**14.0**			**6.8**			
	Lattice	54.1	1.1	7.8	53.8	1.2	2.1			
	Surface	55.2	1.8	6.2	54.8	1.9	4.7			
Mn 3p	**Total**	49.9		**9.5**	49.7		**4.5**	49.7		**13.5**
Mn 3s	**Total**			**8.5**			**4.1**			**13.3**
	A	84.5	2.6	5.5	84.4	2.7	2.5	84.4	2.8	8.2
	B	88.9	3.5	3.0	88.8	3.9	1.6	88.7	3.9	5.1
Mn 2p	**Total**	**642.2**		**6.2**	**642.3**	**2.7**	**2.9**	**642.0**		**10.4**
O 1s	**Total**			**27.5**			**13.5**			**18.1**
	Lattice	529.4	1.4	14.9	529.4	1.6	6.6	529.5	1.2	14.2
	Surface							530.9	1.9	2.4
	CO_3^{2-}, SO_4^{2-}	532.1	2.3	12.6	531.9	2.5	6.4	532.2	2.0	1.5
	C-O, C=O				534.5	2.0	0.5			
C 1s	**Total**			**15.5**			**41.9**			**6.1**
	C-C	285.0	1.5	9.6				284.9	1.6	6.1
	C-O	286.0	2.0	3.2						
	C=O	288.5	1.3	0.7						
	CO_3^{2-}	290.2	1.7	2.0						
S 2p	**Total**	169.5	1.9	**0.9**	169.2	1.7	**0.5**			
F 1s	**Total**						**17.1**			
	CF_2				688.1	2.6	16.3			
	LiF				684.3	1.4	0.8			

Table 3.2.8 Results of XPS quantitative analysis for the manganese oxides. Binding energies (BE) and full width at half maximum (FWHM) are reported in eV.

Orbital	**Assignation**	**Li_2MnO_3 (powder)**			**Li_2MnO_3 (electrode)**			**MnO_2**		
		BE	**FWHM**	**at%**	**BE**	**FWHM**	**at%**	**BE**	**FWHM**	**at%**
Li 1s	**Total**	**54.3**	**2.0**	**15.6**	**54.3**	**2.5**	**12.7**			
Mn 3p	**Total**	**49.7**		**10.3**	**49.8**		**6.7**	**49.7**		**15.6**
Mn 3s	**Total**			**8.9**			**5.6**			**11.8**
	A	84.3	2.7	5.4	84.3	2.8	3.5	84.3	2.7	6.7
	B	88.6	4.3	3.6	88.9	3.7	2.1	88.8	5.0	5.1
Mn 2p	**Total**	**642.5**	**2.6**	**13.1**	**642.4**	**2.8**	**8.9**	**642.1**	**2.3**	**17.5**
O 1s	Total			52.1			32.5			27.7
	Lattice	529.3	1.5	32.7	529.4	1.9	21.1	529.5	1.2	25.8
	CO_3^{2-}	532.2	2.5	19.4	532.2	2.5	11.4	532.1	2.0	1.9
F 1s	**Total**				**688.1**	**2.9**	**21.3**			

Table 3.2.9 Results of HAXPES quantitative analysis for the manganese oxides. Binding energies (BE) and full width at half maximum (FWHM) are reported in eV.

As for Ni and Co core level spectra, the spin-orbit splitting of Mn 3p is small, so that a single line is observed as convolution of both Mn $3p_{3/2}$ and $3p_{1/2}$. An analogous broad satellite at ~62 eV (i.e. 12 eV from the Mn 3p main line) is observed as for the Mn 2p spectra. In all compounds, the shape of asymmetric 3p peak is in line with references for Mn^{IV}. However, the Mn 3p spectra for MnO(OH) and MnO_2 are similar, so the shape of Mn 3p cannot be uniquely considered to determine the oxidation state of Mn ions.

The Mn 3s is more informant with this regard. While for high-valence late transition metals such as Ni^{III} and Co^{III} the charge transfer effect is dominant in the 3s core level spectra, the exchange and correlation splitting prevails for Mn ions [282]. Indeed, a phenomenological relationship between the Mn 3s doublet splitting and Mn average oxidation state was established [283]. The peak splitting was in average 4.4 eV for both Li_2MnO_3 and MnO_2, corresponding to the value reported for Mn^{IV} ions [273,277,280,281,283].

3.2.4.2 Li 1s core level

Since the high-energy tail of Mn 3p overlaps with the Li 1s peak, the following strategy was adopted to analyze these spectra and quantify the Li content. First, an analytical curve for Mn 3p was extracted from the reference MnO_2 by a mathematical fit, which consists of a Shirley background and five pseudo-Voigt GL(30) peaks (see **Annex F** for details). Then, the convolution was used as lineshape for the Mn 3p peak, while the remaining part was fitted with the usual two-peak model for Li 1s spectra. The second peak was not included in HAXPES fit model due to the low sensitivity to Li 1s detection. Note that we followed this procedure due to the similarities in Mn core level spectra between MnO_2 and Li_2MnO_3, reflecting the similar Mn oxidation state and local coordination. Regarding the surface lithium species, the C 1s peaks suggest that the most relevant species is Li_2CO_3, as expected. However, analysis of S 2p and F 1s (only in the electrode) XPS peaks suggest the presence of LiF and Li_2SO_4 as well [6].

---

[6] The origin of sulfur contamination may be assigned to either synthesis conditions or to sample handling and storage in glovebox containing sulfates. However, the atomic concentration of this impurity is very small (< 1%).

3.2.4.3 C 1s core level

The C 1s XPS spectra for the bare Li_2MnO_3 and MnO_2 show contributions from the common surface impurities as observed in previous lithiated and Li-free samples. On the contrary, the spectrum for the electrode has a "bizarre" shape. This can be explained by the high insulating character of Li_2MnO_3. In fact, as for the $LiNiO_2$ electrode, the Li_2MnO_3 electrodes consist of a mixture of Li_2MnO_3 powder, conductive carbon and PVDF. However, Li_2MnO_3 is a strong insulator, while $LiNiO_2$ is a narrow gap semiconductor. Therefore, charge neutralization was employed even for the electrode sample.

Unfortunately, it seems the neutralization shifted the signal due to carbon black (typically at 284.5 eV) to higher binding energies, while compensating well for the insulating Li_2MnO_3 considering the high similarities between the spectra of bare powder and electrode. Due to large complexity of the spectra interpretation already observed for the $LiNiO_2$ electrode, to which this artifact is added, the C 1s was not fitted for this sample. For charge correction, the binding energy scale was shifted to match the position of the O 1s peak at 529.4 eV measured for the bare powder.

3.2.4.4 O 1s core level

Finally, the O 1s XPS and HAXPES spectra were fitted with the typical four-peaks model used above. Notably, the O_{surf} peak at 530-531 eV was only necessary for the MnO_2 sample, while the high-energy part of the O 1s spectra for Li_2MnO_3 was mostly related to surface contaminants. These included in large part Li_2CO_3, in consistency with Li 1s and C 1s analysis, but also SO_4^{2-} groups due to the small S 2p peak measured in this sample.

3.2.4.5 Surface stoichiometry

The surface stoichiometries were deduced for the lithiated manganese oxide samples as explained above (**Table 3.2.10**). The Li/Mn ratio obtained with the two X-ray sources largely differ: in agreement with the results by Quesne-Turin et al. [280], the surface of Li_2MnO_3 samples appears under-lithiated (Li/Mn ~ 1). With the Cr Kα source, we found $1 < Li/Mn < 2$, closer to the expected stoichiometry. Note that the low Li 1s sensitivity with the HAXPES setup generally led to lower-than-expected Li quantification for the previous results for $LiCoO_2$ and $LiNiO_2$, compounds. Remarkably, the Mn/O atomic ratio obtained by HAXPES matches the expected bulk stoichiometries. With XPS, instead, the ratio is closer to 1:2, leading to an overall stoichiometry closer to a stoichiometric $LiMO_2$ oxide. If that were the case, Mn ions should be partially reduced at the extreme surface. However, the Mn core-level qualitative analysis suggest otherwise. Another possibility is that the extreme surface of the particles is instead under-lithiated leading towards δ-MnO_2, with Mn^{IV} ions filling the Li empty slabs.

	XPS	**HAXPES**
Li_2MnO_3 Powder	$Li_{1.0}MnO_{1.8}$	$Li_{1.4}MnO_{3.0}$
Li_2MnO_3 Electrode	$Li_{0.5}MnO_{1.7}$	$Li_{1.8}MnO_{3.0}$
MnO_2 Powder	$MnO_{1.5}$	$MnO_{1.7}$

Table 3.2.10 Surface stoichiometry of manganese oxide samples estimated by XPS and HAXPES quantification.

3.2.5 Section summary

Comparing the results of XPS and HAXPES analysis for pristine $LiCoO_2$, $LiNiO_2$, and Li_2MnO_3 materials, we can draw general trends and common features.

1. **Lithiated surface impurities**

Although lithiated surface impurities (mainly Li_2CO_3) are present in almost all materials, it is evident that their concentration is higher in $LiNiO_2$. This is in line with other findings in the literature and agrees with the higher basicity of this oxide, which therefore tends to react more readily with CO_2 in the environment. However, one must also take into account the synthesis conditions of the materials, which often make use of Li_2CO_3 as a reactant: this may explain the great difference between $LiCoO_2$ thin films and powders.

2. **Surface oxygen sub-stoichiometry**

The most interesting aspect of the surface chemistry of these materials is the deviation from bulk stoichiometry. Co-focused XPS and HAXPES analysis helps to delineate the zone of interest at the first few nanometers from the extreme surface. Here, XPS results indicate a lower O/M ratio than expected and that obtained with HAXPES. Again, this phenomenon is accentuated in $LiNiO_2$, in which the HAXPES result does not lead to the expected stoichiometry either. The sub-stoichiometry is typically followed by the presence of higher binding energy contributions related to sub-oxide or hydroxide contributions. Regarding the application aspect, the identification and characterization of these surface defects is an important step because they can affect the performance of materials in lithium-ion batteries. The composition and structure of the positive solid electrolyte interphase during formation cycles depends on the surface chemistry of the pristine materials. However, the XPS analysis presents a limit for their identification, as it mainly depends on the peak fitting analysis and interpretation, which should be further validated by other techniques. Combining the XPS and HAXPES results with other surface-sensitive techniques such as surface-enhanced Raman spectroscopy could be a promising approach.

3. Surface transition metal reduction

Finally, superficial deoxygenation of materials must be accompanied by a reduction of transition metals in the surface by charge compensation. To verify this, a strategy of identifying the spectral characteristics of transition metals at different oxidation states is necessary. This is not trivial because the local environment plays a major role in the photoemission process. Indeed, there is no unambiguous analytical strategy for decomposing the spectra of transition metals into oxides, although some methods have been discussed in the literature. In the next section, a simple method for associating spectral variation with transition metal reduction will be proposed. Then, some analytical strategies for analyzing core level 2p spectra in these materials will be outlined.

3.3 Empirical analysis of transition metal 2p core level spectra

3.3.1 Inducing surface reduction by Ar-ion beam etching

The results of the previous sections showed that the pristine layered oxides all exhibit some degree of surface reduction. This is expected to increase upon cycling in Li-ion batteries due to surface irreversible reactions with the electrolyte and the degradation pathways explained in Section 1.5.3. To investigate this process, a simple experiment was carried out to observe the changes of transition metal core-level 2p spectra.

It is well known that Ar-ion sputtering damages the surface of transition metal oxides by preferential sputtering of the lighter oxide ions compared to the transition metal ones [284–287]. With decreasing O/M ratio, the M ions are reduced and the crystal structure is damaged. The same effect is expected to occur and to be even more important in lithiated transition metal oxides, due to the presence of extremely light Li^+ ions. Yet, Ar-ion etching is still employed for XPS depth profiling for Li-ion positive electrode materials [288–292]. Meanwhile, no study focused on the beam damage aspect, to our knowledge. Most studies aimed to resolve the composition of the pSEI and not the surface-bulk changes in oxidation state, which is the target here. Indeed, the M 2p spectra were not discussed or even shown in the above-cited articles.

Here, the Ar$^+$ ion beam damage was exploited to induce surface reduction and study the changes in the core level spectra. After XPS and HAXPES characterization, the reference pristine samples were subjected to Ar-ion etching to induce surface reduction. The sputtering treatment consisted of exposing for 3 min the sample to an Ar$^+$ ion beam accelerated by 3 kV with a raster size of 3x3 mm^2. Then, the XPS and HAXPES spectra were re-measured in the same position.

Part of the study presented below was published as research article within the special issue dedicated to the ECASIA'22 conference in the Surface and Interface Analysis (SIA) journal. The article, titled "Revisiting Co 2p core-level photoemission in $LiCoO_2$ by in-lab soft and hard X-ray photoelectron spectroscopy: A depth-dependent study of cobalt electronic structure", is given in **Annex I** (**paper 1**). It presents a detailed core-level analysis for $LiCoO_2$ before and after an Ar-ion sputtering step, including quantitative analysis and an in-depth investigation of the Co 2p spectra, discussed in **Section 3.3.2.1**. Therefore, here we limit to a qualitative discussion of the experimental results.

Figure 3.3.1 shows the TM 2p and O 1s XPS and HAXPES spectra for $LiCoO_2$ thin film, Li_2MnO_3 powder and $LiNiO_2$ powder before (black lines) and after (red lines) the Ar-ion sputter process. For all three materials, a clear change is observed in the 2p XPS spectra, less pronounced although still visible in the HAXPES spectra. As anticipated, the reduction of transition metals (formally, Co^{III} to Co^{II}, Mn^{IV} to Mn^{III}, and Ni^{III} to Ni^{II}) is the cause of this change. However, there is no common trend among the three compounds.

In the case of $LiCoO_2$, the main aspect is the increase in intensity at 786 eV, which can be assigned to the satellite peak of Co^{II} according to the spectra of Co_3O_4 (see above) and CoO [257,258]. For $LiNiO_2$, a large intensity increase is observed, implying larger damage than for $LiCoO_2$. To visualize the qualitative changes in the Ni 2p peaks, the inset figure in **Figure 3.3.1(a2)** shows the normalized background-corrected Ni 2p$_{3/2}$ spectra. The relative intensity of the satellite peak increases and its maximum shifts to higher binding energies. The main line also shifts to higher binding energies, and a broader asymmetric peak is obtained. These changes go in the direction of the characteristic spectrum for NiO, except for the distinct doublet in the main line. Similar spectra were measured for isolated Ni^{II} ions embedded in MgO and SiO_2 oxides [293,294] as well as NMC materials with low Ni content [215,267,272]. For Li_2MnO_3, a relative shift of the Mn 2p peaks toward low binding energies is observed, as for MnOOH, without significant changes in the satellite structure [281].

The O 1s spectra also reveal changes related to the layered lattice itself. Indeed, an increase in intensity between 530-531 eV is observed in all XPS spectra, shifting the main peak position to higher binding energies. This effect is more pronounced for $LiNiO_2$, while it is only slightly observable for $LiCoO_2$. As for the M 2p core level spectra, the same trend is less or not at all observed in the HAXPES spectra. Overall, these experiments confirm the assignation of the peak at 530-531 eV to surface degradation and transition metal reduction in the pristine materials.

3.3.1.1 Testing gas cluster ion beam to minimize the beam damage

The use of Ar-ion beam for sputtering in combination with HAXPES appears promising for characterizing buried layers in multi-layer materials. However, this is not a viable option for studying the evolution of electronic states from the surface to the bulk of cycled battery materials, due to beam damage. However, there are options to perform a softer surface abrasion using polyatomic sources for the ion beam. To test this option, several depth profile experiments were performed with the GCIB gun equipped in the Versaprobe equipment. The results are discussed in **Annex F**: in short, it was concluded that these materials are too reactive for ion beam etching, which is not suitable for studying the distribution of electronic states at different dept. The use of nondestructive methods such as the combination of XPS and HAXPES at different energies is therefore unavoidable for this study.

3.3.2 Transition metal 2p analysis by peak fitting

The experiments discussed above provide a useful tool for qualitative analysis of M 2p and O 1s core level spectra in the layered systems. However, moving beyond simple peak identification and towards quantitative characterization of oxidation states in transition metal compounds is a long-standing challenge. The main reasons for this are (1) the high sensitivity of the photoemission process to the local environment, which makes the analysis material- and core-level-dependent; and (2) that the experimental spectra are a convolution of the initial- and final- state effects, which are not known a priori. Many methods were proposed in the literature for this task, including also works dedicated to battery materials. These can be referred to as empirical methods, opposite to interpreting the XPS spectra with the use of *ab initio* or cluster simulations. As described in **Chapter 2**, both pathways were explored in this thesis, each with a specific aim. This section presents the empirical approaches developed for pristine materials and that will be employed in the next chapter for studying the changes upon cycling.

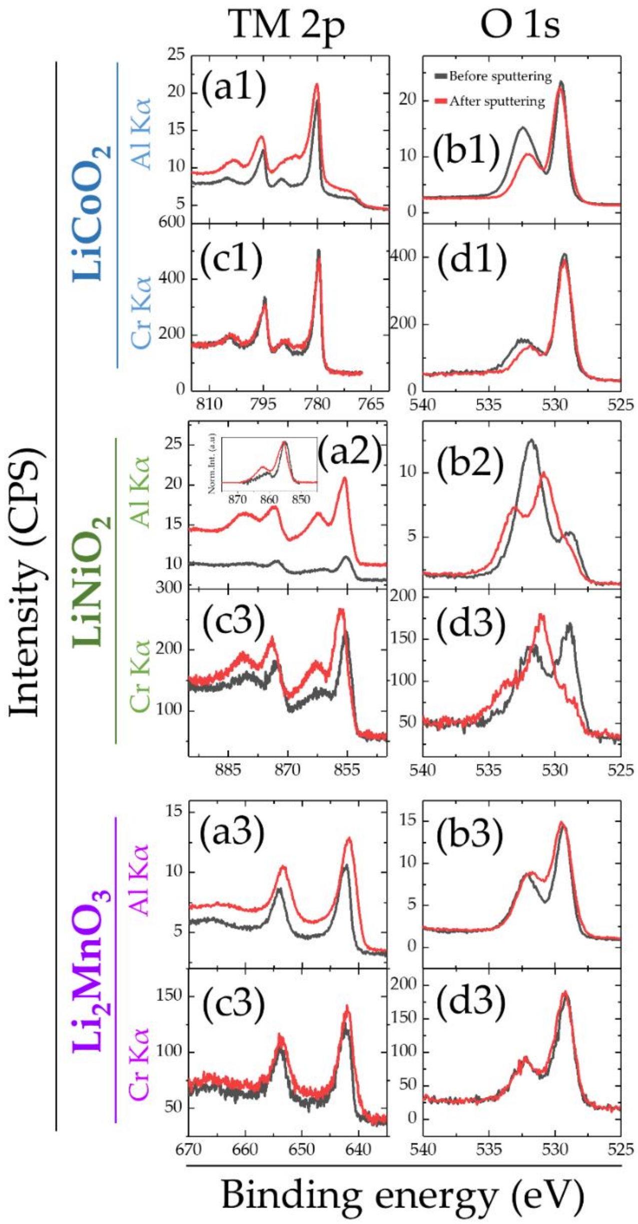

Figure 3.3.1 Surface reduction by Ar-ion beam damage effect for the bare materials. Transition metal (TM) 2p (left-hand panels) and O 1s (right-hand panels) XPS and HAXPES spectra for (a1)-(d1) $LiCoO_2$, (a2)-(d2) $LiNiO_2$, and (a3)-(d3) Li_2MnO_3 before (black line) and after (red line) the Ar-ion sputtering step. The inset in panel (c2) shows the intensity normalized Ni $2p_{3/2}$ XPS spectra after Shirley background subtraction.

3.3.2.1 Co 2p peak fitting model for pristine $LiCoO_2$

Following the previous methods proposed in the literature for Co_3O_4 and other cobalt compounds, the Co 2p XPS and HAXPES spectra of $LiCoO_2$ before and after sputtering as well as Co_3O_4 taken as reference were analyzed by peak fitting using a set of Gaussian-Lorentzian peaks, each associated to a specific final-state effect (**Figure 3.3.2**). The peak model was built with particular concern to consistency between the data acquired with both Al Kα and Cr Kα sources, due to the overlap with Co LMM peaks for the former. From the fits, the Co^{II}/Co^{III} can be semi-quantified at different depths by means of the satellite peaks area ratio. For a detailed description of the model, we refer to the second part of **paper 1** given in the **Annex I**, from which **Figure 3.3.2** was taken.

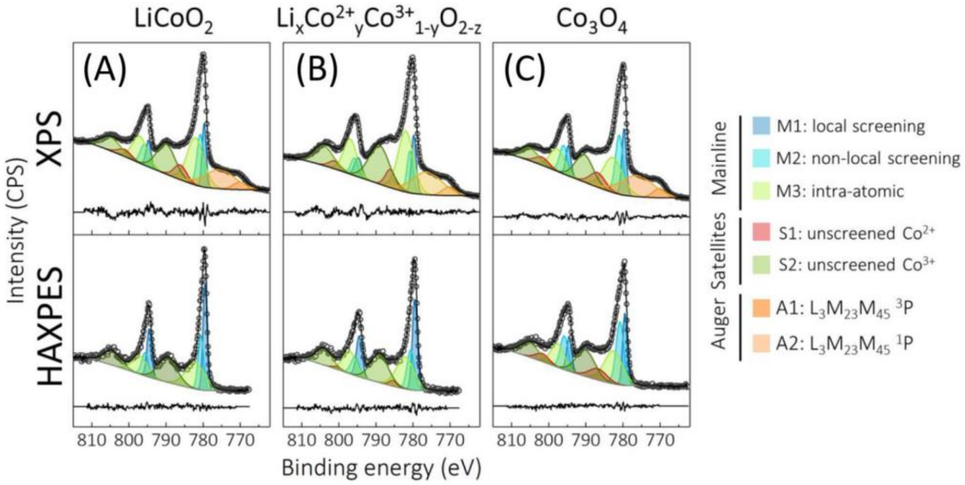

Figure 3.3.2 Co 2p XPS and HAXPES analysis by peak fitting for (A) pristine and (B) sputtered $LiCoO_2$, and (C) spinel Co_3O_4. For each panel, the experimental data, background curve and peak model fit are shown as empty black dots, grey curve, and black line, respectively. The legend on the left-hand side gives the attribution of each peak to a final-state effect or Auger peak. Reprinted from paper 1 (Annex I).

3.3.2.2 Ni 2p analysis of pristine $LiNiO_2$

Numerous efforts have been dedicated to quantifying the surface reduction of nickel in NMC materials, commonly expressed as Ni^{II}/Ni^{III} ratio. In several studies, single peak areas fitting the main line are still used to quantify the Ni^{II}/Ni^{III} to reveal the redox process in battery-related studies [271,295–301]. However, this methodology contrasts with photoemission theory and has been criticized. Other proposed methods in the literature are based on Ni ions multiplets [272,273], satellite analysis by peak fitting [215], and peak fitting using a combination of experimental lineshapes (herein reference-based peak fitting) [141,267]. All the methods proposed in the literature were reviewed and tested for the purpose of this thesis.

3.3.2.2.1 Multiplet templates

The method by Azmi et al. [272,273] is essentially that of Biesinger et al. [257,302,303] applied to Li-ion battery materials. The templates used for peak fitting are built based on the photoemission spectra calculated by Gupta and Sen for isolated 3d transition metal ions [304]. However, there is an actual high degree of freedom for building each peak template, since the simulations neglect metal-ligand hybridization and interatomic screening processes, which typically dominate over multiplets in the XPS spectra for late 3d transition metals. Furthermore, the rigid model template would not be sufficient to appreciate the effects of deintercalation on the electronic structure. Therefore, this approach was not considered in this thesis.

3.3.2.2.2 Satellite analysis by peak fitting

Bondarchuk et al. proposed a peak fitting model with an approach similar to the one used for $LiCoO_2$ in this thesis [215] to quantify the Ni^{II}/Ni^{III} ratio in NMC with different Ni content. In fact, it is expected that in these systems each Mn^{IV} is compensated by a reduction of Ni^{III} to Ni^{II}. Their Ni $2p_{3/2}$ peak model was obtained from NiO, highlighting the spectral similarities between the two oxides. To quantify the Ni^{II}/Ni^{III} ratio, they used the relative intensity of the satellite peak to the main line as figure of merit, based on the assumption that Ni^{III} ions in low-spin d^7 configuration do not contribute at all in the satellite region.

Figure 3.3.3 shows the fit results for $LiNiO_2$ and NiO powders. Applying the formula by Bondarchuk et al. gives $[Ni^{III}]$ = 44 and 31 % for XPS and HAXPES, respectively (see **Annex F** for details). This suggests that a large fraction of Ni ions is reduced at the surface, in agreement with our previous analysis, although the concentration found for XPS quantification higher than the HAXPES one is counterintuitive. More generally, the approximation that Ni^{III} ions do not produce satellite structure is highly questionable. First, it is not necessarily true that low-spin configurations have no satellite, as demonstrated by $LiCoO_2$. Second, the fact that $LiNiO_2$ (and NMC) do have Ni^{III} in formal d^7 is actually a matter of discussion in this thesis. Therefore, the quantification of $[Ni^{III}]$ from this method was not considered as valid. Still, the similarities between $LiNiO_2$ and NiO in their Ni 2p photoemission spectra give insights on the nature of the local electronic structure of Ni ions. Indeed, the peak fitting template derived from NiO will be used in combination with simulations to infer on the electronic structure changes upon deintercalation in **Chapter 5**.

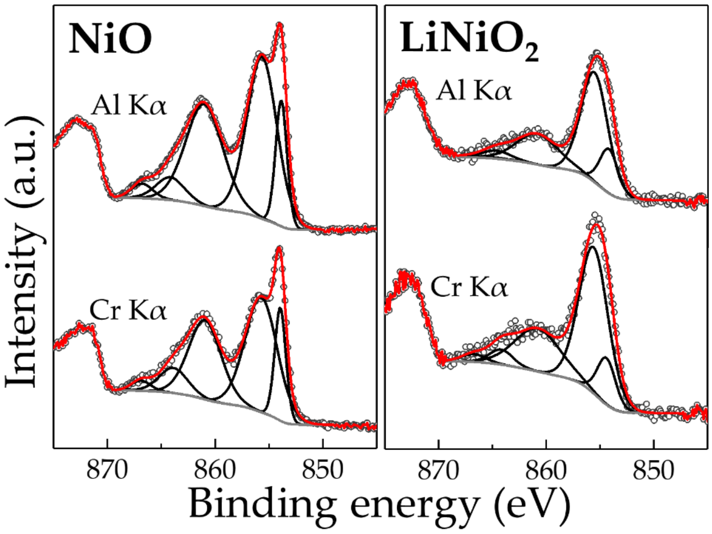

Figure 3.3.3 Ni $2p_{3/2}$ peak fit model for NiO and $LiNiO_2$.

3.3.2.2.3 Reference-based peak fitting

As for the work discussed above, Fu et al. developed a peak fitting model for the 2p peaks of NMC materials with different Ni concentration [267]. They compared the results obtained with two peak models: one based on Gaussian-Lorentzian peaks (a main line and a satellite for Ni^{II} and Ni^{III} each) and another based on non-linear least square (NLLS) fitting. In the latter method, the Ni 2p spectra of NMC111 and $LiNiO_2$ were used as reference spectra for Ni^{II} and Ni^{III} contributions in the overall spectra. Although the general trend of decreasing Ni^{II}/Ni^{III} ratio with increasing Ni content was obtained with both methods, the NLLS method gave more reproducible results and better fits to the experimental spectra.

Similarly, Biao et al. fitted the Ni 2p spectra of charged $Li_{0.17}Ti_{0.58}Ni_{0.25}O_2$ disordered rock-salt oxide using the spectra of fully charged and fully discharged $Li_{1.12}Ni_{0.13}Mn_{0.54}Co_{0.13}O_2$ to characterize the surface reduction as a function of the annealing time [141]. However, in this case they did not apply a NLLS algorithm but described the experimental spectra as a linear combination of the two reference lineshapes.

In both works, the authors employed spectra from reference materials, external to the set of fitted samples, which were referred to specific oxidation states. To minimize the difference in the local environment for the photo emitting ion, the reference materials were taken as much structurally similar as possible. Still, the approach holds on two strong assumptions: (1) the reference spectra of external materials can indeed represent different contributions for a certain sample and (2) the direct linking between specific oxidation states and reference spectra is valid.

In general, reference-base peak fitting is a versatile method that can be easily adapted to specific materials and processes. Therefore, it is suitable for dealing with complex spectra contributions, as in the case of the Ni 2p peaks of $LiNiO_2$. However, the choice of reference spectra plays a major role in both the fit results and the scientific conclusions that can be deduced from it. For example, Fu et al. used the XPS spectra of $LiNiO_2$ powder sample as reference for Ni^{III}, which is here the target of the study and for which subtle differences can be appreciated by comparing the XPS and HAXPES spectra, indicating partial surface reduction.

3.3.2.3 Ni $2p_{3/2}$ peak fitting by combining lab-based and synchrotron HAXPES

To track the evolution of Ni electronic states at different depths and as a function of delithiation, the Ni $2p_{3/2}$ spectra were fitted using three reference spectra. The whole model is discussed in **Section 4.3.2.1**; here we simply present the model for the pristine material, for which only two components were assumed: one for the Ni^{III} bulk-like signal (Ni^{III}_{bulk}) and the second for the Ni^{II} surface contribution (Ni^{II}_{surf}). These were taken as the most bulk-sensitive measure for pristine $LiNiO_2$ and the most surface sensitive spectra for cycled $LiNiO_2$ at discharged state.

Hence, with respect to the previous models proposed in the literature, the data was fitted using reference spectra of materials that are part of the fitted dataset. On the one hand, this reduces even more the difference between local environments of the photo emitting Ni ions; on the other, some experimental spectra will not be fitted as they are used as peak model themselves. Moreover, as with the use of external references, one can only assume that the spectra represent some particular electronic state, without giving further insights on the actual electronic structure. The peak fit model shown in **Figure 3.3.3** and spectra simulations are more suitable for that purpose.

The implementation of the combinative fit model was only possible thanks to the combination of the lab-based XPS and HAXPES with synchrotron HAXPES characterization at different X-ray energies. In fact, a set of Li_xNiO_2 samples that were measured by the lab-based setup in CEA Grenoble were also measured at the Galaxies beamline in the Soleil synchrotron using 2.3, 5.4 and 9.5 keV photon energies and an 80° take-off angle. According to the IMFP calculated with the TPP2M model, the combination of all experiments uniformly allowed scanning the first 30 nm as shown in **Figure 3.3.4(a)**. Thus, the HAXPES spectra taken at 9.5 keV could be used as reference for the bulk-like signal, improving the resolution and bulk-sensitivity of the reference spectra.

A close inspection reveals a slightly larger satellite peak to the mean line and a shift to larger binding energies for the most surface sensitive spectra, as indicated in **Figure 3.3.4(b)**. The reference-based peak fitting was able to track these slight changes, as shown in **Figure 3.3.4(c)**: the Ni^{II}_{surf} component gradually decreases with increasing depth-sensitivity, as expected, giving possibility to perform a non-destructive depth profile of the Ni electronic state distribution in this compound. To validate this method, an EELS study was carried out, as discussed in the next chapter.

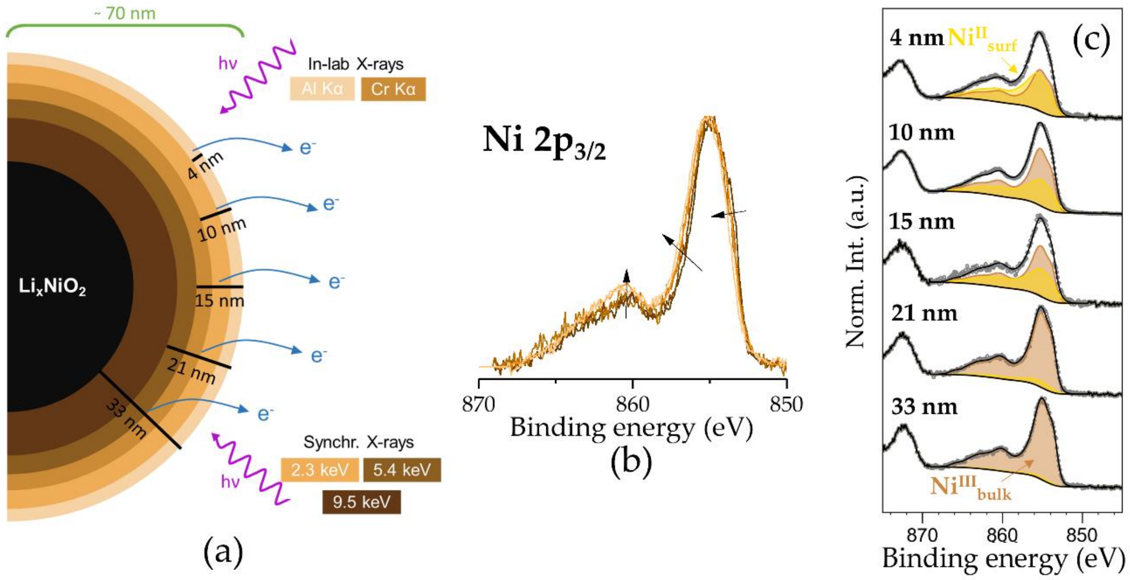

Figure 3.3.4 Non-destructive depth profile of Ni electronic states. (a) Schematic illustration of the experimental approach that combines lab-based and synchrotron X-rays. The figure is scaled to the average size of $LiNiO_2$ single particles estimated by SEM imaging (Annex F) and the sampling depth depending on the X-ray photon energy and take-off angle of lab-based and synchrotron experiments (Annex A). (b) Normalized and background subtracted Ni $2p_{3/2}$ spectra acquired with the five settings illustrated in (a) (same color code). The arrows indicate the changes with increasing surface sensitivity. (c) Same spectra as in (b) but fitted with the use of internal references as component lineshape.

3.3.3 Section summary

We summarize below the main conclusions on the analysis approaches for M 2p spectra from qualitative towards quantitative methods.

1. **Use of beam etching**

The Ar-ion and GCIB depth profile experiments corroborated the analysis done in **Section 3.2** and further established the linking between M 2p and O 1s evolutions upon surface reduction. Moreover, it was highlighted that the high reactivity of lithiated transition metal oxides leads to fast unavoidable damage, imposing the use of non-destructive techniques.

2. **The analysis of M 2p core level spectra is a great challenge.**

The previous works related to $LiCoO_2$ and $LiNiO_2$ were reviewed and new models adapted for these materials were proposed. Two approaches were highlighted: (1) spectra decomposition into single peaks attributed to particular final-state effects and (2) peak fitting using reference spectra as spectral components. For the second, the support from synchrotron HAXPES characterization paved the way to develop a method using internal references.

Beyond the advantages and disadvantages of each method, the fact that they rely on references and therefore assumptions on their assignation is a strong limit of empirical approaches. In fact, no pure reference can be given for charged/discharged materials. Therefore, a study uniquely based on peak fitting can be misleading if the aim is to characterize the charge compensation mechanism and resolve it from surface to bulk. To alleviate this problem, a coupling with simulations and parallel experimental characterizations are necessary for validation.

Chapter 4

Insights on surface degradation of cycled electrodes

In this chapter, the effects of Li^+ deintercalation on the surface chemical composition changes of layered transition metal oxides are investigated by XPS and HAXPES analysis of cycled electrodes. Following the schema outlined in the introduction from the literature review, the pSEI and SRL are distinguished and discussed separately. Especially for the latter, HAXPES quantification contributed to understanding its dependence on the cut-off voltage and deintercalation level and revisiting previous conclusions based on either lab-based XPS or qualitative synchrotron HAXPES analysis only. By discriminating surface degradation contributions, the signatures of the bulk electronic structure are identified, leading toward the study of the bulk charge compensation mechanism discussed in the next chapter.

4.1 Preparation of ex-situ delithiated samples

The samples were prepared by electrochemical delithiation in Li-ion cells. The electrochemical protocols were not chosen for testing the electrochemical performance of the materials, but rather to simply prepare materials at different deintercalation level (hence different cut-off voltage) and after formation of the pSEI. The materials used for the electrolyte and the negative electrode are frequently used in the electrochemical studies for Li-ion battery materials and are considered as standard materials. The general approach was to maintain the same preparation method along the thesis for the studied electrodes. However, the properties of each material eventually led to use slightly different protocols for each of them.

4.1.1 Cycling protocol for $LiCoO_2$ thin films

Because of the special morphology of the $LiCoO_2$ thin film electrodes, a homemade cell case developed in a previous thesis in CEA was employed [305]. The cell consists of two main parts in polyether ether ketone (PEEK): a bottom part with a cavity for the battery components stack and two gasket rings to ensure airtightness and a cover with the two current collectors.

The cell components are listed as follows, in order of assembling: $LiCoO_2$ thin film, Viledon and Celgard separators, 300 μL of a 1 M $LiPF_6$ solution in ethylene carbonate (EC) and ethyl methyl carbonate (EMC) with weight ratio 3:7 (LP57 electrolyte, Sigma Aldrich), and Li foil (Rockwood, 135 μm) larger than the active area of $LiCoO_2$. The $LiCoO_2$ electrodes were cut from the wafer using a diamond knife to fit in the cavity of the cell case. The negative and positive current collector tips were protected by interposing a positive electrode case of CR2032 coin-type cells and covering with Al foil, respectively. Schematics and pictures of the cell case are reported in the Annex.

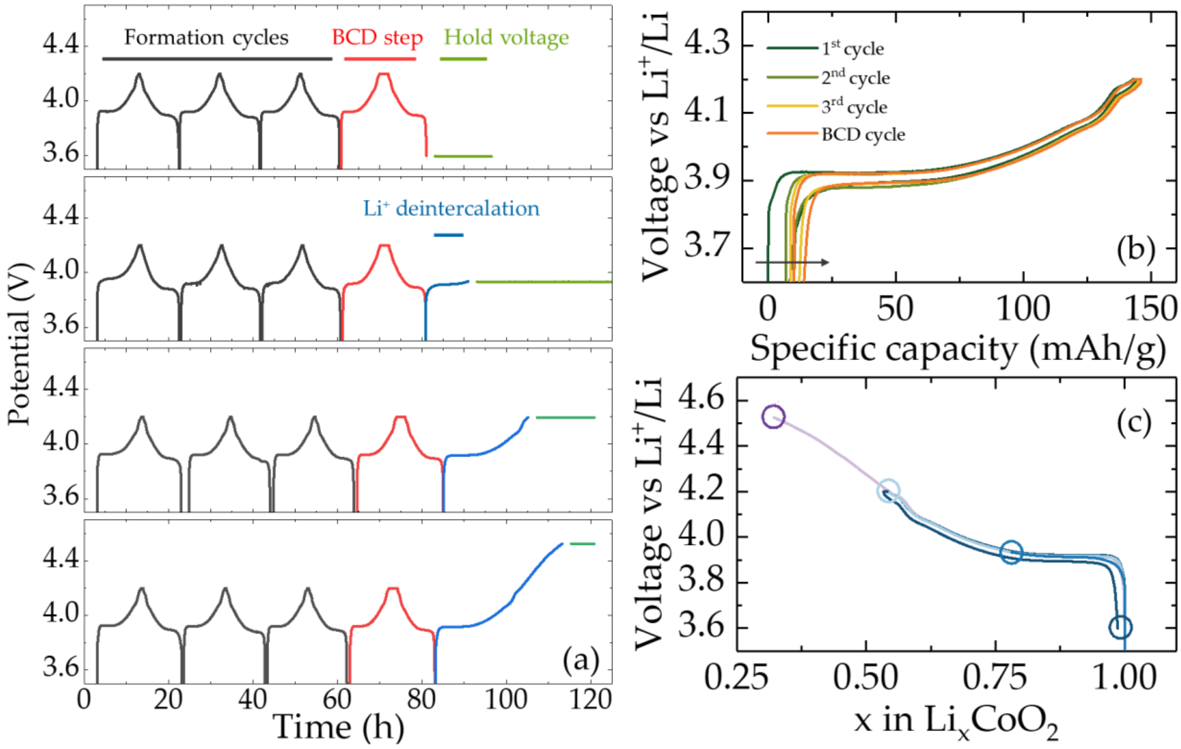

Figure 4.1.1 Electrochemical cycling protocol for Li_xCoO_2 thin films electrodes. (a) Potential vs time highlighting all steps as described in the text. (b) Potential vs capacity for the cell retrieved at discharged state, indicating the total capacity loss at end of the last discharge. (c) Deintercalation curve for the Li_xCoO_2 samples. All curves were shifted to the curve for the material retrieved at discharged state.

The cells were tested with a VMP-300 (Biologic) potentiostat at room temperature. After 3 h of relaxation in open-circuit voltage (OCV) condition, three galvanostatic cycles (herein formation cycles, FC step) were performed between 3.0 and 4.2 V with current density of 13.7 mA/g, which corresponds to a C-rate of C/10 considering the specific active mass of 26.54 mg and the theoretical capacity of 135 mAh/g at 4.2 V. Subsequently, a battery capacity determination (BCD) step was used to measure the capacity with the same voltage range and current used for the formation cycles. Then, the battery was finally charged at C/20 with respect to the as-measured capacity setting the limit time to reach specific intercalation levels of Li_xCoO_2, namely $x \approx 0.75, 0.5, 0.25$. The latter step was not performed for one of the cells. The voltage reached after this step was held until manual stop and cell disassembling. The retrieved thin films were washed in excess dimethyl carbonate (DMC) for about 3 min and finally let drying. Cell (dis)assembling, electrodes washing, and sample storage were all performed in an Ar-filled glovebox.

The (de)intercalation galvanostatic curves for all materials are reported in **Figure 4.1.1(a)**. The capacity loss during the three formation cycles of about ~15 mAh/g have an influence on the delithiation cut-off state "x" by decreasing it of about Δx~0.05 [**Figure 4.1.1(b)**]. Therefore, the thin film retrieved at discharged state will be referred to as $Li_{0.95}CoO_2$. The final charge step plotted against x in **Figure 4.1.1(c)** showing the expected typical behavior of Li_xCoO_2 electrodes in Li-ion batteries.

4.1.2 Cycling protocol for $LiNiO_2$ composite electrodes

CR2032 lithium-ion cells were assembled in an Ar-filled glovebox as follows, in order of assembling: 15 mm diameter graphite anode (CIDETEC), 16 mm Celgard separator, 50 μL of LP57 electrolyte (same used for $LiCoO_2$ cycling), 14 mm diameter $LiNiO_2$ electrode.

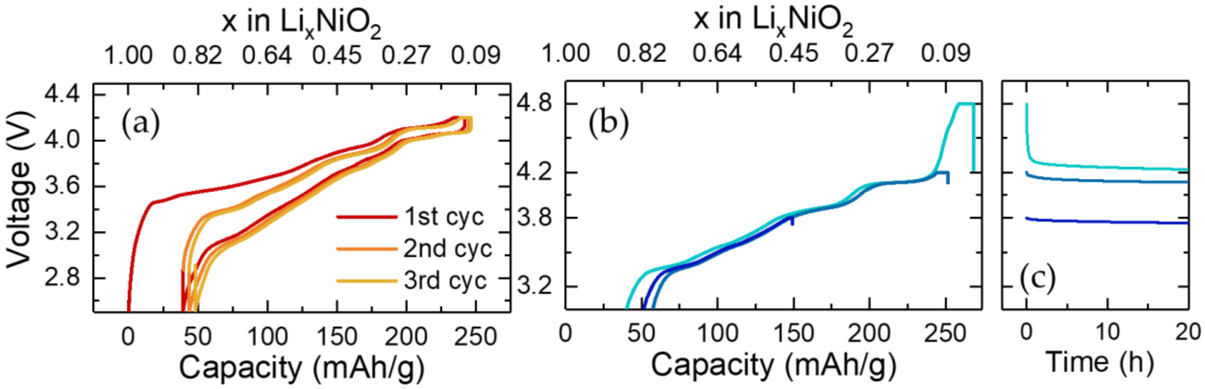

Figure 4.1.2 Electrochemical delithiation of Li_xNiO_2. (a) Formation cycles at C/10 for a reference electrode. Apart for a first cycle capacity loss of ~50 mAh/g, we did not observe significant changes in the voltage curve. (b) Last charge at C/20 stopped at 3.8, 4.2, and 4.8 V. (c) Voltage profile during the final OCV step, which indicates a faster voltage decay with increasing the upper cut-off voltage.

The cells were cycled using a VMP-300 (Biologic) potentiostat at room temperature with the following protocol: (1) 10 hours at the OCV, (2) three galvanostatic cycles between 3.0 and 4.2 V at C/10 (1C = 225 mA/g) including 5h constant voltage step at 4.2 V, (3) galvanostatic charge to 3.8, 4.2, and 4.8 V upper cut-off voltage at C/20, (4) constant voltage until the current was lower than C/100, (5) final relaxation step at OCV. The cycled electrodes were recovered from the disassembled cells and washed with DMC for about 3 min to remove soluble salts from the surface. Cell (dis)assembling, electrodes washing, and sample storage were performed in an Ar-filled glovebox.

Figure 4.1.2(a) shows the typical formation cycles for Li_xNiO_2. Apart for the first cycle capacity loss, we did not observe significant changes in the voltage curve, as highlighted in **Figure 4.1.2(b)** showing the expected behavior of Li_xNiO_2 as reported in the literature. At the end of the charge including the constant voltage step, we collected the Li_xNiO_2 samples with $x \approx 0.5$, 0.1, and 0.01. A sample without the last charge step ($x \approx 0.8$ due to the relatively large capacity loss of 40-50 mAh/g) was also included in the analysis. Because of the staircase-like shape of the deintercalation curve of Li_xNiO_2 along the whole deintercalation range, the BCD step used for $LiCoO_2$ was not necessary.

4.1.3 Cycling protocol for Li_2MnO_3 composite electrodes

The electrochemical delithiation was performed in CR2032 coin cells consisting of 15 mm Li metal (Sigma-Aldrich), 16 mm Celgard separator, 50 µL of LP57 electrolyte, 14 mm diameter Li_2MnO_3 electrode. Despite some electrochemical activity is known for Li_2MnO_3, the electrochemical performances are low, imposing significant changes in the cycling conditions. In fact, the cycling curve of Li_2MnO_3 changes drastically after the first cycle, indicating structural degradation (see **Annex G** for the electrochemical data). Therefore, the material studied by XPS was not subjected to formation cycles. The delithiated material was retrieved immediately after the first charge, which presents a single long plateau at ~5.0 V. In the literature, this voltage plateau is often reported at lower voltages for nanosized Li_2MnO_3. Since our powder presented aggregates of >10 µm (see SEM figures in **Annex F**), we relate the larger overpotential to the large particle size, considering the low electronic conductivity of Li_2MnO_3. The galvanostatic charge was carried out at 10 mA/g (~C/50) with an upper cut-off voltage of 5.2 V, delivering ~220 mAh/g. Assuming that all charge capacity was related to the delithiation redox process, it corresponds to x~1 mols of lithium ions extracted.

4.2 Insights on the pSEI

In principle, HAXPES contribution to the understanding of pSEI formation and evolution is expected to be low due to the larger depth sensitivity. Indeed, part of the information obtained by conventional XPS is lost in the HAXPES measures. This comes as a payback for the larger sensitivity to the buried SRL and bulk material. However, the contribution of quantitative non-destructive depth profiles for binder-free electrodes, including accurate bulk calibration, highlighted important aspects regarding XPS analysis of SEIs that are often overlooked in the literature. Moreover, the present case study allowed quantifying the increased sensitivity to the buried active material. As observed in **Section 3.2.3**, the presence of binder and carbon black significantly complicates the identification of surface species on the electrode active materials. Therefore, the clearest results regarding the pSEI composition were obtained for the cycled Li_xCoO_2 thin films and are presented below. However, some insight could be also obtained for Li_xNiO_2. We omit instead the study of the pSEI for the cycled Li_xMnO_3 material.

4.2.1 Core-level spectra analysis of pSEI components in cycled Li_xCoO_2

The XPS and HAXPES analysis for core levels related to pSEI species are discussed below. The O 1s and Co core-level spectra are discussed in the next section regarding the SRL. Generally, the O 1s peaks related to surface species were consistent with the other core-level spectra analysis. The XPS and HAXPES quantitative results are reported in **Table 4.2.1** and **Table 4.2.2**. The results are overall in agreement with previous XPS studies of the pSEI forming on $LiCoO_2$ [20,108,163,166,170,176,182,306–308]. In particular, lithium fluoride (LiF), lithium fluorophosphate ($Li_xPO_yF_z$), lithium carbonate (Li_2CO_3), polyoxyethylene (POE), and other unresolved carbon-oxygen compounds were recognized, in agreement with the expected products of the decomposition of $LiPF_6$ salt and organic carbonates constituting the electrolyte [306].

		$Li_{0.95}CoO_2$			$Li_{0.75}CoO_2$			$Li_{0.5}CoO_2$			$Li_{0.25}CoO_2$		
Orb.	**Comp.**	**BE**	**FWHM**	**at%**	**BE**	**FWHM**	**at%**	**BE**	**FWHM**	**at%**	**BE**	**FWHM**	**at%**
Li 1s	**Lattice**	54.0	1.0	4.8	54.3	1.2	6.1	54.0	1.5	4.5			
	Surface	56.5	1.2	6.6	55.4	1.6	10.6	55.4	1.5	7.1			
Co 3p		61.1		14.1	61.1		12.7	60.5		17.4	60.7		24.9
Co 2p		779.9		8.4	780.0		6.6	779.6		10.0	779.6		14.9
O 1s	**Lattice**	529.4	1.1	13.3	529.3	1.0	9.9	528.8	1.0	5.6	528.7	1.0	8.1
	Surface	530.2	0.9	2.8	530.0	0.9	3.1	529.6	1.3	9.9	529.6	1.2	11.2
	CO_3^{2-}	531.9	2.4	13.0	531.4	1.9	21.5	531.1	1.9	10.5	531.0	2.4	14.0
	C=O, C-O	533.3	1.6	0.7	532.9	2.3	3.4	532.7	2.3	5.7	532.9	2.3	3.9
	P-O	534.2	2.3	2.2	533.8	2.2	1.3	534.1	1.8	0.8	534.1	1.8	0.3
C 1s	**C-C**	285.1	1.4	5.9	285.0	1.6	2.7	284.8	1.6	4.0	284.7	1.7	4.1
	C-O	286.3	2.1	4.4	286.7	1.8	2.0	286.5	2.1	3.5	286.5	2.0	2.7
	C=O	288.4	2.2	2.5	287.7	1.1	0.4	288.2	2.0	1.4	288.2	2.0	2.0
	CO_3^{2-}	290.3	1.9	1.6	289.5	1.6	4.6	289.3	2.0	2.2	289.7	2.1	1.0
P 2p	**$Li_xPO_yF_z$**	135.4	3.2	0.8	134.3	2.7	0.9	134.5	2.8	1.2	134.3	2.6	1.1
		136.3	3.2	0.4	135.2	2.7	0.4	135.4	2.8	0.6	135.2	2.6	0.5
F 1s	**LiF**	686.0	1.9	16.3	685.0	1.8	10.7	684.9	2.0	12.5	685.2	2.0	8.3
	$Li_xPO_yF_z$	688.3	2.5	2.5	687.4	2.6	3.3	687.5	2.7	3.2	687.6	2.3	3.0

Table 4.2.1 Results of the XPS quantitative analysis for the cycled Li_xCoO_2 samples. Binding energies (BE) and full width at half maximum (FWHM) are reported in eV. The results for pristine $LiCoO_2$ are reported in Table 4.1.

		$Li_{0.95}CoO_2$			$Li_{0.75}CoO_2$			$Li_{0.5}CoO_2$			$Li_{0.25}CoO_2$		
Orb.	**Comp.**	**BE**	**FWHM**	**at%**	**BE**	**FWHM**	**at%**	**BE**	**FWHM**	**at%**	**BE**	**FWHM**	**at%**
Li 1s	**Lattice**	54.2	1.0	4.0	54.5	1.6	6.9						
Co 3p		60.7		17.7	61.0		17.3	60.5		20.4	60.7		22.9
Co 2p		779.8		19.4	779.7		20.0	779.6		24.3	779.6		26.1
O 1s	**Lattice**	529.5	1.2	30.2	529.3	1.2	27.0	528.8	1.2	19.7	528.7	1.2	20.7
	Surface	530.4	1.2	5.6	530.2	1.1	5.4	529.6	1.5	12.6	529.7	1.5	12.7
	CO_3^{2-}	531.8	1.5	6.0	531.3	1.9	14.1	531.2	2.4	10.2	531.2	2.6	8.8
	C=O, C-O	533.3	2.0	2.7	533.1	2.4	2.3	533.5	1.7	1.2	533.7	2.4	1.6
F 1s	**LiF**	685.5	1.9	12.2	684.9	1.8	5.5	684.7	2.0	9.3	684.9	2.0	5.6
	$Li_xPO_yF_z$	687.8	2.9	2.4	687.4	2.5	1.5	687.1	3.0	2.3	687.5	2.2	1.7

Table 4.2.2 Results of the HAXPES quantitative analysis for the cycled Li_xCoO_2 samples. Binding energies (BE) and full width at half maximum (FWHM) are reported in eV. The results for pristine $LiCoO_2$ are reported in Table 4.1.

4.2.1.1 Li 1s and F 1s core-level spectra analysis

The Li 1s and F 1s XPS and HAXPES spectra for the *ex-situ* samples are shown in Figure 4.2.1. The Li 1s spectra show a gradual decrease of the peak addressed to Li_xCoO_2 until reaching the detection limit, consistently with the delithiation of the material and coverage by the pSEI. As for the pristine material, the contributions from lithiated surface species were merged into a single peak. Li_2CO_3, $Li_xPO_yF_z$ and LiF and are expected to be present from the C 1s, P 2p, and F 1s spectra. The related HAXPES spectra show mainly just one broad peak due to the buried active material.

Two components were used to fit the F 1s data, assigned to LiF and $Li_xPO_yF_z$. Well-defined spectra were obtained even with HAXPES, because of the high cross-section for F 1s photoemission. This can also imply that the fluorinated species lie below the organic components forming the pSEI, considering the thin film model system. A substantial shift of ~1 eV to lower binding energies is observed for the pSEI-related peaks in both Li 1s and F 1s spectra upon deintercalation. This is not frequently reported because of the common practice of charge-calibrating to the C 1s peak, that masks the effect of electric potential gradient buildup due the difference in the electronic conductivity between the insulating chemical species of the CEI and the buried Li_xCoO_2. Here, the spectra were instead charge-corrected to the Fermi level of the platinum substrate. Following the model by Maibach et al., the peak shifts can be related to different electric potentials at the interface between the electrode active material and the pSEI [260].

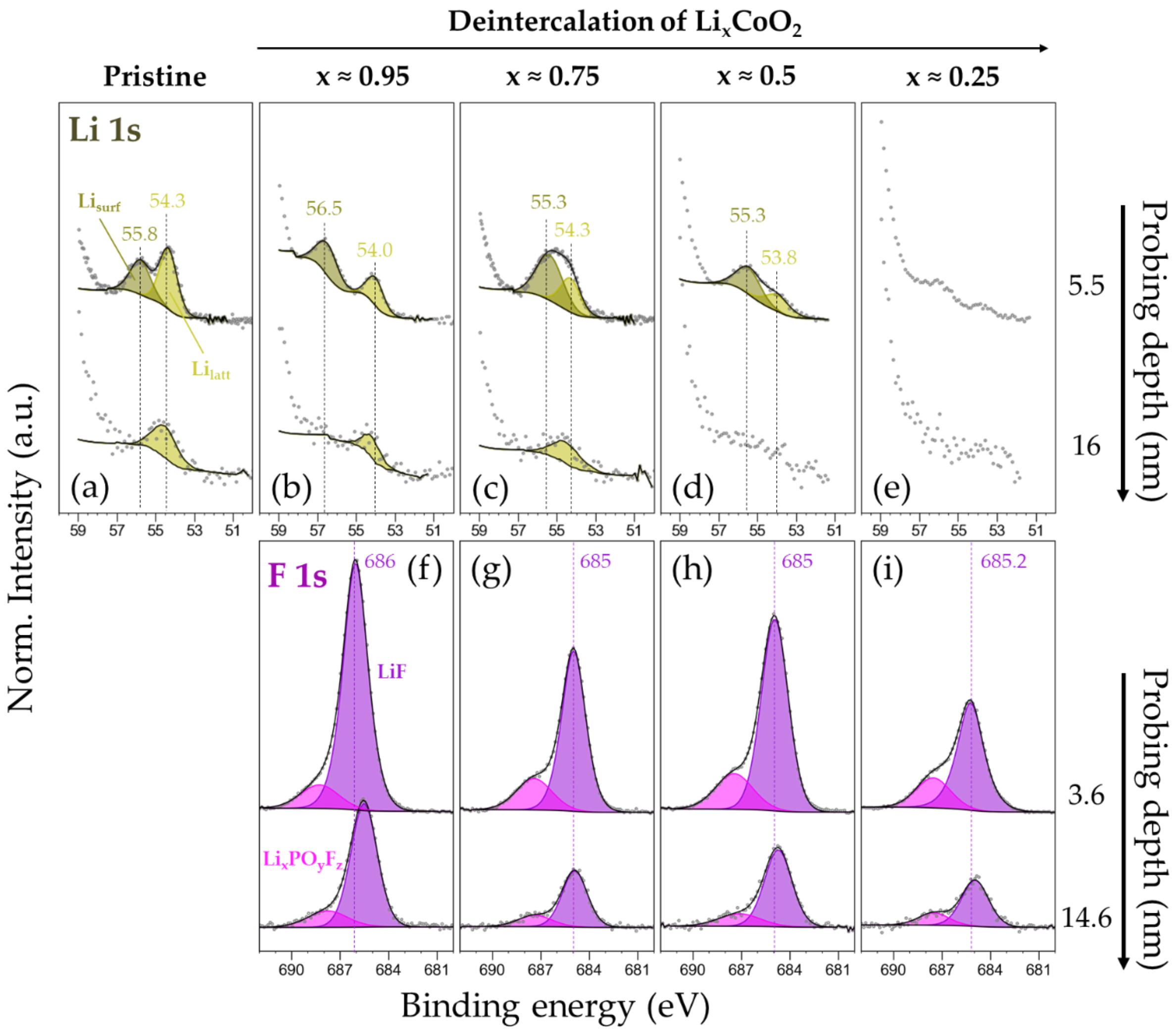

Figure 4.2.1 Li 1s and F 1s core-level spectra for pristine and deintercalated LixCoO2 thin films. The spectra were normalized to the average background intensity on the lower binding energy side of the core level peaks to visualize the changes in relative intensity. In each panel, XPS and HAXPES spectra were stacked as top and bottom spectra. Experimental data, peak components and fits are shown as grey dots, colored-filled areas, and black lines, respectively.

4.2.1.2 C 1s and P 2p core-level spectra analysis

The C 1s and P 2p XPS core level spectra are shown in Figure 4.2.2. As for the pristine electrode analysis, no peak was measured for the C 1s HAXPES spectra. Similarly, the P 2p peaks could be measured only by XPS.

The C 1s spectra show a stark increase in the high binding energy region, which was related to the decomposed electrolyte. However, an accurate identification of the many possible contributions was not achieved, so that the fit is considered an oversimplification of the actual surface chemistry of the sample. With increasing voltage, an initial increase in oxidized carbon-based compounds (mostly Li_2CO_3) is followed by a decrease. This behavior can be explained by the instability of organic carbonates at voltages larger than 4.2 V (x = 0.5), which typically results in CO_2 gas release [205].

The P 2p spectra were fitted with a doublet with energy separation of 0.86 eV because of spin-orbit splitting. The XPS signals were therefore assigned to the $Li_xPO_yF_z$ because the binding energy is on average between the position of fully oxidized Li_3PO_4 and the original salt $LiPF_6$ [19]. Due to the *ex-situ* condition, it is not clear whether $Li_xPO_yF_z$ originated during cycling or from some residual salt on the surface that could not be removed with washing the cathodes.

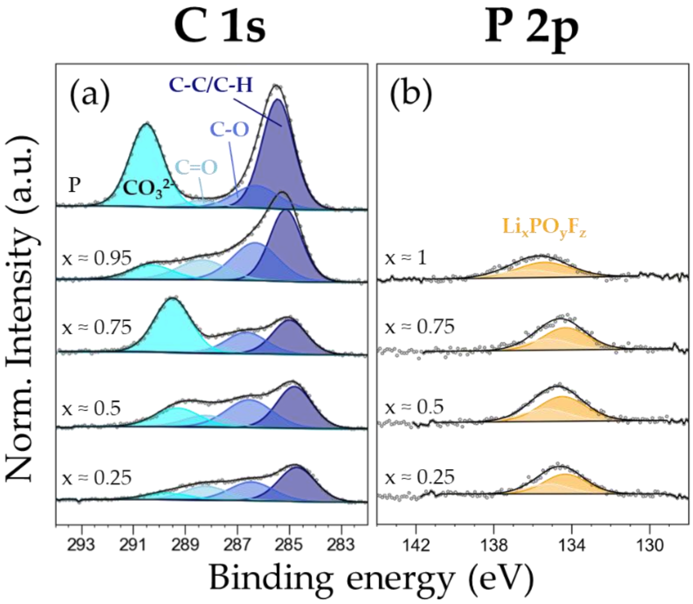

Figure 4.2.2 C 1s and P 2p core-level spectra for pristine and deintercalated Li_xCoO_2 thin films. The spectra were normalized to the average background intensity on the lower binding energy side of the core level peaks to visualize the changes in relative intensity and stacked as indicated by the labels on the left-hand side of each panel.

4.2.1.3 Surface composition and pSEI thickness

From the results of XPS and HAXPES quantification, we reported the surface composition of the electrodes in **Figure 4.2.3**. The stark decrease of (semi-)organic components (Li_2CO_3, POE…) is explained by either the lower photoelectron sensitivity of Li 1s, C 1s, and P 2p or a non-uniform distribution of the inorganic and organic components of the CEI, as already proposed in the literature [166,182]. Due to the fast decomposition of $LiPF_6$ as soon as $LiCoO_2$ is put in contact with the electrolyte, LiF seems to be deposited before the other by-products decomposition reactions occurring at higher voltages [163].

The formation of the pSEI film over the Li_xCoO_2 surface was used as a case of study for comparing the bulk and surface sensitivities of XPS and HAXPES. In the following, we assume a model homogeneous pSEI layer with thickness t formed on the pristine material. Although such model does not accurately represent the complex situation of the real electrode material, it is instructive to estimate the different depth sensitivities of XPS and HAXPES in the case of cycled positive electrode materials.

The thickness t of the pSEI layer was calculated from the area ratio of the peaks due to the buried Li_xCoO_2 before (A) and after (A_0) cycling [163,175]:

$$t = \langle \lambda \rangle \sin\theta \ln \frac{A_0}{A} \qquad \textbf{Equation 4.2.1}$$

where $\langle \lambda \rangle = \frac{\sum_i c_i \lambda_i}{\sum_i c_i}$ is the weighted average IMFP of the pSEI with i the index over each identified phase (LiF, Li_2CO_3, $Li_xPO_yF_z$, POE), c_i their relative percentage atomic concentration as quantified by XPS and HAXPES, λ_i their IMFP as calculated with the QUASES-TPP2M software, and θ = 45° the electron take-off angle. The details about the calculation are found in **Annex G**.

Since the core-level peaks of Li_xCoO_2 change due to deintercalation and surface degradation at higher voltages, we considered only the case for x = 1 i.e. at about the same state of charge as the pristine material. By combining both XPS and HAXPES Co 2p and O 1s results, we estimated the thickness of pSEI to 1.7± 0.5 nm. The result is consistent with the sampling depth of XPS (about 5 nm), since both pSEI and Li_xCoO_2 related spectra are visible, in agreement with literature results by using either XPS or other techniques on similar materials and conditions [163].

With the as-calculated thickness, the O 1s photoelectron intensity exponential decays were calculated as shown in **Figure 4.2.4**. Based on the results for the bilayer model ("pSEI+$LiCoO_2$", thick lines), the integrated sensitivities were then estimated from the area of the curves before (pSEI) and after (Li_xCoO_2) t = 1.7 nm (inset graph). While conventional XPS probes the pSEI and the buried Li_xCoO_2 with similar sensitivity (42 % and 58%, respectively), the O 1s total intensity measured in HAXPES experiments is mostly due to the region below the pSEI (14 % against 86 %). This study allows to directly assess the advantage of combining XPS and HAXPES for resolving both the pSEI and the buried layers.

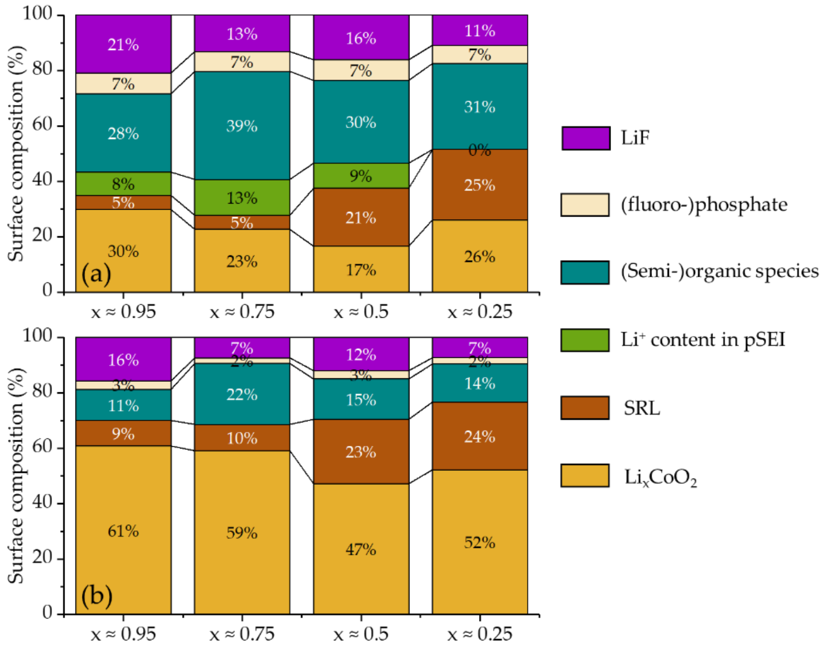

Figure 4.2.3 Surface composition of the cycled thin films determined by (a) XPS and (b) HAXPES quantitative analysis. The components were calculated using the following at% contributions: LiF = F_{LiF}; (fluoro-)phosphate = P 2p + $F_{Li_xPO_yF_z}$ + $O_{P\text{-}O}$, (semi-)organic species = $C_{C\text{-}O}$, $C_{C=O}$ + C_{CO_3} + $O_{C\text{-}O}$ + O_{CO_3}; SRL = O_{surf} + frac(Co_3O_4) x Co 2p; Li_xCoO_2 = O_{latt} + frac($LiCoO_2$) x Co 2p. The at % of Co 2p was divided following the discussion in Section 4.3.1.5.

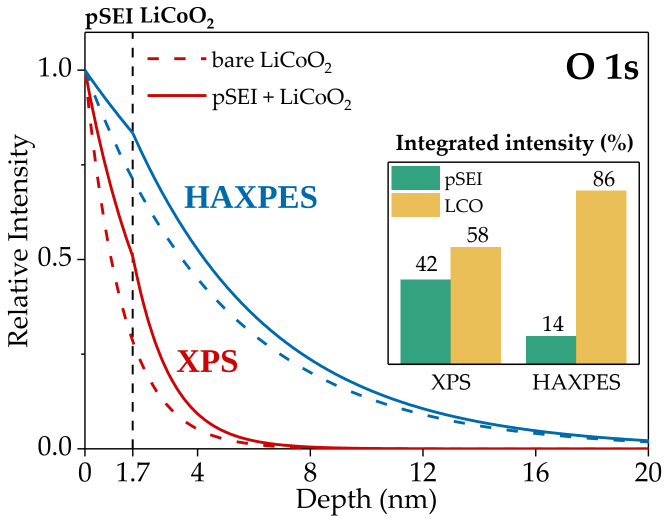

Figure 4.2.4 XPS and HAXPES O 1s attenuation profiles for the model system with homogeneous 1.7 nm-thick pSEI on cycled $LiCoO_2$ (thick lines) compared to pristine $LiCoO_2$ (dashed lines) thin film electrode. Inset: relative area percentage of the curves in the pSEI and $LiCoO_2$ regions.

4.2.2 Insights on the pSEI formed on Li_xNiO_2 electrodes

The characterization of the pSEI formed on the Li_xNiO_2 electrodes by XPS was obstructed by several factors. First, the presence of binder and carbon black complicated the analysis of C 1s peaks. Second, the mechanical scratching step, necessary to observe the Ni 2p spectral features, could in principle alter the composition of the pSEI on the particles. To check the reproducibility of this operation, two electrodes prepared with identical electrochemical protocols were analyzed. Indeed, the only changes in the spectra were attributed to surface species. Further details on mechanical scratching and reproducibility are given in **Annex G**. Finally, the beam damage of synchrotron X-rays significantly affected the C 1s and F 1s spectra. However, some information could be still extracted taking care of the above constraints. The lab-based XPS and HAXPES quantitative results are reported in **Table 4.2.3** and **Table 4.2.4**.

		$Li_{0.8}NiO_2$			$Li_{0.5}NiO_2$			$Li_{0.01}NiO_2$			$Li_{0.01}NiO_2$		
Orb.	**Comp.**	**BE**	**FWHM**	**at%**	**BE**	**FWHM**	**at%**	**BE**	**FWHM**	**at%**	**BE**	**FWHM**	**at%**
Ni 3p		68.1		16.7	67.6		20.9	68.4		20.1	68.5		21.0
Ni 3s		112.5		17.0	112.6		17.1	113.0		17.6	113.2		19.3
Ni 2p		855.0		15.8	855.4		17.6	855.6		15.7	855.4		17.6
O 1s	**lattice**	528.9	1.4	17.2	528.7	1.4	19.1	528.8	1.4	19.3	528.7	1.3	18.1
	surface	530.0	1.7	7.0	530.0	1.4	6.5	530.2	1.3	6.6	530.1	1.8	9.8
	CO_3^{2-}	531.4	1.9	10.5	531.3	1.6	8.7	531.3	1.7	7.8	531.6	1.5	3.3
	C-O, C=O	533.2	2.5	5.3	533.0	1.4	2.0	533.0	2.1	3.0	533.1	2.5	3.4
F 1s	**PVDF**	687.7	2.5	8.0	687.4	2.5	6.8	687.2	2.6	7.4	687.2	2.1	6.1
	LiF	684.5	1.9	2.6	683.8	1.7	1.3	684.0	1.8	2.5	683.7	2.9	1.5

Table 4.2.3 Results of the HAXPES quantitative analysis for the cycled Li_xNiO_2 samples. Binding energies (BE) and full width at half maximum (FWHM) are reported in eV.

		$Li_{0.8}NiO_2$			$Li_{0.5}NiO_2$			$Li_{0.01}NiO_2$			$Li_{0.01}NiO_2$		
Orb.	**Comp.**	**BE**	**FWHM**	**at %**	**BE**	**FWHM**	**at %**	**BE**	**FWHM**	**at %**	**BE**	**FWHM**	**at %**
Li 1s	**Lattice**	53.8	1.2	3.4	53.7	1.4	3.5	53.7	1.3	1.3			
	Surface	55.3	2.0	6.8	55.0	1.5	3.4	55.0	1.8	2.7			
Ni 3p		67.8	4.8	8.9	68.0	4.2	10.6	68.3	4.3	11.7	68.1	4.1	14.4
Ni 2p		855.5	3.9	9.7	855.3	3.2	11.4	855.5	3.2	12.0	855.5	2.9	13.6
O 1s	**lattice**	528.9	1.3	7.8	528.8	1.2	9.5	528.8	1.2	9.0	528.8	1.2	10.8
	surface	530.3	1.7	3.8	530.3	1.7	6.4	530.3	1.8	7.4	530.2	1.8	7.5
	CO_3^{2-}	531.6	2.1	12.9	531.3	1.8	10.5	531.3	2.1	9.8	531.3	2.3	8.9
	C-O, C=O	533.6	2.5	5.0	533.0	2.3	4.0	533.2	2.2	3.2	533.2	2.2	2.7
C 1s	**C=C (CB)**	284.5	1.0	5.1	284.2	1.0	8.8	284.1	1.0	9.7	284.1	1.0	11.4
	C-C	284.8	1.7	8.8	284.8	1.9	10.3	284.8	1.9	10.6	284.8	1.9	9.4
	C-O	286.5	2.0	3.3	286.5	1.8	1.7	286.6	1.9	2.4	286.6	1.9	2.5
	C=O	288.3	2.0	2.6	288.3	2.0	2.8	288.3	2.0	2.5	288.3	1.9	1.9
	CO32-	289.8	1.2	1.0	289.8	1.3	1.9	289.8	1.4	2.0	289.8	1.2	1.8
	CH_2 (PVDF)	286.3	1.7	3.9	286.3	1.3	1.8	286.3	1.3	1.7	286.3	1.3	1.8
	CF_2 (PVDF)	290.8	1.7	3.9	290.8	1.3	1.8	290.8	1.3	1.7	290.8	1.3	1.8
F 1s	**CF_2 (PVDF)**	687.7	2.4	9.9	687.4	2.2	9.3	687.3	2.2	9.4	687.3	2.1	9.7
	LiF	684.6	1.9	3.2	684.2	2.1	2.4	684.1	2.1	3.2	683.7	2.0	1.8

Table 4.2.4 Results of the XPS quantitative analysis for the cycled Li_xNiO_2 samples. Binding energies (BE) and full width at half maximum (FWHM) are reported in eV.

4.2.2.1 Li 1s and F 1s spectra

Figure 4.2.5 shows the Li 1s lab-based XPS and synchrotron HAXPES spectra. The Li 1s spectra were normalized to their background intensity for direct comparison. While the peaks did not appear in laboratory HAXPES, the high flux of synchrotron radiation allowed to characterize Li electronic states at different depths.

As for Li_xCoO_2 study, the spectra were decomposed into two contributions: one for the Li^+ in the oxide lattice structure (Li_{latt}, ~54 eV) and the second including all lithiated surface species (Li_{surf}, ~56 eV). Considering the O 1s and F 1s spectra (discussed below), the lithiated species of the pSEI included LiF and Li_2CO_3, as observed for the Li_xCoO_2 samples.

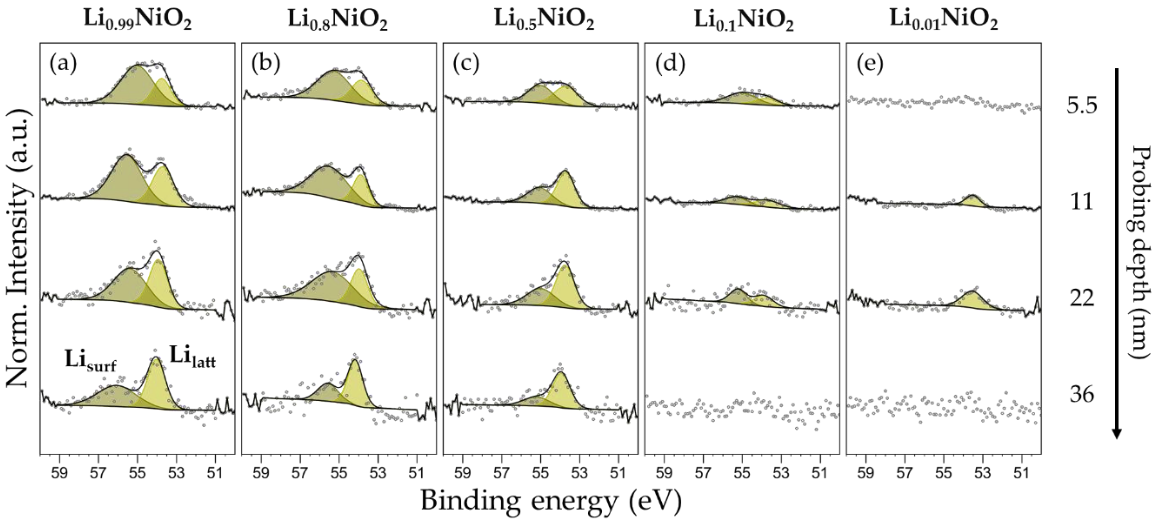

Figure 4.2.5 High-resolution Li 1s core-level spectra of (a) LiNiO$_2$, (b) Li$_{0.8}$NiO$_2$, (c) Li$_{0.5}$NiO$_2$, (d) Li$_{0.1}$NiO$_2$, and (e) Li$_{0.01}$NiO$_2$ electrodes. For each sample, the spectra are shown as stack plots from the most surface (top) to the most bulk-sensitive (bottom) measurement. The spectra were normalized to the average background intensity in the 48-50 eV region to allow peak intensity comparison. Experimental data, peak components and fits are shown as black dots, colored-filled areas, and black lines, respectively.

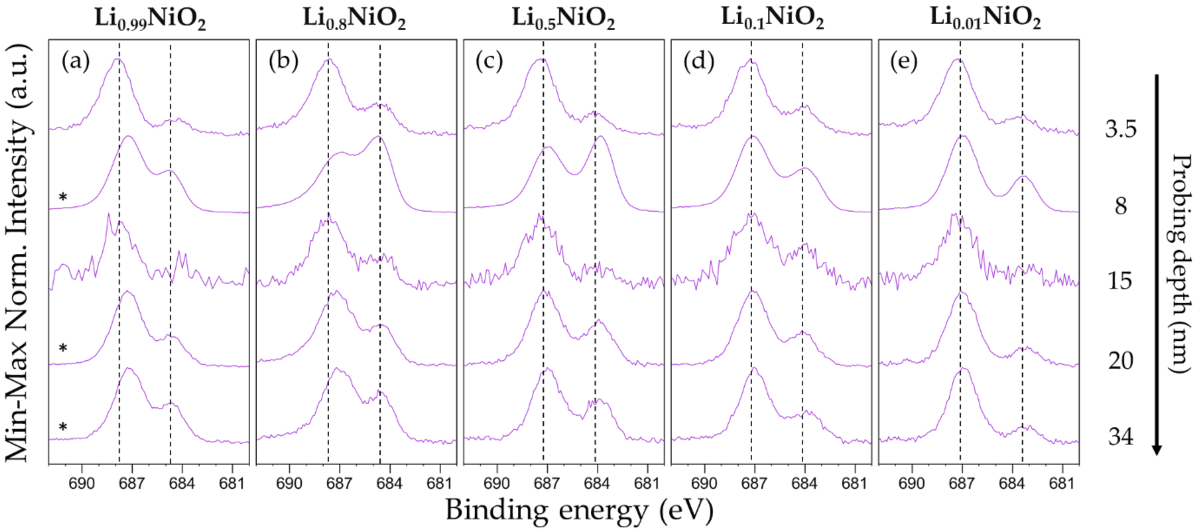

Figure 4.2.6 High-resolution F 1s core-level spectra of (a) LiNiO$_2$, (b) Li$_{0.8}$NiO$_2$, (c) Li$_{0.5}$NiO$_2$, (d) Li$_{0.1}$NiO$_2$, and (e) Li$_{0.01}$NiO$_2$ electrodes. For each sample, the spectra are shown as stack plots from the most surface (top) to the most bulk-sensitive (bottom) measurement. The spectra were normalized to the average background intensity in the 680-681 eV region to allow peak intensity comparison.

The Li$_{surf}$ peak gradually decreases with increasing probing depth and upon deintercalation. This trend is consistent with the results for Li$_x$CoO$_2$ showing that the surface species do not simply accumulates, increasing the pSEI thickness over time. In fact, it has been proposed either a formation-dissolution cycling behavior or the cross-talk with the thicker SEI at the negative electrode (or a contribution of both factors) may rule the pSEI evolution [170,176]. At high states of charges [**Figure 4.2.5(d,e)**], for which the Li concentration in the Li$_x$NiO$_2$ is expected to be below the detection limit of

HAXPES, the Li_{latt} peak was still measured closer to the surface. This suggests the presence of a few nm surface layer of lithium ions trapped in the SRL [191,192,194,309].

The F 1s spectra shown in **Figure 4.2.6** were qualitatively analyzed due to degradation effects discussed in the submitted paper (**Annex I**, **paper 2**). In fact, the two-peaks model employed for the lab-based data and discussed in **Section 3.2.3.3** cannot be applied in this case. The low binding energy peak, assigned to LiF, was always larger in the synchrotron HAXPES (rows indicated by the star symbol) compared to the lab-based spectra. Moreover, it is the highest for the spectra acquired at 2.3 keV, corresponding to the highest flux conditions.

4.2.2.2 pSEI thickness

The thickness of the pSEI after formation cycles was estimated with the same approach developed for Li_xCoO_2 thin film electrodes. We establish the calculation based on the spectra recorded on unscratched electrodes. The calculation is based on the peak area of the low-binding energy O 1s XPS spectra shown in **Annex G**. The as-calculated thickness was 1.6 nm, close to the result obtained for Li_xCoO_2.

4.2.2.3 Assessing the contribution of pSEI on the capacity loss after long-cycling conditions

Despite we observed a similar pSEI for Li_xCoO_2 and Li_xNiO_2 in terms of thickness and chemical composition, the capacity loss after formation cycles for Li_xNiO_2 was significantly larger. To evaluate the contribution of pSEI to the capacity loss, we compared these results to samples retrieved after long cycling conditions. After formation cycles, two cells were let charging and discharging for 100 cycles at fast (1C) and slow (C/10) C-rate. After the prolonged cycling, the discharge capacity loss were 89 and 20 % with respect to the one after formation cycles [**Figure 4.2.7(a)**], in line with other stability tests [309].

Figure 4.2.7(b,c) displays the Li 1s and F 1s lab-based XPS spectra of the two cycled electrodes compared to $LiNiO_2$ before and after formation cycles as well as after soaking the material in the electrolyte. To track the surface composition and concentration of the pSEI, the area percentage of Li_{surf} over the total Li 1s spectra was calculated [**Figure 4.2.7(d)**, green dots], showing a decrease after long cycling. The at% ratio between the F 1s peak related to LiF and the Li_{surf} peak was also considered [**Figure 4.2.7(d)**, pink dots], showing a large increase only for the samples cycled at 1C, indicating a LiF-enrichment. The presence of species like NiF_2, expected at similar binding energy and which may form at high cycling regime conditions, cannot be excluded [164,184]. The slight shift to larger binding energies in the Ni $2p_{3/2}$ peak support this claim, although it is difficult to distinguish its contribution from the SRL.

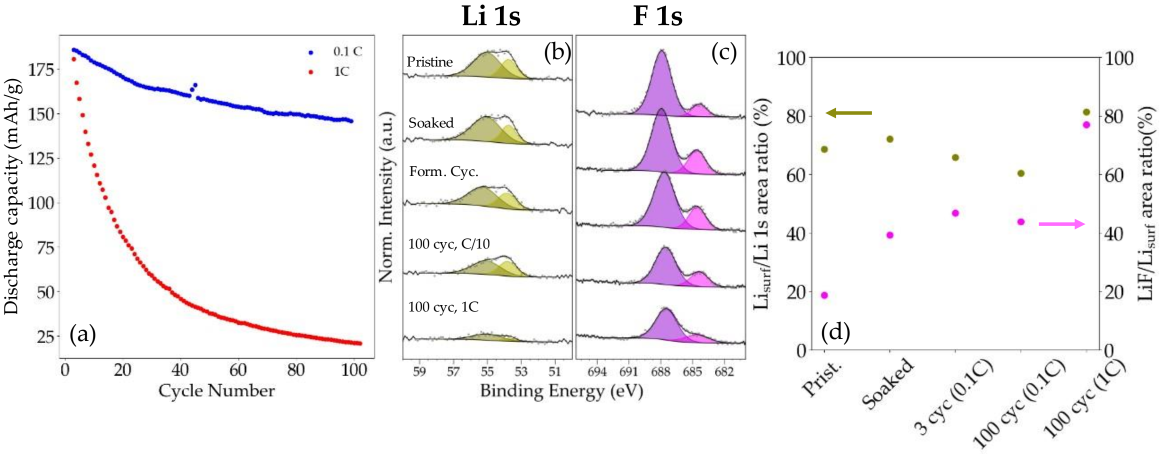

Figure 4.2.7 Study of pSEI composition for Li_xNiO_2 electrodes after long cycling conditions. (a) Discharge capacity as a function of cycle number upon galvanostatic cycling at 0.1C and 1C. Comparison of (b) Li 1s and (c) F 1s normalized XPS spectra for electrode before and after few cycles up to 100 cycles. (d) Figures of merits calculated from the Li 1s and F 1s peak fitting.

Eventually, the analysis points towards a low influence of the pSEI on the capacity loss upon cycling for these positive electrode materials. Although this conclusion should be corroborated by other investigations tailored to characterize the sensitive and ultra-thin pSEI observed in layered transition metal oxides, it does find agreement with recent findings in the literature. Riewald et al. and Xu et al. identified the deactivation of the H3 phase at the end of the charge as the main cause of the charging capacity loss in $LiNiO_2$ and NMC811, respectively [194,210]. The deactivation was ascribed to the interfacial lattice strain between the bulk structure and the SRL. The studies by the Gasteiger's group based on gas release analysis identified the H2/H3 phase transition and associated surface O_2 evolution as the main responsible for surface degradation and cycling stability limit of layered transition metal oxides [152,204]. Moreover, Pan et al. pointed out that surface degradation and SRL specifically has a larger impact on electrochemical performances than particle cracking (in liquid cell setup) [309]. Björklund et al. confirmed this picture overall but also highlighted the electrode slippage (capacity alignment of the electrodes in a full cell relative to initial conditions) contribution, i.e. the role of graphite negative electrode cannot be neglected [310].

In summary, the spotlight on surface degradation mechanisms and role in capacity loss was given to the SRL formation and evolution instead.

4.3 Distinguishing the SRL and bulk by HAXPES

The presence of a SRL in cycled materials is well known in the literature and its influence on the electrochemical performance is more and more recognized as of primary importance. Nevertheless, its characterization by photoelectron spectroscopy techniques is quite rare (**Section 1.5.3.3** and references therein). Unravelling bulk and surface contributions in HAXPES spectra is nontrivial due to the exponential decay of the photoelectron intensity as a function of the depth and the absence of references for cycled bulk materials.

Based on the quantitative analysis and M 2p peak fitting approaches discussed in **Section 3.3**, the study of the SRL formed on Li_xCoO_2 and Li_xNiO_2 samples is presented below. The objective of this study is twofold: (1) to study the influence of cut-off voltage and deintercalation level on the SRL composition and thickness and (2) to discriminate the buried bulk signals to be further analyzed by cluster model-based simulations, which will be the subject of the next chapter.

4.3.1 Surface degradation of Li_xCoO_2

4.3.1.1 Co 2p analysis

Although a peak fitting model for the Co 2p peaks was developed for the pristine $LiCoO_2$, this could not be employed for the cycled materials. In fact, as was later recognized, the deintercalated Li_xCoO_2 is subjected to an insulator-to-metal transition for $0.94<x<0.75$. For deintercalated samples, therefore, the tailing of the Co 2p main lines should be described by asymmetric lineshapes rather than symmetric peaks as proposed in **Section 3.3.2.1**. Therefore, the analysis of the Co 2p core level peaks was kept at a qualitative level for this set of samples.

The Co 2p XPS and HAXPES spectra for pristine and cycled *ex-situ* Li_xCoO_2 samples are shown in **Figure 4.3.1**, respectively. Upon deintercalation, the main changes in the XPS and HAXPES spectra are the more pronounced main line asymmetry and the increasing intensity the satellite structure at ~785 eV. The former is explained by the metallic character of the deintercalated samples [110]. To explain the increase in satellite intensity, we refer to the Ar-ion beam etching experiment discussed in **Section 3.3.1**, where a similar increase in intensity at ~785 eV was related to reduced Co^{II} ions. The comparison of XPS and HAXPES spectra indicate that they are mostly concentrated at the extreme surface for all samples.

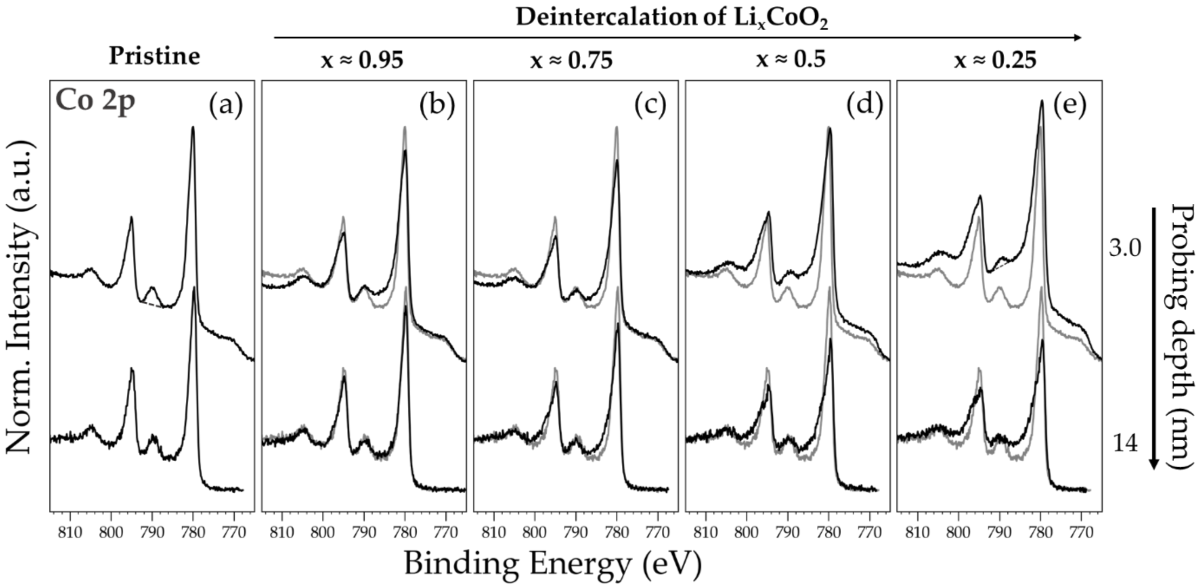

Figure 4.3.1 Co 2p core-level spectra for pristine and deintercalated Li_xCoO_2 thin films. The spectra were normalized to the average background intensity on the lower binding energy side of the core level peaks to visualize the changes in relative intensity. In each panel, XPS and HAXPES spectra were stacked as top and bottom spectra; the related probing depth are reported on the right-hand side. The spectra for pristine $LiCoO_2$ are added to each panel (in grey) to help distinguishing the spectra evolution over deintercalation. In (a) and (e), a background dotted line is shown to illustrate the analysis method by Dahéron et al. based on satellite peak area, commented in the main text.

Regarding the bulk cobalt oxidation that should be tracked upon deintercalation, we do not distinguish the satellite for Co^{IV} ions in the spectra. Indeed, only the main line asymmetry could be related to bulk oxidation of Li_xCoO_2 in the literature, although it only proves the screening of the core hole by unoccupied states above the Fermi level and cannot therefore prove the presence of Co^{IV} ions by itself, as was proposed elsewhere [256,311]. To account for Co^{III} oxidation, Dahéron et al. related the decrease of the Co^{III} satellite peak at 790 eV, measured by tracing a background line between ~787 and 792 eV, to the oxidation to Co^{III} to Co^{IV}, as illustrated in **Figure 4.3.1(a,e)**. However, both the increase of the Co^{II} satellite structure and the broadening of the main line may effectively contribute to such a decrease of the Co^{III} satellite peak, making it an uncertain parameter for tracking bulk oxidation.

Therefore, the analysis of the Co 2p spectrum could not highlight the signature of oxidation from Co^{III} to Co^{IV}. Since the O 1s analysis discussed below shows that the bulk material is probed with our XPS and HAXPES settings, we can exclude that the SRL thickness exceeded the probing depth of these measures. Therefore, another explanation must be given. The combination of experimental HAXPES and cluster model simulations represent a new way to reveal the spectral signatures of Co ions upon deintercalation, as discussed in the next chapter.

4.3.1.2 O 1s analysis

The O 1s XPS and HAXPES spectra of pristine and deintercalated Li$_x$CoO$_2$ electrodes are shown in **Figure 4.3.2**. The peaks were assigned to oxygen in layered lattice (O$_{latt}$, ~529 eV), in the surface layer (O$_{surf}$ at ~530 eV), and in the surface species (O$_{carb}$ at ~531.5, O$_{org}$ at ~533 eV, O$_{P-O}$ at ~534 eV). Herein, we focus on the evolution of the low-binding energy part, fitted by two peaks following the O 1s peak fitting model developed for the pristine materials in **Chapter 3**.

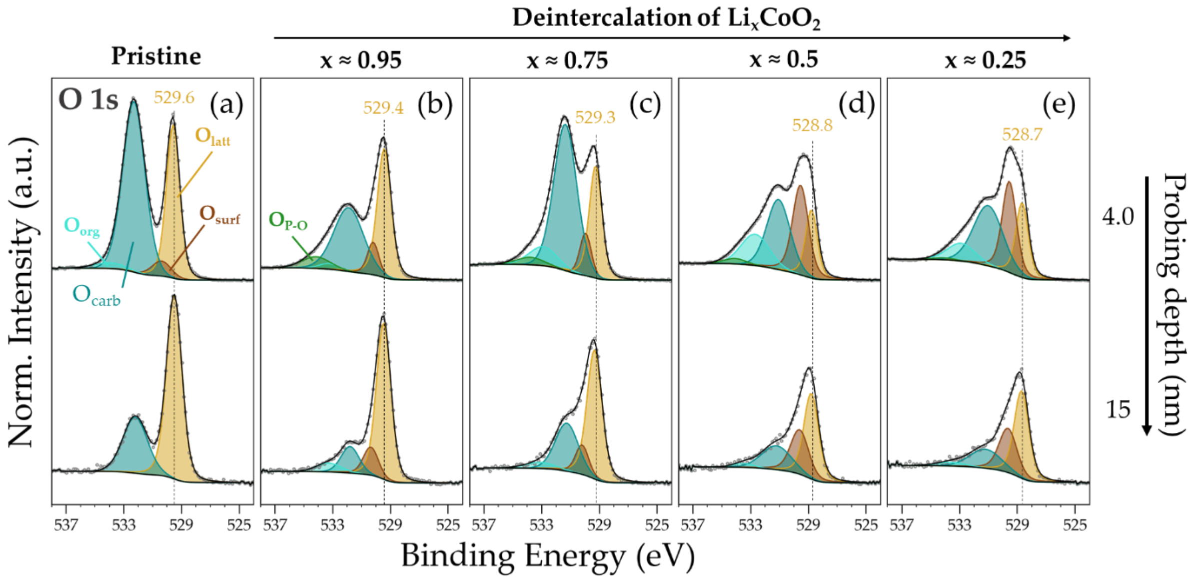

Figure 4.3.2 O 1s core-level spectra for pristine and deintercalated Li$_x$CoO$_2$ thin films. The spectra were normalized to the average background intensity on the lower binding energy side of the core level peaks to visualize the changes in relative intensity. In each panel, XPS and HAXPES spectra were stacked as top and bottom spectra; the related probing depth are reported on the right-hand side. Experimental data, peak components and fits are shown as grey dots, colored-filled areas, and black lines, respectively.

Upon deintercalation, the peaks slightly shift to lower binding energies down to 528.7 eV for the O$_{latt}$ peak of Li$_{0.25}$CoO$_2$, while the O$_{surf}$ peak increases in intensity. For the pristine material, the second peak at 530 eV was referred to the surface layer (**Section 3.2.2.4**). However, further comments are necessary for the cycled materials. In fact, both *ex-situ* XPS and *operando* HAXPES analysis of deintercalated Li$_x$CoO$_2$ assigned this peak to bulk oxygen oxidation [108,256,311]. However, several arguments go against this interpretation for our set of data:

1. The peak is present at all state of charges, including the pristine material.
2. The relative area of the peak is systematically larger in the XPS spectra than that of HAXPES ones, suggesting a depth distribution.
3. The Co 2p analysis indicated surface cobalt reduction.
4. The DFT study of O 1s peaks evolution did not highlight emergence of high-energy components upon deintercalation (see **Section 4.3.1.3** for discussion).

5. The XPS and HAXPES quantification for the O/Co ratio indicates an increase of deoxygenation at the uppermost surface.

The latter argument is further developed in **Figure 4.3.3**, which compares the evolution of the O:Co stoichiometry (top panel) and the O_{surf}/O1s area ratio (bottom panel). A clear correlation between the decrease of the O/Co ratio and the O_{surf} peak area is established. As mentioned in **Section 3.2.2.4**, there is no agreement in the literature on the assignation of this peak. Our results go in favor of the interpretation by Schultz et al., who assigned the peak to surface degradation [166]. The authors labelled the SRL by the generic $(Co^{II},Co^{III})_xO_y(OH)_z$ since the O 1s binding energy of this component is in between the Co^{III}-OH and Co^{II}-OH components of air-exposed $LiCoO_2$ and $Co(OH)_2$.

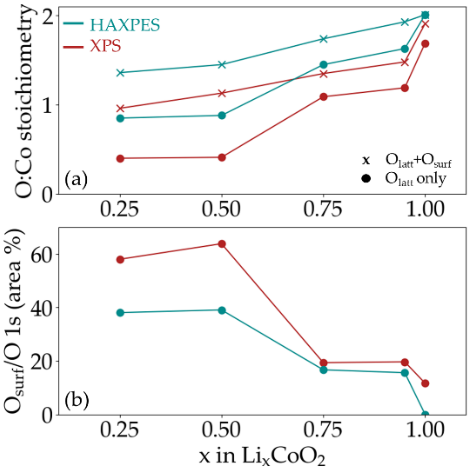

Figure 4.3.3 (a) O:Co stoichiometry in cycled Li_xCoO_2 calculated either taking the sum of both O_{latt} and O_{surf} peaks (cross) or only the O_{latt} peak (dots). The average between Co 2p and Co 3p was used for cobalt quantification. (b) Area percentage of the O_{surf} peak to the sum of O_{surf} and O_{latt}.

However, we disagree with this interpretation: electrochemically-driven surface degradation should not be simply explained based on surface reactivity with air moisture by the pristine material. More generally, it is not possible to determine the precise nature of the SRL by XPS analysis only: to go further, structural information is required. Atomic-resolution STEM is a suitable technique for acquiring such information but could not be carried out for the $LiCoO_2$ samples. Therefore, we based on the several STEM studies reported in the literature, which overall indicate a surface structural degradation towards spinel Co_3O_4-like plus, in some cases, minority CoO at the extreme surface [193,198,312,313].

Although it was not possible to estimate the thickness of the SRL, the fact that the low-binding energy peak was still visible for all samples indicates that it did not exceed the probing depth of XPS (~4 nm). However, as reported by Sharifi-Asl et al. the surface degradation is strongly facet-dependent, meaning that regions with thinner and thicker SRL can be present on the surface of the polycrystalline film [314].

4.3.1.3 Investigation of O 1s peak components by DFT

The question of the origin of the peak at ~530 eV was also approached by *ab initio* calculations, based on the assumption that two populations of oxygen anions with different oxidation state can be expected in delithiated Li_xCoO_2. We considered the case of $Li_{0.5}CoO_2$, since its monoclinic structure presents two different crystallographic oxygen sites showing a different number of first neighbors [**Figure 4.3.4(a)**]. Thus, we posed the following question: does the presence of different local lithium vacancies explain the experimental binding energy difference between the two low-energy peaks as shown in **Figure 4.3.4(b)**? To answer it, we calculated the O 1s binding energy for the two oxygen sites in $Li_{0.5}CoO_2$ and compare it to $LiCoO_2$ using the Janak-Slater method presented in **Section 2.2.1.2**. The calculation was run on supercells to avoid the interaction between neighboring core holes (see **Annex G**). We refer to **Section 5.1** for a general description of the DFT results for these materials and focus here on the binding energy simulations specifically.

The resulting O 1s binding energies are shown in **Figure 4.3.4(c)** as Gaussian distributions with a full width at half middle (FWHM) corresponding to the experimental HAXPES resolution of about 1 eV. In terms of absolute values, both calculations are about 9-10 eV larger than the experimental ones. This can be explained by the missing electronic correlations in the PBE exchange-correlation functional, leading to an overestimation of Co-O covalency. However, the strength of the Janak-Slater method stands in the comparison of binding energy differences [242]. Concerning the two peaks of $Li_{0.5}CoO_2$, the binding energies for the two oxygen local configurations are separated by about 0.3 eV, which falls short to the experimental splitting of about 0.8 eV and is lower than the experimental resolution. This suggests that the two contributions might be unresolved in the experimental peak at ~529 eV.

Moreover, this study offered further insight into the O 1s binding energy shift to lower binding energies. Generally, an increase in binding energy is expected upon oxidation due to the decrease of the electron density screening the interaction between core electrons and the nucleus (see paragraph on chemical shifts in **Annex A**). For the O 1s peaks, however, the opposite trend is observed upon oxidation from $LiCoO_2$ to $Li_{0.5}CoO_2$, qualitatively reproduced by DFT results [**Figure 4.3.4(b,c)**].

We explain this shift by the insulator-metal transition occurring from $x=0.94$ to $x=0.75$ in Li_xCoO_2 [89]. In fact, such a transition to a metallic state (qualitatively reproduced in the PBE calculations, see **Section 5.1.2**) can promote a better screening of the core electrons, decreasing their binding energies. Experimentally, this interpretation is supported by the fact that all peaks related to Li_xCoO_2 shift to lower binding energies upon deintercalation, indicating a general behavior (see **Figure 4.2.1**, **Figure 4.3.1**, **Figure 4.3.2**, and **Figure 5.1.2** for Li 1s, Co 2p, O 1s, and valence band, respectively). A similar behavior is matched in the literature for studies that referred the binding energy scale to a metallic contact as in our study [109,256]; the shifts appear instead masked whenever the binding energy scale was calibrated to carbon contamination [108].

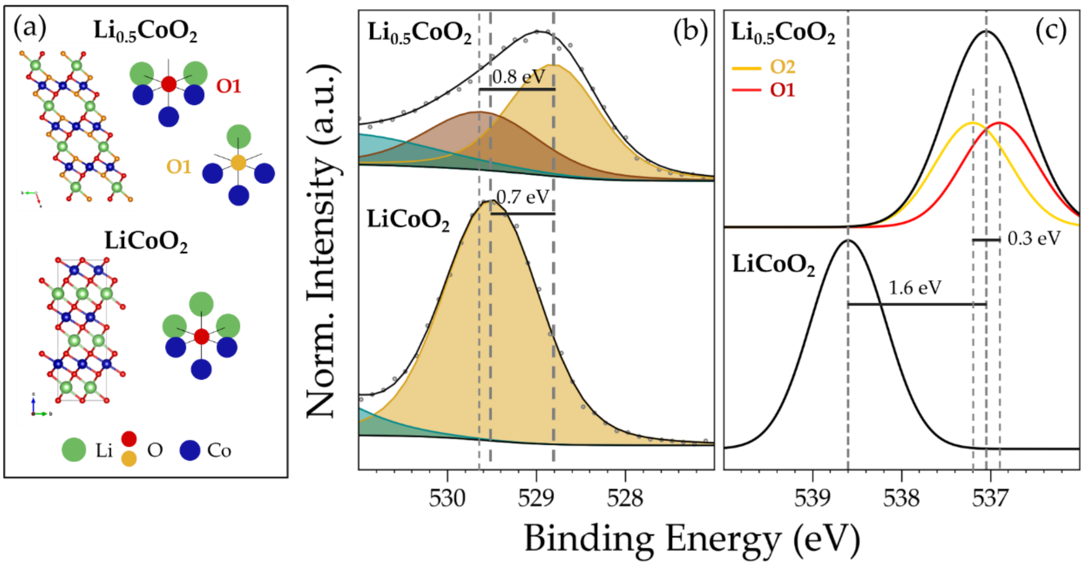

Figure 4.3.4 O 1s peak analysis by DFT calculations. (a) Crystal structures of $LiCoO_2$ and $Li_{0.5}CoO_2$ highlighting the local environment around the O ions. (b) Zoom of the low-energy peaks of the O 1s HAXPES spectra. The spectra are normalized as in Figure 4.3.4. (c) Simulated O 1s contributions for the bulk materials shown as gaussian distributions with FWHM=1 eV and centered at the calculated binding energy. The gaussian functions were normalized to the relative occupation in the crystal structure (i.e. set to 1 for $LiCoO_2$ and 0.5 for $Li_{0.5}CoO_2$). The black line in $Li_{0.5}CoO_2$ shows the sum of the two contributions in $Li_{0.5}CoO_2$. The same energy scale is used in (b) and (c).

In conclusion, while a difference in binding energies can be expected for the two crystallographic sites of $Li_{0.5}CoO_2$, the simulations indicate that they are unresolved in the lowest energy peak. Moreover, this study allowed clarifying the binding energy shifts related to Li_xCoO_2 core levels.

4.3.1.4 Accounting for *ex-situ* conditions: the relation between state-of-charge and surface degradation

It is well documented that cycling Li_xCoO_2 with higher upper-cut off voltages leads to faster surface degradation and larger loss of capacities [111,198]. In fact, Li_xCoO_2 is increasingly unstable for increasing deintercalation levels: at present, intensive research aims to overcome the 4.5 V threshold towards higher energy densities, facing severe degradation issues [51–53,55,111]. In the present study, however, all samples were subjected to the same formation cycling protocol, that brought them to $x = 0.5$ (4.2 V) at the end of charge in each cycle. Only at the last cycle the charge was interrupted at different voltages, meaning that any difference in the surface degradation within the set of samples should be related to this latter step but not just to their end-of-charge voltage. Either (1) a reversible formation/reconstruction for the SRL or an effect happening *after* reaching the end of charge can explain this issue. In the latter case, the larger degradation might be a consequence of (2) the *ex-situ* conditions (surface reconstruction induced by opening the cell) or (3) the voltage holding step. Unfortunately, it was not possible to check (3) by preparing another sample without the final hold step. However, Qin et al. observed by STEM that holding the voltage at 4.7 V for 2 hours or 7 days produced a very similar SRL [313]. Therefore, this effect does not seem likely the dominant one. To investigate options (1) and (2), *operando* HAXPES conditions would be the ideal technique.

Kiuchi et al. studied by *operando* HAXPES the deintercalation of Li_xCoO_2, using a model thin film solid-state battery in the 2.5-4.2 V voltage range [256]. They observed a reversible splitting of the main O 1s peak to a double structure, shifting to lower binding energies at 4.2 V. Because of its reversibility, they related this behavior to bulk oxygen oxidation. However, the results of Kuchi et al. still need further confirmation, especially considering the cycling curves (not representative of the typical behavior of $LiCoO_2$ in a Li-ion cell) and the influence that ultrahigh vacuum conditions and the Au current collector may have on the experiment [7]. In any case, following the discussion given in **Section 1.5.1**, the transformation of $LiCoO_2$ to Co_3O_4 should release O_2, as experimentally observed [204], which makes the process irreversible and option (1) rather unlikely. Moreover, we noticed the O 1s double structure observed by Kiuchi does not seem to be the same as observed in our experiments, as the higher-energy peak does not increase in intensity upon charging, in contrast with our results.

Eventually, we concluded that option (2) i.e. the *ex-situ* conditions may be responsible for the larger surface degradation (larger O_{surf} peak in particular) observed for samples $Li_{0.5}CoO_2$ and $Li_{0.25}CoO_2$, induced by their lower surface stability with respect to samples retrieved at discharge state. It is unclear if the degradation observed for $Li_{0.95}CoO_2$ and $Li_{0.75}CoO_2$ is also in part due to surface reconstruction after the cell opening. Because of the strong similarity in the O 1s and Co 2p spectra for the samples at pristine and discharged states, however, this looks rather a secondary effect.

Note this explanation can be generalized to all *ex-situ* XPS and HAXPES studies of battery materials, and in particular on Li-rich oxides. Indeed, several studies claimed O-bulk redox activity based on apparent reversible increase and decrease of the peak at 530 eV at charge and discharge state (see **Section 1.4.5** and references therein).

---

[7] For instance, we performed preliminary *operando* HAXPES tests with a simplified Pt/$LiCoO_2$/Pt system and observed a very different electrochemical behavior in air or UHV conditions, led by Pt catalytic activity. Also, gold is known to form alloy with lithium shifting the cell potential [315].

However, as for the present study, degradation due to lower stability of deintercalated oxides and induced by *ex-situ* conditions can also explain this effect.

4.3.1.5 Estimating cobalt reduction by a simplified model system

As for the pSEI, further information can be extracted from the quantitative XPS and HAXPES analysis based on a simplified model system. In the following discussions, two major approximations are assumed: (1) the SRL is considered as a homogeneous Co_3O_4 surface layer formed at the surface of cycled Li_xCoO_2 thin films and (2) the O_{surf} peak in the O 1s spectra is uniquely attributed to the as-defined SRL.

Within this simplified model, the atomic concentration of Co^{II} ions can be calculated as follows. Considering the Co_3O_4 stoichiometry and that Co^{II}:Co^{III}=1:2 in Co_3O_4, it follows that the concentration of Co^{II} ions ($N_{Co^{II}}$) is related to that of O atoms in the SRL ($N_{O_{surf}}$) as $N_{Co^{II}} = \frac{1}{3} N_{Co_{surf}} = \frac{1}{3}\frac{3}{4} N_{O_{surf}} = \frac{1}{4} N_{O_{surf}}$. Since the concentration of a chemical species N_i is related to the measured core-level photoelectron peak intensity I_i normalized by its relative sensitivity factor RSF_i ($N_i = I_i/RSF_i$, see **Annex A** for details), the percentage of Co^{II} to the total measured Co concentration can be calculated taking the Co^{II}/Co area ratio (method 1). Alternatively, the concentration of Co can be related to the O_{latt} peak of the O 1s spectrum considering the Li_xCoO_2 stoichiometry (method 2).

Method 1 - from the O/Co atomic concentration:

$$Co^{II}/_{Co}\,(\%) = \frac{\frac{1}{4} N_{O_{surf}}}{\left(\frac{N_{\mathrm{Co3p}} + N_{\mathrm{Co2p}}}{2}\right)} \qquad \textbf{Equation 4.3.1}$$

Method 2 - from the O 1s peak fitting:

$$Co^{II}/_{Co}\,(\%) = \frac{\frac{1}{4} I_{O_{surf}}}{\frac{3}{4} I_{O_{surf}} + \frac{1}{2} I_{O_{latt}}} \qquad \textbf{Equation 4.3.2}$$

The results of both calculations are shown in **Figure 4.3.5** for both XPS and HAXPES. Despite the approximations, the consistency between the results at low deintercalation state obtained by both methods suggests that the SRL consists in part of a Co_3O_4-like material. In fact, while method 2 is entirely based on stoichiometry assumptions, method 1 exploits the Co/O quantification. For the most deintercalated samples, the divergence between the two estimations may indicate the presence of a reduced CoO-like phase in the SRL. Both the XPS and HAXPES results show that the Co^{II} concentration increases along the deintercalation line and is slightly larger for XPS at any point, as expected. From these results, the phase percentages of Co_3O_4 and

Li_xCoO_2 were also calculated[8] and used to construct the percentage charts in **Figure 4.2.3**.

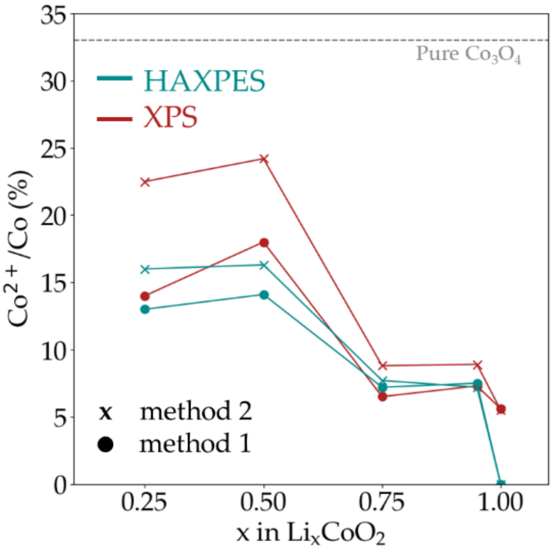

Figure 4.3.5 Percentage of Co^{II} on the total Co content in cycled Li_xCoO_2 calculated from the XPS and HAXPES data.

4.3.1.6 Relating surface reduction and capacity loss

Once the relative amount of Co^{II} was calculated, its increase relative to the pristine material was compared to the electrochemical data to infer on the contribution of the SRL to the capacity loss. Because of the voltage-driven degradation issue explained above, only the sample at discharged state (x ≈ 1) was considered. Based on the Faraday law, the difference in Co^{II} concentration found for the samples at discharged and pristine state was converted into a charge considering the elementary reduction of Co^{III} to Co^{II} and the mass defined by the cylinder probed by XPS/HAXPES given by the X-ray beam spot times the probing depth. All details on the calculations are reported in the **Annex G**.

The results of this calculation give Q_{loss}^{XPS} = 7 mAh/g and Q_{loss}^{HAXPES} = 20 mAh/g, yielding an average of 13.5 ± 6.5 mAh/g. The experimental total capacity loss (charge at first cycle – discharge at last cycle) was 14 mAh/g. Naturally, the result obtained by the model calculation is expected to be quite inaccurate due to the large number of approximations necessary to obtain it. Therefore, the striking similarity between the two values is more likely a coincidence. However, the fact that the capacity loss given

---

[8] $Frac.Co_3O_4(\%) = \frac{\frac{1}{4}AO_{surf}}{\frac{1}{4}AO_{surf}+\frac{1}{2}AO_{latt}}$, $Frac.LiCoO_2(\%) = 1 - \frac{\frac{1}{4}AO_{surf}}{\frac{1}{4}AO_{surf}+\frac{1}{2}AO_{latt}}$

by cobalt surface reduction is of the same order as the total experimental capacity loss is less likely a coincidence and suggests that the evolution of the SRL is quite relevant for the cycle stability of $LiCoO_2$.

4.3.2 Surface degradation of Li_xNiO_2

4.3.2.1 Ni $2p_{3/2}$ analysis

As introduced in **Section 3.3.2.3**, the analysis of Ni 2p core-level spectra of Li_xNiO_2 samples was supported by the reference-based peak fitting exploiting the larger probing depth and finer depth profiling provided by synchrotron HAXPES. The normalized Ni $2p_{3/2}$ spectra are shown in **Figure 4.3.6**. Before discussing the peak fitting results, let us present the information obtained at a qualitative level.

Looking at the surface sensitive spectra (top row), only a lowering of the low-binding energy shoulder at 853 eV can be detected along the delithiated series of materials, while the satellite structure at 860-865 eV is nearly unchanged. On the contrary, the bulk-sensitive HAXPES spectra of delithiated Li_xNiO_2 show clear differences upon delithiation, namely a sharper main line at 855 eV and a satellite structure shifting towards higher binding energies, which is typically associated to a higher oxidation state [257]. Therefore, a surface layer with Ni in reduced state formed upon cycling while bulk Ni oxidation could be observed within the first 30 nm probed by energy-dependent HAXPES.

For the reference-based peak fitting, three components were defined by spectra decomposition with the model templates derived from NiO and presented in **Section 3.3.2.2.2** (see **Annex G** for the fitted spectra). The signature of bulk discharged $LiNiO_2$ (“Ni_{bulk}^{III}”) was defined as the pristine electrode at 9.5 keV. The surface reduced nickel was referred to the lab-based XPS measurement at 1.5 keV (“Ni^{II}_{surf}”). For the bulk charged nickel in deintercalated Li_xNiO_2 (“Ni^{IV}_{bulk}”), the non-negligible surface contribution in the spectra for deintercalated samples was first removed. To this purpose, the spectra for $Li_{0.01}NiO_2$ measured at 9.5 keV was decomposed including the Ni^{II} line shape in the peak model while removing satellite peaks in the 860 - 863 eV range. This approximation is expected to overestimate the percentage of Ni^{II} and therefore the surface layer thickness, presenting an upper limit for its estimate. The as-obtained lines shapes are highlighted by star symbols in **Figure 4.3.6(a,b,e)**. The decomposition of Ni $2p_{3/2}$ into surface and bulk contributions allowed to infer on the thickness estimated for the surface $Li_xNi_{1-x}O$ layer and estimate the Ni/O surface and bulk stoichiometry, as explained below.

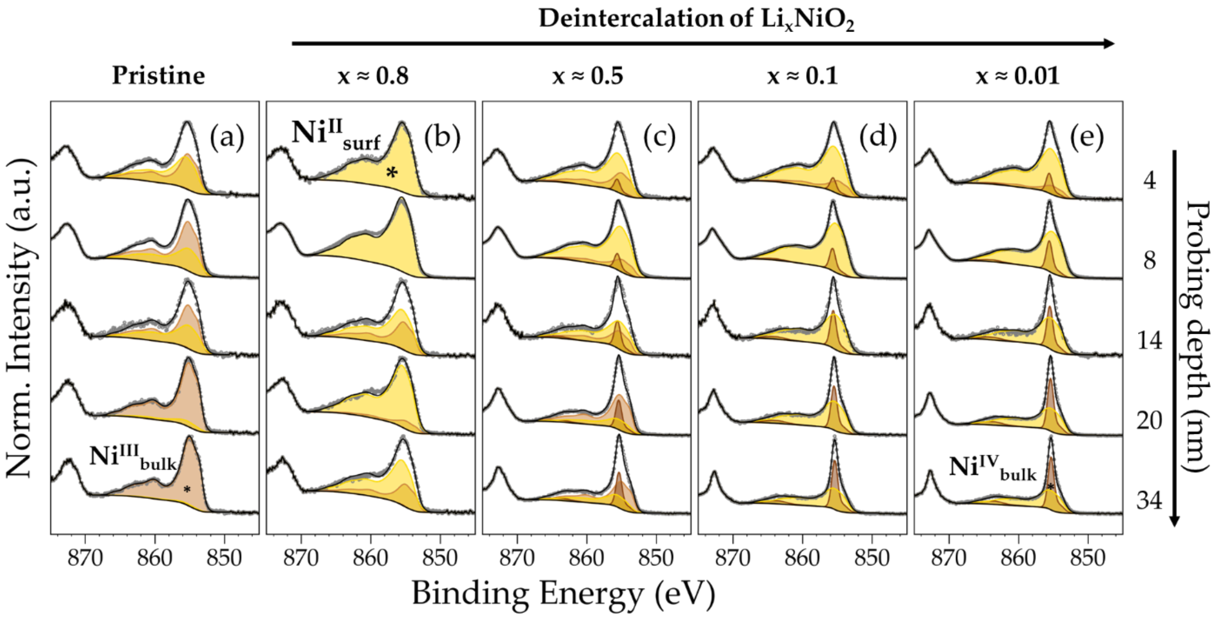

Figure 4.3.6 High-resolution Ni $2p_{3/2}$ spectra of the Li_xNiO_2 series of samples. All spectra are normalized to the peak maximum and are stacked top-to-bottom in the order of increasing bulk sensitivity. Experimental data, peak components and fits are shown as black dots, colored-filled areas, and black lines, respectively. The "Ni^{II}_{surf}", "Ni^{III}_{bulk}" and "Ni^{IV}_{bulk}" components are shown as yellow, brown, and dark-brown area, respectively. The spectra used as line components are marked by a star symbol.

4.3.2.2 SRL thickness estimation: comparing EELS and HAXPES

Visual inspection of the Ni $2p_{3/2}$ spectra, combined with estimated sampling depth for each acquisition mode (**Figure 3.3.4**), suggest that the thickness of such layer would be confined within the first 10 nm (i.e. sampling depth for the measurement at 2.3 keV). However, the spectral shape and fits for the surface-sensitive Al Kα XPS (sampling depth of ~3 nm) measurements already indicate a partial contribution from oxidized $Ni^{III/IV}$. Either a non-uniform or a non-homogeneous surface layer, or a combination of both, might explain this effect.

As first approximation, the surface layer thickness was estimated by assuming a simple homogeneous and uniform model system, leading to $t = \lambda \sin\theta \ln(A_{bulk})$, where $\langle\lambda\rangle$ is the inelastic mean free path ($LiNiO_2$ was assumed), θ the take off angle, and A_{bulk} the area percentage of the Ni $2p_{3/2}$ peak related to bulk material (i.e. $Ni^{III/IV}$), as estimated by reference-based peak fitting. However, this result in a thickness that is photon-energy dependent (**Annex G**), which highlights the influence of inhomogeneity. In this framework, the value of ~10 nm given by the most-bulk sensitive HAXPES measurement represents the upper limit for its estimate as it allows to probe deeper within the inhomogeneous surface layer.

To corroborate this conclusion, Ni L-edge EELS measurements were carried out for the most de-intercalated sample ($Li_{0.01}NiO_2$), for which the contrast between surface and bulk is enhanced (**Annex G** for experimental method). As reported in the literature, the oxidation state of Ni can be qualitatively determined by the position of maximum intensity for the Ni $L_{2,3}$-edge EELS spectrum, which shifts to higher energy going from $Ni^{II/III}$ to Ni^{IV} [195,203]. A similar behavior is typically observed in soft XAS spectra [143]. In fact, the maximum position of the EELS spectrum of Ni L_3 shifts to higher energies when scanning inwards towards the bulk with a 1 nm step. [**Figure 4.3.7(a,b)**]. The peak maximum position plotted in **Figure 4.3.7(c)** indicate that a plateau is reached after about 10 nm, in fair agreement with HAXPES conclusions.

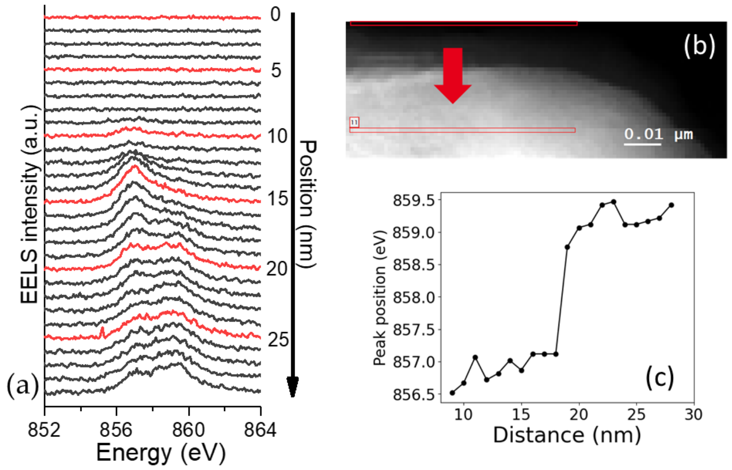

Figure 4.3.7 High-resolution Ni L3-edge EELS spectra acquired from the extreme surface towards the interior of a particle. (b) Corresponding STEM image showing the first and last position where the EELS spectra were acquired. (c) Energy position of the maxima intensity for each scan; the first measures are not included as no peak was registered.

4.3.2.3 O 1s analysis

The O 1s core level spectra are shown in **Figure 4.3.8**. Four pseudo-voigt peaks were used to fit the spectra in the 528-535 eV region. The latter contributions starkly decrease with increasing probing depth, indicating a very thin pSEI layer, in agreement with the calculated thickness of 1.7 nm (**Section 4.2.2.2**). Herein, we focus on the two lower-binding energy peaks, named O_{latt} and O_{surf} in analogy with the Li_xCoO_2 study.

The bulk-sensitive HAXPES spectra at 9.5 keV further confirm the presence of the component at 530 eV even at the pristine state. Its area percentage with respect to O_{latt} is shown in **Figure 4.3.9** for each sample as a function of the probing depth, showing slight voltage dependence but a tendency to decrease towards the bulk. In light of the Ni $2p_{3/2}$ peak analysis and the previous study for the Li_xCoO_2 system, as well as the preliminary quantitative analysis for the pristine $LiNiO_2$ material (**Section 3.2.3**), we can assign the peak at 530 eV to surface defects (pristine material) and degradation i.e. the SRL formed upon cycling.

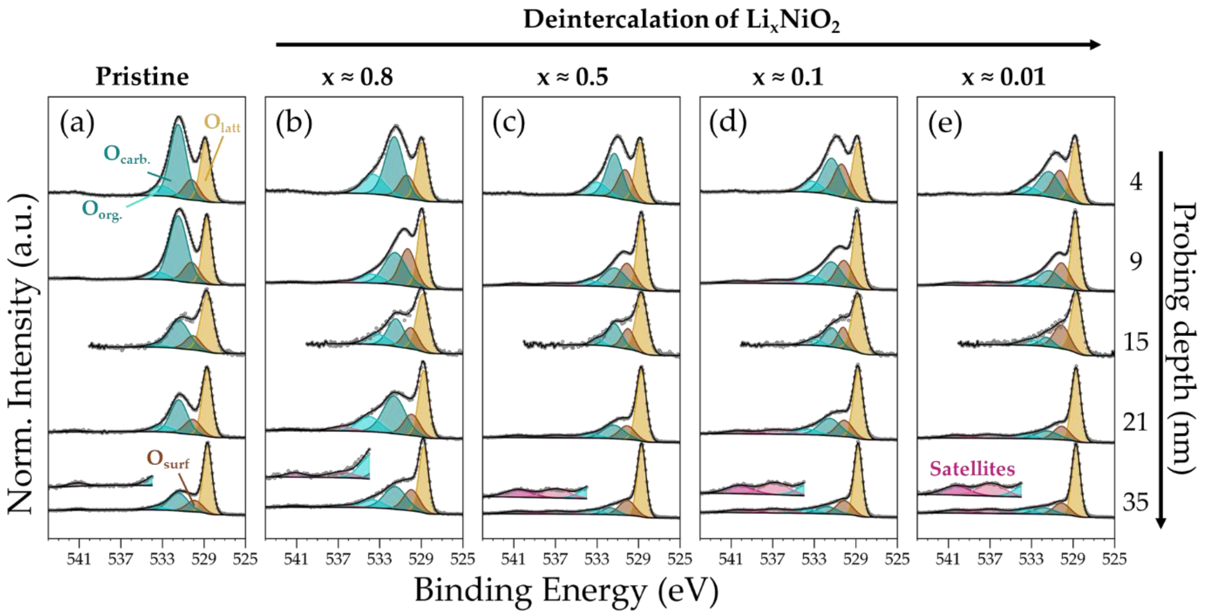

Figure 4.3.8 High-resolution O 1s spectra of the Li$_x$NiO$_2$ series of samples. All spectra were normalized to the lowest-binding energy peak intensity and are ordered from the most surface sensitive (top) to the most bulk sensitive (bottom). Experimental data, peak components and fits are shown as black dots, colored-filled areas, and black lines, respectively. A magnification of the satellite region is shown for each spectrum acquired at 9.5 keV.

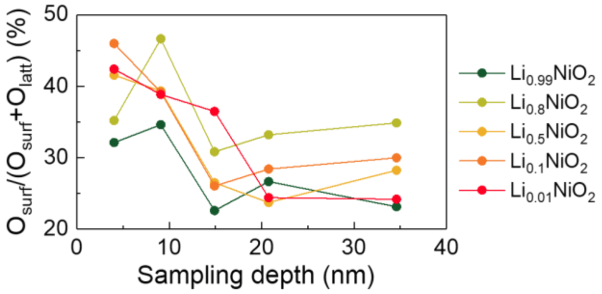

Figure 4.3.9 Calculated area percentage ratio of O$_{surf}$ to the sum of O$_{surf}$ and O$_{latt}$, as a function of the sampling depth for the O 1s photoemission of each XPS setting.

4.3.2.4 Estimate for the O/Ni surface and bulk stoichiometries

Based on O 1s and Ni 2p peak fitting, the O/Ni at% ratio was estimated by lab-based XPS and HAXPES, discriminating the surface and bulk contributions following the above discussion. Reference NiO and Ni(OH)$_2$ are included for comparison. The peak fitting results (the data is summarized in the table given in **Annex G**) were used to calculate the O/Ni stoichiometries shown in **Figure 4.3.10**.

Taking the whole Ni 2p area with respect to the O_{latt} peak gives good agreement with the expected composition in the case of reference samples NiO and $Ni(OH)_2$ but not in the case of real electrodes (“as ref” values). Even adding the higher binding energy O 1s peak in the calculation (“all-in”), e.g. assuming this contribution is related to bulk oxidation, the O/Ni ratio is <2, indicating surface sub-stoichiometry. When Ni 2p and O 1s surface and bulk contributions (“surf” and “bulk”) are separated, a better agreement with the expected ratio for the bulk layered structure (Li_xNiO_2, O/Ni~2) and surface layer (NiO-like, O/Ni ~ 1) is eventually obtained.

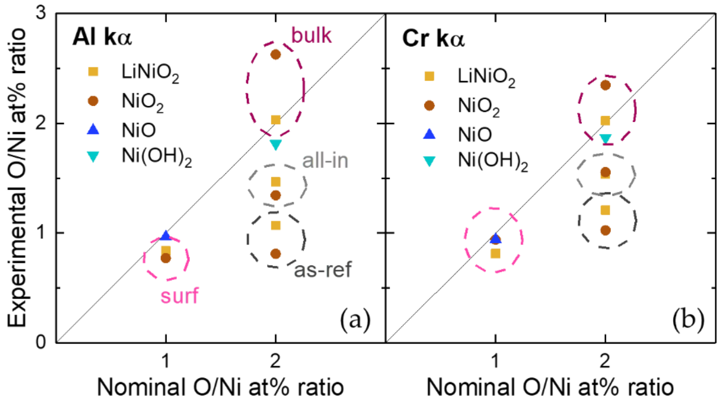

Figure 4.3.10 Lab-based (g) XPS and (h) HAXPES quantification of the O/Ni at% ratio relative to nominal stoichiometry for reference NiO and $Ni(OH)_2$ samples, pristine $LiNiO_2$ and cycled $Li_{0.01}NiO_2$ electrodes.

4.3.2.5 Synchrotron HAXPES revealed O 1s satellite peaks

By performing synchrotron HAXPES measurements, new high-binding energy peaks could be distinguished thanks to the high flux of synchrotron radiation[9]. As highlighted in the zoomed spectra measured at 9.5 keV, only a weak satellite at ~541 eV is observed for the pristine material, whereas two peaks at ~537 eV and ~540 eV arise upon charging towards delithiated NiO_2. The O 1s satellite intensity increased (relative to O_{latt}) by probing deeper and with higher deintercalation stage. These trends indicate that they are related to a bulk process and can possibly give a hint on the charge compensation process of Li_xNiO_2.

Therefore, although we excluded that the 530 eV peak is related to oxygen oxidation, the high-energy satellites observed in O 1s spectra could be a signature of its redox activity. Similar satellites were observed in Li-rich NMCs and other materials

---

[9] Small signatures of these peaks can be seen in the XPS spectra but not in the lab-based HAXPES spectra. Note that the lab-based measurements were carried out before the synchrotron campaign, so the measurement region was limited to increase the count rate. A following test was performed to detect the satellites with lab-based HAXPES conditions for sample $Li_{0.01}NiO_2$, but they could not be observed even after long acquisition time.

suspected of so-called anionic redox, although their origin is not yet understood [129,141]. Clarifying this would help understanding the role of O 2p states in the charge compensation mechanism in these materials. The theoretical study presented in **Section 5.2.2.2.2** gives further insight on this aspect.

4.3.3 Surface degradation of Li_xMnO_3

The Mn 2p and O 1s XPS and HAXPES spectra for pristine and charged Li_2MnO_3 electrodes are shown in **Figure 4.3.11**. The quantification results are given in **Table 4.3.1**. As mentioned in **Section 3.2.4**, this material has been already studied by qualitative synchrotron HAXPES by Lebens-Higgins et al., who concluded that the O 1s peak at 530 eV was related to surface degradation and not bulk anionic oxidation [131]. Our results fit overall well with this interpretation, to which HAXPES quantification is herein added to further corroborate this conclusion. First, no detectable sign of Mn oxidation is observed in the Mn core level spectra. This also includes Mn 3s and 3p core level spectra (see **Annex G**). The Mn 3s exchange-correlation splitting is constantly 4.4 eV. However, the low-binding energy tail of the Mn 3p XPS spectra for the cycled material could not be fitted by the Mn 3p line shape described in **Section 3.2.4.1**, indicating surface Mn reduction. Note that Li extraction was confirmed by the decrease of the Li 1s peak. The O 1s spectra show the largest changes upon deintercalation, in particular concerning the appearance of the O_{surf} peak, referred to the surface degradation. In fact, the O_{latt}/Mn atomic ratio decreased from 1.7 and 2.9 with XPS and HAXPES to 0.6 and 1.7 (note that the Mn at% was averaged for all core levels). Even adding the O_{surf} peak in the calculation, a large deviation is obtained: $(O_{surf}+O_{latt})/Mn = 1.3$ and 2.2 with XPS and HAXPES, respectively.

In summary, while the surface deoxygenation was already observed by Quesne-Turin with conventional Al Kα source, this study proves quantitatively that the O 1s HAXPES signal is still related to such surface effect [316]. In agreement with Rana et al., we conclude that the delithiation is almost completely compensated by O_2 gas release [123].

		XPS			HAXPES		
Orb.	**Comp.**	**BE**	**FWHM**	**at%**	**BE**	**FWHM**	**at%**
Li 1s	**Lattice**	54.6	1.7	5.0			
	Surface	56.1	1.8	6.4			
Mn 3p		50.2		17.1	49.8		9.6
Mn 3s	**Total**						
	A	84.6	3.1	11.5	84.4	2.8	5.2
	B	89.5	3.6	5.9	89.0	5.4	4.2
Mn 2p		642.6		15.0	642.2		14.8
O 1s	**Lattice**	529.7	1.4	10.5	529.6	1.6	18.7
	Surface	530.5	1.7	10.8	530.7	1.8	6.6
	CO_3^{2-}	531.9	1.6	8.6	531.8	2.2	5.4
	C-O/C=O	533.0	1.6	6.5	533.0	2.0	35.5
	P-O	534.2	2.0	2.9			

Table 4.3.1 Results of the XPS quantitative analysis for the charged Li_xMnO_3 samples. Binding energies (BE) and full width at half maximum (FWHM) are reported in eV.

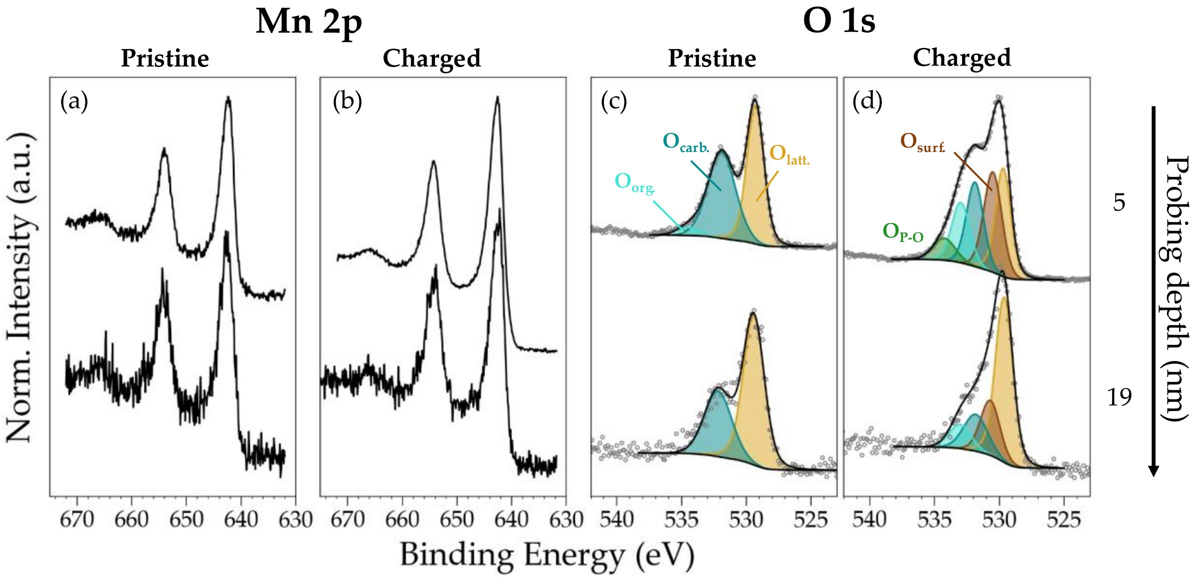

Figure 4.3.11 Mn 2p and O 1s lab-based XPS (top) and HAXPES (bottom) spectra of (a,c) pristine and (b,d) charged Li_2MnO_3 electrodes. The spectra are normalized to the background intensity at the lower binding energy side of each peak.

4.4 Chapter summary

In this chapter, the study of *ex-situ* Li_xCoO_2, Li_xNiO_2 and Li_xMnO_3 cycled materials by lab-based XPS and HAXPES (supported by synchrotron HAXPES for Li_xNiO_2) was presented. The degradation products that constitute the complex multi-layer interphase of cycled layered transition metal oxides were distinguished. In fact, the experimental approach allowed us to study both the products of electrolyte degradation (pSEI) and of positive electrode surface degradation (SRL).

For both Li_xCoO_2 and Li_xNiO_2, a very thin pSEI (1-2 nm) was obtained after few cycles in classical Li-ion cells. Their composition (mainly LiF and Li_2CO_3 plus -- for $LiCoO_2$ thin films -- $Li_xPO_yF_z$, and POE) matched results present in the literature. The support by HAXPES allowed us to refine the XPS analysis but could not improve the current understanding as it is poorly sensitive to this extremely thin pSEI. However, the results support the recent idea of a dynamic pSEI that "breathes" and that in general the evolution of the pSEI is not greatly responsible for the capacity loss upon cycling.

Due to the integrated nature of XPS/HAXPES depth profiling and to the chemical similarity between bulk and SRL materials, their distinction by this technique is not trivial. The presence of the SRL was revealed by O 1s peak fitting supported by quantification as well as M 2p analysis of the satellite features. The interpretation was also supported by DFT calculations for the bulk binding energy contributions. However, the results of the peak fitting analysis were so far exploited based on simplified models that call for further development in terms of surface characterization. Complementing our method with laterally resolved surface characterization analysis and *operando* conditions are considered two promising methodological perspectives.

While the O 1s spectra signatures for Li_xCoO_2 and Li_xNiO_2 were substantially similar, the trends observed for the two series of *ex-situ* samples greatly differ. This was summarized in **Figure 4.4.1**, which reports the O/M sub-stoichiometry z in Li_xMO_{2-z} as a function of the deintercalation level for the ex-situ cycled samples. Starting with the pristine $LiCoO_2$ close to formal stoichiometry, an increase in O sub-stoichiometry at the extreme surface (z=0.5-0.6 with XPS i.e. <5 nm) is observed for cycled Li_xCoO_2 at relatively low state of charge (x>0.5). With further Li^+ deintercalation, the surface degradation increases and becomes significant also in HAXPES results, indicating a thicker SRL (within probing depth of HAXPES, <15 nm). For Li_xNiO_2 instead, the surface sub-stoichiometry is significant even at the pristine state and involves a thicker region as is observed even by lab-based HAXPES. However, it appears almost constant along the whole deintercalation range.

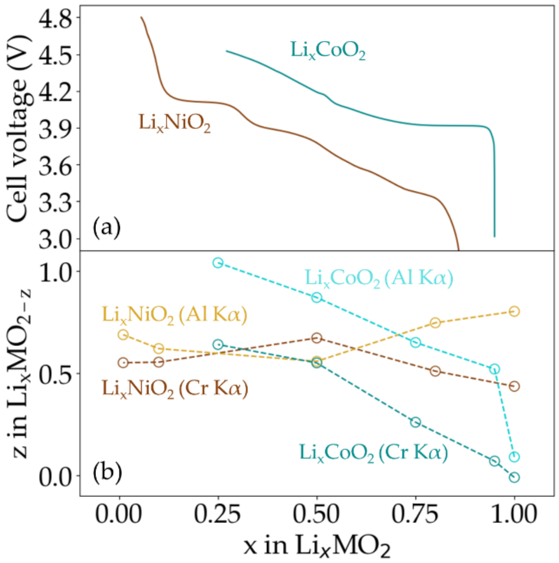

Figure 4.4.1 Comparison of Li_xCoO_2 and Li_xNiO_2 surface degradation upon deintercalation as measured by lab-based XPS and HAXPES. (a) Comparison of deintercalation curves. (b) Surface oxygen sub-stoichiometry calculated by lab-based XPS and HAXPES quantification as $z=2-(O_{surf}+O_{bulk})/M$, where M was quantified as average between M 2p and M 3p core levels. The results for pristine materials are shown at x = 1.

These trends follow well the general electrochemical limits for Ni-based and Co-based positive electrode materials in Li-ion batteries. In fact, both materials can be cycled up to 4.2 V reaching relatively good stability, but this translates to nearly full deintercalation for Li_xNiO_2 but just reaching halfway for Li_xCoO_2. The lower surface stability of Li_xNiO_2 does also agree with other results in the literature. However, the fact that it did not worsen upon deintercalation suggests that (1) the SRL formation is a self-limiting process and (2) it is the voltage and not simply the deintercalation level that impacts on the deoxygenation process.

Eventually, the combination of XPS and HAXPES allowed extracting the surface contributions leading towards bulk-like electronic structure signatures in the transition metal core-level spectra. However, neither the purely qualitative analysis nor the use of reference spectra for peak fitting does give clear insight on the actual electronic structures beneath the core level spectra. For that, *ab initio*-based cluster model simulations were carried out, leading us to the next and final chapter.

Chapter 5

Electron transfer mechanism in model layered transition metal oxides

In this chapter, the experimental photoemission spectra are studied from a theoretical perspective to investigate the bulk charge compensation mechanism in Li_xCoO_2 and Li_xNiO_2. The results of standard DFT calculations are presented first. Then, the introduction of electronic correlations by either empirical fitting or using the results of cRPA calculations is discussed. Finally, the results obtained by the cluster model calculations are presented, highlighting the role of an intrinsic self-regulation mechanism in these systems.

5.1 Preliminary insights by DFT

To study the electron transfer process, the orbital occupations of converged DFT electronic structures were first considered. Band structures and partial densities of states (PDOS) for Li_xMO_2 and Li_2MnO_3 are reported in the **Annex H** and show good agreement with the literature [33,113,147,148,223,228,317,318].

5.1.1 Electron transfer by DFT

Since the electronic charge is a continuous distribution within the crystal lattice, one needs to define a rule for assigning the charges to each ion. The simplest method, based on the definition of atomic or orbital spheres for each atom, has the drawback of neglecting the delocalized charge in the interstitial space. Two more accurate methods for assigning the electronic charge to each atom in the solid are the Bader approach and the wannierization of the DFT eigenfunctions (see **Annex B** for details).

The results obtained by both methods are compared in **Table 5.1.1** for Li_xMO_2 (M = Co, Ni and x = 1, 0.5, 0). The same qualitative trend is obtained for both methods, although the use of localized Wannier functions tends to increase the ionicity of the system. In any case, the calculated oxidation states for the transition metals are significantly lower (ranging between 1 and 2) than the nominal ones ($M^{III/IV}$). In fact, as highlighted in the difference plot in **Figure 5.1.1(a,b)**, a larger electron transfer is observed for the O ions for both systems, in agreement with the literature as reviewed in **Section 1.4.2**.

	Bader		Wannier	
	M	**O**	**M**	**O**
$LiCoO_2$	1.32	-1.11	1.83	-1.40
$Li_{0.5}CoO_2$	1.43	-0.94		
CoO_2	1.51	-0.75	2.07	-1.02
$LiNiO_2$	1.26	-1.08	1.84	-1.42
$Li_{0.5}NiO_2$	1.35	-0.85		
NiO_2	1.42	-0.71	2.10	-1.04

Table 5.1.1 Oxidation state (OS) obtained by DFT calculations using the following expression: OS = Q_{neutr} - Q_{DFT} with Q_{neutr} = 9 (Co) and 10 (Ni) and Q_{DFT} the charge calculated by either the AIM module of Wien2k (Bader) or by integrating the M 3d PDOS calculated with Wannier90 (Wannier). The latter was not performed for $Li_{0.5}MO_2$ due to the rotational issue described in Annex E.

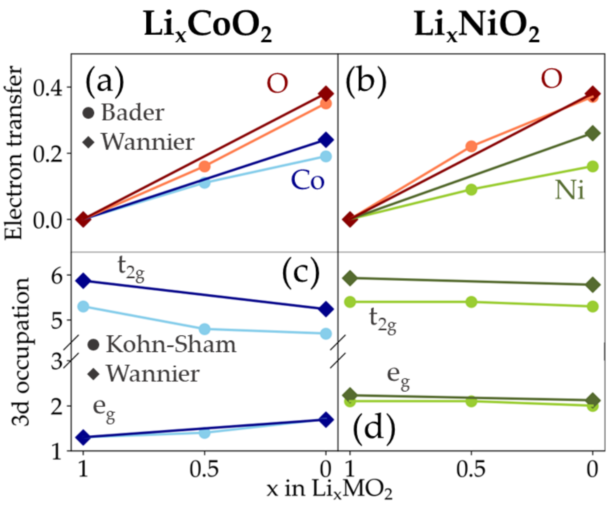

Figure 5.1.1 DFT insight on the charge compensation mechanism for Li_xCoO_2 (left-hand side panels) and Li_xNiO_2 (right-hand side panels). (a,b) Electron transfer calculated from the data shown in Table 5.1.1 and setting x=0 as reference. Results obtained by Bader and Wannier methods are shown as circle and diamond symbols, respectively. (c,d) Transition metal 3d t_{2g} and e_g occupation using the QTL module in Wien2k (Kohn-Sham, circle symbols) and Wien2wannier/Wannier90 (Wannier, diamond symbols) with analogous input local symmetry along the M-O bonds.

By looking at **Figure 5.1.1(a,b)**, a similar trend is observed for Li_xCoO_2 and Li_xNiO_2. However, considering only the total oxidation state of each ion can limit the interpretation of the charge compensation mechanism. As revealed in **Figure 5.1.1(c,d)**, the partial occupations of the t_{2g} and e_g states evolve differently for the two systems. For Li_xCoO_2, the t_{2g} occupation decreases while the number of e_g electrons increases upon deintercalation. For Li_xNiO_2, instead, both occupations slightly decrease. Therefore, electron occupations and not oxidation states will be considered throughout the chapter.

5.1.2 Comparison of DFT and experimental valence band

The results shown above are obtained using a GGA exchange-correlation functional, which is expected to underestimate the local electronic repulsion within the transition metal d-shell. More generally, DFT does not take into account the many-body effects, leading to poor agreement with experimental data (**Section 2.2.1.1**). Within our study, this is verified by comparing the XPS and simulated valence band spectra, as shown below.

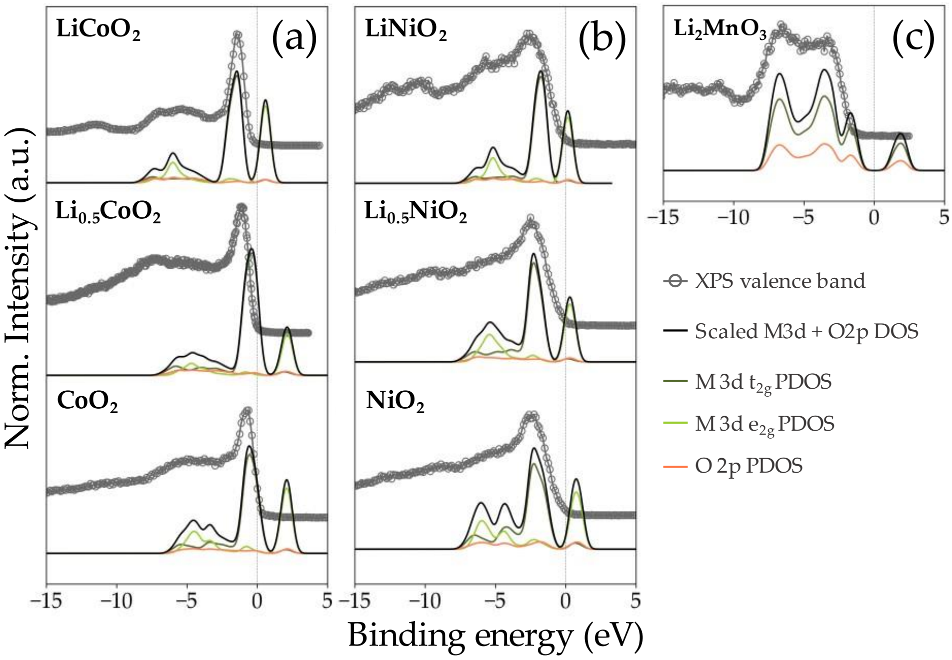

Figure 5.1.2 Comparison between XPS valence band and projected DFT density of states. The M 3d and O 2p PDOS (colored lines) were scaled to the theoretical photoelectron cross section at 1486 eV according to ref. [319] and convoluted with a Gaussian function with FWHM=0.7 eV to consider the experimental conditions. The experimental data (empty gray dots) was min-max normalized to the sum of the as-calculated partial contributions (black line). A vertical dotted line is added at 0 eV to highlight the Fermi level. For all non-metallic cases (LiCoO$_2$, NiO$_2$, and Li$_2$MnO$_3$), a rigid shift to the energy was applied to match with the experiment. All calculations were not-spin polarized except for Li$_2$MnO$_3$.

For the Li$_x$CoO$_2$ [**Figure 5.1.2(a)**] and Li$_x$NiO$_2$ [**Figure 5.1.2(b)**], the overall shape of the valence band consists of a low energy peak and a higher-energy band, that is also reproduced in the calculations. The valence band of Li$_2$MnO$_3$ consists instead of a single broad band to which both the Mn 3d and O 2p states contribute and that is qualitatively well described by the spin-polarized[10] GGA calculation [**Figure 5.1.2(c)**]. However, the predicted density of states obtained by the PBE calculations are not sufficient to describe the experimental spectra. Two main issues can be recognized and both are related to unaccounted electronic correlations: (1) for all materials, the high energy satellite features (beyond -10 eV) are missed in the calculations and (2) for the nickelate system in particular (except for NiO_2), the PBE calculation predicts a metallic ground state in contrast with experimental results from the literature (**Section 1.4.4**).

5.2 Interpretation of core-level spectra changes by theoretical spectroscopy

Since the electronic structure predicted by DFT does not describe the experimental data, the insights given above cannot be considered overall reliable. The theoretical description was improved by introducing many-body effects to better describe the core-level and valence band experimental photoemission spectra. Instead of focusing on the valence band data, however, the transition metal core-level spectra were considered for this study. This allows to decouple the oxygen and transition metal photoemission features, which are convoluted in the valence band, while retaining their local interaction which is exhibited by the observed satellite features. Note that the calculation method gives access to all transition metal core levels: we decided to focus on the 2p core level as it was the most sensitive to bulk delithiation, experimentally.

The overall methodology for the study of the Li_xCoO_2 and Li_xNiO_2 systems is described in **Section 2.2** and detailed in **Annex E**. The results obtained for the cobalt oxide system were published as a research article in the journal Physical Review X Energy with the title "Self-Regulated Ligand-Metal Charge Transfer upon Lithium-Ion Deintercalation Process from $LiCoO_2$ to CoO_2". Therefore, we refer to this paper (given in **Annex I**, **paper 3**) for a detailed description of both the determination of cluster model parameters and the results for the Li_xCoO_2 systems, which will be only summarized in the manuscript to set the basis for the study of the parent Li_xNiO_2 system. Since no changes in Mn core level spectra related to Mn redox activity were observed experimentally, only the Mn 2p spectrum of Li_2MnO_3 was simulated. A fine

---

[10] We choose to include spin-polarization for Li_2MnO_3 because of its high-spin and insulator nature given by the Mn^{IV} ions ($t_{2g}^3e_g^0$, $S=3/2=3\mu_b$). This is qualitatively obtained in the converged ground state, characterized by $S = 2.5\ \mu_b$ and a band gap of ~2 eV. In contrast, in the non-spin-polarized calculation, a metallic state due to half-filled t_{2g} states is obtained.

agreement with the expected local Mn^{IV} (d^3) electronic structure was obtained (see **Annex H** for details).

5.2.1 Determination of cluster model parameters: experimental and *ab initio* approaches

All single-electron interactions for the cluster model Hamiltonian were directly imported from DFT calculations through wannierization (see **Section 2.2.2** and **Annex E** for details). The remaining parameters are distinguished as either strongly screened (U, Δ) or poorly screened (direct multipole and exchange Slater parameters, spin-orbit splitting). The former are the most critical to find as they are more-case dependent, while an atomic-like approximation is generally assumed to be sufficient for the latter.

5.2.1.1 Fitting U and Δ to the experimental spectra

As a first approach, all poorly screened interaction parameters were approximated by scaled Hartree-Fock values obtained for free ions (see **Annex E** for the list of parameters). The strongly screened U and Δ were instead fitted to the experimental background-subtracted transition metal 2p core level HAXPES spectrum. In practice, the spectra simulated by varying U and Δ were shifted and scaled to optimize the agreement with the experimental line shape. Then, the resulted fit was visually inspected to find the range of U and Δ that best represented the experimental data. Note that we focused on the description of the satellite peaks since it is the most sensitive feature to the local screening process. The fits of $LiCoO_2$, CoO_2, $LiNiO_2$, and NiO_2 are given in **Annex H**.

Overall, varying U and Δ had an impact on (1) the position and intensity of the satellite peak to the main line and (2) the shape of the main line reflecting the spin-state of the metal ion. Therefore, knowledge of the overall magnetic properties of the materials (accessible in the literature) and of the surface contributions to the total experimental HAXPES spectra (studied in detail in **Chapter 4** and **5**) was essential for reliably finding the parameters U and Δ describing the bulk electronic structures under study.

For $LiCoO_2$, CoO_2, and NiO_2, these considerations allowed us to find a region of best agreement. For $LiNiO_2$, instead, no simulation could describe altogether the broad satellite peak while predicting the correct low spin state. Both the complex surface contributions and the missing non-local screening channels can in part explain this, although we will show below that the bond disproportionation is also expected to play a decisive role. However, the fact that U and Δ could not be found by empirically fitting the Ni 2p spectrum of $LiNiO_2$ led to the implementation of the *ab initio* cRPA interaction parameters for an alternative estimate.

5.2.1.2 Adopting cRPA calculated Coulomb interactions

The screened Coulomb interactions calculated by the cRPA method and parametrized as Slater parameters are given in **Table 5.2.1** (**Annex D** for computational details). Before discussing the fitting of the 2p spectra using these values, it is worth discussing the insight given by them. In fact, the screened U decrease upon delithiation from $LiMO_2$ to MO_2, in contrast to the expected trend for more localized orbitals, confirmed by the shrinking of the spread of the Wannier functions and that is found for the bare interactions instead. Using the same *d-dp* low-energy model employed in our calculations (**Annex D**), Kim et al. shows the complex interplay between 3d localization and p-d hybridization, which is enhanced by delithiation and therefore allows for a stronger screening by the O 2p orbitals [227].

For the materials whose U could be estimated empirically, a good agreement is found with the cRPA results. However, the F^2_{dd} and F^4_{dd} are significantly smaller than those adopted from free atom calculations, leading to a smaller Hund J. Consequently, no transition between high and low spin regions was observed in this case by varying Δ, as shown in **Figure 5.2.1(a-d)**. We leave the discussion on the ground state electronic structure determined by these simulations to the next section. Since U is already given by the cRPA calculation, the only parameter left to be determined is Δ. **Figure 5.2.1(e-i)** show the simulated spectra fitted to the experimental HAXPES data by varying Δ. The star symbols indicate the best agreement case for each material. In general, we found fine agreement with the values for U and Δ obtained by the two methods. However, it was still not possible to describe the overall satellite structure of $LiNiO_2$ with a single simulated spectrum.

Since the effect of the polarizability given by the O 2p states is included in the screened U within the *d-dp* low energy model, one can question if Δ needs to be fitted at all. In the cluster model theory, Δ is a model parameter implemented in a configuration interaction model to correct the relative position of the M 3d and O 2p onsite energies for the p-d screening interactions. However, these interactions are taken into account for the calculation of the screened Coulomb interactions in the cRPA method. Therefore, the screened 3d-3d interactions calculated by cRPA can in principle set the M 3d and O 2p onsite energies to a reasonable position.

	CoO_2	$LiCoO_2$	NiO_2	$LiNiO_2$	NiO
Formal N_{3d}	5	6	6	7	8
cRPA					
Spread (Å^2)$^{(1)}$	0.41	0.45	0.38	0.40	0.43
U_{bare}	24.7	24.2	26.1	25.6	24.9
U_{cRPA}	3.3	4.6	4.5	4.7	5.6
Δ_{cRPA}	-2.6	-2.3	-6.0	-3.9	2.7
J_{cRPA}	0.71	0.78	0.75	0.77	0.83
$F^2_{dd,cRPA}$	6.1	6.7	6.4	6.6	7.1
$F^4_{dd,cRPA}$	3.8	4.2	4.1	4.2	4.5
HF + empirical fit					
U_{fit}	[3.5, 4.5]	[4.0, 5.5]	4.0	n.d.	7.3
Δ_{fit}	[-3, -1.5]	[3.5, 6.5]	[-6,-2]	n.d.	4.7
J_{HF}	1.3	1.2	1.2	1.1	1.3
$F^2_{dd,HF}$	10.9	10.1	10.0	9.3	11.1
$F^4_{dd,HF}$	6.9	6.3	6.3	5.8	6.9

Table 5.2.1 Comparison of the cluster model parameters calculated by cRPA and obtained from fitting the simulation to experimental data with support by Hartree-Fock (HF) values for multipole terms. n.d. = not determined. (1) Average spread of the 3d MLWF functions.

To test this idea, the charge transfer energy was not injected as input parameter but was calculated as $\Delta_{cRPA} = E[d^{n+1}] - E[d^n]$, with $E[d^{n+1}]$ and $E[d^n]$ the total energies for the constrained ground state calculation configurations with $n+1$ and n electrons in the Ni 3d shell (n being the nominal one). The values are reported in **Table 5.2.1**. A fine agreement with the empirically determined values is found for NiO (a positive charge transfer), NiO_2 and CoO_2 (both negative charge transfer as further discussed below), but not for $LiCoO_2$ (intermediate but predicted as negative charge transfer). The latter is the only case in which the simulation using Δ_{cRPA} did not match with the experiment and therefore requires manual adjustment. Although we cannot fully explain the reason for this particular mismatch, we are tempted to attribute its cause to the intermediate nature of $LiCoO_2$ between Hubbard and charge transfer insulator in the ZSA model (**Section 1.3.2**). For $LiNiO_2$, as argued below, this shall not be the case.

We noticed that the charge transfer energy for $LiNiO_2$ predicted by cRPA is -3.9 eV for $LiNiO_2$. This was also suggested by the simulations discussed in **Section 5.2.1.1,** since it is only the case where the cluster spin matched the experimental data (see **Annex H** for the ground state properties of $LiNiO_2$ obtained by this method). Both conclusions agree with most recent theoretical studies on the $LiNiO_2$ ground state electronic structure, as presented in **Section 1.4.4**. However, in contrast to $LiCoO_2$, there are not many cluster simulation studies in the literature to make a direct comparison: to the best of our knowledge, only Huang et al. reported U and Δ for $LiNiO_2$. Their fit to Ni L-edge XAS led to Δ = -0.5 and -3.5 eV for $LiNiO_2$ and NiO_2, respectively [149]. In addition, the comparison with $NdNiO_3$ is of particular interest, as it exhibits a Ni $2p_{3/2}$ spectrum very similar to that measured for $LiNiO_2$ (see **Figure 3.2.6**) while being indicated as negative charge transfer insulator from Ni L-edge XAS and RIXS analysis [115,275,320].

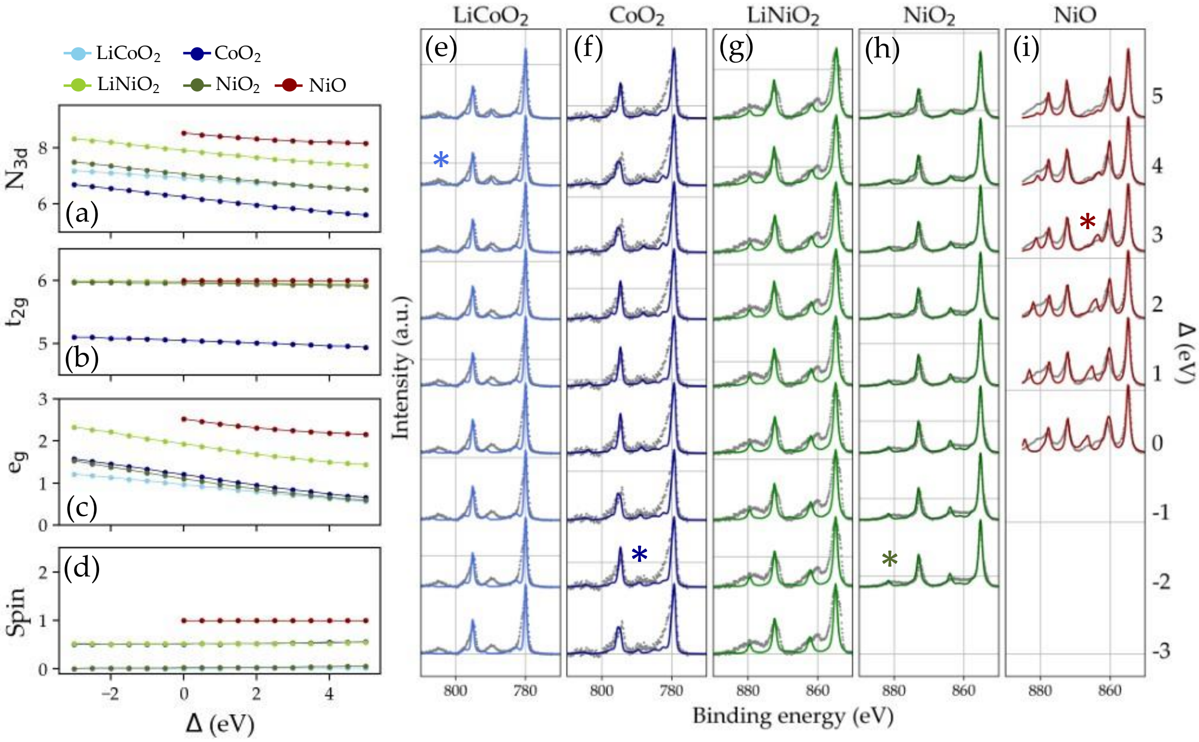

Figure 5.2.1 Cluster model simulations employing the cRPA-derived Slater parameters but manually adjusting Δ. Electronic occupations of the (a) total 3d, (b) t_{2g}, and (c) e_g orbitals and (d) total spin as a function of Δ. Simulated transition metal 2p spectra compared to related HAXPES spectra for (e) $LiCoO_2$, (f) CoO_2, (g) $LiNiO_2$, (h) NiO_2, and (i) NiO. Laboratory-based HAXPES data (5.4 keV) for pristine $LiCoO_2$ and cycled $Li_{0.12}CoO_2$ were used for $LiCoO_2$ and CoO_2 simulations, respectively (see paper in Annex I for details). Synchrotron-based HAXPES (9.5 keV) data for pristine $LiNiO_2$ and cycled $Li_{0.01}NiO_2$ electrodes were employed for $LiNiO_2$ and NiO_2, respectively. The Ni 2p XPS spectrum for $Ni_{0.03}Mg_{0.97}O$ reported by Altieri et al. was used for fitting the NiO simulated spectra [293].

In summary, we consider the results of the cluster model simulations employing cRPA values and with no fit of Δ as reliable for NiO, $LiNiO_2$, and NiO_2. Next, we discuss the insights on the charge compensation mechanism given by these results.

5.2.2 Self-regulation ligand-metal charge transfer in layered lithium transition metal oxides

5.2.2.1 Electron transfer from $LiCoO_2$ to CoO_2

By studying the Co 2p HAXPES spectra using the cluster model calculations as described above, the self-regulation mechanism mentioned in **Section 5.1** eventually found experimental confirmation. We refer to **paper 1** for a detailed description of the results (**Annex I**). A sketch for the electron compensation mechanism from $LiCoO_2$ to CoO_2 deduced from the study is shown in **Figure 5.2.2(a)**. Upon deintercalation, the electrons are withdrawn from the lowest energy t_{2g} band, as conventionally accepted. However, the hole is redistributed around the ionized Co ions by an electron backflow from the O 2p ligands towards the e_g orbitals, increasing the Co-O hybridization while allowing for the Co 3d metallic character due to the partially filled t_{2g} manifold.

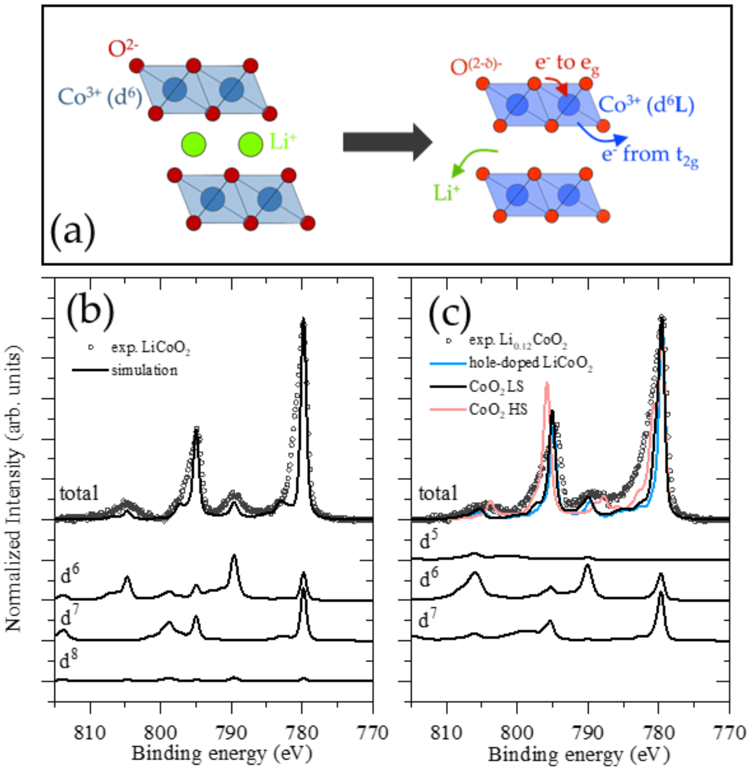

Figure 5.2.2 (a) Sketch of the self-regulation mechanism involved in the electron compensation upon delithiation from $LiCoO_2$ to CoO_2. Simulated and experimental lab-based HAXPES Co 2p core-level photoemission spectra for (b) $LiCoO_2$ and (c) CoO_2. The experimental data are shown as empty circles after background subtraction of an iterated Shirley function. The total simulated spectra (black line) are normalized and shifted to the experimental Co $2p_{3/2}$ peak maximum. The partial spectra refer to constrained spectra calculation. In panel (c), the red and blue lines refer to a high-spin solution ($U = \Delta = 4.5$ eV) and to the spectrum simulated using the $LiCoO_2$ cluster model Hamiltonian but removing one electron (see the related paper for details).

This mechanism answers the question that arose in **Section 4.3.1.1** about the missing signature of oxidized Co^{IV} ions upon deintercalation. As shown in **Figure**

5.2.2(b,c), the satellite peak did not change significantly going from $LiCoO_2$ to CoO_2 because the net electronic state of CoO_2 is not the formally expected d^5 ($t_{2g}^5e_g^0$) but $d^6\mathbf{L}^{-1}$ ($t_{2g}^5e_g^1\mathbf{L}^{-1}$), due to a positive-to-negative charge transfer transition induced by delithiation. Although the simulations in the paper were carried out without employing the cRPA calculations, the same result is obtained also in that case [Figure 5.2.1(a-d)]. The missing features in the spectra simulation with respect to the experimental data are related to non-local (metallic) screening and surface reduction as described in Section 4.3.1.1.

Despite we studied only the end members, the series of Co 2p XPS and HAXPES spectra discussed in Section 4.3.1.1 suggests that the self-regulation mechanism is playing a role along the whole delithiation process. The progressive increase of hole density in the O 2p states, combined with the high cell voltage, eventually reaches an upper limit beyond which severe surface degradation is triggered, as observed in the O 1s XPS and HAXPES spectra evolution (Section 4.3.1.2).

The proposed mechanism for Li_xCoO_2 improves the previous description given by soft XAS analysis (see Figure 1.4.5 and related discussion) and sets the link between experimental spectroscopy and the qualitative description given at both DFT (Figure 5.1.1 and Figure 1.4.4) and DFT+DMFT levels [Figure 1.4.9(a)]. Noteworthy, a recent study based on electron diffraction investigations also reached a similar conclusion, although in their case the O 2p – Co 3d charge transfer is even much larger, leading to an inversion of t_{2g} and e_g occupations that appears unlikely [321]. Although conceptually similar, we stress that our conclusions go beyond the "rehybridization" mechanism proposed by other groups because it involves a net electron transfer and an electronic phase transition from positive to negative charge transfer. Moreover, the study allowed to clarify the XPS signatures observed in the Co 2p spectra, which were previously analyzed based on qualitative interpretation[11]. The comparison with simulation was crucial to move forward from the classical picture based on the Co^{3+}/Co^{4+} redox reaction.

5.2.2.2 Electron transfer from $LiNiO_2$ to NiO_2

In Section 5.2.1.2, we concluded that the electronic structure of $LiNiO_2$ belongs to the negative charge transfer regime. However, the experimental satellite structure of the Ni 2p core level spectrum could not be interpreted by our method. Before

---

[11] We highlight that a recently accepted manuscript supported the previous interpretation by the same authors of a $Co^{3+/4+}$ redox below the "intrinsic limit" of 4.2 V vs Li^+/Li [322] using the approach introduced by Dahéron et al. and commented in Section 4.3.1.1 for the analysis of Co $2p_{3/2}$ satellite [108].

discussing the charge compensation mechanism for the Li_xNiO_2 system, this aspect needs clarification.

5.2.2.2.1 Insights by Ni 1s HAXPES analysis

To this purpose, we studied the Ni 1s core level spectra, accessible by synchrotron HAXPES at 9.5 keV. For such a deep core level, the core-valence multiplet effects are negligible, allowing to isolate the charge-transfer processes [323]. As shown in **Figure 5.2.3(a)**, the Ni $2p_{3/2}$ and Ni 1s spectra measured at 9.5 keV for the pristine $LiNiO_2$ are very similar, suggesting that the Ni $2p_{3/2}$ satellites are also due to ligand-metal charge transfer processes. For the deeply delithiated sample [**Figure 5.2.3(b)**], such comparison does not hold due to the SRL formation and the smaller IMFP of the Ni 1s core level (2.2 nm) compared to Ni 2p (11.3 nm) photoemission when measured at 9.5 keV. Indeed, the Ni 1s spectrum shows some similarities to the Ni 2p spectrum acquired at 2.3 keV (2.6 nm), at similar probing depth.

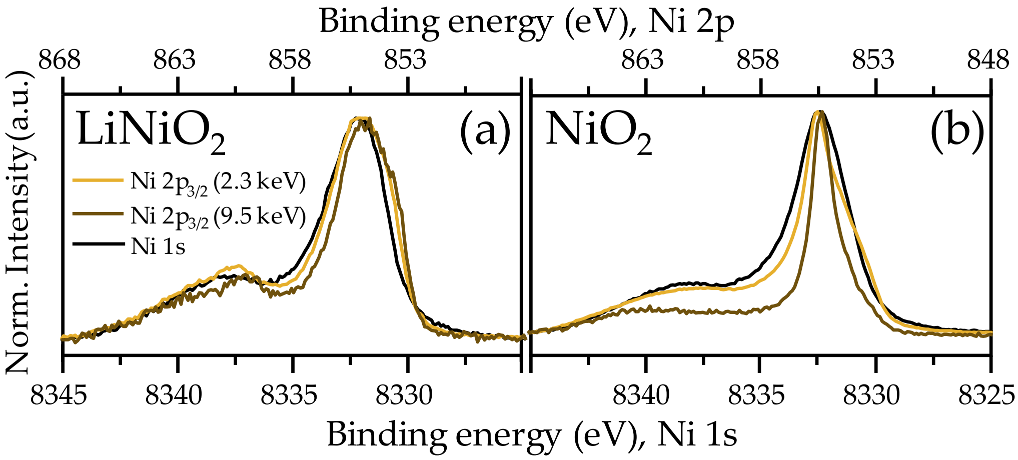

Figure 5.2.3 Comparison of Ni 1s (at 9.5 keV) and Ni $2p_{3/2}$ (at 2.3 and 9.5 keV) spectra for pristine $LiNiO_2$ (top) and deeply deintercalated $Li_{0.01}NiO_2$ (bottom). To allow direct comparison, the spectra were normalized and shifted to the peak maximum. For reference, absolute binding energies for the Ni 1s and 2p spectra are shown in the bottom and top axes, respectively.

5.2.2.2.2 Accounting for disproportionation in the Ni $2p_{3/2}$ HAXPES satellite structure

Since the Ni $2p_{3/2}$ satellite is due to charge transfer processes, which are expected to be well interpreted by cluster model theory, a likely reason for the disagreement between the experimental and simulated spectra is that the global electronic structure cannot be interpreted by a single local electronic environment. Indeed, this approximation might not be valid for $LiNiO_2$ according to the literature. In particular, we considered the bond- and charge-disproportionation model for the $LiNiO_2$ ground state proposed by Foyevtsova et al. (see **Section 1.4.4**) [112]. In their model, the electronic structure of $LiNiO_2$ is described as a random distribution of three different local electronic structures with the same Ni 3d occupation but different numbers of ligand holes [$|d^8\boldsymbol{L}^{-2}\rangle$, $|d^8\boldsymbol{L}^{-1}\rangle$, and $|d^8\rangle$] and therefore different cluster sizes. Within such a model, it becomes clear that more than a single cluster simulation is required to fully describe the overall Ni 2p satellite structures.

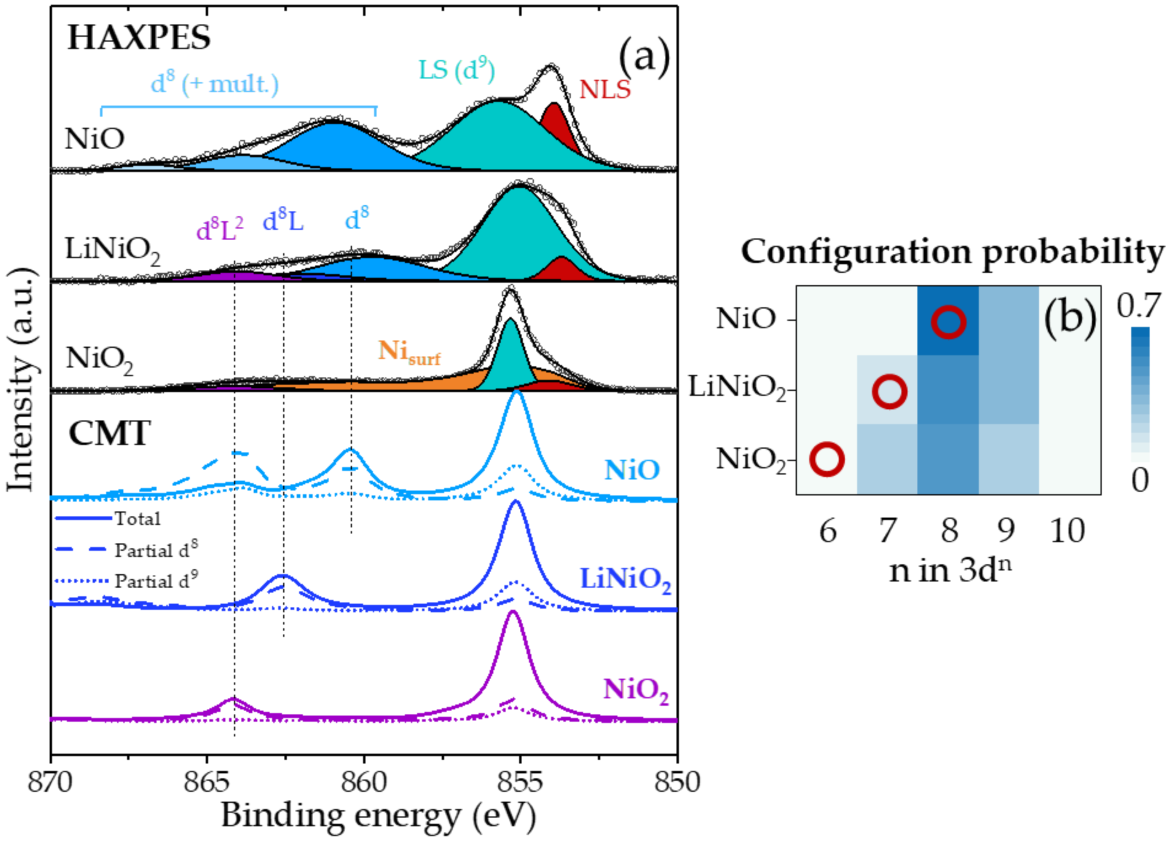

Figure 5.2.4 (a) Comparison of experimental and simulated Ni 2p$_{3/2}$ spectra. All spectra were normalized to the maximum intensity. A Shirley background subtraction was applied to the experimental data. See the text for details on the peak fitting approach. For each simulated total spectra, partial contributions for d^8 and d^9 configurations are shown as dashed and dotted lines, respectively. LS = Local screening; NLS = non-local screening. (b) Occupation probabilities for the 3d^n configurations in NiO, $LiNiO_2$, and NiO_2 cluster model ground states. The red circles are added to indicate the formal occupation.

In **Figure 5.2.4(a)**, the Ni 2p experimental and simulated spectra for NiO, $LiNiO_2$, and NiO_2 are compared. The experimental spectra are fitted as described in **Section 3.3.2.2.2** except for NiO_2, where the "Ni$^{II}_{surf}$" component described in **Section 4.3.2.1** was used to fit the surface contribution. **Figure 5.2.4(b)** shows the related ground state occupation probabilities for the Ni 3d states in NiO, $LiNiO_2$, and NiO_2, showing that they all have a dominant d^8 character. In all three materials the t$_{2g}$ states are completely filled and only the occupation of the e$_g$ states changes upon delithiation [**Figure 5.2.1(b,c)**].

Focusing on the Ni 2p spectrum of $LiNiO_2$, the cluster simulations of NiO, $LiNiO_2$, and NiO_2 can therefore represent the small, medium, and large clusters with $|d^8\boldsymbol{L}^{-2}\rangle$, $|d^8\boldsymbol{L}^{-1}\rangle$, and $|d^8\rangle$ electronic structures for the bond- and charge-disproportionation model by Foyevtsova et al. [112]. In fact, the satellite structure of $LiNiO_2$ is globally well described by superposing the Ni 2p cluster simulations for the three cluster models. Upon delithiation, the holes are localized on the O 2p ligands, leaving the Ni 3d states nearly unchanged. In fact, the Ni $2p_{3/2}$ spectra of NiO_2 show a spectral weight transfer to the higher energy satellite peak identified as $|d^8\boldsymbol{L}^{2}\rangle$. As for the CoO_2 spectra, a significant contribution by the SRL is observed between the main line and this satellite peak.

However, the experimental spectra of all three structure present a non-local screening (NLS) peak at low energy that is not reproduced in the simulations. This calls for further improvement by either multi-cluster simulations or other methods (e.g. DMFT) to fully resolve the experimental final states. Experimentally, it can be concluded that the spectral weight of the NLS final state decreases upon oxidation. A similar trend was observed by Kumara et al. concerning Li-substitution of NiO [324]. Both the disproportionation character of $LiNiO_2$ and the influence of NLS indicate the need to consider longer-range interactions to improve the theoretical understanding of these materials.

Therefore, the self-regulation mechanism observed to occur from $LiCoO_2$ to CoO_2 system is also verified for the Li_xNiO_2 system, although in this case there is no reorganization of the electronic charge in the 3d orbitals. This can be explained by the different initial state for the two materials: in $LiCoO_2$, the lowest energy states are of t_{2g} character, less hybridized to the O 2p bands; in $LiNiO_2$, the strongly hybridized e_g orbitals are already partially filled due to the additional electron in the system. The same disproportionation nature of $LiNiO_2$ can be fundamentally related to the self-regulation mechanism since both have the effect of minimizing the hole density accumulation in the metal ion. However, the electronic disordered character of $LiNiO_2$ seems to decrease upon delithiation according to the Ni 2p spectra analysis for NiO_2. A parallel Raman spectroscopy analysis, given in **Annex H**, supports this interpretation.

As for the Li_xCoO_2 system, the increase of oxygen hole density explains the surface instability at high voltage. Moreover, the significant surface oxygen sub-stoichiometry measured in pristine $LiNiO_2$ can be related to its negative charge transfer character, leading to overall lower cycling stability and faster degradation (upon cycling within the stability limit for $LiCoO_2$).

5.2.2.2.3 O 1s HAXPES satellites are due to interatomic plasmonic excitations

The theoretical investigation allowed to clarify the origin of the O 1s HAXPES satellites observed to increase upon delithiation for the Li_xNiO_2 samples (**Section 4.3.2.5**). According to the dynamically screened Coulomb interaction calculated by the cRPA method, we concluded that the O 1s satellites are related to plasmonic excitations. In fact, the divergence of the real part of the U(ω) curve at the plasmon frequency ω_p is a footprint of plasmonic excitations [325], as observed for $LiNiO_2$ (ω_p = 8.5 eV) and NiO_2 (ω_p = 8.5 and 11 eV) in **Figure 5.2.5(a-c)**. While a good quantitative agreement is obtained for NiO_2 even at the DFT level, the same cannot be said for $LiNiO_2$, possibly due to the limitations of DFT for describing the electronic structure of $LiNiO_2$ (wrong prediction of a metallic state without local disproportionation).

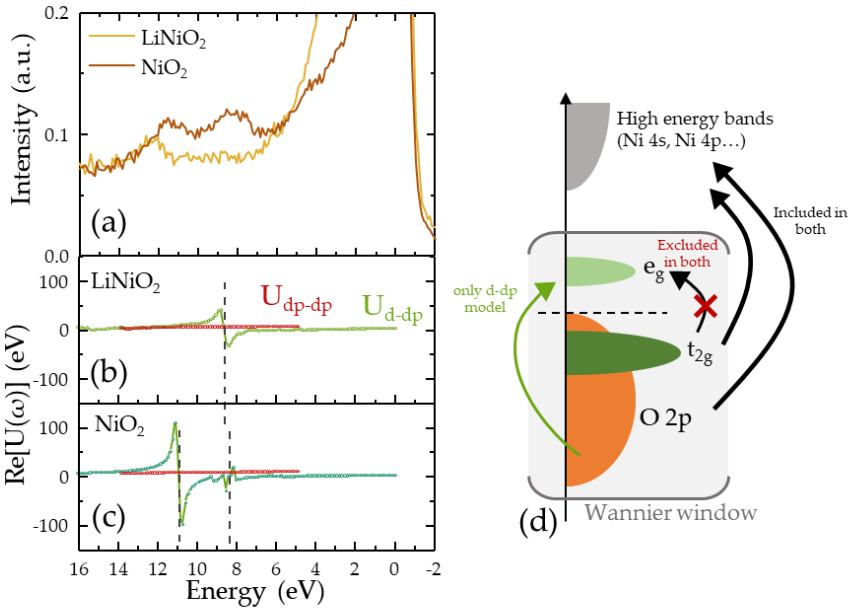

Figure 5.2.5 (a) Zoomed O 1s HAXPES spectra highlighting the high-energy satellites of $LiNiO_2$ and $Li_{0.01}NiO_2$ (see Figure 4.3.8 for the full spectra). Dynamically screened Coulomb interaction U(ω) calculated by cRPA for (b) $LiNiO_2$ and (c) NiO_2 using the *d-dp* (green) or *dp-dp* (red) low-energy screening models. The zero is set to the main peak of the O 1s spectra. Vertical dotted lines are shown to indicate the position of the plasmonic excitations. (d) Schematic representation of the screening channels available in the low-energy *d-dp* and *dp-dp* models used for the cRPA calculations. An approximation of the density of states in NiO_2 is used as example.

To understand the origin of the strong plasmonic excitations in the O 1s HAXPES spectrum for NiO_2, two screening models were compared. In fact, depending on the choice of the low-energy model, electronic transitions constituting screening channels to the Coulomb interaction can be switched on or off. Following the nomenclature in the field, we refer to *d-dp* as the model in which only the Ni 3d to Ni 3d transitions are excluded within the *dp* window, while the *dp-dp* model is defined by excluding all reciprocal Ni 3d and O 2p transitions [**Figure 5.2.5(d)**]. Therefore, the main difference between the two models is that the latter does exclude O 2p to Ni 3d transitions. Since no divergence was found in the *dp-dp* model, the plasmons are related to p-to-d (i.e.

charge transfer) transitions, indicating an increase of such screening channels going from $LiNiO_2$ to NiO_2, in agreement with the results from the Ni 2p analysis. Further investigation on the nature of these oscillations is expected to shed more light on the Li^+ diffusion mechanism and the structural evolution of the layered host.

5.2.2.2.4 Summary

The theoretical photoemission study allowed to resolve the Ni 2p and O 1s HAXPES satellite structures of $LiNiO_2$ and delithiated Li_xNiO_2 with high accuracy. Both features are related to the O 2p - Ni 3d interaction, which is enhanced upon delithiation and acquires non-local character as revealed by the plasmonic nature of O 1s satellites.

As for $LiCoO_2$, understanding the photoemission spectra required departing from the conventional interpretation based on Ni^{3+}/Ni^{4+} redox. In fact, the study of the core-level spectroscopy satellite peaks highlighted the negative charge transfer character of both $LiNiO_2$ and NiO_2. This conclusion goes along recent experimental (XAS [148,149] and RIXS [137]) and theoretical (DFT+U [112] and DMFT [148]) studies. Moreover, we gave the first photoemission spectroscopy insight on the bond- and charge-disproportionation proposed by Foyevtsova et al., so far supported by diffraction experiments [112], and suggest that this characteristic fades upon deintercalation.

Since the theoretical analysis of the Ni 2p HAXPES satellite structure was strongly dependent on various experimental findings as described above and further in **Section 4.3.2** (Ni 2p and O 1s peak fitting and quantification, Ni 1s analysis), the results presented here constitute part of a publication that is under submission at the time this paragraph was written (January 2024, see **Annex I**, **paper 4**).

5.3 Chapter summary

In this chapter, we presented our theoretical approach for studying the bulk-related signatures of HAXPES spectra to access the bulk electronic structure of model layered transition metal oxides. This combinative method is based on (1) examination of the experimental spectra by non-destructive depth profiling (**Chapter 4**) and (2) subsequent cluster model theory calculations. The determination of model parameters related to transition metal 3d correlations and p-d charge transfer was essential for this task. The application of *ab initio* interaction parameters from cRPA was assessed as an alternative method to overcome the limits of the classical semi-empirical method.

The results brought new contributions to the long-standing question of the fundamental redox compensation mechanism of Li_xCoO_2 and Li_xNiO_2. For both systems, we identified a mechanism that explains the experimental spectroscopy evidence and attributes a dominant role to metal-oxygen interactions driven by the reduction of local hole charge accumulation on the transition metal 3d orbitals. However, the electronic structure changes are different in the two systems due to the different "starting point" for the delithiation process, considering that the ligand-metal charge transfer involves the e_g states predominantly.

In fact, $LiCoO_2$ is an intermediate insulator with filled t_{2g}^6 and an overall empty e_g orbitals (just partially occupied by hybridization with O 2p). Upon delithiation, the electronic structure evolves towards a metal due to electron withdrawing from t_{2g}, compensated by electron transfer towards the e_g states. For $LiNiO_2$ the electronic structure is already in the negative charge transfer regime with the higher energy e_g states half-filled. Therefore, electron withdrawing from these states is directly compensated by O 2p charge transfer and the hole distribution is carried out by the strongly mixed e_g-O 2p bands.

Although finding agreement with experimental and theoretical results, including most recent findings in the literature, these conclusions dispute the conventional picture based on cationic redox and eventually anionic redox at end of charge, highlighting the strong interactions between cation and anions. Moreover, our study suggests that the mere presence of oxygen holes in the layered oxide does not represent an intrinsic limit for application, as proposed in the literature (**Figure 1.4.6** and related discussion): otherwise, $LiNiO_2$ should not work at all as a Li-ion positive electrode material. Instead, the surface instability and related loss of electrochemical performance seems to be ruled not only by the presence of O holes but also by the cell potential and the structure of the SRL.

The cluster model calculations developed in this thesis have shown some limitation related to:

1. Only the end members could be studied, leaving open the question of linking crystal phase transitions with the observed electronic behavior. For example, concerning Li_xCoO_2, the positioning of the positive-negative charge transfer transition along the deintercalation level can shed further insights on its actual bulk stability limits.
2. The contribution from long-range interactions (metallic screening and NLS effects) are missed in the simulation but clearly present in the experiment. In the case of Li_xNiO_2, the NLS spectral weight clearly decreases, suggesting a relevant role of non-local charge transfer upon delithiation. More generally, as we argued above, the larger differences observed between the two systems involve non-local interactions which shall therefore be introduced for a better understanding.

3. Third, the proposed presence of disproportionation in $LiNiO_2$ cannot be confirmed within single cluster model calculations.

All the above issues can be improved by developing multi-cluster or extended model simulations [324,326–329]. Despite being already presented since a long time for simpler cases, their actual implementation in the context of this thesis e.g. involving DFT tight binding models for edge-sharing MO_6 octahedra organized in layered structures is still a challenge. Concerning the metallic and NLS screening in particular, DFT+DMFT simulations of core-level photoemission spectra are considered a valuable improvement [323,330–332].

In this chapter, most of the discussion was based on M 2p simulations. However, we expect that the O 1s HAXPES spectra could also be investigated by this method. In fact, both the binding energy simulations by DFT (**Section 4.3.1.3**) and the study of O 1s satellites by cRPA (**Section 5.2.2.2.3**) gave important contributions to our study. However, O 1s HAXPES simulation by cluster model theory is non-trivial as both the O 1s core hole potential and the O 2p correlations need to be carefully examined. In fact, only a few examples of similar calculations were found in the literature for simplified systems (either XAS simulations -- no oxygen correlations -- or no 3d transition metal as central ion) [333,334]. In principle, this problem could be treated by departing from the configuration interaction model and adopting a *dp-dp*-like model as described within cRPA theory in **Section 5.2.2.2.3**. Noteworthy, the introduction of oxygen self-interaction seemed to improve the theoretical description of NiO at the DFT+DMFT level [335]. Therefore, we consider the examination of O 1s HAXPES by theoretical methods as a promising route.

At the level of the materials, we recall that our conclusions are for model materials with a single transition metal. However, the most technologically and commercially relevant materials are NMC solid solutions, in which Ni, Co, and Mn are disordered in each MO_2 layer. Therefore, understanding the electronic behavior of these materials requires adding this additional dimension of complexity. On the one hand, the non-local interactions seen in $LiCoO_2$ and $LiNiO_2$ are strongly perturbed; on the other hand, new ones are potentially added, related to the topological distribution of each transition metal. From the perspective of cluster model theory, a first approximation would be to consider each MO_6 entity separately, similar to what was done for $LiNiO_2$ disproportionation. However, this does not provide access to global information on the evolution of the electronic structure of the system since the mutual interaction between each transition metal bridged by the O 2p orbitals is missing. Indeed, considering the self-regulation mechanism, we speculate that the compensation mechanism is similarly based on charge transfer by the oxygen ion network. Clearly, the technical advances proposed above are partly necessary to be able to approach this problem.

General conclusions

Given the ongoing debate regarding the nature of the charge compensation mechanism in classic and Li-rich layered oxides based electrodes, the role of transition metals and oxygen in the redox process is yet to be clarified and resolved. In this thesis, we focused on two main questions: (1) what is the contribution of transition metals and oxygen to the charge compensation mechanism considering the strong M 3d-O 2p covalency and M 3d correlations of $LiMO_2$ (M = Ni, Co, Mn)? (2) can we distinguish surface and bulk electronic structures given the formation and evolution upon battery cycling of the positive solid electrode-electrolyte interphase (pSEI) and surface reduced layer (SRL)? Throughout this thesis, we addressed these questions and provided methodological approaches to answer them.

Core-level spectroscopies are amongst the most effective techniques for this challenge but quantitative analysis and coupling with electronic structure simulations are required for an accurate interpretation of the experimental spectra. In this framework, we have developed a methodology based on soft and hard X-ray photoelectron spectroscopy (XPS, HAXPES) to perform qualitative and quantitative depth analysis in combination with a suite of computational techniques (DFT, Wannier functions, CMT, cRPA).

We based our study on $LiCoO_2$ thin films and $LiNiO_2$ and Li_2MnO_3 powder electrodes, chosen as model systems for the family of NMC materials. The advantages and limits of quantitative lab-based XPS/HAXPES and empirical peak fitting analysis of transition metal and oxygen core-level spectra were first established using the pristine electrode materials. The link between surface transition metal reduction and deviation from ideal stoichiometry (surface deoxygenation) was evinced from M 2p and O 1s spectra analysis. These insights formed the basis for studying the materials cycled at different states of charge and characterizing their surface degradation distinguished into pSEI (1-2 nm), SRL (2-10 nm), and bulk (probed down to 15-20 nm with lab-based HAXPES). The three materials displayed different behaviors consistent with their electrochemical stability limit. For the pSEI, the use of a co-localized XPS and HAXPES enabled surface contributions to be better discriminated in terms of thickness and chemical composition.

However, the SRL formation and evolution was considered more relevant concerning battery performance stability. Upon cycling, we observed changes in M 2p and O 1s spectra related to degradation processes. For the M 2p spectra, the surface reduction was identified in changes of the satellite peaks based on reference spectra. This was related to the apparition of a peak in the O 1s spectra shifted at ~1 eV to the high- binding energies side of the main peak related to bulk lattice oxygen atoms. The peak fitting interpretation was supported by quantitative analysis that showed a decrease in the O/M atomic ratio. The comparison of XPS and HAXPES results allowed localizing these processes at the extreme surface and so to identify the signatures of different surface and bulk electronic states. However, the voltage dependence of these surface chemical changes differ for each material: in Li_2MnO_3, surface degradation dominates since the first charge; in $LiCoO_2$, the SRL growth accelerates when deintercalating more than 0.5 atoms of Li per unit formula; in $LiNiO_2$, we observed a small voltage dependence, but the surface is already altered at the pristine state in contrast to the other two materials. Moreover, we highlighted the advantage of combining lab-based HAXPES quantification with the higher sensitivity to bulk spectral features of synchrotron-based HAXPES characterization. This allowed resolving the depth distribution of Ni and O electronic states in cycled Li_xNiO_2 by photoemission spectroscopy for the first time. From a methodological point of view, we also addressed the question of synchrotron radiation beam damage and remarked on the significant advantage of carrying out lab-based HAXPES analysis before the synchrotron campaign.

Subsequently, we studied the bulk electronic structures of $LiMO_2$ and MO_2 (M=Ni, Co) by simulating the M 2p core level HAXPES spectra compared to the experimental signatures related to the bulk material. The determination of transition metal 3d coulombic interaction (U) and p-d charge transfer energy (Δ) was approached both experimentally (fitting the simulation to the experiment) and theoretically (results from the cRPA method). Generally, we observed a tendency of decreasing Δ toward the negative charge transfer regime with increasing formal transition metal valence. By studying the changes in the local electronic structure upon delithiation, we highlighted the dominant role of metal-oxygen interactions driven by the minimization of local hole charge accumulation on the transition metal 3d orbitals (self-regulation mechanism), explaining (part of) the subtle changes in the Ni 2p and Co 2p HAXPES spectra.

With our understanding of the surface stability issues and bulk electron compensation mechanism studied in this thesis, we can draw some perspectives on the candidates for next-generation positive electrode materials. Rather than referring to cationic and/or anionic redox, our study focused on the metal-oxygen interaction and showed that the electron removal mainly affects the occupation of the O 2p states. Also, the high-voltage-driven degradation caused by oxidized surface oxygen ions was noticed by comparing the behavior of the unstable Li_2MnO_3 to the more stable $LiNiO_2$ (with $LiCoO_2$ falling in between considering the whole deintercalation line). In this perspective, designing materials that exploit the self-regulation mechanism seems a promising direction for developing next-generation materials.

Nowadays, many efforts focus on high-voltage anionic redox based on electron-hole localization, as in Li-rich Mn-rich NMC, disordered rocksalt oxides, and oxyfluorides [8,44,57,142,336,337]. Among other issues, transition metal dislocation and phase degradation drastically affect their performance upon cycling due to cycle hysteresis, voltage fade, and capacity loss. Favoring the self-regulation mechanism through substitution anions (e.g. oxygen to other chalcogens) and cations (e.g. 3d to 4d) that strengthen mutual interactions and hole delocalization seems more appealing for stable, larger capacities. Interestingly, this approach has been recently proposed in the literature highlighting the compromise to undertake due to a lower average voltage of the as-substituted electrodes [338–342]. Studying these new candidate materials based on the results and methods described in this thesis seems therefore a promising direction.

In fact, this study established a method for studying the depth-dependent changes in the electronic structure of functional materials in the field of Li-ion batteries. We note that the approach can be extended not only to NMC and next-generation electrode materials but also to a broader range of applications within and beyond the energy storage sector. Meanwhile, there are various experimental and theoretical challenges to face for a better understanding of the electronic structure of layered transition metal oxides. Although we characterized the evolution of surface chemical structure upon cycling, the impact of cell opening and exposure of cycled surface to different environments is yet to be clarified. Coupling our quantitative XPS/HAXPES characterization with *in-situ/operando* conditions to clarify surface degradation mechanisms and to study the dynamics of the redox process is clearly an upcoming challenge. We also identified the main limitations of the theoretical method. Two main aspects need further improvement: (1) access to partial lithiation states and (2) inclusion of longer-range interactions that expand the single-cluster model. In addition, we note that so far we have addressed only the bulk electronic structure through simulations; surface structures should also be considered for a complete joint experimental and theoretical depth-dependent study.

Annex

A. X-ray photoelectron spectroscopy

A.1. Introduction

Based on the photoelectron effect discovered in 1905 by A. Einstein, the X-ray photoelectron spectroscopy (XPS) was developed in the '50s by Siegbahn group as characterization method of surface chemical species. Nowadays, the application of this technique spans a broad range of scientific fields that can be divided into two categories. One the one hand, XPS is a widely employed technique for the characterization of surface chemistries of all classes of materials, from metals to organic samples. On the other, XPS can serve as probing tool for the electronic structure of materials. In this case, the focus of the technique is on the response of the electronic structure to the photoemission process itself, which can be used to infer on the microscopic nature of the material. Because of such variety of applications, the XPS technique is also referred to as electron spectroscopy for chemical analysis (ESCA) or photoemission spectroscopy (PES) in different communities. In this section, we shortly review the basic aspects of the technique. A more complete overview of XPS (and HAXPES) can be found in ref. [213,217].

A.2. Introduction Basic principles

The basic principle behind the XPS technique is the photoemission process: the ejection of an electron from a sample, whether solid, liquid or gas, by the annihilation of a photon with energy hv. The process occurs if the energy of the incident photon is greater than the energy that binds the electron to the system. In a typical XPS experiment, schematized in **Figure A.2.1(a)**, a monochromatic X-ray beam excites the sample and the emitted electrons are counted as a function of their kinetic energy E_K, given by the following equation:

$$E_K = h\upsilon - E_B - \phi_{sample} \qquad \textbf{Equation A.2.1}$$

Where ϕ_{sample} is the work function of the sample and E_B the binding energy [**Figure A.2.1(b)**]. For a conducting sample in electronic contact with the electron detector, $\phi_{sample} = \phi_{detector}$, which is a value given by the manufacturer; for insulators the absolute value in energy is obtained by correction of the measured energy by a reference value. Thus, **Equation A.2.1** can be used to obtain the binding energy E_B, which contains information about the chemical nature of the atoms from which the photoelectron was ejected. In fact, all core-levels of each element in the periodic table starting from lithium are distinguishable by means of their electrons' binding energy.

Beyond the atomic orbital characteristics, the binding energy is influenced by the chemical environment, which gives a so-called chemical shift. Therefore, it is possible to distinguish atoms in different oxidation states and their involvement in different chemical bounds.

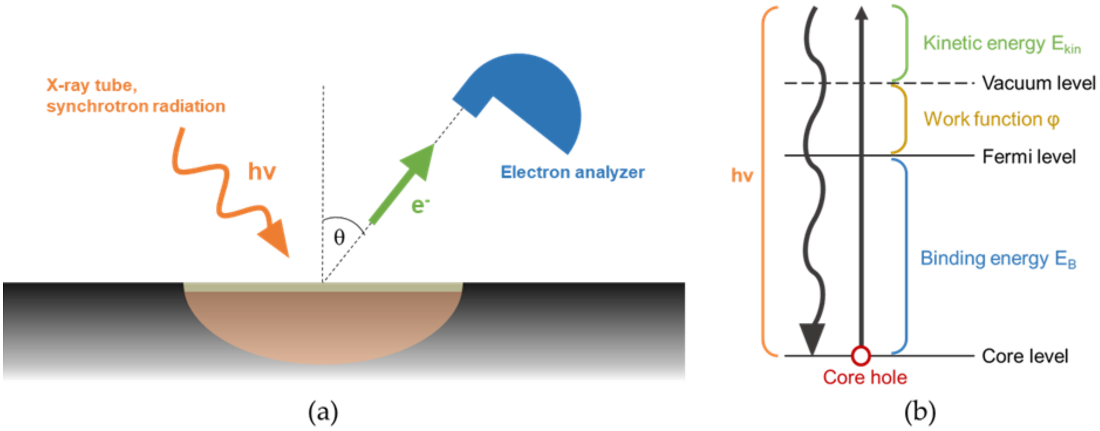

Figure A.2.1 Fundamentals of an XPS experiments. (a) Schematics of the experiment. They orange area represents the X-ray penetration depth, generally much larger than the escape depth of photoelectrons, represented by the grey area. (b) Energy schema of the fundamental law of XPS.

The probability of a photoemission process depends on the probability of collision between the incident photon and the core or valence state, characterized by a set of quantum numbers ($|n, l, j\rangle$). Without going into detail, it is important to note that this probability decreases with increasing hν. Hence, while gaining access to deeper core levels would require high photon energies belonging in the hard X-ray regime (hν > 2 keV), the decrease of the photoionization cross-section prevents the effective measurement of photoemitted electrons. As a compromise, nowadays most laboratory instruments use X-ray tubes based on Al Kα (1.486 keV) and Mg Kα (1.253 keV) X-ray emission.

In a photoemission experiment, after the photoexcitation the electron needs to move through the sample and reach the detector to be measured. In fact, the full process is generally described using a three-step model, shown in **Figure A.2.2**, of which the photoexcitation represents the initial one.

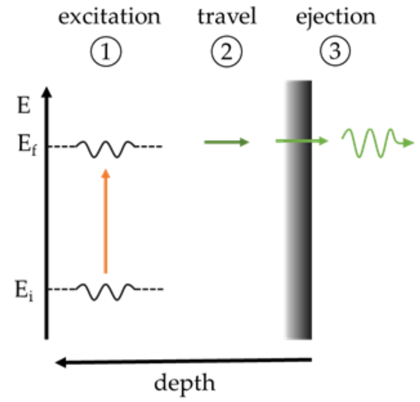

Figure A.2.2 The three-step model, adapted from ref. [217]. E_f and E_i are initial and final state energies.

While the penetration of matter by X-rays is in the order of few micrometers or greater, depending on hν and the material itself, electrons strongly interact with matter. Therefore, even if photoexcitation can occur at large depths, only the electrons excited from the first few nanometers can reach the sample surface. This phenomenon is at the basis of the success of XPS as surface-sensitive technique. Considering a homogeneous solid with flat surface as model system, the attenuation of the detected photoelectron intensity I follows an exponential decay as a function of the depth z and the angle θ with respect to the surface:

$$I(z) = I(0)e^{\left({-z}/{\lambda \sin\theta}\right)}dz$$ **Equation A.2.2**

Where λ is the inelastic mean free path (IMFP), formally defined as the distance an electron beam can travel before its intensity is damped by e^{-1} or equivalently representing the distance an electron can travel between two consecutives collisions. Consequently, the 99.7 % of the total intensity comes from a herein defined sampling depth SD:

$$SD = 3\,\lambda\,\sin\vartheta$$ **Equation A.2.3**

The IMFP is an intrinsic property of each material whose accurate determination requires to know the scattering channels that can damp the electron travel towards the surface. The group of S. Tougaard developed tools for such calculation that rely on supporting Reflection Electron Energy Loss Spectroscopy (REELS) characterization but are practically available only for model systems [294]. However, it has been found that the IMFP of most materials follow the same tendency with respect to the kinetic energy of the travelling electron, which allowed defining the TPP2M relation by Tanuma, Powell, and Penn [343–345]:

$$\lambda = \frac{E_K}{E_p^2\,(\beta \ln(\gamma E_K) - \frac{C}{E_K} + \frac{D}{E_K^2})}$$ **Equation A.2.4**

Where E_p is the free electron plasmon energy and β, γ, C, D are parameters empirically related to the bulk density, the number of valence electron per unit formula, the molecular weight, and the band gap of the investigated material, which are all quantities easily obtainable to some degree of accuracy.

The intensity I in **Equation A.2.2** is due to photoelectrons that did not incur into inelastic collisions hence kinetic energy loss. For all other photoelectrons, their kinetic energy will be lowered by a certain amount, which appears as an apparent higher binding energy following **Equation A.2.1**. The intensity collected from these inelastically scattered photoelectrons is modeled as a background contribution in XPS analysis, which focuses on the analysis of the elastic peaks instead.

Regarding the last step of the photoemission process as schematized in the three-step model, i.e. the electron ejection from the surface to vacuum, we simply note that the electron position and momentum can be used to perform spatially-resolved X-ray photoemission microscopy (XPEEM) and angle-resolved photoemission spectroscopy (ARPES, k-PEEM), that allows to measure the band dispersion of a solid. However, the successful application of these techniques has strict requirements, for example on sample flatness, which are not typically met by battery materials [346].

Overall, it is important to note that XPS experiments involve an ionization process, meaning that a core hole (assuming photoemission from a core level) is created. By applying the energy conservation principle to the photoemission process:

$$h\nu + E_i[N] = E_K + E_f[N-1]$$ **Equation A.2.5**

Where $E_i[N]$ and $E_f[N-1]$ are the total energy of the system at initial and final state with N and N-1 electrons, respectively. Combining equations **Equation A.2.1** and **Equation A.2.5**, the fundamental definition of binding energy emerges as:

$$E_B = E_f[N-1] - E_i[N] - \phi$$ **Equation A.2.6**

A.3. Core-level spectra analysis by peak fitting

The XPS spectra consist of the photoelectron intensity measured as a function of the binding energy. It can be distinguished into two regions: the valence band and the core-levels. While the former tends to have a band-like character and is typically approximated by the density of states obtained by electronic structure calculations, core level spectra have an atomic-like character, although they still reflect the nature of the electronic structure because of its role in screening the core hole. In this section, the analysis of core-level spectra is shortly reviewed, from theoretical to practical aspects.

A.3.1. Chemical shifts: qualitative analysis of surface chemistry

The main information of a core-level peak is its binding energy position, which is influenced by the above-mentioned chemical shift. This concept is strongly linked to the effective screening of the nuclear charge by the other electrons in the atom as well as its surrounding chemical environment. The latter can be explained by considering the case of a bond between two atoms with different electronegativity: the electron density is shifted towards the most electronegative one.

In principle, extracting an electron from an electron-depleted environment requires more energy, as the photo-excited electron is more strongly bound to its nucleus: consequently, its binding energy will be higher than an equivalent atom with a more electron-rich environment. Such chemical shifts are often discussed on this qualitative basis and with supporting reference material that can be found in dedicated databases and previous publications. For example, **Figure A.3.1** shows the typical binding energy range of different chemical species as measured in the O 1s spectra.

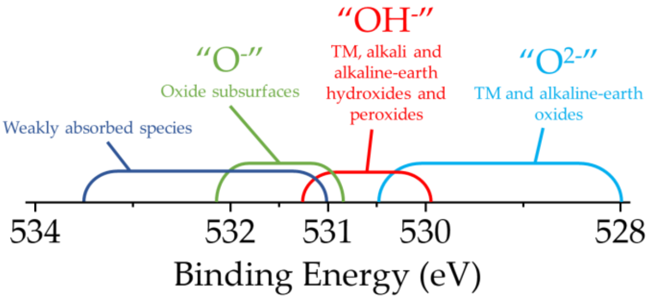

Figure A.3.1 General binding energy scale of O 1s peak. Adapted from Ref. [249].

It must be noted that the absolute value of binding energy assigned to the same formal chemical specie can significantly vary in the literature for battery-related materials, as shown in the example of **Figure A.3.2**. In fact, the substrate and measurement conditions can significantly influence on the measured binding energy for surface species. This is a consequence of the large heterogeneities present in the SEI, which can present differential charging effects that shift components with different conductivities with respect to each other. For this reason, it is often more insightful to consider binding energy differences between different core levels.

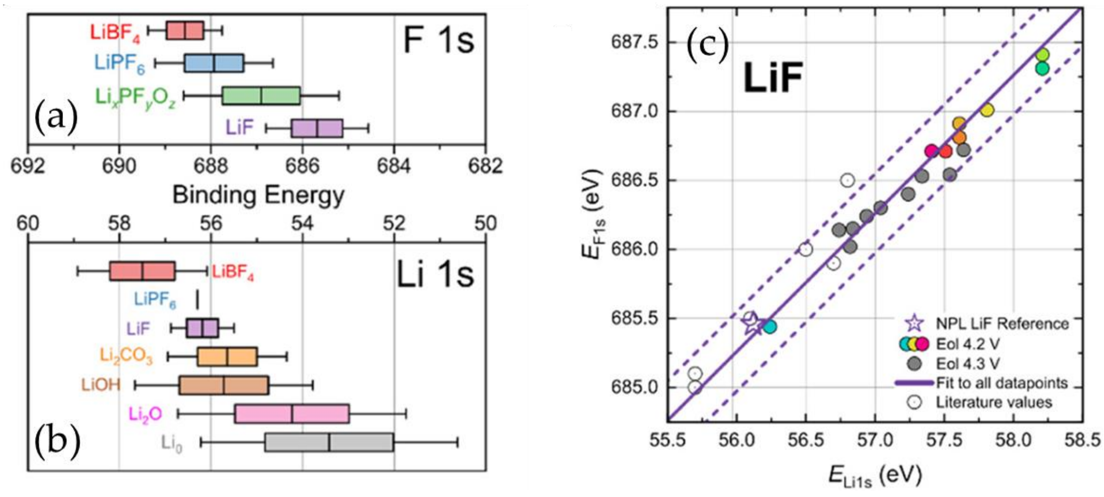

Figure A.3.2 Literature review of reported binding energy values for Li salts relevant in Li-ion battery application. Binding energy range of (a) F 1s and (b) Li 1s peaks. (c) Comparing Li 1s and F 1s binding energies for several LiF-containing electrode samples reveal that, while binding energy shift may be significant, the difference remains overall constant. Reprinted from Ref. [347].

A.3.2. XPS quantification

Studying the core-level spectra intensities allows to quantify the relative concentration of surface species in a sample. In general, the XPS intensity I for a measured core-level peak is given by:

$$I = N\,F\,\sigma\,\varphi\,T\,\lambda = RSF \cdot N \qquad \text{Equation A.3.1}$$

where:

- N is the concentration of the chemical specie (at/cm^3)
- F is the X-ray flux (photon/cm^2)
- σ is the partial photo-ionization cross section
- φ is the angular distribution
- T is the efficiency detection of the spectrometer i.e. the transmission function
- λ is the inelastic mean free path

Overall, all instrumental and intrinsic properties enter into the Relative Sensitivity Factor (RSF). Knowing these parameters allows one to estimate the relative atomic concentration of a given atomic specie X as:

$$n_X = \frac{I_X/_{RSF_X}}{\sum_i I_i/_{RSF_i}}$$ **Equation A.3.2**

A.3.3. Data treatment

In general, the measured core-level spectra might contain more than one contribution from different chemical specimens, which need to be distinguished for both qualitative and quantitative analysis. This is routinely performed by the peak fitting method presented below, which aims to extract the main physical information i.e. the binding energy position, peak width, and the intensity for each chemical component.

A peak fitting model is defined in terms of component peaks, each characterized by a certain position, full width at half maximum (FWHM), lineshape, and intensity, and a background function. The sum of these constituents gives the data envelope, which is optimized to reproduce the experimental spectra by modifying the adjustable parameters of peak components using a mathematical algorithm based on e.g. the minimization of the square residuals.

A.3.3.1. Background subtraction

To extract the elastic contribution from a core-level spectrum, it is first necessary to subtract the intensity due to inelastic losses by defining a background function. There are three commonly adopted backgrounds: linear, Shirley [348], and Tougaard [349].

- Shirley is the most general choice as it well describes the typical “step” in the background intensity following an elastic peak. In fact, its mathematical derivation is based on the assumption that the change in background intensity is proportional to the peak intensity above the background.
- Tougaard’s background has instead a physical basis as it is calculated from the inelastic scattering cross section, which can be the universal’s one or, if proper parameters are found, be finely tuned for each material. Although appealing, its dependence on materials-dependent parameters and requirement of a large energy range (more than 30 eV) in the background at lower kinetic energy to the peak makes it hardly employable for unknown heterogeneous samples as in the case of battery materials. Note that, beyond imposing constrains on data acquisition, it cannot be used in case of overlapping peaks within this range.
- The linear background is generally employed for symmetric peaks with similar intensity for the lower and upper continuous inelastic background. It is also used when the background function mentioned before does not work for complex spectrum feature.

A.3.3.2. Resolving spectral components

Once defined the region of interest and its background subtraction, the spectrum is analyzed by defining the number and properties of components constituting it. Each component is characterized by a position, linewidth, lineshape and area.

The binding energy measured for a certain specimen is subjected to intrinsic and instrumental broadening that define the overall linewidth of the peak, typically expressed as FWHM. The intrinsic broadening is linked to the core-hole lifetime τ via the Heisenberg's principle ($\Delta E_L = {}^{\hbar}/_{\tau}$) leading to a Lorentzian distribution function in absence of any instrumental broadening. Instrumental factors lead instead to a Gaussian contribution, which is in principle convoluted to the Lorentzian distribution giving the Voigt lineshape.

For practical reasons, the convolution is approximated by either a sum or product of Gaussian and Lorentzian contribution, leading to the most commonly adopted pseudo-Voigt line shapes. Therefore, the choice reduces to define the relative amount of Gaussian or Lorentzian contribution in the pseudo-Voigt function, which modifies the peak tails. While these are symmetric functions by definition, in certain cases (e.g. metals) asymmetric line shapes are best suited to describe the core-level spectra. In light of the large number of parameters that enter into the minimization algorithm, fit constraints become increasingly relevant for complex spectra. By making use of database and references, the binding energy range of a certain specimen can be generally defined; it is also possible to constrain the position of a peak to be at certain distance from another, as in the case of two spin-orbit components. Similar considerations apply for the FWHM and areas.

In practical routine, the peak fitting is performed iteratively by progressively releasing the starting constraints. However, it should be highlighted that the algorithm does not consider physical or chemical meaningfulness of the fit, which is given by proper selection of number of the parameters to be used for the peak fitting. This includes the number of components, the line shape, the background region and shape, and the parameter constrains (e.g. the binding energy range for a given component).

Overall, XPS peak fitting is a challenging practice, which requires certain experience by the user and can even be disfavored over a more qualitative and general description of the spectral shape, which can already give valuable insight (i.e. sometimes "the best fit is no-fit"[12]). In fact, nowadays the XPS data analysis represents a crucial issue for the photoelectron community: according to expert's opinions, the spreading of accessible XPS equipment and user-friendly software led to proliferation of erroneous and faulty data analysis in the literature [350,351].

The core-level spectra analysis of 3d transition metal systems falls into this category. For these materials, more than one peak is measured for the same chemical specimen, leading to non-trivial line shapes that requires fundamental understanding of the photoemission process. This is treated in **Chapter 3** as a core theme of this thesis. Unfortunately, it needs to be pointed out that such considerations are not always taken into account in the literature, leading to an increasing list of publications where the nature of the transition metal ions in the sample (in most cases, the oxidation state) is wrongly extracted by chemical shifts considerations [189,271,295–301,352–354].

A.4. Theory of photoemission spectroscopy

A.4.1. The Fermi's Golden Rule

From the conceptual division established in the three-step model concerning non-interacting core-hole creation, electron travelling, and electron ejection, the photoelectron process can be approached by distinguishing three subsystems:

- The core-electron system $|\psi_c\rangle$ of energy ε_c;
- The photoelectron system $|\psi_{n\boldsymbol{k}}\rangle$ of energy $\varepsilon_{n\boldsymbol{k}}$, n and **k** being Bloch and plane-wave indexes inside and outside the system, respectively;
- The low-energy (valence) electron system, involving the TM 3d (and possibly the O 2p) electrons.

The first step involves a creation of a core hole, defined as the absence of an electron in a core level. A core hole created by XAS or by XPS experiments lives for about 1 fs before it decays via radiative or non-radiative decay channels.

Within this framework, the core-hole creation probability (w) can be described by means of the Fermi's Golden Rule:

$$w \propto \frac{2\pi}{\hbar}\left|\langle\Psi_f|\boldsymbol{p}\cdot\boldsymbol{e}|\Psi_i\rangle\right|^2\delta(E_f - E_i - \hbar\omega) \qquad \textbf{Equation A.4.1}$$

---

[12] Anass Benayad is acknowledged for this mantra.

Where the dipole approximation was assumed for the transition operator ($\boldsymbol{p}\cdot\boldsymbol{e}$) and Ψ_f and Ψ_i are the initial and final many-body states with energies E_f and E_i, respectively.

Following the three-step model, one can separate the core electron as single electron wavefunction ($\psi_c \to \psi_{i,k}$) from the remaining system in the initial state:

$$\Psi_i(N) = \psi_{i,k}\Psi_{i,R}^{k}(N-1) \qquad \textbf{Equation A.4.2}$$

and similarly for the final state ($\psi_{nk} \to \psi_{f,k}$):

$$\Psi_f(N) = \psi_{f,k}\Psi_{f,R}^{k}(N-1) \qquad \textbf{Equation A.4.3}$$

Substituting these expressions in **Equation A.4.1** gives:

$$\begin{aligned}\langle\Psi_f|\boldsymbol{p}\cdot\boldsymbol{e}|\Psi_i\rangle = {} & \langle\psi_{f,k}|\boldsymbol{p}\cdot\boldsymbol{e}|\psi_{i,k}\rangle \\ & \times \langle\Psi_{f,R}^{k}(N-1)|\Psi_{i,R}^{k}(N-1)\rangle\end{aligned} \qquad \textbf{Equation A.4.4}$$

Hence, the photoemission intensity depends on the overlap integral between (N-1) initial and final states as well as single-electron matrix elements. Of particular concern is the latter moiety because of its many-electron nature. In fact, all possible final states are taken into account in the total photoemission intensity, leading to the following expression:

$$\begin{aligned}I \propto {} & \sum_{f,i,k}\left|\langle\psi_{f,k}|\boldsymbol{p}\cdot\boldsymbol{e}|\psi_{i,k}\rangle\right|^2 \sum_{s}\left|c_{s,i}\right|^2 \\ & \times \delta\big(E_{f,kin} - E_s(N-1) - E_{\mathrm{i}}(N) - \hbar\omega\big)\end{aligned} \qquad \textbf{Equation A.4.5}$$

where $c_s = \langle\Psi_{s,R}^{k}(N-1)|\Psi_{i,R}^{k}(N-1)\rangle$ is the probability that removing an electron from $\Psi_{i,R}^{k}(N-1)$ leads to the s-th excited state $\Psi_{s,R}^{k}(N-1)$ and the Dirac delta function expresses the definition of binding energy. Considering the ground state energy ($E_{\mathrm{i}}(N) = E_0$):

$$A(\omega) = \sum_{s}|c_s|^2\delta\big(E_{f,kin} - E_s(N-1) - E_0 - \hbar\omega\big) \qquad \textbf{Equation A.4.6}$$

is the spectral function, with s the index running over the possible (N-1) excited states obtained by the ejected photoelectron.

In the case of weak correlations, all s-th states beyond the lowest one (conventionally, s = 0) are negligible and the overlap between final and initial ground state is significant, i.e. $c_{s=0} \approx 1$. This leads to a single sharp line in the photoemission spectra, corresponding to the conceptual framework upon which are developed the analytical methods presented in **Section A.3**. This condition corresponds to a common assumption called frozen-orbital or Koopmans' approximation.

In case of transition metal core level spectra, such approximation does not hold since the spectra is composed by various lines which in principle correspond to different s-th excited states. The electronic correlations leading to different final states in the XPS spectra can be distinguished into intra-atomic and inter-atomic effects, summarized below.

A.4.2. Intra-atomic effects

The photo-induced core-hole should not be interpreted only as a punctual positive charge created in the atom: it retains the character of the core level from which the photoelectron was excited. Therefore, atomic physics is the first level of theory to be introduced to interpret this process. In particular, the N-electrons atomic Hamiltonian contains two terms that can play a major role in the photoemission spectra: the electron-electron interactions and the spin-orbit coupling:

$$H_{ATOM} = \sum_{N} \frac{\boldsymbol{p}_i^2}{2m} + \sum_{N} \frac{-Ze^2}{\boldsymbol{r}_i} + \sum_{i,j} \frac{e^2}{\boldsymbol{r}_{ij}} + \sum_{i} \zeta_i \, \boldsymbol{l}_i \cdot \boldsymbol{s}_i \qquad \textbf{Equation A.4.7}$$

with **p** the electron momenta, m the electron mass, e the electron charge, r its position, l and s the angular and spin momenta, respectively, and ζ the spin-orbit coupling energy.

A.4.2.1. Spin-orbit coupling

The spin-orbit coupling terms becomes relevant only for electrons for which the orbital angular momenta is non-zero ($L \neq 0$), which includes all photoelectrons emitted except from s shells. Because of the broken degeneracy of the total angular momenta $J = \left|L \pm \frac{1}{2}\right|$, a doublet is observed in XPS experiments with energy separation that depends on ζ, increasing with Z and for deeper core levels. The intensity ratio follows the degeneracy of each spin-orbit peak, given by all possible states ranging from –j, -j+1,…, j.

For 3d transition metals, the 2p core-levels split into $2p_{3/2}$ and $2p_{1/2}$ (where the value of J is given in pedix) with a separation in the order of 10 eV and theoretical intensity ratio of 2:1. The spin-orbit splitting for 3p and 3d electrons is instead so small that the two components are convoluted in each other.

A.4.2.2. Exchange splitting

The other term of H_{ATOM} that can impact on the shape of the photoelectron spectra is the electron-electron interactions, which are of Coulomb and exchange type. The unfilled core-shell of the final state can interact with the partially filled 3d shell, leading to many microstates as the electrons can be differently arranged in core and valence shells. Because electron-electron interactions are not negligible in 3d transition metals, the presence of such multitude of microstates called multiplets can lead to non-trivial spectral shapes.

A particular core-valence interaction is the so-called exchange splitting, which is well-known for 3s core levels of 3d transition metals. When an electron is emitted from a 3s core-level, it leaves a core level with either a spin-up or spin-down electron, which interacts by exchange with unpaired electrons in the valence shell leading to two spectral contributions, whose energy separation was calculated by van Vleck theorem [217]:

$$\Delta E_s = \left(\frac{2S+1}{2l+1}\right) G^2(3s, 3d) \qquad \textbf{Equation A.4.8}$$

where S is the total spin of the ground state of the 3d electrons, l is the orbital quantum number ($l = 0$, for 3s core level) and $G^2(3s, 3d)$is the Slater exchange integral. Therefore, the exchange splitting of a 3s core level can give insight on the total spin of the 3d shell. However, for late transition metal it tends to overlap with or even disappear in favor of charge transfer satellites.

A.4.2.3. Multiplet splitting

Beyond 3s core levels, both Coulomb and exchange core-valence interactions need to be taken into account, which is only possible by supporting simulations. Gupta and Sen first calculated the spectral shapes arising from multiplet splitting for isolated 3d transition metal ions [304], which are nowadays used by part of the photoemission community to build ad-hoc line shapes (often referred to as Biesinger's templates) for each transition metal specie in the sample [257,302,303]. This approach is finding application in fields such as corrosion and catalysis, where XPS is employed to characterize the oxidation state of transition metal in the surface of the active system. The method is further commented in **Chapter 3**.

A.4.3. Inter-atomic effects

To analyze photoemission spectra of solid samples, the chemical environment around the photoelectron emitting ion needs to be included as it reacts to the core hole creation. As it turned out, it is often sufficient to introduce only the local (i.e. first neighbor) environment, leading to small molecular-like models in most cases.

A.4.3.1. Crystal field splitting

Even before introducing explicitly the final-state interactions between the transition metal and its surroundings, the first aspect to include is the charge felt by the central cation due to the surrounding ligand orbitals. This well-known effect is described within solid-state chemistry by crystal field theory and leads to a splitting of the 3d orbitals into subshells depending on the coordination of the transition metal ion e.g. octahedral, tetrahedral, and distortions evolving from it.

The inclusion of crystal field splitting to the atomic Hamiltonian described above (i.e. including multiplet splitting and spin-orbit coupling) leads to so-called crystal field multiplet theory, which is often sufficient for a first-approximation description of XAS spectra, but fails for XPS [66,219]. Indeed, because the final state is ionized, the core hole potential is not “self-screened” as in XAS and this turns on strong screening channels that largely modifies the final state with respect to initial state.

A.4.3.2. Charge-transfer satellites

The response of the system to core hole creation by ligand-to-metal charge transfer in the final state was readily recognized as the origin of large satellites structures measured in XPS core-level spectra of 3d transition metal compounds. In fact, the first charge transfer models developed by Asada and Sugano in the ’70 initially neglected all effects listed above, finding good agreement for dihalides [355]. Hybridization, crystal fields and intra-atomic effects were later included towards the so-called charge transfer multiplet theory (or multiplet ligand field theory) [64,65,243,244,356–358].

Herein, the main concept of charge transfer satellite will be given, for which the original simple model by Asada and Sugano shown in **Figure A.4.1** is more appropriate. The extension of the charge transfer concept to the more general case that includes metal-ligand hybridization and all the effects presented above is straightforward by maintaining the configuration interaction approach sketched in the figure.

In this model, two configurations are assumed for the transition metal – ligands system: one with formal occupancies $|d^n\rangle$ and another where an electron was transferred from the ligands orbitals to the transition metal $|d^{n+1}\boldsymbol{L}^{-1}\rangle$, with $\boldsymbol{L}^{-1}$ indicating the ligand hole. The energy separating this latter excited state from the ground state is the charge transfer energy Δ presented in **Section 1.3.2**.

In the final state, the core-hole potential U_{cd} lowers the energy of the $|\boldsymbol{c}^{-1}d^{n+1}\boldsymbol{L}^{-1}\rangle$ (with $\boldsymbol{c}^{-1}$ representing the core-hole). Thus, two peaks will appear in the photoemission spectra, namely a main line and a satellite, whose character depends on the U_{cd}/Δ ratio. The case $U_{cd} > \Delta$, for which the lowest energy peak (the mainline) is the $|d^{n+1}\boldsymbol{L}^{-1}\rangle$ is the most frequent [31] for late transition metal oxides, although it depends on the ligand's nature as well. For this reason, main line and satellite peaks are also addressed to as well-screened and poorly screened states in the literature. The formal derivation for this simplistic charge transfer model derived is found in ref. [217].

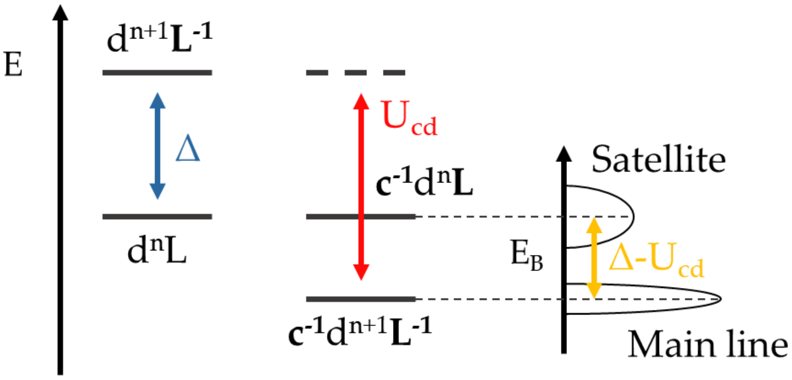

Figure A.4.1 Sketch of the Asada-Sugano charge-transfer model ($\Delta < U_{cd}$).

A.4.3.3. Non-local screening

In some cases and particularly for late transition metal oxides it was demonstrated that fine details of the mainline could only be explained including screening channels going beyond the first neighbor shell, i.e. non-local screening processes. The difference between local and non-local screening is shown schematically in **Figure A.4.2**, for a square plane model that often represents cuprate systems such as CuO [326]. The former final state is due to electron transfer from a neighbor square planar cluster, leading to a filled d-shell for the photo emitting ion and a so-called Zhang-Rice singlet, whose name is due to the authors that first studied this electronic state [359]. In the Zhang-Rice state, the hole in the central ion cohabits with the hole delocalized in the ligand shell. This property was shown to be crucial for interpreting the electronic structure and photoemission of CuO as well as other high-temperature cuprate superconductors [326].

However, the first theoretical study of non-local screening process was dedicated to interpreting the characteristic mainline doublet of NiO. Proof that this structure was due to non-local screening came from both an experimental investigation of the $Mg_xNi_{1-x}O$ system, revealing its disappearance for x~1 [293], and by performing multi-cluster calculations that correctly simulated the shoulder peak [327].

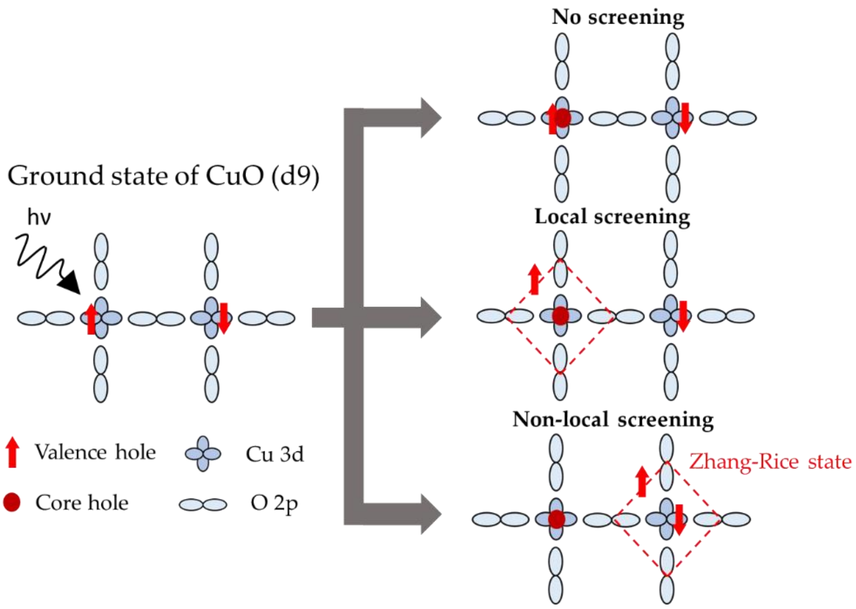

Figure A.4.2 Comparison of not screened, locally and non-locally screened final states for the CuO square planar model system. Adapted from Ref. [326].

A.5. Experimental details

A.5.1. Laboratory setup

Laboratory XPS and HAXPES measurements were performed with a QUANTES spectrometer (ULVAC-PHI) equipped with a co-localized Al kα (1486.6 eV) and Cr kα (5414.9 eV) dual X-ray source. Both X-ray sources are monochromated scanning microprobes, whose lateral resolution can be tuned delivering an X-ray spot size with radius varying from ~10 μm to 200 μm. The choice of lateral resolution is related to the X-ray beam power hence the photoelectron intensity, which is why in most cases beam spots of 100 or 200 μm were employed, corresponding to 25 W (Al) and 50 W (Cr), respectively. X-ray induced secondary electron imaging (SXI) can be performed to select the region of analysis, allowing also to select a line or an area in which the selected microprobe acquires the measurement by scanning on the sample surface.

High-resolution spectra were typically acquired with a pass energy of 55 eV (or 69 eV), corresponding to an energy resolution of about and 0.71 (0.81) and 0.93 (1.16) eV for Al kα and Cr kα, respectively, as estimated from the FWHM of the Ag $3d_{5/2}$ of a reference clean Ag sample. In case of insulating samples (typically all powders), automatic dual electron and Ar-ion charge neutralization was enabled.

Ar-ion depth profile can be performed on the Quantes system with acceleration voltages hence impact energies in the range of 0.5 - 5 keV and on square areas with sides of 1-3 mm. As discussed in **Chapter 3**, to evaluate capabilities of different depth profiling approaches, Gas Cluster-ion Beam (GCIB) depth profiles were also performed, using a Versaprobe II equipment (ULVAC-PHI) similar to the Quantes by means of lateral and energy resolution but enabled only with the conventional Al X-ray source.

The samples can be introduced by a standard entry or by a side entry dedicated for air-sensitive samples, which can be introduced using a dedicated air-tight transfer vessel. All air-sensitive samples were introduced by this latter entry. On one hand, this allows to prevent air contamination; on the other, the take-off angle had to be restricted to only 45° due to construction specification. This value will be taken as standard conditions. While the pressure in the entry chamber required pressures below $2x10^4$ Pa, the measurements were carried out in the main chamber in ultra-high vacuum conditions ($p < 10^{-7}$ Pa). Generally, all samples were mounted on the sample holder using conductive copper double tape. Unless otherwise specified, sample preparation was carried out in an Ar-filled glovebox for all positive electrode materials.

A.5.2. Synchrotron HAXPES

The lab-based study for Li_xNiO_2 electrodes was complemented by a twenty-four hour synchrotron HAXPES campaign at Soleil synchrotron. Synchrotron HAXPES was performed in the Galaxies beamline using monochromatic X-rays with three photon energies: 2300, 5400, and 9500 eV. The incident and take-off angles were 10° and 80°, respectively. The X-ray beam spot was 20x80 um^2 (oval shaped). A different spot of previously unexposed sample was used for each X-ray energy. The pass energy was 200 eV corresponding to an energy resolution from 0.3 eV for the measures at 2300 and 9500 eV and 1.0 eV for the one at 5400 eV. No charge calibration was employed. A cut of the same electrodes measured by lab-based XPS/HAXPES was transferred using double thermally sealed pouches to prevent air contamination. The samples were prepared in an Ar-filled glovebox using copper double tape.

A.5.3. Data analysis

All spectra were analyzed with the CasaXPS software. The corrected relative sensitivity factor (RSF) for both X-ray sources were exported from the MultiPak library to take into account the transmission function of the spectrometer. Generally, peak decomposition was performed using an iterated Shirley function for modeling the background and Pseudo-Voigt Gaussian-Lorentzian product functions having 30% and 70% of Lorentzian and Gaussian weight as peak lineshape.

To quantify the different sampling depths of XPS and HAXPES techniques, the inelastic mean free paths (IMFPs) were calculated with the Tanuma-Powell-Penn method by the Quases-IMFP-TPP2M software [343]. The values are shown in the table below and were used to calculate the sampling depth as $3\lambda \sin\vartheta$, with ϑ the take-off angle of 45° and 80° for lab-based and synchrotron experiment, respectively.

	XPS (Al Kα)			**HAXPES (Cr Kα)**			**2.3 keV**	**9.5 keV**
Core level	**Li_2MnO_3**	**$LiCoO_2$**	**$LiNiO_2$**	**Li_2MnO_3**	**$LiCoO_2$**	**$LiNiO_2$**	**$LiNiO_2$**	**$LiNiO_2$**
Li 1s	3.3	2.6	2.6	9.9	7.6	7.7	3.7	12.2
TM 3p	3.3	2.6	2.6	9.9	7.6	7.7	3.7	12.2
TM 3s	3.3	2.6	2.6	9.8	7.6	7.5	3.6	12.2
C 1s	2.9	2.3	2.3	9.5	7.4	7.4	3.4	12.0
O 1s	2.4	1.9	1.9	9.1	7.1	7.1	3.1	11.7
TM 2p	2.2	1.4	1.4	9.0	6.7	6.7	2.6	11.3
TM 2s	1.9	1.3	1.2	8.8	6.6	6.6	2.4	11.2
TM 1s								2.2

Table A.5.1 Inelastic mean free path for all core level accessible by the lab-based HAXPES equipment. All values are given in nm. The following parameters were used as input for the QUASES-IMFP software. Bulk density in g/cm^3: 2.34 (Li_2MnO_3), 4.92 ($LiCoO_2$), 4.80 ($LiNiO_2$). Number of valence electrons per formula unit: 21 (Li_2MnO_3), 18 ($LiCoO_2$), 19 ($LiNiO_2$). Atomic mass: 116.82 (Li_2MnO_3), 97.893 ($LiCoO_2$), 97.63 ($LiNiO_2$). Band gap energy in eV: 5 (Li_2MnO_3), 2.2 ($LiCoO_2$), 0.4 ($LiNiO_2$).

B. Density functional theory

B.1. Introduction

The main aim of solid-state physics is solving the full many-body Schrödinger equation of a given system, which essentially consists of a collection of N electrons and nuclei interacting with each other. In general, the Hamiltonian of such N-particles system includes all kinetic and potential terms plus an electron-nuclei Coulomb interaction, taking the following form (in Hartree atomic units) [360]:

$$\begin{aligned} H = -\sum_i \frac{\boldsymbol{\nabla}_i^2}{2} - \sum_I \frac{\boldsymbol{\nabla}_I^2}{2M_I} - \sum_{i,I} \frac{Z_I}{|\boldsymbol{r}_i - \boldsymbol{R}_I|} \\ + \frac{1}{2}\sum_{i \neq j} \frac{1}{|\boldsymbol{r}_i - \boldsymbol{r}_j|} + \frac{1}{2}\sum_{I \neq J} \frac{Z_I Z_J}{|\boldsymbol{R}_I - \boldsymbol{R}_J|} \end{aligned} \qquad \textbf{Equation B.1.1}$$

where uppercase and lowercase symbols are referred to nuclei and electrons, respectively.

The Hamiltonian is simplified by the Born-Oppenheimer approximation that assumes the nuclei dynamics to be significantly slower than that of electrons (m<<M). Thus, the nuclei-related terms can drop off the Hamiltonian while the electron-nuclei interaction is formally defined as the external potential acting on the electron-only system.

$$\mathrm{V}_{ext}(\boldsymbol{r}_i) = -\sum_{i,I} \frac{Z_I}{|\boldsymbol{r}_i - \boldsymbol{R}_I|} \qquad \textbf{Equation B.1.2}$$

Still, the remaining many-electron Schrödinger equation

$$\left[-\sum_i \frac{\boldsymbol{\nabla}_i^2}{2} + \frac{1}{2}\sum_{i \neq j} \frac{1}{|\boldsymbol{r}_i - \boldsymbol{r}_j|} + \mathrm{V}_{ext}(\boldsymbol{r}_i)\right]\Psi_n = E_n \Psi_n \qquad \textbf{Equation B.1.3}$$

is analytically insoluble and requires further strategies able to retain the physics of the problem while making it computationally solvable.

The success of DFT stands on replacing this many-electron equation for the wave function $\Psi_n(\boldsymbol{r}_1, \dots, \boldsymbol{r}_N)$, characterized by 3N variables, with a one-electron problem based on the electron density $\rho_n(\boldsymbol{r})$, defined in the $\mathbb{R}^3$ space. Thus, the many-electron problem can be solved without introducing empirically adjusted parameters. Only atomic positions and physical constants are used as input for the calculation, which is why DFT and similar methods are generally called *ab initio* or by first principles.

The strength of *ab initio* approaches is two-fold: first, it has a strong prediction power, as it allows computing properties of a system without (or before) measuring it; secondly, it relieves the need for searching proper empirical parameters to describe the system, which effectively simplifies the computational work.

In this thesis, the advantage of moving from semi-empirical towards *ab initio* calculations in the sense of the second argument given above will be expressed in **Chapter 5**, related to CMT calculations. Nevertheless, *ab initio* methods accuracy relies on the approximation chosen to describe the system. In the case of 3d transition metal oxides, this translates into the choice of how electronic correlations are treated, which is a critical point for DFT calculations. An extended description of the DFT method for materials science is found in ref. [360].

B.2. Basic principles

The core idea of DFT is to express the energy of the system not as a functional of the wave function using the typical expression for an observable in quantum mechanics, i.e.

$$E_n = \langle \Psi_n(\boldsymbol{r}_1, \dots, \boldsymbol{r}_N) | H | \Psi_n(\boldsymbol{r}_1, \dots, \boldsymbol{r}_N) \rangle \qquad \textbf{Equation B.2.1}$$

but as a functional of the electron density only, independent of the external potential:

$$E[\rho(\boldsymbol{r})] = F[\rho(\boldsymbol{r})] + \int \mathrm{V}_{ext}(\boldsymbol{r})\, \rho(\boldsymbol{r})\, d\boldsymbol{r} \qquad \textbf{Equation B.2.2}$$

This is known as the first Hohenberg-Kohn theorem, which states that there exists a biunivocal correspondence between the energy of an N-electron system and the external potential acting on it [361]. The second theorem affirms that the ground state energy E_0 is found by minimization of E to the electron density, in agreement with the variational principle:

$$E_0 = \min_{[\rho(\boldsymbol{r})]} E[\rho(\boldsymbol{r})] \qquad \textbf{Equation B.2.3}$$

Therefore, the framework defined by Hohenberg and Kohn allows obtaining information on the ground state properties from the electron density, reducing the problem to its determination. It must be emphasized that this is valid for the ground state only: because of the importance of final excited states in the photoemission process, the physics underlying the photoemission spectra can be fully captured only by moving beyond the DFT method.

The Hohenberg-Kohn theorems are exploited by the Kohn-Sham equations, which refer to an effective non-interacting electron system that replaces the interacting one. In fact, the Kohn-Sham equations are a set of single-electron Schrödinger equations where the effective Kohn-Sham potential V_{KS} is defined by construction such that the ground state electron density is equal to that of the many-electron system [362]:

$$\left[-\frac{\boldsymbol{\nabla}_i^2}{2}+\mathrm{V}_{KS}[\rho(\boldsymbol{r})](\boldsymbol{r})\right]\psi_{n,k}=\varepsilon_{n,k}\psi_{n,k}$$ **Equation B.2.4**

where $\varepsilon_{n,k}$ and $\psi_{n,k}$ are the Kohn-Sham eigenvalues and eigenfunctions.

Solving this system of single-electron equations yield an electron density

$$\rho(\boldsymbol{r})=\sum_{n,k}^{N}\left|\psi_{n,k}\right|^2$$ **Equation B.2.5**

formally equivalent to that of the target many-electron, that can be reinjected in **Equation B.2.4** to solve again the Kohn-Sham equations until the lowest energy, i.e. the ground state according to the variational principle, is found by convergence.

The Kohn-Sham approach would be exact if $\mathrm{V}_{KS}[\rho]$ was known; this is typically not true as the electron-electron interactions are only approximated in the single-electron picture by the so-called exchange correlation potential, which enters in the Kohn-Sham potential as follows:

$$\mathrm{V}_{KS}(\boldsymbol{r})=\mathrm{V}_{ext}(\boldsymbol{r})+\mathrm{V}_{Hartree}(\boldsymbol{r})+\mathrm{V}_{xc}(\boldsymbol{r})$$ **Equation B.2.6**

where:

- $\mathrm{V}_{ext}(\boldsymbol{r})$ is the electron-nuclei interaction (**Equation B.1.2**),
- $\mathrm{V}_{Hartree}(\boldsymbol{r})=\int\frac{\rho(\boldsymbol{r'})}{|\boldsymbol{r}-\boldsymbol{r'}|}d\boldsymbol{r'}$ is the Hartree potential describing the Coulomb interaction between an electron and the mean field created by the remaining electron cloud,
- V_{xc} is the exchange-correlation potential defined as:

$$\mathrm{V}_{xc}(\boldsymbol{r})=\frac{\delta E_{xc}[\rho(\boldsymbol{r})]}{\delta\rho(\boldsymbol{r})}$$ **Equation B.2.7**

where E_{xc} is the exchange-correlation functional accounting for all what remains to obtain the total energy of the system (**Equation B.2.2**):

$$E_{xc}[\rho(\boldsymbol{r})] = E[\rho(\boldsymbol{r})] - T[\rho(\boldsymbol{r})] - \int \mathrm{V}_{ext}(\boldsymbol{r})\, \rho(\boldsymbol{r}) d\boldsymbol{r} - \int \mathrm{V}_{Hartree}(\boldsymbol{r})\, \rho(\boldsymbol{r}) d\boldsymbol{r}$$ **Equation B.2.8**

with $T[\rho(\boldsymbol{r})]$ the electron kinetic energy.

The accuracy of a DFT calculation relies on the choice of the approximation for the exchange-correlation functional E_{xc}, for which there exist no exact formulation. Many functionals have been proposed and employed in the literature with either a general purpose or a specific target of systems or properties in mind.

Among the most popular functionals are the so-called semilocal approximations, which describe the local exchange and correlation interactions by means of the known expression for the homogeneous electron gas ε_{xc} (the "jellium" system) expressed as a function of the density (local density approximation, LDA), its derivative (Generalized Gradient Approximation, GGA), and so on. In the simplest case of LDA, the functional reads:

$$E_{xc}^{LDA}[\rho(\boldsymbol{r})] = \int \rho(\boldsymbol{r})\, \varepsilon_{xc}(\rho(\boldsymbol{r})) d\boldsymbol{r}$$ **Equation B.2.9**

Semilocal approximations are often successful in describing the fundamental properties of materials. However, they fail when the local interactions significantly deviate from those of the dummy jellium system. Such is typically the case of strongly correlated systems such as 3d transition metal oxides, in which LDA and GGA tend to underestimate the local interactions. For these materials, other approximations are typically employed to improve the description of 3d correlations, such as on-site methods. However, as discussed in **Section 2.2.1.1**, the DFT calculations performed in this thesis employed the GGA exchange-correlation functional in the form given by Perdew-Burke-Ernzerhof (PBE). Then, the electronic correlations are considered within the subsequent cluster model calculations.

B.3. Linearized augmented-plane-wave method

There exist various computational methods for solving the Kohn-Sham equations within the chosen approximation for exchange-correlation interactions. In fact, each DFT code implements a specific basis set ϕ_i for describing the Kohn-Sham wave functions in a numerically solvable way:

$$\Psi_{n,k} = \sum_i c_{n,k}^i \phi_i$$ **Equation B.3.1**

One of the most accurate codes is Wien2k, used throughout this thesis, which is based on the linearized augmented plane wave (LAPW) method [242]. In this approach, the unit cell is decomposed into atomic “muffin-tin” spheres with radii R_{MT} separated by an interstitial space (**Figure B.3.1**). Based on this distinction, the LAPWs are defined as radial functions times spherical harmonics within the spheres S_t and plane waves in the interstitial space I:

$$\phi_{\boldsymbol{k}+\boldsymbol{K}}^{LAPW} = \begin{cases} \sum_{l,m} \left[A_{t,l,m}^{\boldsymbol{k}+\boldsymbol{K}} u_{t,l}(r, E_{t,l}) + B_{t,l,m}^{\boldsymbol{k}+\boldsymbol{K}} \dot{u}_{t,l}(r, E_{t,l})\right] Y_{l,m}(\boldsymbol{r}), & \boldsymbol{r} \in S_t \\ \frac{1}{\sqrt{\Omega}} e^{i(\boldsymbol{k}+\boldsymbol{K})\cdot \boldsymbol{r}}, & \boldsymbol{r} \in I \end{cases} \qquad \text{Equation B.3.2}$$

where:

- l and m are the atomic angular and magnetic indexes for the target orbital),
- $\boldsymbol{k}$ and $\boldsymbol{K}$ are the wave vector inside the first Brillouin zone and the reciprocal lattice vector, respectively,
- $u_{t,l}$ is the solution of the radial Kohn-Sham equation for the energy $E_{t,l}$, taken as the center of the band with l-like character,
- $A_{t,l,m}^{\boldsymbol{k}+\boldsymbol{K}}$ and $B_{t,l,m}^{\boldsymbol{k}+\boldsymbol{K}}$ are coefficients chosen such that $\phi_{\boldsymbol{k}+\boldsymbol{K}}^{LAPW}$ is continue and differentiable at the sphere boundary,
- Ω is the unit cell volume

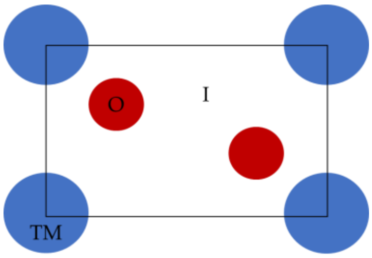

Figure B.3.1 Schematic unit cell for a general transition metal oxide as studied within the LAPW scheme. The blue and red sphere represent transition metal and oxygen muffin-tin spheres while the in-between space is the interstitial region *I*.

The as-defined LAPW constitute the basis set for calculating the Kohn-Sham wavefunctions as expressed in **Equation B.3.1**, where the coefficients $c_{n,k}^{i}$ are determined by the variational principle. The accuracy of this expansion depends on the size of LAPW basis, determined by the cut-off value $|\boldsymbol{k} + \boldsymbol{K}| \leq K_{max}$ and dependent on the type and size of the smallest atom whose radius is R_{MT}^{min} [242]. In practice the two parameters are controlled by setting their product $R_{MT}^{min} K_{max}$ ranging from 3 for hydrogen atoms to 9 for 4f lanthanides. In this thesis, the smallest radii was either due to lithium or, if absent to oxygen, both sp-elements for which $R_{MT}^{min} K_{max} = 7$ is considered a good convergence parameter and was therefore typically employed in all calculations [242].

The Wien2k code is an all-electron method, in the sense that all electrons starting from the 1s core orbitals are included in the calculation. The wave function of core states is defined to be completely confined inside the atomic spheres (i.e. only the top line of **Equation B.2.1**). This definition does not correspond to the formally assumed distinction between core and valence states because the wave function of shallow core levels can leak out the sphere. These states are defined as "semi-core" states and treated as the valence ones in the calculation.

In the LAPW scheme, each self-consistent cycle iterates the calculation of $\psi_{n,k}$ and $\rho(\boldsymbol{r})$ starting from an initial guess, given by a superposition of atomic electron densities in the unit cell, and mixing the (core plus valence) calculated electron density with the one of the previous cycle until the desired convergence criteria are obtained. Beyond the energy convergence, the position-dependent charges and forces can be used. Unless otherwise specified, energy and convergence criteria of 0.0001 Ry/cell and 0.001 electrons/cell have been employed, respectively.

B.4. Electronic structure properties

Once a converged electronic structure is obtained, its electron density can be used to compute properties of the system. In Wien2k, this operation consists of following a workflow of various steps, including the preparation of input files, execution of dedicated programs, and visualization of the results. Among the vast possibility of properties that can be computed by DFT, in this thesis we focused on three main aspects, discussed below.

B.4.1. Density of states

The DFT density of states (DOS) can be seen as a single-electron approximation of the experimental valence band measured by XPS. In Wien2k, the DOS is calculated from the Kohn-Sham eigenvalues evaluated on a k-grid in the irreducible Brillouin Zone using the tetrahedron method. Beyond the total DOS, partial DOS (PDOS) can be evaluated by decomposing the (normalized) total charge into interstitial I and atomic sphere t contributions, including the distinction from different l orbitals:

$$1 = \sum_{t,l} q_{t,l} + q_I$$

Equation B.4.1

Accessing the PDOS information allows to discriminate the contribution of the different valence states to the experimental valence band. Nevertheless, beyond the missing many-electron final state effects, describing the experimental valence band by means of DOS does not take into account the renormalization of each PDOS by means of the photoionization cross-section. However, this can be readily done now in Wien2k within the *pes* module, described in ref. [363].

By integrating the PDOS in the positive binding energy scale, the partial electron charge for each set of t, l Kohn-Sham states ($Q_{t,l}$) is obtained. This allows inquiring about the redox compensation mechanism and ligand-metal charge transfer at the DFT level of theory. However, this is not directly related to the concept of oxidation state of atoms in a solid [91–94]. Moreover, the interstitial charge cannot be decomposed further by construction of the LAPW scheme. To alleviate this problem, the PDOS can be renormalized so that their sum yields the total DOS, neglecting the interstitial contribution. Still, the electron charge inside an atomic sphere and related PDOS obtained by LAPW calculations depend on the choice of the input R_{MT} radii. One on hand, this imposes to fix these parameters to allow direct comparison within a series of calculations. On the other, a parameter-free alternative was also considered, as described below.

B.4.2. Bader charges

In his "Atoms in Molecule" (AIM) theory, R. W. F. Bader proposed a topological analysis of the electron density to distinguish single atomic volumes in a collection of atoms [364]. This is essentially constructed by imposing a zero-flux boundary and can be extended from limited molecular systems to crystal structures. Therefore, the AIM theory allows to uniquely assign charges to each atom in the unit cell, which are the Bader charges $Q_{t,l}^{Bader}$. Inspection of both $Q_{t,l}^{Bader}$ and $Q_{t,l}$ should highlight a similar qualitative trend but different amount of charge transfer, which can give information on charge localization.

B.4.3. Binding energy calculations with the Janak-Slater method

Within DFT, the Kohn-Sham eigenvalue approximates the binding energy within the frozen orbital approximation [240]:

$$E_B \approx -\varepsilon_c^{KS} \qquad \textbf{Equation B.4.2}$$

with ε_c^{KS} is $\varepsilon_{n,k}$ for a core level c in **Equation B.2.4**. Such approximation neglects any screening of the core hole, and indeed is typically off by several tens of eV to the experimental value. A better approximation relies on the Janak's theorem, which states that the Kohn-Sham core eigenvalues represent the variation of DFT total energy E to the occupation of the core level n_c itself [365]:

$$\varepsilon_c^{KS} = \frac{\partial E}{\partial n_c}$$

Equation B.4.3

Combining this relation (independent on the choice of exchange-correlation functional) with the fundamental definition of binding energy (**Equation A.2.6**) gives:

$$E_B = E_f[N-1] - E_i[N] = \int_0^1 \varepsilon_c^{DFT}(n_c)dn_c$$

Equation B.4.4

The calculation is subsequently done by approximating the integral, whose exact calculation would require calculating the electronic structure hence the core level eigenvalue for infinitely small variations of core-hole occupation increasing from 0 (ground state) to 1 (full core hole). Two approximations exist for this calculation. The so-called ΔSCF method consists of computing both the ground state and the full core hole excited state, and subsequently taking the difference between the two eigenvalues. However, the latter calculation can become computationally expensive, and since a compensating opposite charge must be injected in the unit cell to maintain charge neutrality, artificial effects can occur more easily with a larger perturbation. A softer approach relies on the Slater transition state approximation and is therefore called Janak-Slater method [366,367]. In this case, the integral is approximated by its midpoint by applying the mean value theorem:

$$E_B = \int_0^1 \varepsilon_c^{DFT}(n_c)dn_c \approx \varepsilon_c^{DFT}\left(\frac{1}{2}\right)$$

Equation B.4.5

which implies that the binding energy can be calculated from a single DFT calculation in which half a core electron is removed. This approach is therefore less stressful for the electronic structure. The compensating charge is either added to an unoccupied low energy level (more frequently done for XAS simulations as reflecting the absorption process) or by a homogeneous charge, as performed in this thesis. From a practical point of view, the periodical boundary conditions within LAPW calculations imply that the creation of the core hole in the unit cell [13] is replicated in the whole crystal. To avoid spurious hole-hole interactions, the calculation must be performed on a sufficiently large supercell.

---

[13] Note : in Wien2k, this is done by manually changing the occupation of a core level in the case.in1c file and compensating the hole by adding a negative charge in the case.inm files. For more practical details, the reader is referred to ref. [230].

C. Maximally localized Wannier functions

C.1. Wannierization

The Kohn-Sham wave functions resulting from a converged DFT calculation for a bulk solid respect the Bloch's theorem, which affirms that any solution of a Hamiltonian including a periodic potential can be expressed as a plane wave modulated by a periodic function:

$$\psi_{n,\boldsymbol{k}}(\boldsymbol{r}) = e^{i\boldsymbol{k}\cdot\boldsymbol{r}} u_{n,\boldsymbol{k}}(\boldsymbol{r}), \quad u_{n,\boldsymbol{k}}(\boldsymbol{r}) = u_{n,\boldsymbol{k}}(\boldsymbol{r}+\boldsymbol{R}) \qquad \textbf{Equation C.1.1}$$

with $\boldsymbol{R}$ a vector in the Bravais lattice and n the band index.

Wannier functions $\{w_{m,\boldsymbol{R}}(\boldsymbol{r})\}$ represent an alternative basis set to the Bloch one $\{\psi_{n,\boldsymbol{k}}(\boldsymbol{r})\}$ that is often preferred in solid-state physics and chemistry as it can give a more straightforward picture of the chemical bonding in materials and can improve significantly the computational efficiency. Although Wannier functions are not eigenfunctions for the Kohn-Sham Hamiltonian, they can be formally obtained by their Fourier transform through a unitary transformation:

$$w_{m,\boldsymbol{R}}(\boldsymbol{r}) = \frac{V}{8\pi^3} \int_{BZ} \left(\sum_{n,m} U^{(\boldsymbol{k})}{}_{n,m} \psi_{n,\boldsymbol{k}}(\boldsymbol{r}) \right) e^{-i\,\boldsymbol{k}\cdot\boldsymbol{R}} d\boldsymbol{k} \qquad \textbf{Equation C.1.2}$$

Since the relation between Bloch and Wannier functions is given by a unitary transformation, both give a valid description for the DFT bands. However, the advantage of working with Wannier functions is that they are localized in space with a strong atomic- and orbital-like character.

In practice, the choice of the unitary transform matrix $U^{(\boldsymbol{k})}{}_{n,m}$ is non-unique, which led to different wannierization criteria in the literature. Among them, the maximally localized Wannier functions (MLWF) as obtained by the Wannier90 code constitute one of the most successful ones and was chosen for this study [368,369] since it was well interfaced with other codes. The criteria for obtaining MLWF is via minimization of the quadratic spread functional:

$$\Omega = \sum_{m} \langle w_{m,\boldsymbol{R}} | \boldsymbol{r}^2 | w_{m,\boldsymbol{R}} \rangle - \langle w_{m,\boldsymbol{R}} | \boldsymbol{r} | w_{m,\boldsymbol{R}} \rangle^2 \qquad \textbf{Equation C.1.3}$$

In this thesis, wannier90 was simply used as a toolbox to create MLWFs, limiting to the standard protocol defined in available sources. Therefore we do not give here the computational details on this operation that can be found in refs. [368,369] but limit to the physically relevant aspects. Essentially, the wannierization procedure requires to define a set of Kohn-Sham bands within a selected energy window W in which the MLWFs are obtained by projection onto the bands starting from a trial set of functions. Typically, W contains the bands with stronger correlation effects and is therefore called correlated subspace, where the low-energy model for studying the correlation effects is constructed.

C.2. Computational details

In practice, the linking between the LAPWs functions obtained by *Wien2k* and the MLWFs was carried out using the dedicated *wien2wannier* package, which prepares all necessary input files starting from a converged DFT electronic structure [370]. The correlated subspace included all transition metal 3d and oxygen 2p bands, constituting the so-called *dp*-model. Thus, each MLWF is expected to have a distinguishable atomic- and orbital-like character and to be centered to the appropriate atomic site. Moreover, the *dp* band manifold was always separated from lower energy occupied states (e.g. O 2s) or higher energy bands (e.g. metal 4sp): no disentanglement procedures were therefore necessary. While computationally straightforward and typically successful, the wannierization procedure had to be manually corrected to account for the local symmetry in 3d lithium transition metal oxides. Indeed, while the global cell was typically hexagonal (see **Chapter 1**), re-symmetrized MLWFs in the local (distorted) octahedral symmetry of the TMO_6 were required to perform the cluster model calculations. For that, a manual orientation was given as input for the wannierization algorithm. This technical aspect will be discussed in more detail in **Section E.4.1**.

C.2.1. Tight binding Hamiltonian from MLWF

Because of their localized character, Wannier functions are the natural choice as basis set of tight-binding model Hamiltonians. In fact, the matrix elements of the tight binding Hamiltonian using a MLWF basis set are simply evaluated as overlaps between each other:

$$H_{m,n}(\boldsymbol{R}) = \langle w_{m,\boldsymbol{0}} | H | w_{n,\boldsymbol{R}} \rangle \qquad \textbf{Equation C.2.1}$$

which typically gives non-negligible values only for local interactions.

Because of their link with the original Kohn-Sham functions, any observable based on the MLWFs can be Fourier retransformed to give the same observable in the reciprocal space. This can be applied to the tight binding Hamiltonian to obtain the band structure in a procedure called band interpolation, as it allows to significantly increase the number of k-points (hence the resolution of the band plot) due to the limited size of the basis set.

$$H_{m,n}(\boldsymbol{k}') = \sum_{\boldsymbol{R}} e^{-i\boldsymbol{k}'\boldsymbol{R}} H_{m,n}(\boldsymbol{R}) \qquad \textbf{Equation C.2.2}$$

Comparing the interpolated band structure with the original one obtained by DFT allows to visually confirm the successful wannierization. Moreover, it delivers an *ab initio* tight binding model, which constituted the first building block of the cluster model Hamiltonian for photoemission simulations, as described in **Section E.2**.

D.Constrained Random phase approximation

D.1. General theory

A main topic in the physics of strongly correlated materials concerns the determination of electron-electron interactions in materials, typically identified in the Hubbard U parameter. In solids, the Coulombic interaction between two electrons is shielded by the remaining electron density. The multi-electron character of these interactions makes its access non-banal leading to the frequent tendency to treat the Hubbard U as a semi-empirical parameter. However, nowadays there are schemes to obtain this information by first principles: this is the case of the constrained random phase approximation method. As for the section above, we will not discuss the technical details of the method but only the essential physics and practical aspects in the context of this study. Further details can be found in ref. [371,372].

The first step of the cRPA method is to separate the electronic structure into two regions, in total analogy with the strongly correlated subspace definition defined concerning wannierization (see **Figure D.1.1**). The idea underlying the cRPA method is that single-electron calculation methods (e.g. DFT) can describe all interactions but those internal to the strongly correlated subspace, for which multi-electron models are necessary. This conceptual separation is formalized in the polarization calculation, divided as follows:

$$P = P_d + P_r \qquad \textbf{Equation D.1.1}$$

where P_d is related to the contribution from the correlated subspace and P_r is all the remaining polarization. Since the polarization depends on the electronic screening due to inter-band transitions, P_r can be visualized as shown in **Figure D.1.1**: it contains all transitions but those within the strongly correlated subspace. The cRPA method allows to calculate the polarization from the Kohn-Sham eigenvalues and eigenfunctions $\{\varepsilon_{n,k}, \psi_{n,k}\}$ [371]:

$$\begin{aligned} &P(\boldsymbol{r}, \boldsymbol{r}', \omega) \\ &= \sum_{n,k}^{occ} \sum_{n',k'}^{unocc} \left\{ \frac{\psi^*_{n,k}(\boldsymbol{r}) \psi_{n',k'}(\boldsymbol{r}) \psi^*_{n',k'}(\boldsymbol{r}') \psi_{n,k}(\boldsymbol{r}')}{\omega - \varepsilon_{n',k'} + \varepsilon_{n,k} + i\delta} \right. \\ &\left. - \frac{\psi_{n,k}(\mathbf{r}) \psi^*_{n',k'}(\mathbf{r}) \psi_{n',k'}(\boldsymbol{r}') \psi^*_{n,k}(\boldsymbol{r}')}{\omega + \varepsilon_{n',k'} - \varepsilon_{n,k} - i\delta} \right\} \end{aligned} \qquad \textbf{Equation D.1.2}$$

The same formula can be applied to obtain P_d and P_r restricting the set of $\{\varepsilon_{n,k}, \psi_{n,k}\}$ as schematized in **Figure D.1.1**. Finally, the shielded interaction is calculated from the bare (non-frequency-dependent) interaction normalized by the dielectric function, given by:

$$U = \frac{v}{\varepsilon} = \frac{v}{1 - vP_r} \qquad \textbf{Equation D.1.3}$$

Therefore, one can see U as the bare Coulomb interaction within the correlated low-energy subspace, which in turn depends on the total polarization due to the whole electronic structure of the material i.e. it is partially screened by channels out of such subspace. Moreover, since the polarization is frequency dependent, U also depends on the frequency ω. This allows to explore the frequency-dependent screening processes such as plasmonic excitations.

The $U(\omega)$ matrix is then evaluated within the set of localized Wannier orbitals w_m (m indicating position and angular moment) leading to the $U_{ijkl}(\omega)$ matrix elements:

$$U_{ijkl}(\omega) = \langle w_i w_j | U(\omega) | w_k w_l \rangle \qquad \textbf{Equation D.1.4}$$

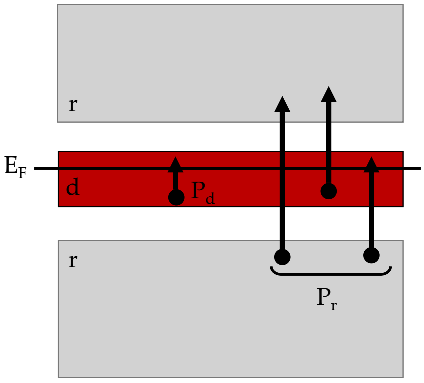

Figure D.1.1 Schematic picture of the repartition of the band structure within the cRPA scheme.

In the case of a 3d shell, the matrix U_{ijkl} contains 5^4 = 625 elements for each frequency. However, in practice the matrix is typically reduced to retain only the essential interactions, since many matrix elements of the full four-index matrix are negligible. The two-indexes reduced interaction matrices are defined as follows:

$$U_{m,m'}^{\sigma,\sigma'} = \langle w_m w_{m'} | U | w_m w_{m'} \rangle$$ **Equation D.1.5**

$$J_{m,m'} = \langle w_m w_{m'} | U | w_{m'} w_m \rangle$$ **Equation D.1.6**

$$U_{m,m'}^{\sigma,\sigma} = U_{m,m'}^{\sigma,\sigma'} - J_{m,m'}$$ **Equation D.1.7**

An even more drastic but often effective approximation is the Slater parametrization. The Slater parameters represent the radial component in the expansion of the Coulomb interaction into harmonic spheres, which in the case of a 3d shell is given by the monopole (F^0), dipole (F^2), and quadrupole (F^4) terms. The Slater parametrization is obtained from the following relations [372,373]:

$$U = \frac{1}{25} \sum_{m,m'} U_{m,m'}^{\sigma,\sigma'} = F^0$$ **Equation D.1.8**

$$J = \frac{1}{25} \sum_{m,m'} J_{m,m'} = \frac{F^2 + F^4}{14}$$ **Equation D.1.9**

where $F^4/F^2 = 0.63$ as an approximation corresponding to the atomic limit [373].

D.2. Computational details

The MLWFs obtained by Wannier90 for the DFT converged electronic structures based on the *dp*-model were used to compute the screened coulomb interactions using the *gap2c* code based on constrained random phase approximation (cRPA) theory [374]. A 5x5x5 kmesh and upper-cut-off energy of 15 Ry were found sufficient to obtained converged static U and J values within less than 0.01 eV. Two models were considered by excluding both metal 3d and O 2p states or only the metal 3d states in the correlated subspace, referred to as *dp-dp* and *d-dp* models in the main manuscript, respectively.

E. Cluster model theory

E.1. Introduction

Herein, the theoretical framework for the simulation of XPS spectra based on the charge transfer multiplet theory or cluster model theory (CMT) is presented. We follow the formalism by Haverkort et al., adapted to our setup, which is based on the Quanty script language that was employed for the calculations [375]. A more general description of the theory including applications for studying XAS and XPS spectra is found in ref [218].

E.2. Initial and final state Hamiltonians

In the following, we will refer to the specific case of layered lithium transition metal oxides as subject of this thesis. The single cluster model calculations are carried out on transition metal-centered TMO_6 octahedral clusters (TM = Mn, Co, Ni). For the ground state calculations, only the low-energy TM 3d and O 2p states were considered, with 46 fermionic states. The model Hamiltonian for the cluster includes the onsite and hopping energies i.e. one-electron interactions $H^{(1)}$ as well as the spin-orbit H_d^{SO} and Coulomb interactions H_{dd}^{ee} for the central TM 3d states.

$$H^{cluster} = H^{(1)} + H_{dd}^{ee} + H_d^{SO} - H_{dc}^{AMF} \qquad \textbf{Equation E.2.1}$$

Technically, an additional term H_{dc}^{AMF} is taken into account to correct for the correlations already taken into account at the DFT level with the exchange-correlation functional. This procedure, described below, is referred to as double counting correction and is typical for post-DFT many-body methods [376].

In second quantization formalism, the single electron Hamiltonian $H^{(1)}$ of the cluster is:

$$H^{(1)} = \sum_{i} \varepsilon_i d_i^\dagger d_i + \sum_{i \neq j} t_{ij} d_i^\dagger d_j + \sum_{i} \varepsilon_i p_i^\dagger p_i + \sum_{i \neq j} t_{ij} p_i^\dagger p_j + \sum_{i,j} t_{ij} \left(d_i^\dagger p_j + h.c. \right) \qquad \textbf{Equation E.2.2}$$

with ε, t being the on-site and hopping energies, respectively, $d^\dagger$ and d ($p^\dagger$ and p) the creation and annihilation operators for the Co 3d shell (O 2p shell), and i, j spin-orbital indices.

To treat correlations more conveniently, the Coulomb interactions are expanded in spherical harmonics to separate radial and spherical parts. With a basis set of spherical symmetry, the Coulomb interactions are rewritten as sum of direct and exchange terms consisting of analytically solvable spherical harmonics times Slater integrals. For the latter, no analytical solution exists so the common procedure is to describe each by a single parameter, which can be obtained by different strategies as described below. The number of direct F^k and exchange G^k terms depend on the angular momenta of the interacting shell or shells. In case of 3d-3d interactions, only direct Slater integrals are present:

$$H_{dd}^{ee} = \sum_{k=0,2,4} F_{dd}^k H^{F^k} \qquad \textbf{Equation E.2.3}$$

with F^k being the Slater integrals and H^{F^k} the spherical harmonic of the k-th order pole.

The spin-orbit coupling is formally defined as:

$$H_{SO}^d = \xi_{3d} \sum_i l_i \cdot s_i \qquad \textbf{Equation E.2.4}$$

where ξ_{3d} is an atom- and orbital-dependent constant. For 3d valence shell, it is generally very small and it does not play a major role, but for deeper core levels it becomes relevant reflecting the discussion given in **Section A.4.2.1**.

On top of the as-defined Hamiltonian $H^{cluster}$, a configuration-interaction model is taken into account to introduce the ligand-to-metal charge transfer Δ that corrects the onsite energies of the 3d and 2p orbitals. The model is built following the usual definition of charge transfer energy $\Delta = E(|3d^{n+1}L^{-1}\rangle) - E(|3d^n\rangle)$ and including the electronic correlations acting on each configuration modeled by the Hubbard U_{dd} parameter:

$$U_{dd} = F_{dd}^0 - \frac{2}{63}\left(F_{dd}^2 + F_{dd}^4\right) \qquad \textbf{Equation E.2.5}$$

In practice, the problem reduces to solve the following system of equations (note that since there are only two unknowns, the first two configurations are actually necessary).

$$\begin{cases} N_L\varepsilon_L + N_d\varepsilon_d + \dfrac{N_d(N_d-1)U_{dd}}{2} = 0 \\ (N_L-1)\varepsilon_L + (N_d+1)\varepsilon_d + \dfrac{N_d(N_d+1)U_{dd}}{2} = \Delta \end{cases}$$

Equation E.2.6

which gives the following solutions where $N_L = 36$ for the TMO_6 cluster:

$$\varepsilon_d = \frac{36\,\Delta - \mathrm{n}\,(N_d + 71)\,\frac{U_{dd}}{2}}{N_d + 36}$$

Equation E.2.7

$$\varepsilon_L = N_d \cdot \frac{(N_d+1)\,\frac{U_{dd}}{2} - \Delta}{N_d + 36}$$

Equation E.2.8

The solution of the as defined Hamiltonian $H^{cluster}\Psi_n = \mathrm{E}_n\Psi_n$ is thus found by exact diagonalization, leading to the ground state many-body wave function Ψ_0. From this calculation, the properties of the ground state can be obtained by computing observables as $O = \langle\Psi_n|\hat{O}|\Psi_n\rangle$, with $\hat{O}$ being the operator related to the target property. For example, this allows computing the weight or partial occupation of the $|d^{N_d+i}\rangle$ configuration in the ground state or the average occupation of the 3d orbitals, which are relevant information for understanding the redox mechanism upon delithiation.

In case of core-level photoemission spectroscopy, a core electron is missing in the final state. Therefore, the cluster model is augmented with the related core-level shell; we take the example of the TM 2p core levels as the most studied in this thesis. This results in $42 + N_d$ fermionic states. Accordingly, the final-state model Hamiltonian $H_f^{cluster}$includes all interactions present in the initial state plus those relevant for the implemented core-shell. These include the spin-orbit $H_{SO}^{TM_{2p}}$ and the core-valence Coulomb interactions H_{pd}^{ee}, which leads to the multiplet splitting described in Section A.4.2.3.

$$H_f^{cluster} = H^{cluster} + H_{SO}^{TM_{2p}} + H_{pd}^{ee}$$

Equation E.2.9

In analogy with the above formalism, we have

$$H_{SO}^{TM_{2p}} = \xi_{TM_{2p}} \sum_i l_i \cdot s_i$$

Equation E.2.10

and

$$H_{pd}^{ee} = F_{pd}^0 H^{F^0} + F_{pd}^2 H^{F^2} + G_{pd}^1 H^{G^1} + G_{pd}^3 H^{G^3}$$

Equation E.2.11

where the expansion of H_{pd}^{ee} for the p-d inter-shell interactions leads to both direct and exchange terms.

Again, the onsite energies were set to the configuration interaction model, this time including the core-valence Coulomb interaction $U_{pd} = F_{pd}^{0} - \frac{1}{15} G_{pd}^{1} - \frac{3}{70} G_{pd}^{3}$, giving:

$$\begin{cases} N_c\varepsilon_c + N_L\varepsilon_L + N_d\varepsilon_d + \dfrac{N_d(N_d-1)U_{dd}}{2} + N_cN_dU_{pd} = 0 \\ N_c\varepsilon_c + (N_L-1)\varepsilon_L + (N_d+1)\varepsilon_d + \dfrac{N_d(N_d+1)U_{dd}}{2} + N_c(N_d+1)U_{pd} = \Delta \\ (N_c-1)\varepsilon_c + N_L\varepsilon_L + N_d\varepsilon_d + \dfrac{N_d(N_d-1)U_{dd}}{2} + (N_c-1)N_dU_{pd} = 0 \end{cases}$$

Equation E.2.12

Leading to:

$$\varepsilon_c = -\,nU_{pd}$$ **Equation E.2.13**

$$\varepsilon_d = \frac{36\,\Delta - \mathrm{n}\,(n+71)\,\frac{U_{dd}}{2} - 216U_{pd}}{n+36}$$ **Equation E.2.14**

$$\varepsilon_L = \varepsilon_d + nU_{dd} + 6U_{pd} - \Delta$$ **Equation E.2.15**

with N_L = 36 and N_c = 6 for the TM 2p core level. While the same approach used for the initial-state Hamiltonian could be performed, in practice the final state Hamiltonian was directly employed to simulate the XPS spectra as described in the following section.

E.3. Spectra simulations within Green's function formalism

By solving both initial and final states Hamiltonians, one could calculate the spectral function as expressed in **Equation A.4.6**, based on the Fermi Golden Rule. However, this requires including all final states in the calculation, which is not computationally practical. Instead, the most common method is based on the analysis of the correlation function or Green's function[14]. In this thesis, the Green's function was employed as a

---

[14] In solid state physics, the term Green's function is commonly used for any correlation function, although the formal definition of Green's function as a mathematical tool to solve inhomogeneous

computational tool to simulate the XPS spectra. However, we give the essential physics behind it in the context of a photoemission process [377] and proceed with the practical case following the above definitions for the TMO_6 cluster model system. A detailed description of the formalism is found in ref. [60,378].

In general, the Green's function describes the probability that a certain excitation acting into a system persists after a certain time passed from its beginning. In the case of a photoemission process, this means inspecting the correlation between the system at the moment of the photoexcitation t = 0 and its evolution after a time t > 0. Considering an N-electron system, the electron removal at t = 0 acts on its ground state wave function $|\Psi_0\rangle$ as:

$$|\Psi(t=0)\rangle = c_k|\Psi_0\rangle \qquad \textbf{Equation E.3.1}$$

with c_k the annihilation operator for the k-th electron. After a certain time, the system evolves as:

$$|\Psi(t)\rangle = \mathrm{e}^{-\mathrm{i}\mathrm{H}t} c_k|\Psi_0\rangle \qquad \textbf{Equation E.3.2}$$

While if the photoemission happened at the same time t > 0 the time evolution of the system would have been instead:

$$|\Psi_h\rangle = c_k \mathrm{e}^{-\mathrm{i}\mathrm{H}t}|\Psi_0\rangle \qquad \textbf{Equation E.3.3}$$

The Green's function describes the correlation at time t between the system evolving after the photoemission process $|\Psi(t)\rangle$ and the same system at the fundamental state $|\Psi_0\rangle$ without interacting with the core hole $|\Psi_h\rangle$:

$$i\,G(k,t) \equiv \langle\Psi_h|\Psi(t)\rangle = \langle\Psi_0\big|\mathrm{e}^{\mathrm{i}\mathrm{H}t}c_k^\dagger\big|\mathrm{e}^{-\mathrm{i}\mathrm{H}t}c_k\big|\Psi_0\rangle \qquad \textbf{Equation E.3.4}$$

In the non-interacting case, the Green's function becomes a simple phase function whose Fourier transform leads to a Dirac delta function centered at the energy of the excitation. Otherwise, the interactions in the final states progressively lower the coherence between initial and excited state, so the correlation function decreases until complete loss of coherence is obtained; the lifetime of the excitation represents the characteristic time for this process.

---

differential equations coincides only with the case of the non-interacting two-particles correlation function.

To study the interactions that reacts to the excitation, the Green's function can be studied by spectral decomposition. By applying the Fourier transformation, the Green's function can be expressed in the energy domain as:

$$G(\omega) = \left\langle \Psi_0 \middle| T^{\dagger} \frac{1}{\omega - H - i\Gamma/2} T \middle| \Psi_0 \right\rangle \qquad \textbf{Equation E.3.5}$$

where T is the general transition operator acting on the initial system ($T = c_k$ in the example above) and Γ describes the broadening due to the excitation lifetime. Finally, applying the identity $(x + iy)^{-1} = P(1/x) + i\pi\delta(x)$ the spectral function as defined in **Equation A.4.6** is obtained as the imaginary part of the Green's function:

$$\begin{aligned} A(\omega) &= -\frac{1}{\pi} \operatorname{Im} G(\omega) \\ &= -\frac{1}{\pi} \operatorname{Im} \left\langle \Psi_0 \middle| T^{\dagger} \frac{1}{\omega - H - i\Gamma/2} T \middle| \Psi_0 \right\rangle \end{aligned} \qquad \textbf{Equation E.3.6}$$

with the advantage that only three ingredients are necessary for its calculation, namely the ground state wave function, the transition operator, and the final state Hamiltonian.

E.4. Practical aspects

The cluster model calculations were performed using the Quanty code [375,379], which implements the formalism of second quantization and Green's functions presented above in a Lua-based script language. The main advantages of this choice are the high versatility and overall good performance. Nonetheless, there was no interface between Quanty and the other computational tools used in this thesis, so this was developed throughout this work to improve the calculations.

Indeed, one objective of the study was to push forward the theoretical description by progressively reducing the number and impact of empirically adjusted parameters towards a complete *ab initio* method. In general, all terms constituting the cluster model Hamiltonian of **Equation E.2.1** are defined by sets of parameters describing the interactions. Below we summarize the main strategies carried out in this thesis for the choice of such parameters.

E.4.1. Tight binding

In ref. [219], a method to extract the one-particle term from Wannier tight binding Hamiltonian is presented. In Quanty, this can be obtained by built-in functions working for the FPLO DFT code but not for the Wien2k-Wannier90 routine. Based on the FPLO examples, a homemade python script was written to obtain all hopping and onsite terms written with respect to the TMO_6 cluster. The general workflow is described as follows.

In practice, the terms of the tight binding Hamiltonian $H^{(1)} = \sum_i t_i a_i^{\dagger} a_i$ are explicitly written in Quanty format based on Hamiltonian matrix elements (**Equation C.2.1**) stored in the case_hr.dat output file of Wannier90. To improve computational efficiency only the elements > 10^{-5} eV are actually considered.

A critical point is the definition of the proper translation vectors **R** to obtain the desired octahedral cluster, as the centers of the Wannier functions do not typically sit within the primary primitive cell but in some other position due to the convergence algorithm of Wannier90. Therefore, the proper R definitions were found by manually comparing the positions given in *case_centres.xyz* file with respect to the crystal structure.

A second important aspect regarded the local symmetry of the cluster, which generally did not match with the crystal symmetry as determined by the initialization step of Wien2k. This is due to the typical rhombohedral symmetry of $LiTMO_2$ where the TMO_6 octahedra are slightly distorted into a lower D3d symmetry. This was adjusted by applying an input rotation to the coordinate system for the projection of the MLWFs in Wien2wannier, which generally resulted in successful orientation of the TM 3d and O 2p MLWFs to the TM-O bonds in the TMO_6. Typically, the rotation left small but non-zero non-diagonal terms in the order of 0.01 eV. This approximation was necessary for three reasons: 1) to properly distinguish t_{2g} and e_g states, simplifying the interpretation 2) to reduce off-diagonal terms, improving the computational efficiency, and 3) to validate the on-site energy correction of the configuration interaction model, that otherwise would miss to correct an important part of the interactions.

Although successful for many relevant cases, this “manual” orientation before wannierization failed for all systems significantly deviating from the octahedral symmetry, namely for the monoclinic structures. To sort this problem out, a different approach was employed. In this case, a block band diagonalization is first used to reduce the basis set from 46 to 20 states: the O 2p orbitals were linearly combined to form a ligand shell with d symmetry that boosts the computational efficiency. The reduced Hamiltonian was thus rotated by a unitary transformation matrix so that the d- and L-blocks were diagonal, which effectively acts as local rotation to the cluster symmetry without changing the physics of the system. This way, the octahedral approximation could be implemented for MLWF basis set of any symmetry.

E.4.2. Coulomb interactions

Different approaches were adopted for the Coulombic interactions. First, it is important to distinguish between the well screened and poorly screened interactions. Following Slater parametrization, the direct monopole interactions are typically more sensitive to the screening processes from the surrounding electronic structure than the multipoles and exchange terms.

The first approach is to approximate all interactions but the monopole ones by atomic-like parameters. The multipole and exchange Slater parameters as well as the spin-orbit parameters were taken from the Hartree-Fock solutions for free ions available published libraries [380,381]. As common in the literature, an 80% scaling factor was employed with respect to the free-ion values for the Slater parameters. Within this approximation, the monopole Slater integral is obtained from **Equation E.2.5** by adjusting the U_{dd} parameter to the experimental spectra, together with the charge transfer Δ parameter. The core-valence interaction was instead set as $U_{pd} = 1.2U_{dd}$ [65]. All semi-empirical parameters used in this thesis are shown below.

	$LiCoO_2$	CoO_2	NiO	$LiNiO_2$	NiO_2	Li_2MnO_3
F^2_{dd}	10.1	10.9	11.1	9.3	10.0	9.93
F^4_{dd}	6.3	6.9	6.9	5.8	6.3	6.26
ξ_{3d}	0.1	0.1	0.1	0.1	0.1	0.05
F^2_{pd}	6.3	6.8	6.7	5.8	6.3	6.13
G^1_{pd}	4.8	5.2	4.9	4.4	4.8	4.62
G^3_{pd}	2.7	3.0	2.8	2.5	2.8	2.63
ξ_{2p}	9.7	9.7	11.5	11.5	11.5	6.85

Table E.4.1 Semi-empirical parameters used for TM 2p simulations in this thesis. The values are in eV and correspond to 80% scaled Slater parameters computed for isolated ions in the formal oxidation state for each compound, as reported in ref. [381]. For Li2MnO3, we took the parameters from the library within the Crispy software [380].

However, the above method typically resulted in large Hund's coupling $J = \frac{F^2+F^4}{14}$ that overestimate the exchange interaction leading to abrupt spin transitions in the U_{dd}-Δ phase diagram. The implementation of Slater parameters from *ab initio* cRPA calculations not only solved this issue but also allowed to avoid fitting U_{dd} and, in some cases, even Δ. This aspect is further discussed in **Section 5.2.1.1**.

Whatever the approximation for H^{ee}_{dd}, a double counting correction was necessary to account for the correlations described by the PBE functional at the DFT step. Various approximations exist for this critical part, as described elsewhere. In this thesis, the well-known around mean field (AMF) approximation was employed. It is based on calculating the mean field version of the operators contributing to $H_{dd'}^{ee}$, e.g. the F^k and G^k in case of Slater parametrization or the $U_{m,m'}^{\sigma,\sigma'}$ and $U_{m,m'}^{\sigma,\sigma}$ in case of the cRPA matrices. This means replacing all two-particles terms with the expectation values of the density matrix obtained by the exact diagonalization of the $H^{(1)}$, containing only DFT-imported interactions.

E.4.3. Exact diagonalization

For the exact diagonalization, Quanty employs the Krylov convergence algorithm starting from a given occupation of the system. Unless specified otherwise, the nominal occupation was also taken as starting point (e.g. for NiO, 8 electrons and 6 electrons were assigned to the Ni 3d and O 2p shells, respectively) and the convergence limit was set to 10^{-10} eV.

Typically, a few lowest eigenstates were calculated. However, since we typically found that $E_n - E_0 \gg k_B T$, with n > 0 and T = 300 K (considering all experiments were carried out at room temperature), the results are discussed only by means of the lowest energy state.

Finally, a set of restrictions were also employed for the ground state calculation to reduce the convergence time. In fact, only the most relevant TM configurations were included in the calculations according to the configuration interaction model. Thus, the TM 3d occupation was restricted between N_d and $N_d + 2$, with N_d being the nominal occupation in ionic limit.

F. Supplementary information for Chapter 3

F.1. Structural characterization

F.1.1. $LiCoO_2$

F.1.1.1. Scanning electron microscopy

Scanning electron microscopy (SEM) images of $LiCoO_2$ were collected using PHI-700 spectrometer from ULVAC-PHI using a primary electron beam of 10 kV.

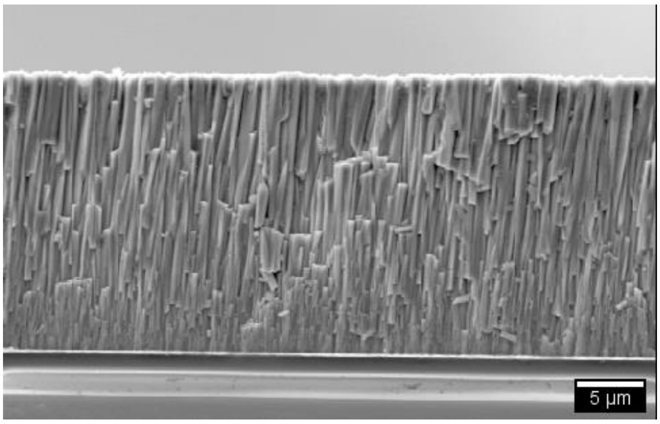

Figure F.1.1 Cross section of the $LiCoO_2$ thin film, realized by cutting the thin film with a diamond knife.

F.1.1.2. Raman Spectroscopy

Raman spectroscopy analyses were performed using a Renishaw inVia Raman microscope in backscattering configuration with 532 nm laser excitation. The $LiCoO_2$ sample was transferred and measured in air. Raman spectroscopy was used to track the crystallization of $LiCoO_2$ upon annealing of the PVD deposed amorphous films. When annealed at intermediate temperatures (400 °C), the material begins to order itself in a cubic spinel structure, known as the low-temperature (LT) phase. When higher temperatures are reached, the typical layered hexagonal structure of $LiCoO_2$ (HT phase) is formed [382,383]. All samples discussed in the manuscript were annealed at 700 °C.

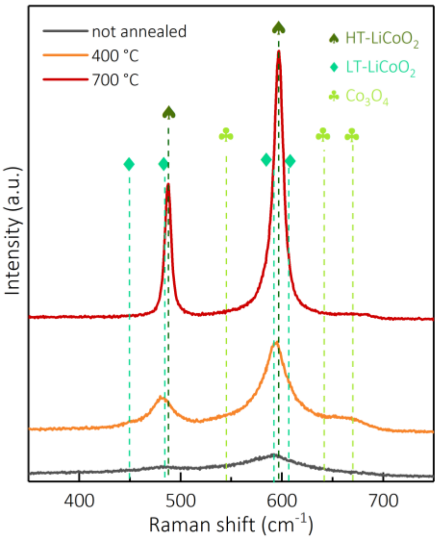

Figure F.1.2 Raman spectra of LiCoO$_2$ thin films after PVD deposition (black), after subsequent annealing at 400°C (orange) and 700°C (red). Colored symbols in the figure indicate the modes for Co$_3$O$_4$ (triangles), LT-LiCoO$_2$ (diamonds), and High-Temperature HT-LiCoO$_2$ (spades) phases.

F.1.2. LiNiO$_2$

F.1.2.1. Scanning electron microscopy

Scanning electron microscopy (SEM) images of LiNiO$_2$ were collected using a MEB-LEO microscope using an acceleration electron beam of 5 kV.

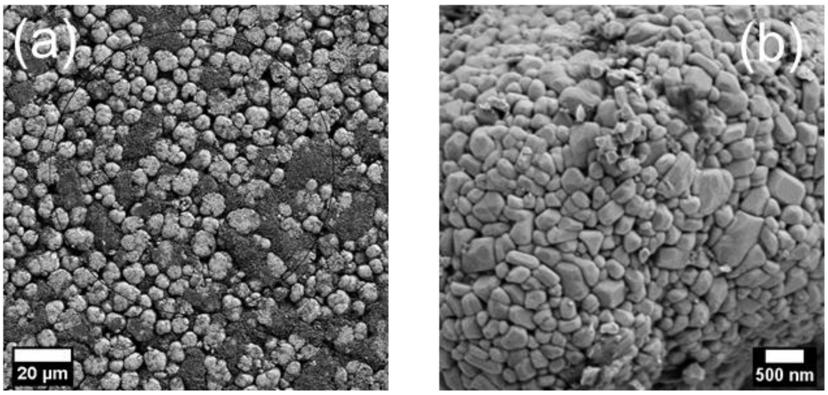

Figure F.1.3 Morphology and particle size analysis of LiNiO$_2$ particles. (a) Low and (b) high magnification SEM images for the pristine LiNiO$_2$ electrode. As typical commercial-grade Ni-rich electrodes, the morphology of LiNiO$_2$ consists of spherical aggregates with diameter d = 6.9 ± 1.7 µm (average over ~100 particles in Figure F.1.3 Morphology and particle size analysis of LiNiO2 particles. (a) Low and (b) high magnification SEM images for the pristine LiNiO2 electrode. (b) that are constituted of smaller primary particles with irregular and prismatic-like shapes randomly oriented. The average dimension was estimated as 300 - 400 nm considering ~50 single particles in four different aggregates. Approximating the particles as spheres gives a radius of about 150 - 200 nm, which was compared to XPS and HAXPES depth sensitivities in the manuscript.

F.1.2.2. X-ray diffraction

Synchrotron X-ray diffraction of $LiNiO_2$ electrode was performed at beamline BM32, at the European Synchrotron Radiation Facility using a beam energy set to 27 keV. The beam had a size of about 150µm × 550µm and a flux of about $3 \cdot 10^{10}$ph/s. The XRD patterns of the *ex situ* samples were recorded in transmission geometry (Debye-Scherrer) with a moveable 2D CdTe detector, calibrated and integrated into intensity *vs.* angle 1D-patterns using the pyFAI multigeometry module [384]. The setup and the data integration process provided an angular resolution of $7.8 \cdot 10^{-3\circ}$ in the range [2.5°, 32.7°]. The $LiNiO_2$ electrodes were covered by polyimide tape to limit air contamination before the measurement. The covered electrodes were brought to the beamline in pouch casings sealed in water free (<1ppm) argon atmosphere. The patterns were analyzed with the Fullprof software [385] by Rietveld refinement. Lattice parameters, oxygen position, Ni/Li anti-site default, thermal movement of the Ni in the layer and strain of the H3 phase were refined. The peaks were fitted using pseudo-Voigt functions.

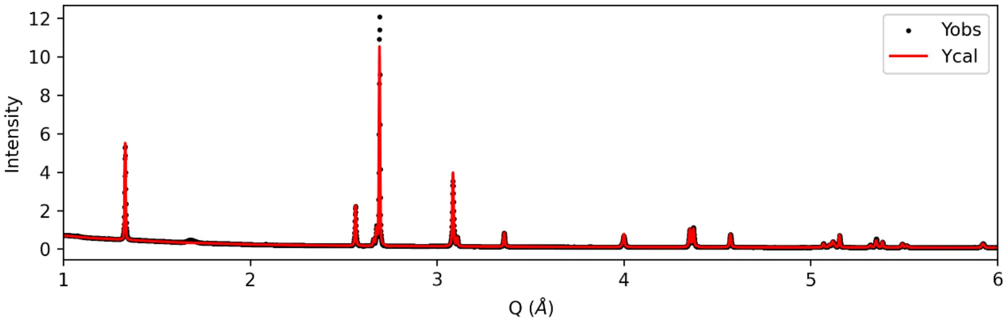

Figure F.1.4 Ex-situ crystal structure characterization of the cycled samples by synchrotron XRD. Experimental data and refinements are shown as black dots and red lines, respectively.

Sample	Phase	Space Group	a (Å)	b (Å)	c (Å)	z_O	Phase fraction (%)
P	H1	R -3 m	2.875	2.875	14.176	-0.26	100

Table F.1.1 Parameters obtained by Rietveld refinement of the XRD patterns. An additional phase for Aluminum (Fm-3m, a = 4.04 Å) was also included in the fits.

F.1.3. $NaNiO_2$

F.1.3.1. Scanning electron microscopy

Scanning electron microscopy (SEM) images of $NaNiO_2$ were collected using a MEB-LEO microscope using an acceleration electron beam of 5 kV.

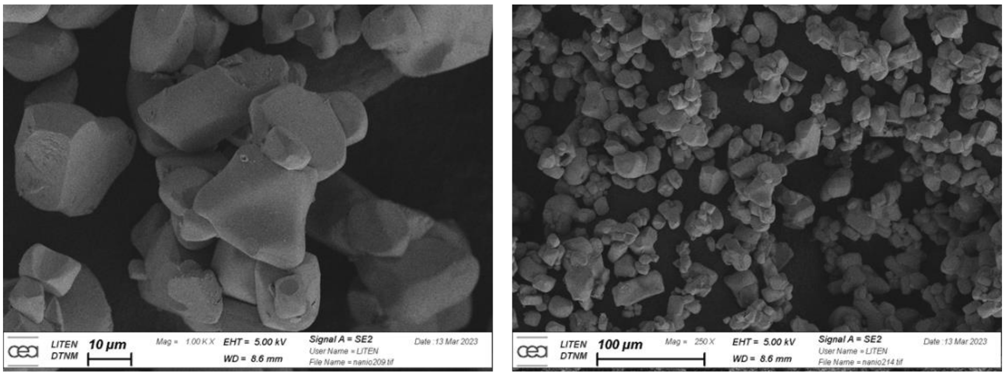

Figure F.1.5 SEM images of the $NaNiO_2$ powder.

F.1.3.2. X-ray diffraction

The XRD pattern was obtained with a Bruker D8 Advance diffractometer equipped with a Cu anode (x-ray beam of wavelength 1.542 Å) and using an anti-scattering filter.

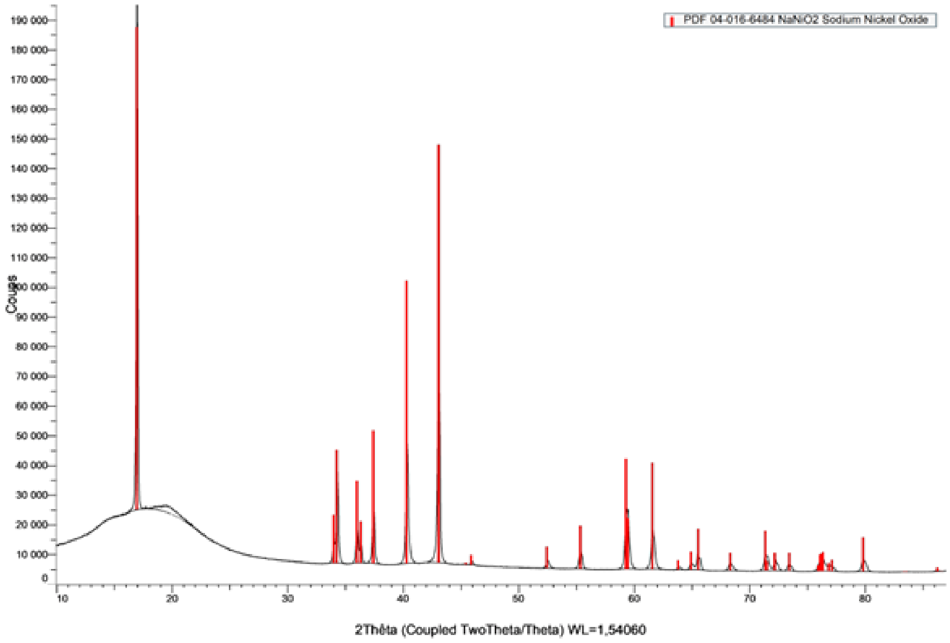

Figure F.1.6 XRD pattern of $NaNiO_2$ compared to reference PDF 04-016-6484

F.1.4. Li_2MnO_3

F.1.4.1. Scanning electron microscopy

Scanning electron microscopy (SEM) images of Li_2MnO_3 were collected using a MEB-LEO microscope using an acceleration electron beam of 3 kV.

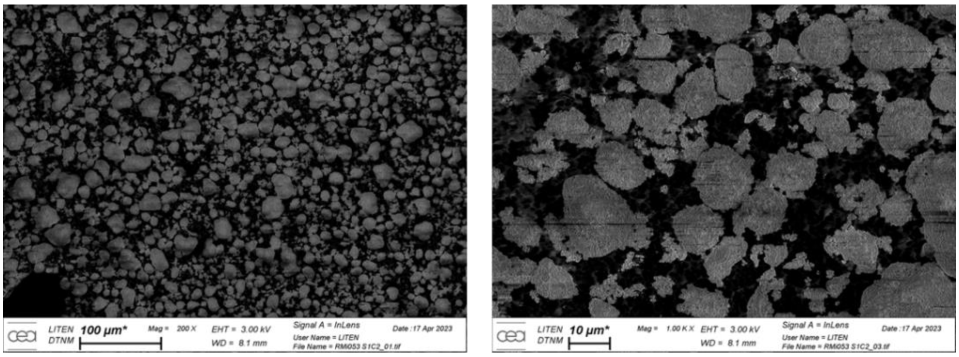

Figure F.1.7 SEM images of the Li_2MnO_3 powder.

F.1.4.2. X-ray diffraction

The XRD pattern was obtained with a Bruker D8 Advance diffractometer equipped with a Cu anode (x-ray beam of wavelength 1.542 Å) and using an anti-scattering filter.

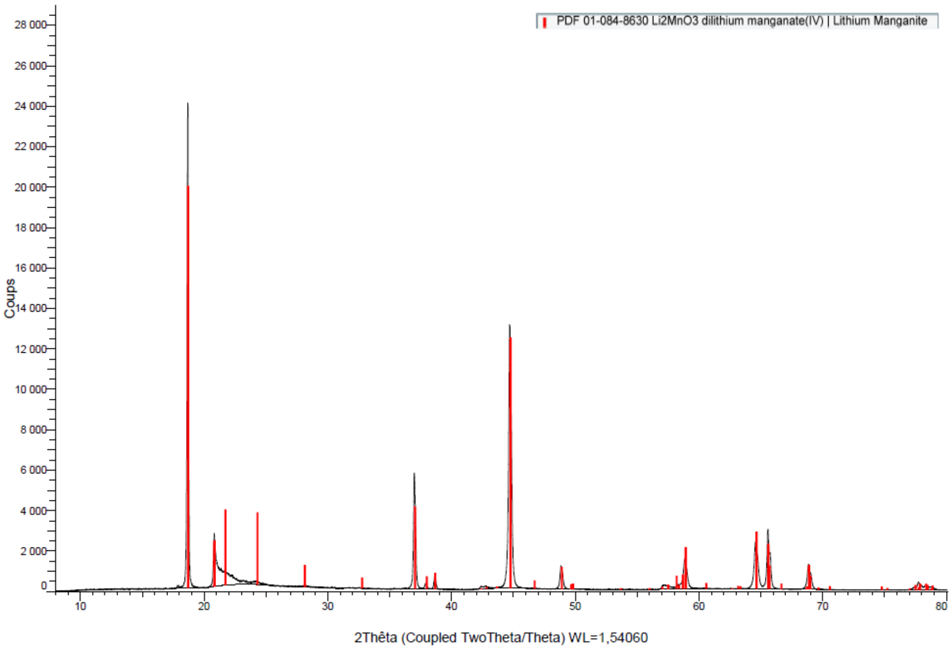

Figure F.1.8 XRD pattern of Li_2MnO_3, compared to reference PDF 01-084-8630.

F.2. Supporting information for XPS and HAXPES analysis

F.2.1. Modeling the main O 1s peak of transition metal oxides

In general, we noticed that the use of standard GL(30) peak could not describe properly the low binding energy-tail of the O_{latt} peak in the O 1s XPS and HAXPES spectra of transition metal oxides. This is shown in **Figure F.2.1(a)** using the O 1s HAXPES spectrum of pristine $LiCoO_2$ thin films and looking at the residual curve in particular. Playing with the percentage weight of Gaussian and Lorentzian functions within the same lineshape model does not improve significantly the fit [**Figure F.2.1(b)**] while moving to the more recent numerical approximation for the Voigt function introduced in CasaXPS does [**Figure F.2.1(c)**]. In the LA(α,m) function, α describes tail asymmetries (α=1 for symmetric peak) and $0<m<1401$ indicates the weight of the convolution with a Gaussian [15]. To correct for the mathematical issue of this approximation that leads to non-zero intensity at infinite, a damping parameter w is also introduced in the LF(α, α, w, m) function [**Figure F.2.1(d)**].

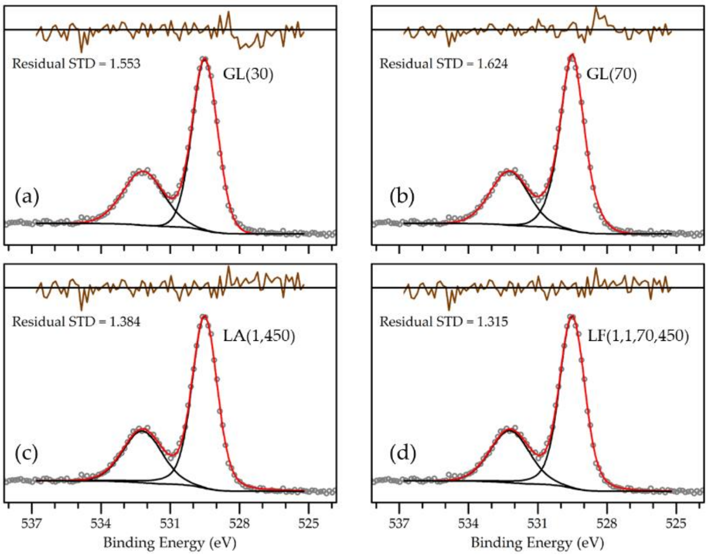

Figure F.2.1 O 1s HAXPES peak fitting models for the pristine $LiCoO_2$ thin film using different lineshapes for the low-binding energy main peak at ~529.5 eV: (a) GL(30), (b) GL(70), (c) LA(1,450), and (d) LF(1,1,70,450). The residual standard deviations (STD) calculated in CasaXPS are indicated in the figure.

---

[15] See http://www.casaxps.com/help_manual/manual_updates/LA_Lineshape.pdf for details on the lineshape mathematical definition. Note that in our version of CasaXPS (2.3.23) the upper limit for m was set to 1401 and not 499 as indicated in the reference.

F.2.2. XPS and HAXPES analysis of Li_2CO_3 and Na_2CO_3

Orbital	Assignation	Li_2CO_3 (XPS)			Na_2CO_3 (XPS)			Na_2CO_3 (HAXPES)		
		BE	FWHM	at%	BE	FWHM	at%	BE	FWHM	at%
Li 1s	**Li_2CO_3**	55.4	1.8	28.8						
Na 1s	**Na_2CO_3**				1071.5	2.0	34.5	1071.5	2.2	36.2
C 1s	**C - C**	285.0	1.8	4.9	285.0	1.9	7.1	285.0	2.0	1.6
	C-O	286.5	2.0	0.6	286.5	1.5	0.6	286.6	2.0	0.7
	C=O	288.3	1.4	0.6	288.0	1.5	0.5			
	CO3	290.1	1.5	14.9	289.4	1.6	14.6	289.6	2.0	13.4
O 1s	**CO3**	531.9	1.9	50.4	531.3	1.9	42.7	531.4	2.1	44.4
	C-O							533.5	2.1	3.8
	N KLL Auger				535.8	2.5				

Table F.2.1 Quantification results for Li_2CO_3 and Na_2CO_3.

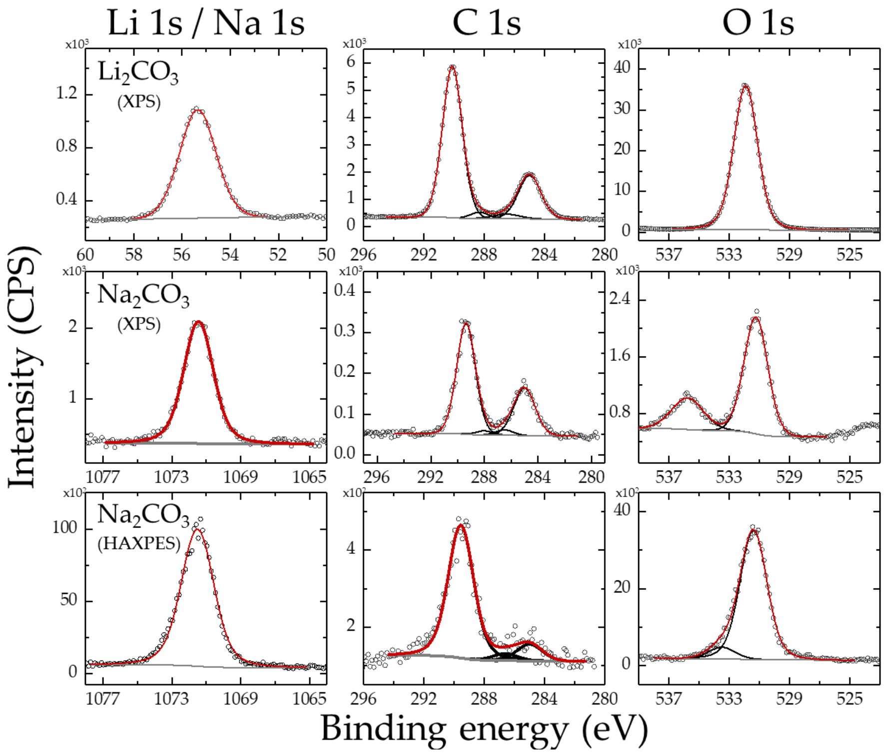

Figure F.2.2 Core-Level spectra analysis for Li_2CO_3 and Na_2CO_3. Due to the overlap between Na KLL and O 1s, HAXPES spectra were also measured for Na_2CO_3.

F.2.3. XPS analysis of commercial-grade electrodes: technical details

The LiNiO$_2$ electrode samples suffered beam damage-induced modifications when measured in the same conditions as LiCoO$_2$ thin films, especially for the F 1s, C 1s, and O 1s core levels. Moreover, the signal of LiNiO$_2$ particles was nearly completely obscured by the PVDF binder and carbon black additive. To minimize these effects, a different protocol was performed, involving the following precautions:

1. The electrodes were manually scratched with a ceramic knife in the glovebox before the measurement. This led to effective decrease of binder intensity in the XPS measurement (**Figure F.2.3**).
2. No charge neutralization was used during the acquisition, exploiting the. intimate mixing of LiNiO$_2$ particles and conductive carbon.
3. To reduce the X-ray exposure time, the area of analysis was increased to a square of 500x500 μm^2, scanned by the X-ray probe of 100 μm in diameter. With this procedure, no significant changes on the XPS spectra were observed even after long exposures of >10 h (typical time for HAXPES experiments).

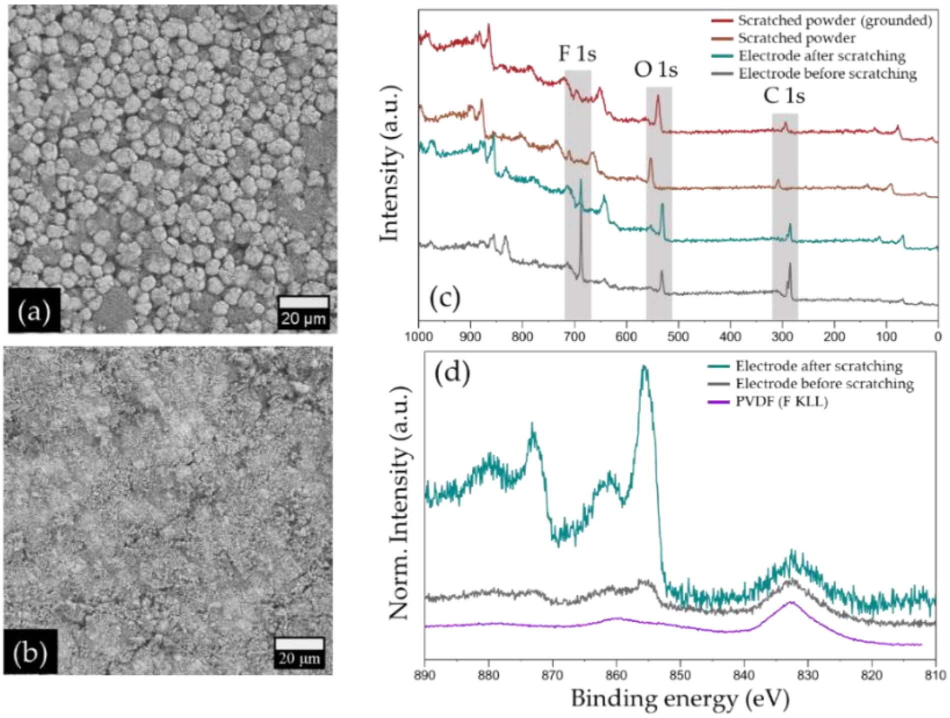

Figure F.2.3 SEM top view image of (a) unscratched and (b) mechanically scratched pristine LiNiO$_2$ electrodes. (c) Stack plot of normalized XPS survey spectra for pristine LiNiO$_2$ prepared in four ways, from bottom to top: unscratched electrode, mechanically scratched electrode, powder retrieved after scratching, and ground powder retrieved after scratching. Note that the spectra were not charge calibrated, showing that the powder samples suffered charging effects in contrast to the electrode samples.

The mechanism and effect of X-ray induced beam damage on $LiNiO_2$ electrodes were investigated during the synchrotron campaign at Soleil since, as expected, the effect of beam damage was enhanced with the synchrotron radiation. These results were submitted to Surface and Interface Analysis and accepted for publication as a short article titled "Surface analysis insight note: Accounting for X-ray beam damage effects in positive electrode-electrolyte interphase investigations" (**Annex I**, **paper 2**).

F.2.3.1. XPS analysis of carbon black and PVDF

Both powders were stored in Ar-filled glovebox and were transferred to Quantes with the airtight transfer vessel as usual. However, oxygen and water contamination were found for PVDF (but not for the carbon black), as evident in the unexpected large O 1s peak shown below. Since the electrodes were fabricated elsewhere (BASF in the frame of BIG-MAP European project), it is not clear if such contamination can be expected in the electrode samples as well. However, from the analysis of $LiNiO_2$ samples, such a contamination was not observed. For fitting the C 1s peak of carbon black, a LF(0.65,1.15,100,100,3) lineshape was used in combination with a GL(30) peak for the π-π* satellite.

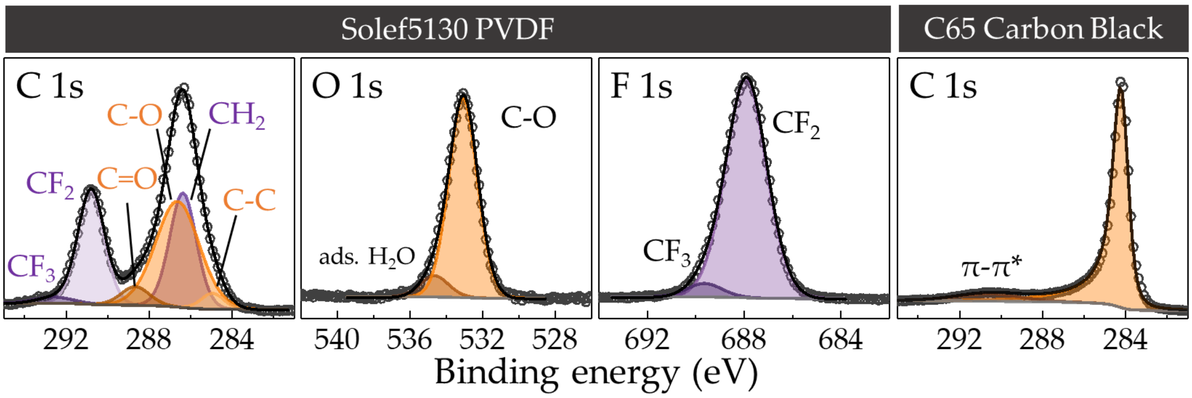

Figure F.2.4 Core-level spectra for bare PVDF and carbon black used to produce the $LiNiO_2$ electrode samples.

Orbital	Component	BE (eV)	FWHM (eV)	at %
C 1s	C-C/C-H	284.9	1.3	1.7
	CH_2 (PVDF)	286.3	1.5	14.2
	C-O	286.6	2.5	21.5
	C=O	288.6	1.6	2.5
	CF_2 (PVDF)	290.8	1.5	14.2
	CF_3 (PVDF)	292.6	2.2	1.1
O 1s	C-O/C=O	533.0	1.9	10.2
	Ads. H_2O	534.6	1.8	1.1
F 1s	CF_2 (PVDF)	687.9	2.0	31.9
	CF_3 (PVDF)	689.6	1.7	1.7

Table F.2.2 Quantification results for PVDF bare powder.

F.2.4. Mn 3p lineshape

To extract characteristic Mn 3p lineshape of Mn^{IV} in octahedral environment, we used the XPS and HAXPES spectra of reference MnO_2 powder. The approach is similar to the one discussed in ref. [281].

Peak	BE	FWHM	Area %
A	49.7	1.8	65.0
B	51.0	1.8	17.1
C	52.4	1.8	8.5
D	47.9	1.8	6.0
E	53.9	1.8	3.4

Table F.2.3 Mn 3p peak fitting model used to fit the Mn 3p XPS and HAXPES for MnO_2.

F.2.5. On GCIB beam damage for layered lithium transition metal oxides

The underlying principle of GCIB is that the kinetic energy of the atomic aggregate is distributed among the ions composing itself. For example, while an Ar^+ ion accelerated to 1 keV impacts the surface with that energy (1 keV/at), a cluster of 1000 Ar^+ ions accelerated to the same energy impacts the material with an energy of 1 eV/at. Some examples have already been brought for cycled NMC materials: Chang et al compared sputtering using C60 and Ar^+, showing that the former allows reduction of surface damage, while Bondarchuk et al. used a gas cluster ion beam (GCIB) to remove the surface reduced layer [215,386]. However, the Ni 2p evolution is either not shown [386] or difficult to understand from figure (Supporting Information of ref. [215]).

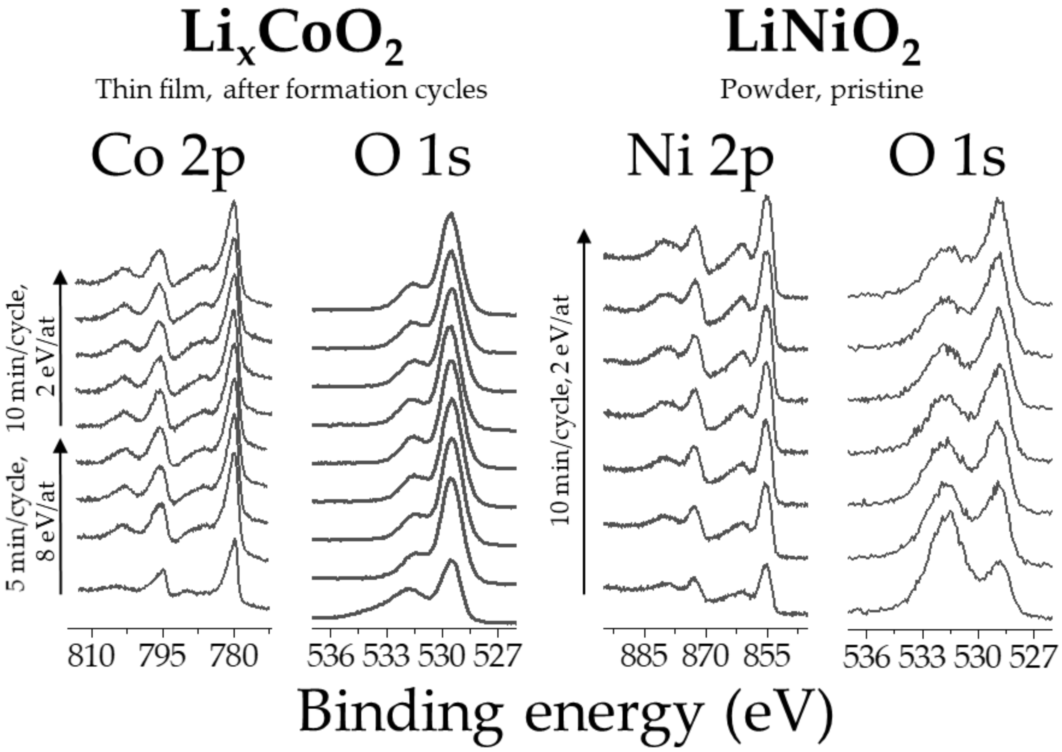

Figure F.2.5 GCIB experiments of cycled $LiCoO_2$ thin films and pristine $LiNiO_2$ powders. A constant shift was applied to each core level spectra starting from the first scan (without sputter) at the bottom and following the arrows indicated at the left-hand side of the TM 2p stack plots.

Figure F.2.5 shows the changes of (a) Co 2p and (b) O 1s spectra for cycled Li_xCoO_2 and of (c) Ni 2p and (d) O 1s spectra for $LiNiO_2$ upon GCIB sputtering, taken as representative for testing the damage produced by GCIB depth profile. In practice, the goal was to remove the surface layer and to get a "clean" signal to reduce the relatively large noise in HAXPES spectra. However, it was not possible to avoid altering the 2p spectra of the transition metals. Even with the softest GCIB conditions available in our equipment (2eV/at), $LiNiO_2$ reacted instantaneously. Still, the beam damage was effectively reduced with respect to Ar-ion sputtering, as observed in the evolution of the O 1s spectra. However, this comes with the drawback of less efficient sputtering of the surface inorganic species (e.g. LiF and Li_2CO_3), for which higher impact energy is required.

F.2.6. Ni 2p$_{3/2}$ peak fitting models and quantification using the method by Bondarchuck et al.

With the data shown in Table F.2.4, the Ni^{III} percentage concentration [Ni^{III}] was calculated using the following formula proposed by Bondarchuk et al. [215]:

$$[Ni^{III}] = 100 \times \frac{A(main\ line) - R \times A(satellite)}{A(main\ line)}$$

Where $A(ML) = \sum_i A(ML_i)$, $A(SAT) = \sum_i A(SAT_i)$, and R is the intensity ratio "main peak-to-satellite" from NiO fits, i.e. the area ratio $A(ML)/A(SAT)$, equal to 1.3 for XPS (in agreement with ref. [215]) and 1.4 for HAXPES.

	NiO XPS			LiNiO$_2$ XPS		
Peak	**BE**	**FWHM**	**Area %**	**BE**	**FWHM**	**Area %**
ML$_1$	853.9	1.2	12.9	854.2	2.0	15.4
ML$_2$	855.7	3.3	44.2	855.5	2.9	55.1
SAT$_1$	861.0	4.1	34.3	860.8	4.6	23.8
SAT$_2$	864.2	3.1	5.9	864.7	3.1	4.3
SAT$_3$	866.8	2.3	2.8	866.8	6.1	1.4
	NiO HAXPES			**LiNiO$_2$ HAXPES**		
Peak	**BE**	**FWHM**	**Area %**	**BE**	**FWHM**	**Area %**
ML$_1$	854.0	1.2	14.9	854.4	2.0	11.4
ML$_2$	855.7	3.5	43.9	855.6	3.2	56.0
SAT$_1$	861.0	3.6	30.5	860.8	5.0	25.6
SAT$_2$	863.9	3.1	8.4	864.2	2.6	4.6
SAT$_3$	866.9	2.1	2.3	866.8	2.6	2.5

Table F.2.4 Ni 2p$_{3/2}$ peak fitting models for NiO and LiNiO$_2$.

G. Supplementary information for Chapter 4

G.1. Electrochemistry: additional information

G.1.1. Cell cases for Li_xCoO_2 thin films

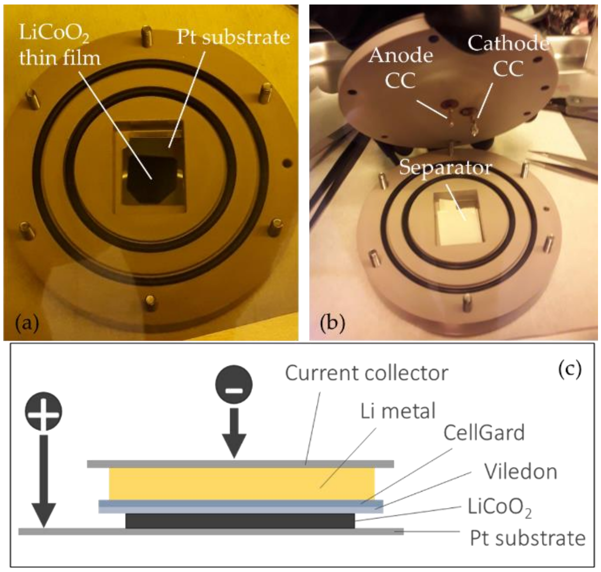

Figure G.1.1 Pictures of the cell case for cycling $LiCoO_2$ thin films. (a) Bottom part with a $LiCoO_2$ cathode. (b) Top and bottom parts. (c) Side-view schematics of the electrochemical cell.

G.1.2. Electrochemical data for Li_2MnO_3

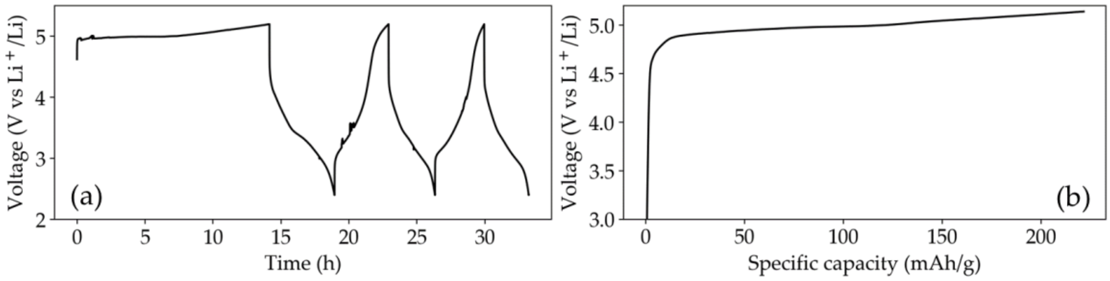

Figure G.1.2 Electrochemical data for Li_2MnO_3. (a) Three formation cycles at C/50, showing the typical large voltage fade after the first charge. (b) Galvanostatic charge for the cycled material studied in Chapter 5.

G.2. XPS study of cycled materials: technical details

G.2.1. pSEI thickness calculation

Upon cycling, the pSEI covering the layered oxide effectively reduces the photoelectron intensity for the core level peaks related to the buried material from A to A_0 as sketched in the figure below. Assuming a homogeneous bilayer model as shown in the figure allows to estimate the pSEI thickness as discussed in the main text.

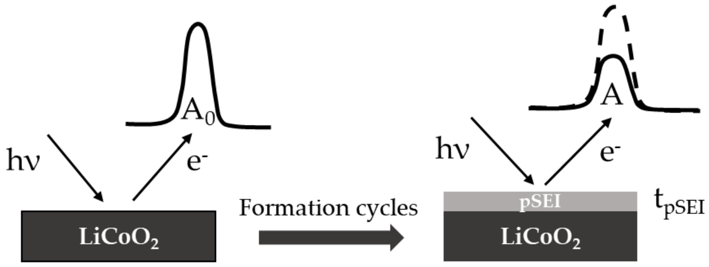

Figure G.2.1 Schematics for the photoelectron intensity decay for cycled Li_xCoO_2 thin films due to pSEI formation.

	LiF	Li_3PO_4	Li_2CO_3	POE
Bulk density (g/cm³)	2.64	2.39	2	1.23
N° valence electrons	8	32	24	18
Molecular weight	25.94	115.79	73.89	44.05
Band gap	14.2	5.8	5.1	0

Table G.2.1 Parameters used for the IMFP calculation of pSEI. The band gap of POE was taken as 0 after observing the final IMFP was not largely affected by its change: changing from a band gap of 0 to 2 eV returned IMFPs from 3.90 to 3.95 nm for Al kα photon energy.

	O 1s		Co 2p	
	XPS	HAXPES	XPS	HAXPES
E_K (eV)	957	4885	707	4635
λ_{LiF} (nm)	3.9	14.5	3.1	13.8
$\lambda_{Li_3PO_4}$ (nm)	2.6	9.7	2.1	9.3
$\lambda_{Li_2CO_3}$ (nm)	2.7	10.2	2.2	9.7
λ_{POE} (nm)	2.7	10.5	2.2	10

Table G.2.2 Estimated IMFP (λ) for the O 1s and Co 2p photoelectrons travelling through the four main pSEI species according to the XPS analysis, excited by the Al Kα and Cr Kα photon energy.

		XPS	HAXPES
pSEI composition (at%)	F 1s - LiF	18.6	14.5
	F 1s - $Li_xPO_yF_z$	2.8	2.9
	O 1s – CO_3^{2-}	9.4	11.4
	O 1s - C-O	7.0	2.8
O 1s	A (CPS eV)	19306	601
	A_0 (CPS eV)	46351	764
	$\langle\lambda^{O1s}_{pSEI}\rangle$ (nm)	2.8	12.1
	t^{O1s}_{pSEI} (nm)	1.8	2.1
Co 2p	A (CPS eV)	92421	2550
	A_0 (CPS eV)	150866	2808
	$\langle\lambda^{Co2p}_{pSEI}\rangle$ (nm)	2.3	9.3
	t^{Co2p}_{pSEI} (nm)	0.79	0.63
	$\langle t_{pSEI}\rangle$ (nm)	1.3 ± 0.5	1.3 ± 0.7

Table G.2.3 Calculation of the average pSEI thickness $\langle t_{pSEI}\rangle$ for the cycled $Li_{0.95}CoO_2$ electrode following Eq. 5.2.1. XPS and HAXPES quantitative analysis results are used to estimate the pSEI chemical composition. The results from O 1s and Co 2p core levels are averaged. The semi-difference is used as error for the estimate.

For the cycled Li_xNiO_2 composite electrodes, the calculation was not carried out in such detail: the pSEI was approximated by the LiF IMFP noting that it is larger than all other species i.e. giving an upper limit for its estimate. The calculation was carried out using unscratched samples, whose O 1s spectra are shown below.

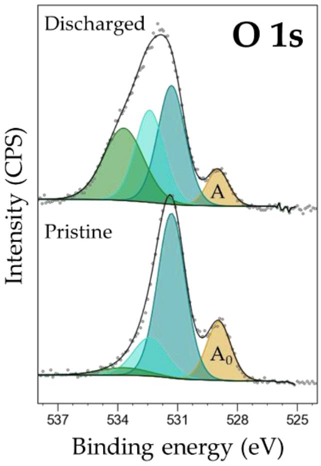

Figure G.2.2 O 1s core-level spectra of the unscratched pristine and cycled (x~0.8) Li_xNiO_2 electrodes. The low energy peak was used for the pSEI thickness calculation.

G.2.2. Reproducibility tests for Li$_x$NiO$_2$ electrodes

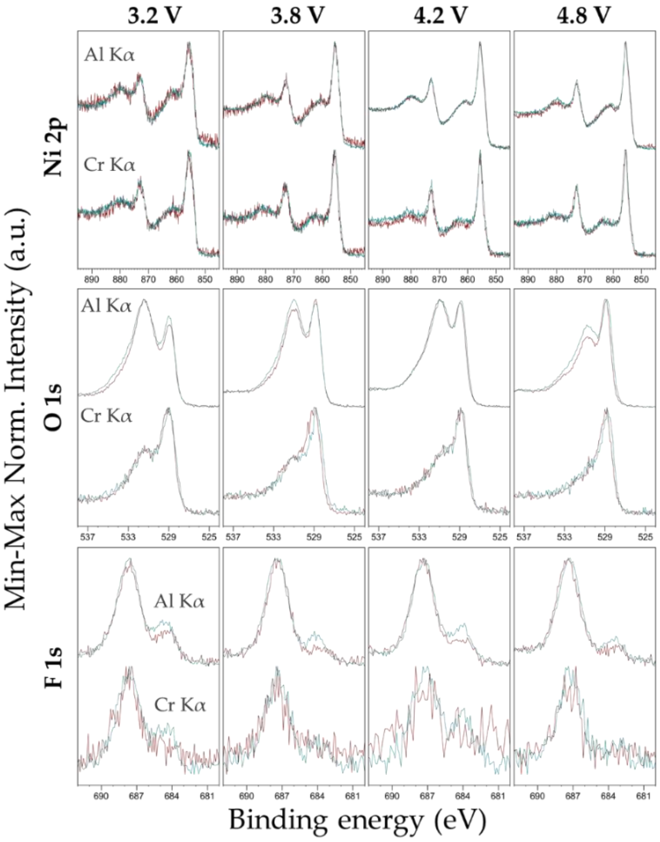

Figure G.2.3 Comparison of the Ni 2p, O 1s, and F 1s XPS and HAXPES spectra of two cycled electrodes subjected to the same electrochemical protocol.

G.2.3. Calculation of the capacity loss by Co reduction

The increase of surface percentage Co^{II} ions ($C_{Co^{II}}$) from pristine to cycled $LiCoO_2$ thin film electrodes (calculated in 5.3.1.5) is due to electrochemical reduction of Co^{III}. Therefore, the new moles of Co^{II} ($n_{Co^{II}} = C_{Co^{II}} n_{Co}$, with n_{Co} the total moles of Co ions) are linked to the charge q_{red} by the Faraday law as $q_{red} = F\frac{n_{Co^{II}}}{m}$, with m the mass of the system and F the Faraday constant (26801 mAh/mol). This charge should contribute to the Li-ion cell capacity loss assuming the reduction process to be irreversible. To estimate q_{red} we proceeded with calculating m and $n_{Co^{II}}$ by considering the portion of matter probed by XPS and HAXPES experiments as cylinders whose volume is $V = \pi r^2 \cdot 3 \sin\theta\, \lambda_{hv}$, with r the beam spot radius (50 µm) and λ_{hv} the IMFP for the XPS and HAXPES measures. With the as-obtained volume the mass of $LiCoO_2$ (m) and total moles of Co ions (n_{Co}) are obtained using the known density and molar weight of $LiCoO_2$ (4.5 g/cm^3 and 98.90 g/mol). All the values are given in the table below.

	HAXPES	XPS
$C_{Co^{II}}$ (%)	7.4	2.6
λ (nm)	6.8	2.3
V (cm^3)	1.1*10^{-10}	3.8*10^{-11}
m (ng)	0.51	0.17
n_{Co} (10^{-12} mol)	5.2	1.7
$n_{Co^{II}}$ (10^{-14} mol)	38	4.4
q_{red} (mAh/g)	20	7.0

Table G.2.4 Estimation of the charge capacity related to cobalt reduction by XPS and HAXPES.

G.2.4. Components for reference-based Ni 2p$_{3/2}$ peak fitting

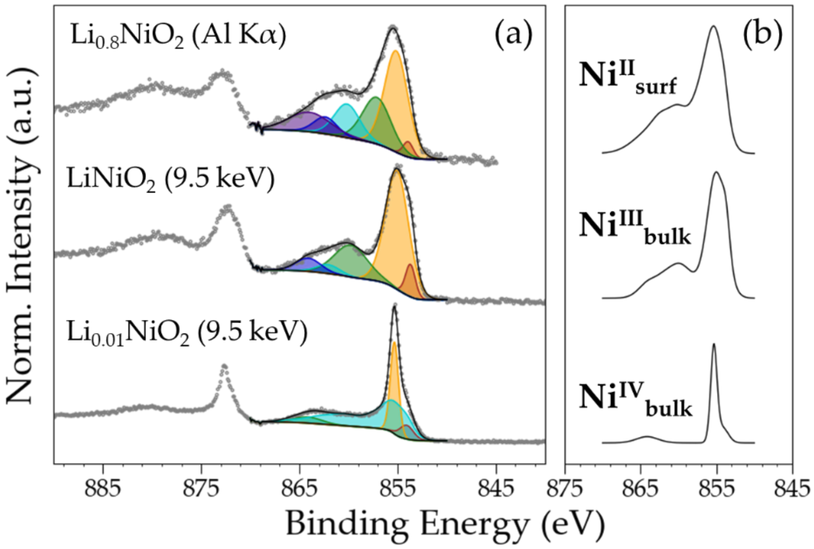

Figure G.2.4 (a) Ni 2p$_{3/2}$ peak fitting model and (b) related convolution line used as line shapes to fit the set of Ni 2p$_{3/2}$ samples.

G.2.5. SRL thickness calculation for cycled Li_xNiO_2 samples

	$Li_{0.8}NiO_2$	$Li_{0.5}NiO_2$	$Li_{0.1}NiO_2$	$Li_{0.01}NiO_2$
Al Kα	--	1.1	1.5	1.2
2.3 keV	--	3.7	5.9	4.7
Cr Kα	4.0	3.9	4.8	3.9
5.4 keV	10.9	1.7	3.9	3.9
9.5 keV	13.5	3.3	10.6	10.0

Table G.2.5 Surface layer thickness calculated by XPS and HAXPES using a bilayer homogeneous model. All values are in nm.

G.2.6. Ni $2p_{3/2}$ and O 1s quantification

	XPS			HAXPES		
	Component	**BE (eV)**	**%at**	**Component**	**BE (eV)**	**%at**
NiO	O 1s		61	O 1s		52
	O_{latt}	529.5	38	O_{latt}	529.5	45
	$O_{carb/hydr}$	531.3	22	$O_{carb/hydr}$	531.2	8
	O_{org}	533.3	1			
	Ni 2p	854.1	39	Ni 2p	853.7	48
$Ni(OH)_2$	O 1s		73	O 1s		68
	O_{latt}	531.1	49	O_{latt}	531.1	62
	O_{org}	533.2	24	O_{org}	532.6	6
	Ni 2p	856.1	27	Ni 2p	855.5	32
Pristine $LiNiO_2$	O 1s		79	O 1s		73
	O_{latt}	528.8	23	O_{latt}	528.7	36
	O_{surf}	530.1	8	O_{surf}	529.9	10
	$O_{carb/hydr}$	531.4	41	$O_{carb/hydr}$	531.4	26
	O_{org}	533.0	6	O_{org}	533.4	2
	Ni 2p		21	Ni 2p		27
	Ni^{II}	855.5	10	Ni^{II}	855.5	11
	Ni^{III}	855.2	11	Ni^{III}	855.2	16
	Ni^{IV}	855.6	0	Ni^{IV}	855.5	0
Charged $LiNiO_2$	O 1s		69	O 1s		60
	O_{latt}	528.8	25	O_{latt}	528.7	33
	O_{surf}	530.2	17	O_{surf}	530.1	17
	$O_{carb/hydr}$	531.3	21	$O_{carb/hydr}$	531.6	6
	O_{org}	533.3	6	O_{org}	533.1	5
	Ni 2p		31	Ni 2p		40
	Ni^{II}	855.5	22	Ni^{II}	855.1	22
	Ni^{III}	854.9	7	Ni^{III}	855.2	9
	Ni^{IV}	855.6	3	Ni^{IV}	855.5	9

Table G.2.6 Lab-based XPS and HAXPES quantification results of Ni 2p and O 1s for reference samples and electrodes.

G.2.7. Mn 3s, Mn3p, and Li 1s spectra of charged Li$_2$MnO$_3$

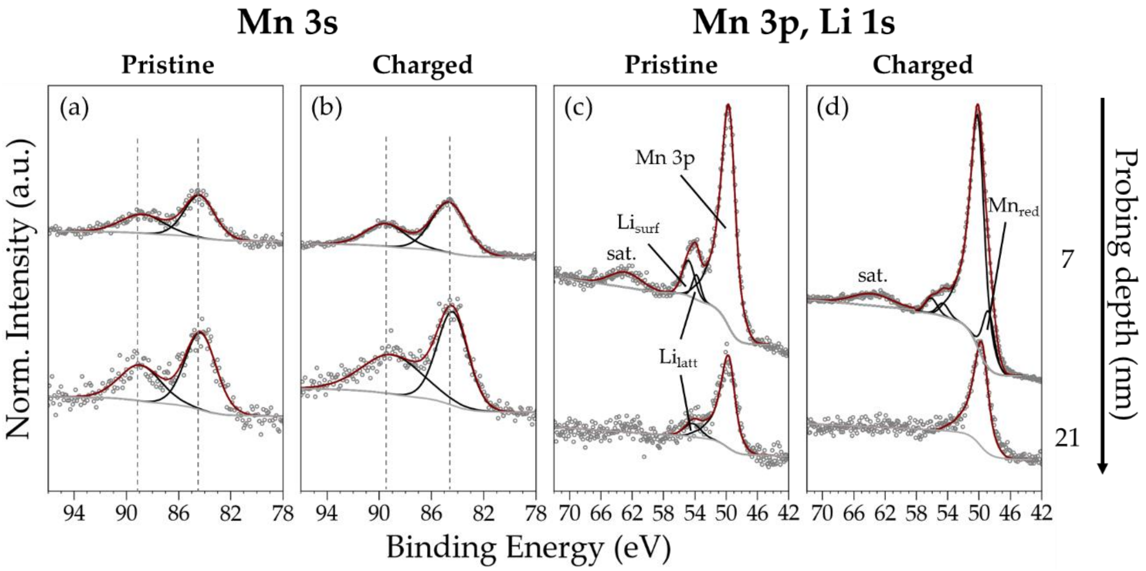

Figure G.2.5 Mn 3s, Mn 3p and Li 1s lab-based XPS (top) and HAXPES (bottom) spectra of (a,c) pristine and (b,d) charged Li$_2$MnO$_3$ electrodes. The spectra are normalized to the background intensity at the lower binding energy side of each peak. Note that the inverted Mn 3s/Mn 3p intensity ratio switching from XPS to HAXPES is related to the change in photoelectron cross section.

G.3. O 1s binding energy calculations for bulk Li$_x$CoO$_2$

The supercell size was progressively increased to check convergence for the binding energy calculation. The most important criterion was identified as the smallest distance between the independent O atom in which the (half-)core hole was imposed. For this system, a $\mathbf{d_{hole\text{-}hole}}$ > 5 Å was considered sufficient for the comparison with the experimental data, for which an error of 0.1 eV is below experimental resolution.

Cell Size	**N$_{atoms}$**	**d$_{hole\text{-}hole}$ (Å)**	**E$_{TOT}$ (keV/at)**	**E$_{fermi}$ (eV)**	**E$_{O1s}$ (eV)**	**BE (eV)**
Primitive (G.S.)	4.0	0.0	-10.56	6.48		
1x1x3 SC	12.0	2.8	-10.53	6.42	-532.30	538.7
2x2x3 SC	48.0	5.6	-10.55	6.42	-532.17	538.6

Table G.3.1 DFT calculation of the O 1s binding energy for LiCoO$_2$. The total and Fermi energies for the ground state calculation (G.S., no core hole) is added for reference. SC= supercell. All values are in eV.

Cell Size	N_{atoms}	$d_{hole-hole}$ (Å)	E_{TOT} (keV/at)	E_{fermi} (eV)	E_{O1s} (eV)	BE (eV)
Primitive (G.S.)	7	0	-12.03	4.74		
Primitive (=1x1x2)	7	2.8	-12.00	4.01	-532.70	536.7
2x2x2 SC	28	5.1	-12.02	4.31	-532.54	536.8
3x3x2 SC	63	5.1	-12.03	4.36	-532.54	536.9

Table G.3.2 DFT calculation of the O 1s binding energy for the O1 oxygen configuration in $Li_{0.5}CoO_2$. The total and Fermi energies for the ground state calculation (G.S., no core hole) is added for reference. SC= supercell. All values are in eV.

Cell Size	N_{atoms}	$d_{hole-hole}$ (Å)	E_{TOT} (keV/at)	E_{fermi} (eV)	E_{O1s} (eV)	BE (eV)
Primitive (G.S.)	7	0	-12.03	4.74		
Primitive (=1x1x2)	7	2.8	-12.00	4.16	-532.86	537.0
2x2x2 SC	28	5.1	-12.02	4.35	-532.86	537.2
3x3x2 SC	63	5.1	-12.03	4.38	-532.81	537.2

Table G.3.3 DFT calculation of the O 1s binding energy for the O2 oxygen configuration in $Li_{0.5}CoO_2$. The total and Fermi energies for the ground state calculation (G.S., no core hole) is added for reference. SC= supercell. All values are in eV.

G.4. STEM-EELS: experimental details

STEM images and EELS spectra were acquired on a probe Cs-corrected TFS Titan Themis microscope operating at 200 kV. EELS spectra were collected in spectrum imaging mode with a Gatan GIF Quantum electron spectrometer using a dispersion of 0.25 eV per channel and a 2.5 mm aperture. Concerning the sample preparation, powders were ground and deposited on a lacey carbon coated grid. For the observations, grids were transferred from the glovebox to the microscope using a vacuum transfer holder to protect the sample from air exposure.

H. Supplementary information for Chapter 5

H.1. Density functional theory calculations

H.1.1. Computational details

The electronic structures were calculated with the full-potential linearized augmented plane-wave method of WIEN2K, using the Perdew-Burke-Ernzerhof (PBE) generalized-gradient approximation (GGA) for the exchange-correlation potential. The planewave cutoff was set to $R_{MT}^{min}K_{max} = 7$, where R_{MT}^{min} is the smallest atomic sphere radius and K_{max} is the largest k vector. The paramagnetic ground-state electronic density was obtained with a 10 × 10 × 10 wave-vector grid in the primitive full Brillouin zone with convergence criteria of 1.36 meV/f.u. (where "f.u." denotes formula unit) for the total energy and 10^{-3} electrons/f.u. for the charge, respectively. The table below summarizes the crystal structures and material-dependent parameters used.

Name	Li	TM	O
$LiCoO_2$	1.77	1.94	1.67
$Li_{0.5}CoO_2$	1.71	1.81	1.56
CoO_2		1.9	1.66
$LiNiO_2$	1.69	1.9	1.63
$Li_{0.5}NiO_2$	1.69	1.9	1.63
NiO_2		1.9	1.63
Li_2MnO_3	1.7	1.92	1.65
NiO		2.11	1.81

Table H.1.1 Muffin-tin radii employed in the DFT calculations.

Name	**Space group**	**a (Å)**	**b (Å)**	**c (Å)**	**γ (°)**	**Li**	**TM**	**O**	**Ref.**
LiCoO$_2$	R-3m	2.816	2.816	14.052	120	0,0,0	0, 0, 1/2	0, 0, 0.7600	[79]
								0, 0, 0.2401	
Li$_{0.5}$CoO$_2$	P2/m	4.865	2.809	5.063	90 (1)	0, 0, 0	1/2, 0, 1/2	0.2334, 0, 0.7042	[387]
							0, 1/2, 0	0.7666, 0, 0.29579	
								0.7379, 1/2, 0.7095	
								0.2621, 1/2, 0.2905	
CoO$_2$	P-3m1	2.822	2.822	4.293	120		0, 0, 0	1/3, 2/3, 0.2341	[79]
								2/3, 1/3, 0.7659	
LiNiO$_2$	R-3m	2.878	2.878	14.198	120	0, 0, 1/2	0, 0, 0	0, 0, 0.2578	us(2)
								0, 0, 0.7422	
Li$_{0.5}$NiO$_2$	P2/m	5.073	4.940	2.826	109.3478	1/2, 0, 1/2	0,0,0	0.2150, 1/4, 1/2	us(2)
							0, 1/2, 1/2	0.7850, 3/4, 1/2	
								0.2150, 3/4, 0	
								0.7850, 1/4, 0	
NiO$_2$	R-3m	2.814	2.814	13.494	120		0, 0, 0	0, 0, 0.7369	us(2)
								0, 0, 0.2631	
Li$_2$MnO$_3$	C2/m	4.937	5.030	8.532	109.46	0, 0, 1/2	0, 0, 0.83292	0.2189, 0.2273, 0	PDF 01-084-8630
						0, 1/2, 0	0, 0, 0.16708	0.7811, 0.7727, 0	
						0, 1/2, 0.6606		0.2540, 0.2233, 0.3212	
						0, 1/2, 0.3394		0.7460, 0.7767, 0.6788	
								0.2540, 0.2233, 0.6788	
								0.7460, 0.7767, 0.3212	
NiO	Fm-3m	4.177	4.177	4.177	90		0, 0, 0	0.5, 0.5, 0.5	[219]

Table H.1.2 Structural parameters used for DFT calculations. (1) β= 108.68°. (2) The structure was obtained from synchrotron XRD refinements of related pristine and cycled electrodes (the atomic occupancy was rounded to unity).

H.1.2. Band structures and density of states

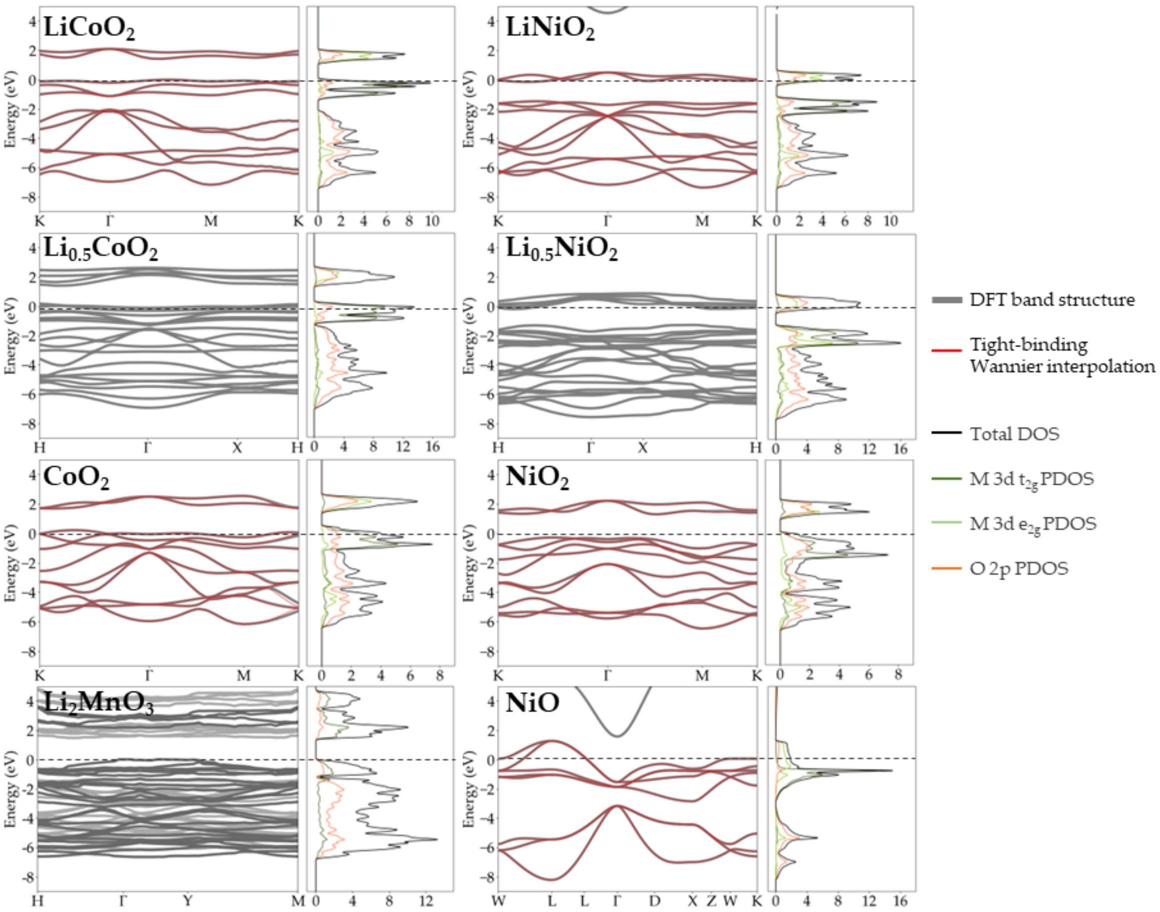

Figure H.1.1 Band structures and density of states calculated with DFT method. The partial density of states was computed with qtl program of Wien2k rotating to the local distorted octahedral symmetry. The Wannier tight binding model is added for comparison, showing a successful interpolation with the input band structure. For Li_2MnO_3 (only spin-polarized calculation), dark and light grey were used to indicate the spin polarization in the band structure plot and the green line represents overall 3d PDOS.

H.2. Transition metal 2p simulations

H.2.1. Li_xMO_2 (M=Co, Ni; x=0,1)

Below we show the Co 2p and Ni 2p spectra simulated for $LiCoO_2$, CoO_2, $LiNiO_2$, and NiO_2, respectively. The simulated spectra are compared to background-corrected and normalized HAXPES data to find the best-agreement values for U and Δ, which are highlighted by the yellow background. The remaining parameters used for the calculations are reported in **Table E.4.1**.

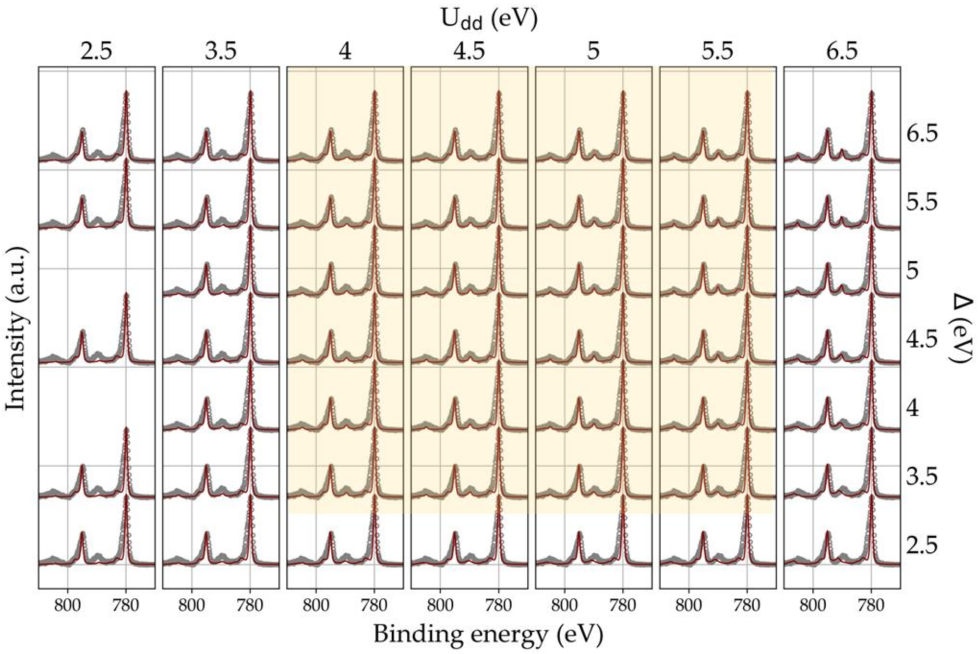

Figure H.2.1 Co 2p simulations (red line) compared to experimental HAXPES (grey dots) for LiCoO$_2$.

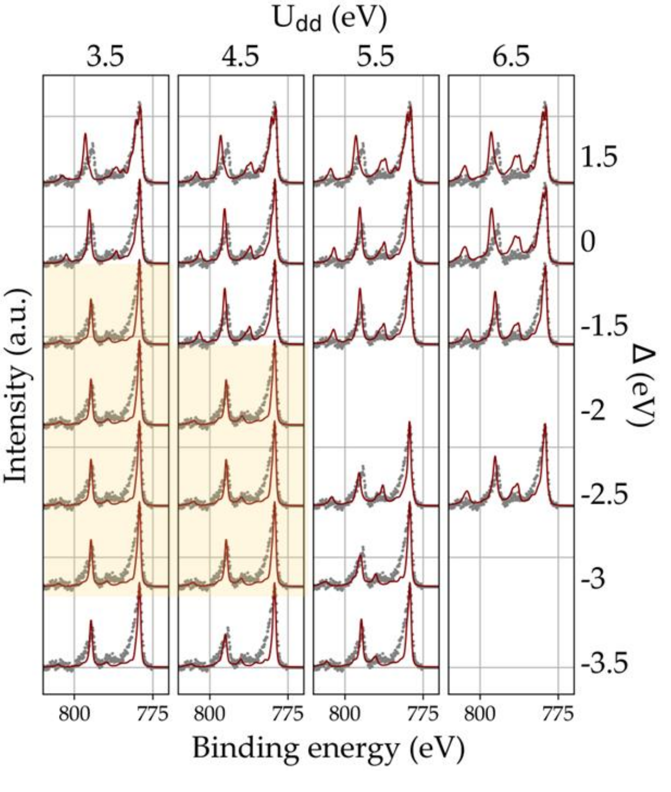

Figure H.2.2 Co 2p simulations (red line) compared to experimental HAXPES (grey dots) for CoO$_2$.

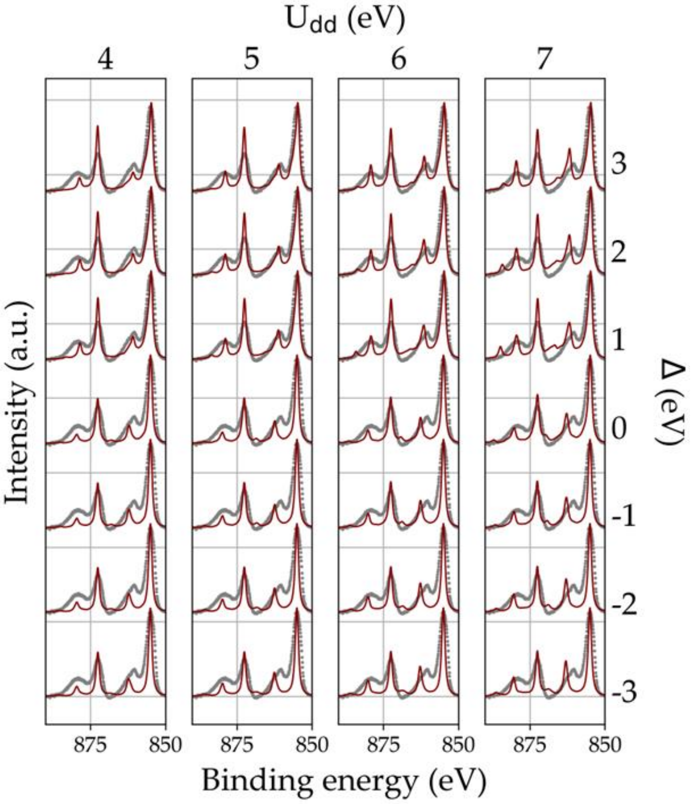

Figure H.2.3 Ni 2p simulations (red line) compared to experimental HAXPES (grey dots) for $LiNiO_2$.

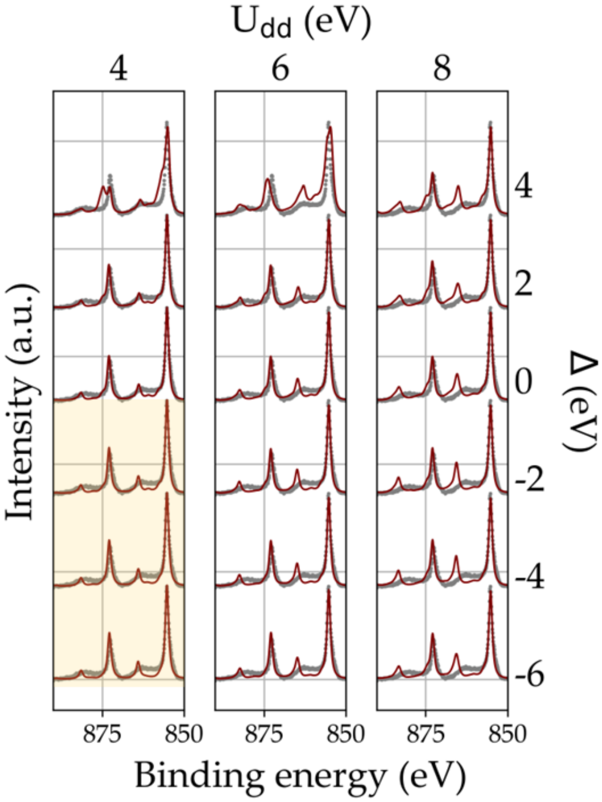

Figure H.2.4 Ni 2p simulations (red line) compared to experimental HAXPES (grey dots) for NiO_2.

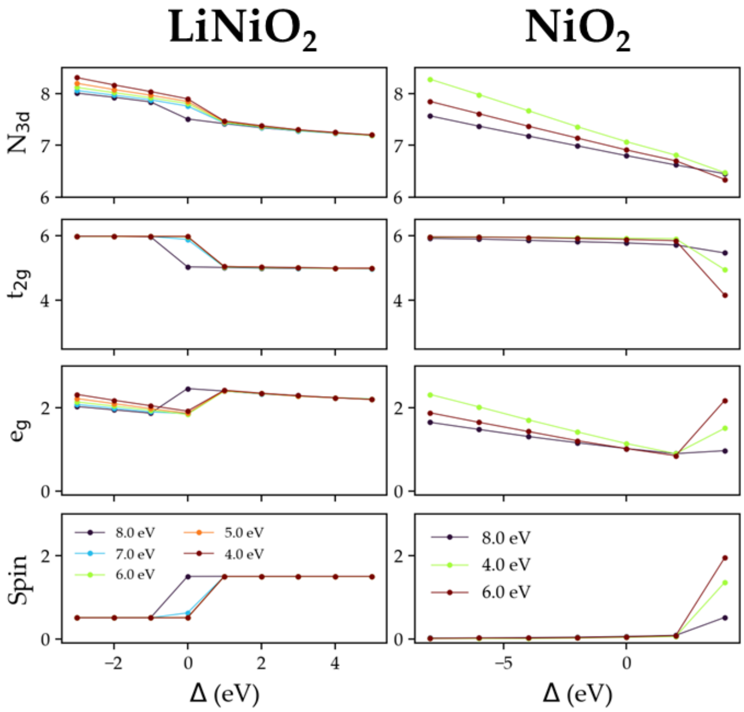

Figure H.2.5 Ground state properties for $LiNiO_2$ and NiO_2 using atomic-like Slater parameters as a function of U and Δ. See paper 3 in Annex I for the $LiCoO_2$ and CoO_2 data obtained with an analogous method.

H.2.2. Li_2MnO_3

We could not treat Li_2MnO_3 the same way as for $LiCoO_2$ and $LiNiO_2$. However, the interpretation of the Mn 2p spectra was less complicated than for the other two materials. The cluster model calculation was performed using the Crispy interface for Quanty based on an approximated MnO_6 octahedra where the O 2p orbitals are combined by linear combination forming a set of five ligand orbitals L [219,380]. The crystal field (10Dq) and overlap (V) parameters for the model are $10Dq_{3d}$ =1.6 eV, $10Dq_L$ = 1.1 eV, V_{eg} = 2.6 eV, and V_{t2g} = 1.2 eV. These parameters were found by comparing the simulation with Mn 2p HAXPES as for U = 5.5 eV and Δ = 3.0 eV, starting from other studies in the literature [279,333]. We emphasize here the strength of the method proposed for Li_xCoO_2 and Li_xNiO_2 systems, as it allows for a more robust determination of the many parameters involved in the simulation.

As shown below, the simulation reproduced overall the experimental Mn 2p spectra including the satellite peak at ~675 eV. We attribute the mismatch in intensity to the background subtraction approximation by the Shirley method. However, as noticed in Chapter 3, the experimental spectrum does not show the characteristic doublet in the main line, which is instead obtained in the simulation. Morita et al. also found this feature, which was confirmed experimentally for Li_2MnO_3 single crystals. Either the powder morphology or surface effects can explain the difference with our experimental observation.

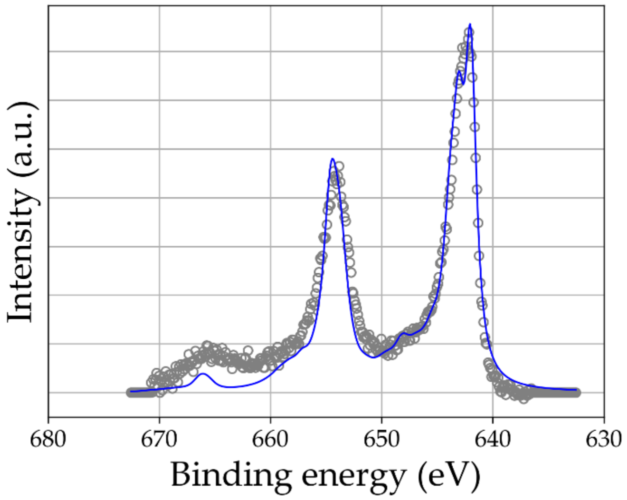

Figure H.2.6 Mn 2p simulation (blue line) compared to experimental HAXPES (grey dots).

Concerning the ground state properties, both the occupation N_d=3.38 and the spin S=2.5 μ_b indicated the $t_{2g}^3e_g^0$ configuration for Mn 3d states as expected for Mn^{IV}. In agreement with Morita et al, we also concluded that Li_2MnO_3 is a charge transfer insulator ($\Delta/U < 1$) [279]. In absence of a strong hybridization with the Mn 3d states (as observed instead for the Li_xCoO_2 and Li_xNiO_2 system), this suggests that the O 2p states are directly involved in the charge compensation mechanism upon delithiation, differing from the participation via the self-regulation mechanism proposed for the other two materials. The valence band analysis (**Section 5.1.2**) and the absence of changes in the experimental Mn 2p spectra for charged Li_xMnO_3 (**Section 4.3.3**) fit with this interpretation. As discussed by Rana et al., however, this mechanism is apparently not stable as it readily destabilizes the oxygen framework by deoxygenation [123].

H.3. Raman spectroscopy analysis of Li_xNiO_2 electrodes

H.3.1. Experimental details

Raman spectroscopy was performed using a Renishaw inVia Raman microscope in backscattering configuration with 532 nm laser excitation and low power (< 0.1 mW/µm² on the sample). The Li_xNiO_2 electrodes were prepared in an Ar-filled glovebox and transferred with a custom dedicated airtight optical sample holder to avoid air exposure. The lateral spatial resolution of the microscope (~1.5 µm) allowed laser focusing on individual Li_xNiO_2 spherical aggregates. Multiple aggregates were systematically analyzed to assess homogeneity of both pristine electrode materials and electrochemical charging process. The estimated laser penetration depth is comparable to the radius of primary $LiNiO_2$ particles (100-200 nm based on reported extinction coefficients [388,389]) and it increases for cycled electrodes [389].

The Raman spectra are shown below. The two main bands are attributed to Ni-O vibration models perpendicular (E_g) and parallel (A_{1g}) to the c-axis according to the R-3m space group. Theoretically, the E_g mode is related to JT-like octahedra distortions, while the A_{1g} mode relates to overall NiO_6 cluster expansion/contraction [47]. Therefore, the bond disproportionation model supported by our HAXPES analysis would perturb the E_g mode while enhancing the A_{1g} one. This is experimentally verified for $LiNiO_2$: its E_g band is particularly broad and with low intensity compared to delithiated samples and even $LiCoO_2$, for which there is no supposed disproportionation and with similar long-range hexagonal crystal structure. Upon delithiation, the lifting of the bond-disproportionation in favor of a more homogeneous and strongly covalent electronic structure is reflected by the narrowing and increased intensity maximum of the E_g mode. Therefore, the local bonding evolution upon deintercalation studied by Raman spectroscopy agrees overall well with the electronic mechanism deduced by HAXPES analyses.

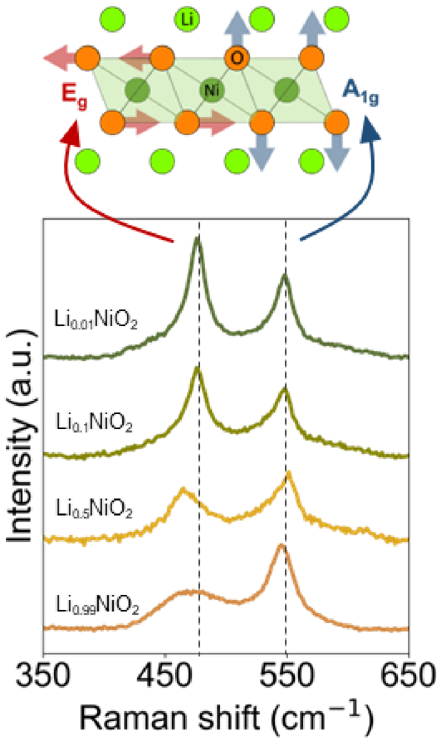

Figure H.3.1 Evolution of local Ni-O bonding investigated by Raman spectroscopy. The dynamical effect of E_g and A_{1g} Raman modes is sketched above the spectra.

I. List of Publications

Paper 1

R. Fantin, A. Van Roekeghem, and A. Benayad, *Revisiting Co 2p Core-level Photoemission in* $LiCoO_2$ *by In-lab Soft and Hard X-ray Photoelectron Spectroscopy: A Depth-dependent Study of Cobalt Electronic Structure*, Surface and Interface Analysis **55**, 489-495 (2023). https://doi.org/10.1002/sia.7167

Paper 2

R. Fantin, A. Van Roekeghem, J.-P. Rueff, and A. Benayad, *Surface analysis insight note: Accounting for X-ray beam damage effects in positive electrode-electrolyte interphase investigations*, Surface and Interface Analysis, **56**, 353-358 (2024). https://doi.org/10.1002/sia.7294

Paper 3

R. Fantin, A. van Roekeghem, and A. Benayad, *Self-Regulated Ligand-Metal Charge Transfer upon Lithium-Ion Deintercalation Process from* $LiCoO_2$ *to* CoO_2, Physical Review X Energy **2**, 043010 (2023). https://doi.org/10.1103/PRXEnergy.2.043010

Paper 4

R. Fantin, T. Jousseaume, R. Ramos, L. Gauthier, A. Van Roekeghem, J.-P. Rueff, and A. Benayad, *Depth-Resolving the Redox Compensation Mechanism in* Li_xNiO_2, ACS Energy Letters, **9**, 1507-1515 (2024). https://doi.org/10.1021/acsenergylett.4c00360

Acknowledgments

Most of the work carried out in this thesis was performed at the LCAE laboratory of CEA-LITEN Grenoble, with punctual but periodic visits to the LMPS laboratory for the simulation part. I thank the respective laboratory directors Jessica Thery and Marion Chandesris for their hosting throughout these years. I am also grateful to the Focus Battery program of CEA for funding this thesis.

My deepest gratitude goes to my advisors Anass Benayad and Ambroise Van Roekeghem, whose merits cannot be adequately expressed in these few lines. Thank you for the daily discussions that fueled my passion for scientific research and for supporting me throughout these three years of scientific and professional growth with outstanding dedication. Your advice on which of the many doors had to be passed through, just opened to have a look inside, or better avoided (facing my stubbornness) has been crucial for me.

I had the opportunity to collaborate with many experienced scientists who helped me throughout the thesis. I thank the LCAE colleagues Johannes Ast, Raphael Ramos, and Gauthier Lefevre for their help with XRD, Raman Spectroscopy, and Scanning Electron Transmission Spectroscopy analyses, respectively. I would like to thank also Thibaut Jousseaume for the synchrotron XRD characterization. I express my gratitude to Christophe Secouard and Maude Bert for their help with the preparation of the $LiCoO_2$ thin films. Many thanks also to David Peralta for the preparation and characterization of the Li_2MnO_3 electrodes and $NaNiO_2$ powder. I am also grateful to Jean-Pascal Rueff for the incredible opportunity to perform synchrotron HAXPES in the Galaxies beamline and for his expertise and support during the experiments. I thank the Hybdriden platform of CEA-IRIG for hosting my battery-related activities and Quentin Jacquet for the stimulating discussions. Furthermore, I thank Renaud Bouchet for supporting ideas outside my main research activities by hosting me for a short time at LEPMI.

Sur une note plus personnelle, je tiens à remercier tous les stagiaires, thésards et post-docs qui j'ai eu le plaisir de croiser pendant ces trois années. Merci bien pour les beaux moments passés ensemble, des pauses café aux soirées amicales : Claire G., Claire S., Guillaume, Joel, Julia, Khawla, Loan, Nicolas, Palmerina, Patrice, Pierre, Pierre-Maire, Thibaut, Thomas J. et Vincent, avec mes excuses pour ceux que j'ai oubliés dans la liste. J'adresse en particulier Roman, Thomas M. et Tarek qui, avec moi, ont formé le bureau des Fantastic Four (avec tout ce que cela implique).

Grazie a tutti coloro che, piombando a Grenoble come me, non solo mi hanno fatto sentire un po' più a casa ma con i quali ho potuto fare nuove esperienze nello sfondo

di questa città, dalle serate in compagnia alle avventure in montagna. Grazie dunque a Lorenzo, Giovanni, Ivana, Riccardo, Marta, Alessio, Ihsane, Lisa, Emanuele, Cecilia, Tommaso, Beatrice, Michele e tutti coloro che avrò dimenticato in questa già lunga lista di fantastiche persone.

Ringrazio inoltre la mia famiglia, che da Jesolo, Granada e Grezzana ha sempre sostenuto le mie scelte e nella quale ho sempre trovato sostegno. Un pensiero in particolare va ai miei genitori, che ogni giorno mi insegnano a non mollare mai e ai quali dedico questo manoscritto di tesi.

Infine, sono certo che queste pagine non esisterebbero senza il sostegno di Giulia. Grazie ancora una volta per la tua infinita pazienza e per tutto il conforto nei momenti più difficili durante questa avventura che è stata il dottorato.

References

[1] United Nations, *THE 17 GOALS | Sustainable Development*, https://sdgs.un.org/goals.

[2] European Council, *Fit for 55*, https://www.consilium.europa.eu/en/policies/green-deal/fit-for-55-the-eu-plan-for-a-green-transition/.

[3] *Battery2030+*, https://battery2030.eu/.

[4] *Roadmap Battery 2030+*, https://battery2030.eu/wp-content/uploads/2023/09/B-2030-Science-Innovation-Roadmap-updated-August-2023.pdf.

[5] J. Amici et al., *A Roadmap for Transforming Research to Invent the Batteries of the Future Designed within the European Large Scale Research Initiative BATTERY 2030+*, Adv. Energy Mater. **12**, 2102785 (2022).

[6] *FOCUS Battery Program*, https://www.cea.fr/cea-tech/liten/english/Pages/Medias/News/Batteries/Focus-batteries.aspx.

[7] S. P. Kühn, K. Edström, M. Winter, and I. Cekic-Laskovic, *Face to Face at the Cathode Electrolyte Interphase: From Interface Features to Interphase Formation and Dynamics*, Adv. Mater. Interfaces **9**, 8 (2022).

[8] M. Zhang et al., *Pushing the Limit of 3d Transition Metal-Based Layered Oxides That Use Both Cation and Anion Redox for Energy Storage*, Nat. Rev. Mater. **7**, 7 (2022).

[9] D. Atkins et al., *Understanding Battery Interfaces by Combined Characterization and Simulation Approaches: Challenges and Perspectives*, Adv. Energy Mater. **12**, 17 (2022).

[10] J. B. Goodenough and K.-S. Park, *The Li-Ion Rechargeable Battery: A Perspective*, J. Am. Chem. Soc. **135**, 1167 (2013).

[11] J. S. Edge et al., *Lithium Ion Battery Degradation: What You Need to Know*, Phys. Chem. Chem. Phys. **23**, 8200 (2021).

[12] M. Bianchini, V. Lacivita, D.-H. Seo, and H. Kim, *Advances and Challenges in Multiscale Characterizations and Analyses for Battery Materials*, J. Mater. Res. **37**, 3113 (2022).

[13] D. Atkins et al., *Accelerating Battery Characterization Using Neutron and Synchrotron Techniques: Toward a Multi-Modal and Multi-Scale Standardized Experimental Workflow*, Adv. Energy Mater. **12**, 2102694 (2022).

[14] J.-M. Tarascon and M. Armand, *Issues and Challenges Facing Rechargeable Lithium Batteries*, Nature **414**, 359 (2001).

[15] D. Atkins et al., *Understanding Battery Interfaces by Combined Characterization and Simulation Approaches: Challenges and Perspectives*, Adv. Energy Mater. **12**, 2102687 (2022).

[16] C. Julien, A. Mauger, K. Zaghib, and H. Groult, *Comparative Issues of Cathode Materials for Li-Ion Batteries*, Inorganics **2**, 132 (2014).

[17] J. T. Frith, M. J. Lacey, and U. Ulissi, *A Non-Academic Perspective on the Future of Lithium-Based Batteries*, Nat. Commun. **14**, 420 (2023).

[18] M. D. Radin, S. Hy, M. Sina, C. Fang, H. Liu, J. Vinckeviciute, M. Zhang, M. S. Whittingham, Y. S. Meng, and A. Van der Ven, *Narrowing the Gap between Theoretical and Practical Capacities in Li-Ion Layered Oxide Cathode Materials*, Adv. Energy Mater. **7**, 1602888 (2017).

[19] J. B. Goodenough and Y. Kim, *Challenges for Rechargeable Li Batteries*, Chem. Mater. **22**, 587 (2010).

[20] M. Gauthier et al., *Electrode–Electrolyte Interface in Li-Ion Batteries: Current Understanding and New Insights*, J. Phys. Chem. Lett. **6**, 4653 (2015).

[21] A. Manthiram, *A Reflection on Lithium-Ion Battery Cathode Chemistry*, Nat. Commun. **11**, 1550 (2020).

[22] R. Schmuch, R. Wagner, G. Hörpel, T. Placke, and M. Winter, *Performance and Cost of Materials for Lithium-Based Rechargeable Automotive Batteries*, Nat. Energy **3**, 267 (2018).

[23] E. J. Berg, C. Villevieille, D. Streich, S. Trabesinger, and P. Novák, *Rechargeable Batteries: Grasping for the Limits of Chemistry*, J. Electrochem. Soc. **162**, A2468 (2015).

[24] N. Nitta, F. Wu, J. T. Lee, and G. Yushin, *Li-Ion Battery Materials: Present and Future*, Mater. Today **18**, 252 (2015).

[25] A. Manthiram, B. Song, and W. Li, *A Perspective on Nickel-Rich Layered Oxide Cathodes for Lithium-Ion Batteries*, Energy Storage Mater. **6**, 125 (2017).

[26] C. Delmas, C. Fouassier, and P. Hagenmuller, *Structural Classification and Properties of the Layered Oxides*, Phys. BC **99**, 81 (1980).

[27] J. M. Tarascon, G. Vaughan, Y. Chabre, L. Seguin, M. Anne, P. Strobel, and G. Amatucci, *In Situ Structural and Electrochemical Study of* $Ni_{1-x}Co_xO_2$ *Metastable Oxides Prepared by Soft Chemistry*, J. Solid State Chem. **147**, 410 (1999).

[28] M. Bianchini, M. Roca-Ayats, P. Hartmann, T. Brezesinski, and J. Janek, *There and Back Again—The Journey of* $LiNiO_2$ *as a Cathode Active Material*, Angew. Chem. Int. Ed. **58**, 10434 (2019).

[29] L. de Biasi, B. Schwarz, T. Brezesinski, P. Hartmann, J. Janek, and H. Ehrenberg, *Chemical, Structural, and Electronic Aspects of Formation and Degradation Behavior on Different Length Scales of Ni-Rich NCM and Li-Rich HE-NCM Cathode Materials in Li-Ion Batteries*, Adv. Mater. **31**, 1900985 (2019).

[30] D.-H. Seo, J. Lee, A. Urban, R. Malik, S. Kang, and G. Ceder, *The Structural and Chemical Origin of the Oxygen Redox Activity in Layered and Cation-Disordered Li-Excess Cathode Materials*, Nat. Chem. **8**, 692 (2016).

[31] M. Saubanère, E. McCalla, J.-M. Tarascon, and M.-L. Doublet, *The Intriguing Question of Anionic Redox in High-Energy Density Cathodes for Li-Ion Batteries*, Energy Environ. Sci. **9**, 984 (2016).

[32] A. Urban, D.-H. Seo, and G. Ceder, *Computational Understanding of Li-Ion Batteries*, Npj Comput. Mater. **2**, 16002 (2016).

[33] M. K. Aydinol, A. F. Kohan, G. Ceder, K. Cho, and J. Joannopoulos, Ab Initio *Study of Lithium Intercalation in Metal Oxides and Metal Dichalcogenides*, Phys. Rev. B **56**, 1354 (1997).

[34] K. Mizushima, P. C. Jones, P. J. Wiseman, and J. B. Goodenough, Li_xCoO_2 $(0<x<1)$*: A New Cathode Material for Batteries of High Energy Density*, Mat Res Bull **15**, 783 (1980).

[35] A. Manthiram and J. B. Goodenough, *Layered Lithium Cobalt Oxide Cathodes*, Nat. Energy **6**, 323 (2021).

[36] M. Zhang et al., *Pushing the Limit of 3d Transition Metal-Based Layered Oxides That Use Both Cation and Anion Redox for Energy Storage*, Nat. Rev. Mater. **7**, 522 (2022).

[37] Y. Tokura, *Correlated-Electron Physics in Transition-Metal Oxides*, Phys. Today **56**, 50 (2003).

[38] G. Kotliar and D. Vollhardt, *Strongly Correlated Materials: Insights From Dynamical Mean-Field Theory*, Physics Today **57**, 53 (2004).

[39] *The Hubbard Model at Half a Century*, Nat. Phys. **9**, 523 (2013).

[40] A. Georges, *The Beauty of Impurities: Two Revivals of Friedel's Virtual Bound-State Concept*, Comptes Rendus Phys. **17**, 430 (2016).

[41] A. Lagendijk, B. van Tiggelen, and D. S. Wiersma, *Fifty Years of Anderson Localization*, Phys. Today **62**, 24 (2009).

[42] G. A. Sawatzky and R. J. Green, *G. Sawatzky and R. J. Green, The Explicit Role of Anion States in High-Valence Metal Oxides*, in *Quantum Materials: Experiments and Theory* (Forschungszentrum, Zentralbibliothek, Jülich, 2016).

[43] J. Zaanen, G. A. Sawatzky, and J. W. Allen, *Band Gaps and Electronic Structure of Transition-Metal Compounds*, Phys. Rev. Lett. **55**, 418 (1985).

[44] J. H. Yang, H. Kim, and G. Ceder, *Insights into Layered Oxide Cathodes for Rechargeable Batteries*, Molecules **26**, 3173 (2021).

[45] A. Awan, H. Truong, and R. J. Lancashire, *Crystal Field Theory*, in *CHEM 211: Foundational Inorganic Chemistry (Nataro)* (Libretexts, 2023).

[46] A. Manthiram, A. Vadivel Murugan, A. Sarkar, and T. Muraliganth, *Nanostructured Electrode Materials for Electrochemical Energy Storage and Conversion*, Energy Environ. Sci. **1**, 621 (2008).

[47] C. A. Marianetti, D. Morgan, and G. Ceder, *First-Principles Investigation of the Cooperative Jahn-Teller Effect for Octahedrally Coordinated Transition-Metal Ions*, Phys. Rev. B **63**, 224304 (2001).

[48] J. B. Goodenough, *Covalent Exchange vs Superexchange in Two Nickel Oxides*, J. Solid State Chem. **127**, 126 (1996).

[49] C. Liu, Z. G. Neale, and G. Cao, *Understanding Electrochemical Potentials of Cathode Materials in Rechargeable Batteries*, Mater. Today **19**, 109 (2016).

[50] A. Manthiram, *A Reflection on Lithium-Ion Battery Cathode Chemistry*, Nat. Commun. **11**, 1550 (2020).

[51] Y. Lyu et al., *An Overview on the Advances of $LiCoO_2$ Cathodes for Lithium-Ion Batteries*, Adv. Energy Mater. **11**, 2000982 (2021).

[52] W. Kong, D. Wong, K. An, J. Zhang, Z. Chen, C. Schulz, Z. Xu, and X. Liu, *Stabilizing the Anionic Redox in 4.6 V $LiCoO_2$ Cathode through Adjusting Oxygen Magnetic Moment*, Adv. Funct. Mater. **32**, 2202679 (2022).

[53] J.-N. Zhang et al., *Trace Doping of Multiple Elements Enables Stable Battery Cycling of $LiCoO_2$ at 4.6 V*, Nat. Energy **4**, 594 (2019).

[54] E. Hu et al., *Oxygen-Redox Reactions in $LiCoO_2$ Cathode without O–O Bonding during Charge-Discharge*, Joule **5**, 720 (2021).

[55] W. E. Gent, G. M. Busse, and K. Z. House, *The Predicted Persistence of Cobalt in Lithium-Ion Batteries*, Nat. Energy **7**, 1132 (2022).

[56] M. Okubo and A. Yamada, *Molecular Orbital Principles of Oxygen-Redox Battery Electrodes*, ACS Appl. Mater. Interfaces **9**, 36463 (2017).

[57] G. Assat and J.-M. Tarascon, *Fundamental Understanding and Practical Challenges of Anionic Redox Activity in Li-Ion Batteries*, Nat. Energy **3**, 373 (2018).

[58] A. Grimaud, W. T. Hong, Y. Shao-Horn, and J.-M. Tarascon, *Anionic Redox Processes for Electrochemical Devices*, Nat. Mater. **15**, 121 (2016).

[59] Y. Xie, M. Saubanère, and M.-L. Doublet, *Requirements for Reversible Extra-Capacity in Li-Rich Layered Oxides for Li-Ion Batteries*, Energy Environ. Sci. **10**, 266 (2017).

[60] E. Pavarini and E. Koch, *Simulating Correlations with Computers* (Forschungszentrum Jülich GmbH, Institute for Advanced Simulation, Jülich, 2021).

[61] V. I. Anisimov, I. V. Solovyev, M. A. Korotin, M. T. Czyżyk, and G. A. Sawatzky, *Density-Functional Theory and NiO Photoemission Spectra*, Phys. Rev. B **48**, 16929 (1993).

[62] G. A. Sawatzky and J. W. Allen, *Magnitude and Origin of the Band Gap in NiO*, Phys. Rev. Lett. **53**, 2339 (1984).

[63] E. Pavarini, E. Koch, J. van den Brink, G. Sawatzky, *Quantum Materials: Experiments and Theory: Lecture Notes of the Autumn School on Correlated Electrons 2016* (Forschungszentrum, Zentralbibliothek, Jülich, 2016).

[64] A. E. Bocquet, T. Mizokawa, K. Morikawa, A. Fujimori, S. R. Barman, K. Maiti, D. D. Sarma, Y. Tokura, and M. Onoda, *Electronic Structure of Early 3*d *-Transition-Metal Oxides by Analysis of the 2* p *Core-Level Photoemission Spectra*, Phys. Rev. B **53**, 1161 (1996).

[65] A. E. Bocquet, T. Mizokawa, T. Saitoh, H. Namatame, and A. Fujimori, *Electronic Structure of 3* d *-Transition-Metal Compounds by Analysis of the 2*p *Core-Level Photoemission Spectra*, Phys. Rev. B **46**, 3771 (1992).

[66] F. M. F. de Groot et al., *2p X-Ray Absorption Spectroscopy of 3d Transition Metal Systems*, J. Electron Spectrosc. Relat. Phenom. **249**, 147061 (2021).

[67] M. S. Whittingham, *Electrical Energy Storage and Intercalation Chemistry*, Science **192**, 1126 (1976).

[68] A. Yoshino, *The Birth of the Lithium-Ion Battery*, Angew. Chem. Int. Ed. **51**, 5798 (2012).

[69] Lithium-Ion Batteries - Scientific Background on the Nobel Prize in Chemistry 2019, The royal swedish academy of sciences, 2019.

[70] J. R. Dahn, U. von Sacken, M. W. Juzkow, and H. Al-Janaby, *Rechargeable $LiNiO_2$ / Carbon Cells*, J. Electrochem. Soc. **138**, 2207 (1991).

[71] J. R. Dahn, U. von Sacken, and C. A. Michal, *Structure and Electrochemistry of $Li_{1+y}NiO_z$ and a New Li_2NiO_2 Phase with the $Ni(OH)_2$ Structure*, Solid State Ion. **44**, 87 (1990).

[72] T. Ohzuku, A. Ueda, and M. Nagayama, *Electrochemistry and Structural Chemistry of $LiNiO_2$ (R3m) for 4 Volt Secondary Lithium Cells*, J. Electrochem. Soc. **140**, 1862 (1993).

[73] T. Ohzuku, A. Ueda, M. Nagayama, Y. Iwakoshi, and H. Komori, *Comparative Study of $LiCoO_2$, $LiNi_{1/2}Co_{1/2}O_2$ and $LiNiO_2$ for 4 Volt Secondary Lithium Cells*, Electrochimica Acta **38**, 1159 (1993).

[74] M. G. S. R. Thomas, W. I. F. David, J. B. Goodenough, and P. Groves, *Synthesis and Structural Characterization of the Normal Spinel $Li[Ni_2]O_4$*, Mater. Res. Bull. **20**, 1137 (1985).

[75] J. van Elp, J. L. Wieland, H. Eskes, P. Kuiper, G. A. Sawatzky, F. M. F. de Groot, and T. S. Turner, *Electronic Structure of CoO, Li-Doped CoO, and LiCoO 2*, Phys. Rev. B **44**, 6090 (1991).

[76] J. van Elp, H. Eskes, P. Kuiper, and G. A. Sawatzky, *Electronic Structure of Li-Doped NiO*, Phys. Rev. B **45**, 1612 (1992).

[77] P. Kuiper, G. Kruizinga, J. Ghijsen, G. A. Sawatzky, and H. Verweij, *Character of Holes in $Li_xNi_{1-x}O$ and Their Magnetic Behavior*, Phys. Rev. Lett. **62**, 221 (1989).

[78] J. N. Reimers and J. R. Dahn, *Electrochemical and In Situ X-Ray Diffraction Studies of Lithium Intercalation in Li_xCoO_2*, J. Electrochem. Soc. **139**, 2091 (1992).

[79] G. G. Amatucci, J. M. Tarascon, and L. C. Klein, *CoO_2, The End Member of the Li_xCoO_2 Solid Solution*, J. Electrochem. Soc. **143**, 1114 (1996).

[80] L. Croguennec, C. Pouillerie, and C. Delmas, *NiO_2 Obtained by Electrochemical Lithium Deintercalation from Lithium Nickelate: Structural Modifications*, J. Electrochem. Soc. (2000).

[81] L. Croguennec, C. Pouillerie, A. N. Mansour, and C. Delmas, *Structural Characterisation of the Highly Deintercalated $Li_xNi_{1.02}O_2$ Phases (with $x \leq 0.30$)*, J. Mater. Chem. **11**, 131 (2001).

[82] W. Li, J. N. Reimers, and J. R. Dahn, *In Situ X-Ray Diffraction and Electrochemical Studies of Li_xNiO_2*, Solid State Ion. **67**, 123 (1993).

[83] H. Li, N. Zhang, J. Li, and J. R. Dahn, *Updating the Structure and Electrochemistry of Li_xNiO_2 for $0 \leq x \leq 1$*, J. Electrochem. Soc. **165**, A2985 (2018).

[84] P. Chien, X. Wu, B. Song, Z. Yang, C. K. Waters, M. S. Everett, F. Lin, Z. Du, and J. Liu, *New Insights into Structural Evolution of $LiNiO_2$ Revealed by Operando Neutron Diffraction*, Batter. Supercaps **4**, 1701 (2021).

[85] M. Mock, M. Bianchini, F. Fauth, K. Albe, and S. Sicolo, *Atomistic Understanding of the* $LiNiO_2$ *–* NiO_2 *Phase Diagram from Experimentally Guided Lattice Models*, J. Mater. Chem. A **9**, 14928 (2021).

[86] K. Mukai, T. Uyama, and T. Nonaka, *Revisiting* $LiCoO_2$ *Using a State-of-the-Art* In Operando *Technique*, Inorg. Chem. **59**, 11113 (2020).

[87] J. Rouxel, *Anion–Cation Redox Competition and the Formation of New Compounds in Highly Covalent Systems*, Chem. - Eur. J. **2**, 1053 (1996).

[88] M. E. Arroyo y de Dompablo, A. Van der Ven, and G. Ceder, *First-Principles Calculations of Lithium Ordering and Phase Stability on* Li_xNiO_2, Phys. Rev. B **66**, 064112 (2002).

[89] A. Van der Ven, M. K. Aydinol, G. Ceder, G. Kresse, and J. Hafner, *First-Principles Investigation of Phase Stability in* Li_xCoO_2, Phys. Rev. B **58**, 2975 (1998).

[90] C. Wolverton and A. Zunger, *First-Principles Prediction of Vacancy Order-Disorder and Intercalation Battery Voltages in* Li_xCoO_2, Phys. Rev. Lett. **81**, 606 (1998).

[91] H. Raebiger, S. Lany, and A. Zunger, *Charge Self-Regulation upon Changing the Oxidation State of Transition Metals in Insulators*, Nature **453**, 763 (2008).

[92] R. Resta, *Charge States in Transition*, Nature **453**, 735 (2008).

[93] M. Jansen and U. Wedig, *A Piece of the Picture-Misunderstanding of Chemical Concepts*, Angew. Chem. Int. Ed. **47**, 10026 (2008).

[94] H. Raebiger, S. Lany, R. Resta, and A. Zunger, *Oxidation Numbers as Social Security Numbers: Are They Predictive or Postdictive?*, Nat. Preced. (2009).

[95] N. C. Norman and P. G. Pringle, *In Defence of Oxidation States*, Dalton Trans. **51**, 400 (2022).

[96] A. J. Webster, C. M. Mueller, N. P. Foegen, P. H.-L. Sit, E. D. Speetzen, D. W. Cunningham, and J. S. D'Acchioli, *Oxidation States "Naturally": A Natural Bond Orbital Method for Determining Transition Metal Oxidation States*, Polyhedron **114**, 128 (2016).

[97] L. Jiang, S. V. Levchenko, and A. M. Rappe, *Rigorous Definition of Oxidation States of Ions in Solids*, Phys. Rev. Lett. **108**, 166403 (2012).

[98] A. Rougier, C. Delmas, and A. V. Chadwick, *Non-Cooperative Jahn-Teller Effect in* $LiNiO_2$*: And EXAFS Study*, Solid State Commun. **94**, 123 (1995).

[99] I. Nakai, K. Takahashi, Y. Shiraishi, T. Nakagome, and F. Nishikawa, *Study of the Jahn–Teller Distortion in* $LiNiO_2$*, a Cathode Material in a Rechargeable Lithium Battery, Byin SituX-Ray Absorption Fine Structure Analysis*, J. Solid State Chem. **140**, 145 (1998).

[100] Z. Lu, D. D. MacNeil, and J. R. Dahn, *Layered* $Li[Ni_xCo_{1-2x}Mn_x]O_2$ *Cathode Materials for Lithium-Ion Batteries*, Electrochem Solid-State Lett **4**, A200 (2001).

[101] D. D. MacNeil, Z. Lu, and J. R. Dahn, *Structure and Electrochemistry of* $Li[Ni_xCo_{1-2x}Mn_x]O_2$ $(0 < x < 1/2)$, J. Electrochem. Soc. **149**, A1332 (2002).

[102] H.-J. Noh, S. Youn, C. S. Yoon, and Y.-K. Sun, *Comparison of the Structural and Electrochemical Properties of Layered* $Li[Ni_xCo_yMn_z]O_2$ *(*$x = 1/3, 0.5, 0.6, 0.7, 0.8$ *and 0.85) Cathode Material for Lithium-Ion Batteries*, J. Power Sources **233**, 121 (2013).

[103] *Cutting Cobalt*, Nat. Energy **5**, 825 (2020).

[104] H. Li, M. Cormier, N. Zhang, J. Inglis, J. Li, and J. R. Dahn, *Is Cobalt Needed in Ni-Rich Positive Electrode Materials for Lithium Ion Batteries?*, J. Electrochem. Soc. **166**, A429 (2019).

[105] T. Mizokawa, Y. Wakisaka, T. Sudayama, C. Iwai, K. Miyoshi, J. Takeuchi, H. Wadati, D. G. Hawthorn, T. Z. Regier, and G. A. Sawatzky, *Role of Oxygen Holes in* Li_xCoO_2 *Revealed by Soft X-Ray Spectroscopy*, Phys. Rev. Lett. **111**, 056404 (2013).

[106] W.-S. Yoon, K.-B. Kim, M.-G. Kim, M.-K. Lee, H.-J. Shin, J.-M. Lee, J.-S. Lee, and C.-H. Yo, *Oxygen Contribution on Li-Ion Intercalation−Deintercalation in* $LiCoO_2$ *Investigated by O K-Edge and Co L-Edge X-Ray Absorption Spectroscopy*, J. Phys. Chem. B **106**, 2526 (2002).

[107] L. A. Montoro, M. Abbate, and J. M. Rosolen, *Changes in the Electronic Structure of Chemically Deintercalated $LiCoO_2$*, Electrochem Solid-State Lett (2000).

[108] L. Dahéron, R. Dedryvère, H. Martinez, M. Ménétrier, C. Denage, C. Delmas, and D. Gonbeau, *Electron Transfer Mechanisms upon Lithium Deintercalation from $LiCoO_2$ to CoO_2 Investigated by XPS*, Chem. Mater. **20**, 583 (2008).

[109] D. Ensling, G. Cherkashinin, S. Schmid, S. Bhuvaneswari, A. Thissen, and W. Jaegermann, *Nonrigid Band Behavior of the Electronic Structure of $LiCoO_2$ Thin Film during Electrochemical Li Deintercalation*, Chem. Mater. **26**, 3948 (2014).

[110] K. Ikedo, Y. Wakisaka, T. Mizokawa, C. Iwai, K. Miyoshi, and J. Takeuchi, *Electronic Structure of Li_xCoO_2 Studied by Photoemission Spectroscopy and Unrestricted Hartree-Fock Calculations*, Phys. Rev. B **82**, 075126 (2010).

[111] Z. Chen and J. R. Dahn, *Methods to Obtain Excellent Capacity Retention in $LiCoO_2$ Cycled to 4.5 V*, Electrochimica Acta **49**, 1079 (2004).

[112] K. Foyevtsova, I. Elfimov, J. Rottler, and G. A. Sawatzky, *$LiNiO_2$ as a High-Entropy Charge- and Bond-Disproportionated Glass*, Phys. Rev. B **100**, 165104 (2019).

[113] Dm. M. Korotin, D. Novoselov, and V. I. Anisimov, *Paraorbital Ground State of the Trivalent Ni Ion in $LiNiO_2$ from DFT+DMFT Calculations*, Phys. Rev. B **99**, 045106 (2019).

[114] S. Sicolo, M. Mock, M. Bianchini, and K. Albe, *And Yet It Moves: $LiNiO_2$, a Dynamic Jahn–Teller System*, Chem. Mater. **32**, 10096 (2020).

[115] V. Bisogni et al., *Ground-State Oxygen Holes and the Metal–Insulator Transition in the Negative Charge-Transfer Rare-Earth Nickelates*, Nat. Commun. **7**, 13017 (2016).

[116] A. D. Poletayev, J. P. Cottom, B. J. Morgan, and M. S. Islam, *Temperature-Dependent Dynamic Disproportionation in $LiNiO_2$*, (2022).

[117] Z. Lu and J. R. Dahn, *Understanding the Anomalous Capacity of $Li/Li[Ni_xLi_{(1/3-2x/3)}Mn_{(2/3-x/3)}]O_2$ Cells Using In Situ X-Ray Diffraction and Electrochemical Studies*, J. Electrochem. Soc. **149**, A815 (2002).

[118] K. Luo et al., *Anion Redox Chemistry in the Cobalt Free 3d Transition Metal Oxide Intercalation Electrode $Li[Li_{0.2}Ni_{0.2}Mn_{0.6}]O_2$*, J. Am. Chem. Soc. **138**, 11211 (2016).

[119] K. Luo et al., *Charge-Compensation in 3d-Transition-Metal-Oxide Intercalation Cathodes through the Generation of Localized Electron Holes on Oxygen*, Nat. Chem. **8**, 684 (2016).

[120] P. Kalyani, S. Chitra, T. Mohan, and S. Gopukumar, *Lithium Metal Rechargeable Cells Using Li_2MnO_3 as the Positive Electrode*, J. Power Sources **80**, 103 (1999).

[121] A. D. Robertson and P. G. Bruce, *Mechanism of Electrochemical Activity in Li_2MnO_3*, Chem. Mater. **15**, 1984 (2003).

[122] D. Y. W. Yu, K. Yanagida, Y. Kato, and H. Nakamura, *Electrochemical Activities in Li_2MnO_3*, J. Electrochem. Soc. **156**, A417 (2009).

[123] J. Rana et al., *Quantifying the Capacity Contributions during Activation of Li_2MnO_3*, ACS Energy Lett. **5**, 634 (2020).

[124] Z. Lu, D. D. MacNeil, and J. R. Dahn, *Layered Cathode Materials $Li[Ni_xLi_{(1/3-2x/3)}Mn_{(2/3-x/3)}O_2$ for Lithium-Ion Batteries*, Electrochem Solid-State Lett **4**, A191 (2001).

[125] M. M. Thackeray, S.-H. Kang, C. S. Johnson, J. T. Vaughey, R. Benedek, and S. A. Hackney, *Li_2MnO_3-Stabilized $LiMO_2$ (M = Mn, Ni, Co) Electrodes for Lithium-Ion Batteries*, J. Mater. Chem. **17**, 3112 (2007).

[126] H. Koga, L. Croguennec, M. Ménétrier, K. Douhil, S. Belin, L. Bourgeois, E. Suard, F. Weill, and C. Delmas, *Reversible Oxygen Participation to the Redox Processes Revealed for $Li_{1.20}Mn_{0.54}Co_{0.13}Ni_{0.13}O_2$*, J. Electrochem. Soc. **160**, A786 (2013).

[127] H. Koga, L. Croguennec, M. Ménétrier, P. Mannessiez, F. Weill, C. Delmas, and S. Belin, *Operando X-Ray Absorption Study of the Redox Processes Involved upon Cycling of the Li-Rich Layered Oxide* $Li_{1.20}Mn_{0.54}Co_{0.13}Ni_{0.13}O_2$ *in Li Ion Batteries*, J. Phys. Chem. C **118**, 5700 (2014).

[128] H. Koga, L. Croguennec, M. Ménétrier, P. Mannessiez, F. Weill, and C. Delmas, *Different Oxygen Redox Participation for Bulk and Surface: A Possible Global Explanation for the Cycling Mechanism of* $Li_{1.20}Mn_{0.54}Co_{0.13}Ni_{0.13}O_2$, J. Power Sources **236**, 250 (2013).

[129] G. Assat, A. Iadecola, D. Foix, R. Dedryvère, and J.-M. Tarascon, *Direct Quantification of Anionic Redox over Long Cycling of Li-Rich NMC via Hard X-Ray Photoemission Spectroscopy*, ACS Energy Lett. **3**, 2721 (2018).

[130] W. E. Gent et al., *Coupling between Oxygen Redox and Cation Migration Explains Unusual Electrochemistry in Lithium-Rich Layered Oxides*, Nat. Commun. **8**, 2091 (2017).

[131] Z. W. Lebens-Higgins et al., *How Bulk Sensitive Is Hard X-Ray Photoelectron Spectroscopy: Accounting for the Cathode–Electrolyte Interface When Addressing Oxygen Redox*, J. Phys. Chem. Lett. **11**, 2106 (2020).

[132] M. Sathiya et al., *Reversible Anionic Redox Chemistry in High-Capacity Layered-Oxide Electrodes*, Nat. Mater. **12**, 827 (2013).

[133] G. Assat, C. Delacourt, D. A. D. Corte, and J.-M. Tarascon, *Practical Assessment of Anionic Redox in Li-Rich Layered Oxide Cathodes: A Mixed Blessing for High Energy Li-Ion Batteries*, J. Electrochem. Soc. **163**, A2965 (2016).

[134] D. Foix, M. Sathiya, E. McCalla, J.-M. Tarascon, and D. Gonbeau, *X-Ray Photoemission Spectroscopy Study of Cationic and Anionic Redox Processes in High-Capacity Li-Ion Battery Layered-Oxide Electrodes*, J. Phys. Chem. C **120**, 862 (2016).

[135] K. Shimoda, T. Minato, K. Nakanishi, H. Komatsu, T. Matsunaga, H. Tanida, H. Arai, Y. Ukyo, Y. Uchimoto, and Z. Ogumi, *Oxidation Behaviour of Lattice Oxygen in Li-Rich Manganese-Based Layered Oxide Studied by Hard X-Ray Photoelectron Spectroscopy*, J. Mater. Chem. A **4**, 5909 (2016).

[136] W. Yang and T. P. Devereaux, *Anionic and Cationic Redox and Interfaces in Batteries: Advances from Soft X-Ray Absorption Spectroscopy to Resonant Inelastic Scattering*, J. Power Sources **389**, 188 (2018).

[137] A. S. Menon et al., *Oxygen-Redox Activity in Non-Lithium-Excess Tungsten-Doped* $LiNiO_2$ *Cathode*, PRX Energy **2**, 013005 (2023).

[138] J.-C. Dupin, D. Gonbeau, P. Vinatier, and A. Levasseur, *Systematic XPS Studies of Metal Oxides, Hydroxides and Peroxides*, Phys. Chem. Chem. Phys. **2**, 1319 (2000).

[139] G. Assat, D. Foix, C. Delacourt, A. Iadecola, R. Dedryvère, and J.-M. Tarascon, *Fundamental Interplay between Anionic/Cationic Redox Governing the Kinetics and Thermodynamics of Lithium-Rich Cathodes*, Nat. Commun. **8**, 2219 (2017).

[140] A. J. Naylor et al., *Depth-Dependent Oxygen Redox Activity in Lithium-Rich Layered Oxide Cathodes*, J. Mater. Chem. A **7**, 25355 (2019).

[141] B. Li et al., *Capturing Dynamic Ligand-to-Metal Charge Transfer with a Long-Lived Cationic Intermediate for Anionic Redox*, Nat. Mater. **21**, 1165 (2022).

[142] B. Li et al., *Correlating Ligand-to-Metal Charge Transfer with Voltage Hysteresis in a Li-Rich Rock-Salt Compound Exhibiting Anionic Redox*, Nat. Chem. **13**, 1070 (2021).

[143] N. Li, S. Sallis, J. K. Papp, J. Wei, B. D. McCloskey, W. Yang, and W. Tong, *Unraveling the Cationic and Anionic Redox Reactions in a Conventional Layered Oxide Cathode*, ACS Energy Lett. **4**, 2836 (2019).

[144] G. Lee, J. Wu, D. Kim, K. Cho, M. Cho, W. Yang, and Y. Kang, *Reversible Anionic Redox Activities in Conventional* $LiNi_{1/3}Co_{1/3}Mn_{1/3}O_2$ *Cathodes*, Angew. Chem. Int. Ed. **59**, 8681 (2020).

[145] Z. W. Lebens-Higgins et al., *Revisiting the Charge Compensation Mechanisms in* $LiNi_{0.8}Co_{0.2-y}Al_yO_2$ *Systems*, Mater. Horiz. **6**, 2112 (2019).

[146] K. Wang, J. Wan, Y. Xiang, J. Zhu, Q. Leng, M. Wang, L. Xu, and Y. Yang, *Recent Advances and Historical Developments of High Voltage Lithium Cobalt Oxide Materials for Rechargeable Li-Ion Batteries*, J. Power Sources **460**, 228062 (2020).

[147] E. B. Isaacs and C. A. Marianetti, *Compositional Phase Stability of Correlated Electron Materials within DFT + DMFT*, Phys. Rev. B **102**, 045146 (2020).

[148] A. R. Genreith-Schriever, H. Banerjee, A. S. Menon, E. N. Bassey, L. F. J. Piper, C. P. Grey, and A. J. Morris, *Oxygen Hole Formation Controls Stability in* $LiNiO_2$ *Cathodes*, Joule **7**, 1623 (2023).

[149] H. Huang et al., *Unusual Double Ligand Holes as Catalytic Active Sites in* $LiNiO_2$, Nat. Commun. **14**, 2112 (2023).

[150] J. Reed and G. Ceder, *Role of Electronic Structure in the Susceptibility of Metastable Transition-Metal Oxide Structures to Transformation*, Chem. Rev. **104**, 4513 (2004).

[151] J. Reed and G. Ceder, *Layered-to-Spinel Phase Transition in* Li_xMnO_2, Electrochem Solid-State Lett **4**, A78 (2001).

[152] R. Jung, M. Metzger, F. Maglia, C. Stinner, and H. A. Gasteiger, *Oxygen Release and Its Effect on the Cycling Stability of* $LiNi_xMn_yCo_zO_2$ *(NMC) Cathode Materials for Li-Ion Batteries*, J. Electrochem. Soc. **164**, A1361 (2017).

[153] F. Kong, C. Liang, L. Wang, Y. Zheng, S. Perananthan, R. C. Longo, J. P. Ferraris, M. Kim, and K. Cho, *Kinetic Stability of Bulk* $LiNiO_2$ *and Surface Degradation by Oxygen Evolution in* $LiNiO_2$ *-Based Cathode Materials*, Adv. Energy Mater. **9**, 1802586 (2019).

[154] S. Han, Y. Xia, Z. Wei, B. Qiu, L. Pan, Q. Gu, Z. Liu, and Z. Guo, *A Comparative Study on the Oxidation State of Lattice Oxygen among* $Li_{1.14}Ni_{0.136}Co_{0.136}Mn_{0.544}O_2$, Li_2MnO_3 , $LiNi_{0.5}Co_{0.2}Mn_{0.3}O_2$ *and* $LiCoO_2$ *for the Initial Charge–Discharge*, J. Mater. Chem. A **3**, 11930 (2015).

[155] L. Hartmann, D. Pritzl, H. Beyer, and H. A. Gasteiger, *Evidence for* Li^+/H^+ *Exchange during Ambient Storage of Ni-Rich Cathode Active Materials*, J. Electrochem. Soc. **168**, 070507 (2021).

[156] A. O. Kondrakov et al., *Charge-Transfer-Induced Lattice Collapse in Ni-Rich NCM Cathode Materials during Delithiation*, J. Phys. Chem. C **121**, 24381 (2017).

[157] A. O. Kondrakov, A. Schmidt, J. Xu, H. Geßwein, R. Mönig, P. Hartmann, H. Sommer, T. Brezesinski, and J. Janek, *Anisotropic Lattice Strain and Mechanical Degradation of High- and Low-Nickel NCM Cathode Materials for Li-Ion Batteries*, J. Phys. Chem. C **121**, 3286 (2017).

[158] D. J. Miller, C. Proff, J. G. Wen, D. P. Abraham, and J. Bareño, *Observation of Microstructural Evolution in Li Battery Cathode Oxide Particles by In Situ Electron Microscopy*, Adv. Energy Mater. **3**, 1098 (2013).

[159] S. Schweidler, M. Bianchini, P. Hartmann, T. Brezesinski, and J. Janek, *The Sound of Batteries: An Operando Acoustic Emission Study of the* $LiNiO_2$ *Cathode in Li–Ion Cells*, Batter. Supercaps **3**, 1021 (2020).

[160] E. Trevisanello, R. Ruess, G. Conforto, F. H. Richter, and J. Janek, *Polycrystalline and Single Crystalline NCM Cathode Materials—Quantifying Particle Cracking, Active Surface Area, and Lithium Diffusion*, Adv. Energy Mater. **11**, 2003400 (2021).

[161] R. Ruess, S. Schweidler, H. Hemmelmann, G. Conforto, A. Bielefeld, D. A. Weber, J. Sann, M. T. Elm, and J. Janek, *Influence of NCM Particle Cracking on Kinetics of Lithium-Ion Batteries with Liquid or Solid Electrolyte*, J. Electrochem. Soc. **167**, 100532 (2020).

[162] F. Friedrich, B. Strehle, A. T. S. Freiberg, K. Kleiner, S. J. Day, C. Erk, M. Piana, and H. A. Gasteiger, *Capacity Fading Mechanisms of NCM-811 Cathodes in Lithium-Ion Batteries Studied by X-Ray Diffraction and Other Diagnostics*, J. Electrochem. Soc. **166**, A3760 (2019).

[163] N. Schulz, R. Hausbrand, C. Wittich, L. Dimesso, and W. Jaegermann, *XPS-Surface Analysis of SEI Layers on Li-Ion Cathodes: Part II. SEI-Composition and Formation inside Composite Electrodes*, J. Electrochem. Soc. **165**, A833 (2018).

[164] W. Li, A. Dolocan, P. Oh, H. Celio, S. Park, J. Cho, and A. Manthiram, *Dynamic Behaviour of Interphases and Its Implication on High-Energy-Density Cathode Materials in Lithium-Ion Batteries*, Nat. Commun. **8**, 14589 (2017).

[165] R. Jung, R. Morasch, P. Karayaylali, K. Phillips, F. Maglia, C. Stinner, Y. Shao-Horn, and H. A. Gasteiger, *Effect of Ambient Storage on the Degradation of Ni-Rich Positive Electrode Materials (NMC811) for Li-Ion Batteries*, J. Electrochem. Soc. **165**, A132 (2018).

[166] N. Schulz, R. Hausbrand, L. Dimesso, and W. Jaegermann, *XPS-Surface Analysis of SEI Layers on Li-Ion Cathodes: Part I. Investigation of Initial Surface Chemistry*, J. Electrochem. Soc. **165**, A819 (2018).

[167] H. S. Liu, Z. R. Zhang, Z. L. Gong, and Y. Yang, *Origin of Deterioration for $LiNiO_2$ Cathode Material during Storage in Air*, (2004).

[168] A. Laurita, L. Zhu, P.-E. Cabelguen, J. Auvergniot, J. Hamon, D. Guyomard, N. Dupré, and P. Moreau, *Pristine Surface of Ni-Rich Layered Transition Metal Oxides as a Premise of Surface Reactivity*, ACS Appl. Mater. Interfaces **14**, 41945 (2022).

[169] L. Mu et al., *The Sensitive Surface Chemistry of Co-Free, Ni-Rich Layered Oxides: Identifying Experimental Conditions That Influence Characterization Results*, J. Mater. Chem. A **8**, 17487 (2020).

[170] J.-N. Zhang, Q. Li, Y. Wang, J. Zheng, X. Yu, and H. Li, *Dynamic Evolution of Cathode Electrolyte Interphase (CEI) on High Voltage $LiCoO_2$ Cathode and Its Interaction with Li Anode*, Energy Storage Mater. **14**, 1 (2018).

[171] E. Peled, D. Golodnitsky, and G. Ardel, *Advanced Model for Solid Electrolyte Interphase Electrodes in Liquid and Polymer Electrolytes*, J. Electrochem. Soc. **144**, L208 (1997).

[172] A. Benayad, J. E. Morales-Ugarte, C. C. Santini, and R. Bouchet, *Operando XPS: A Novel Approach for Probing the Lithium/Electrolyte Interphase Dynamic Evolution*, J. Phys. Chem. A **125**, 1069 (2021).

[173] B. Philippe, M. Hahlin, K. Edström, T. Gustafsson, H. Siegbahn, and H. Rensmo, *Photoelectron Spectroscopy for Lithium Battery Interface Studies*, J. Electrochem. Soc. **163**, A178 (2016).

[174] R. Dedryvère, S. Laruelle, S. Grugeon, L. Gireaud, J.-M. Tarascon, and D. Gonbeau, *XPS Identification of the Organic and Inorganic Components of the Electrode/Electrolyte Interface Formed on a Metallic Cathode*, J. Electrochem. Soc. **152**, A689 (2005).

[175] S. Malmgren, K. Ciosek, M. Hahlin, T. Gustafsson, M. Gorgoi, H. Rensmo, and K. Edström, *Comparing Anode and Cathode Electrode/Electrolyte Interface Composition and Morphology Using Soft and Hard X-Ray Photoelectron Spectroscopy*, Electrochimica Acta **97**, 23 (2013).

[176] G. Cherkashinin, K. Nikolowski, H. Ehrenberg, S. Jacke, L. Dimesso, and W. Jaegermann, *The Stability of the SEI Layer, Surface Composition and the Oxidation State of Transition Metals at the Electrolyte–Cathode Interface Impacted by the Electrochemical Cycling: X-Ray Photoelectron Spectroscopy Investigation*, Phys. Chem. Chem. Phys. **14**, 12321 (2012).

[177] S. Fang, D. Jackson, M. L. Dreibelbis, T. F. Kuech, and R. J. Hamers, *Anode-Originated SEI Migration Contributes to Formation of Cathode-Electrolyte Interphase Layer*, J. Power Sources **373**, 184 (2018).

[178] P. Verma, P. Maire, and P. Novák, *A Review of the Features and Analyses of the Solid Electrolyte Interphase in Li-Ion Batteries*, Electrochimica Acta **55**, 6332 (2010).

[179] I. Takahashi, H. Kiuchi, A. Ohma, T. Fukunaga, and E. Matsubara, *Cathode Electrolyte Interphase Formation and Electrolyte Oxidation Mechanism for Ni-Rich Cathode Materials*, J. Phys. Chem. C **124**, 9243 (2020).

[180] C. Lee, Y. Yokoyama, Y. Kondo, Y. Miyahara, T. Abe, and K. Miyazaki, *Cathode-Electrolyte-Interphase Film Formation on a $LiNiO_2$ Surface in Conventional Aqueous Electrolytes: Simple Method to Improve the Electrochemical Performance of $LiNiO_2$ Electrodes for Use in Aqueous Li-Ion Batteries*, Adv. Energy Mater. **11**, 2100756 (2021).

[181] S. Oswald, D. Mikhailova, F. Scheiba, P. Reichel, A. Fiedler, and H. Ehrenberg, *XPS Investigations of Electrolyte/Electrode Interactions for Various Li-Ion Battery Materials*, Anal. Bioanal. Chem. **400**, 691 (2011).

[182] K. Edström, T. Gustafsson, and J. O. Thomas, *The Cathode–Electrolyte Interface in the Li-Ion Battery*, Electrochimica Acta **50**, 397 (2004).

[183] D. Ensling, A. Thissen, and W. Jaegermann, *On the Formation of Lithium Oxides and Carbonates on Li Metal Electrodes in Comparison to $LiCoO_2$ Surface Phases Investigated by Photoelectron Spectroscopy*, Appl. Surf. Sci. **255**, 2517 (2008).

[184] N. Gauthier, C. Courrèges, J. Demeaux, C. Tessier, and H. Martinez, *Probing the In-Depth Distribution of Organic/Inorganic Molecular Species within the SEI of LTO/NMC and LTO/LMO Batteries: A Complementary ToF-SIMS and XPS Study*, Appl. Surf. Sci. **501**, 144266 (2020).

[185] S.-K. Otto, Y. Moryson, T. Krauskopf, K. Peppler, J. Sann, J. Janek, and A. Henss, *In-Depth Characterization of Lithium-Metal Surfaces with XPS and ToF-SIMS: Toward Better Understanding of the Passivation Layer*, Chem. Mater. **33**, 859 (2021).

[186] P. Niehoff and M. Winter, *Composition and Growth Behavior of the Surface and Electrolyte Decomposition Layer of/on a Commercial Lithium Ion Battery $Li_xNi_{1/3}Mn_{1/3}Co_{1/3}O_2$ Cathode Determined by Sputter Depth Profile X-Ray Photoelectron Spectroscopy*, Langmuir **29**, 15813 (2013).

[187] L. Wheatcroft, N. Klingner, R. Heller, G. Hlawacek, D. Özkaya, J. Cookson, and B. J. Inkson, *Visualization and Chemical Characterization of the Cathode Electrolyte Interphase Using He-Ion Microscopy and* In Situ *Time-of-Flight Secondary Ion Mass Spectrometry*, ACS Appl. Energy Mater. **3**, 8822 (2020).

[188] Y. Yamagishi, H. Morita, Y. Nomura, and E. Igaki, *Visualizing Lithium Distribution and Degradation of Composite Electrodes in Sulfide-Based All-Solid-State Batteries Using* Operando *Time-of-Flight Secondary Ion Mass Spectrometry*, ACS Appl. Mater. Interfaces **13**, 580 (2021).

[189] H. Sheng et al., *An Air-Stable High-Nickel Cathode with Reinforced Electrochemical Performance Enabled by Convertible Amorphous Li_2CO_3 Modification*, Adv. Mater. **34**, 2108947 (2022).

[190] Z. Zhang et al., *Cathode-Electrolyte Interphase in Lithium Batteries Revealed by Cryogenic Electron Microscopy*, Matter **4**, 302 (2021).

[191] E. Bautista Quisbert, F. Fauth, A. M. Abakumov, M. Blangero, M. Guignard, and C. Delmas, *Understanding the High Voltage Behavior of $LiNiO_2$ Through the Electrochemical Properties of the Surface Layer*, Small 2300616 (2023).

[192] F. Lin, I. M. Markus, D. Nordlund, T.-C. Weng, M. D. Asta, H. L. Xin, and M. M. Doeff, *Surface Reconstruction and Chemical Evolution of Stoichiometric Layered Cathode Materials for Lithium-Ion Batteries*, Nat. Commun. **5**, 3529 (2014).

[193] J. Kikkawa, S. Terada, A. Gunji, T. Nagai, K. Kurashima, and K. Kimoto, *Chemical States of Overcharged $LiCoO_2$ Particle Surfaces and Interiors Observed Using Electron Energy-Loss Spectroscopy*, J. Phys. Chem. C **119**, 15823 (2015).

[194] C. Xu et al., *Bulk Fatigue Induced by Surface Reconstruction in Layered Ni-Rich Cathodes for Li-Ion Batteries*, Nat. Mater. **20**, 84 (2021).

[195] F. Lin, D. Nordlund, I. M. Markus, T.-C. Weng, H. L. Xin, and M. M. Doeff, *Profiling the Nanoscale Gradient in Stoichiometric Layered Cathode Particles for Lithium-Ion Batteries*, Energy Environ. Sci. **7**, 3077 (2014).

[196] T. Li, X.-Z. Yuan, L. Zhang, D. Song, K. Shi, and C. Bock, *Degradation Mechanisms and Mitigation Strategies of Nickel-Rich NMC-Based Lithium-Ion Batteries*, Electrochem. Energy Rev. **3**, 43 (2020).

[197] A. Boulineau, L. Simonin, J.-F. Colin, C. Bourbon, and S. Patoux, *First Evidence of Manganese–Nickel Segregation and Densification upon Cycling in Li-Rich Layered Oxides for Lithium Batteries*, Nano Lett. **13**, 3857 (2013).

[198] Y. Jiang, C. Qin, P. Yan, and M. Sui, *Origins of Capacity and Voltage Fading of $LiCoO_2$ upon High Voltage Cycling*, J. Mater. Chem. A **7**, 20824 (2019).

[199] W. Wang, Q. Yang, K. Qian, and B. Li, *Impact of Evolution of Cathode Electrolyte Interface of $Li(Ni_{0.8}Co_{0.1}Mn_{0.1})O_2$ on Electrochemical Performance during High Voltage Cycling Process*, J. Energy Chem. **47**, 72 (2020).

[200] R. Fantin, E. Trevisanello, R. Ruess, A. Pokle, G. Conforto, F. H. Richter, K. Volz, and J. Janek, *Synthesis and Postprocessing of Single-Crystalline $LiNi_{0.8}Co_{0.15}Al_{0.05}O_2$ for Solid-State Lithium-Ion Batteries with High Capacity and Long Cycling Stability*, Chem. Mater. **33**, 2624 (2021).

[201] X. Liu et al., *Revealing the Surface-to-Bulk Degradation Mechanism of Nickel-Rich Cathode in Sulfide All-Solid-State Batteries*, Energy Storage Mater. **54**, 713 (2023).

[202] Z. Wang, D. Santhanagopalan, W. Zhang, F. Wang, H. L. Xin, K. He, J. Li, N. Dudney, and Y. S. Meng, *In Situ STEM-EELS Observation of Nanoscale Interfacial Phenomena in All-Solid-State Batteries*, Nano Lett. **16**, 3760 (2016).

[203] Y. Koyama, T. Mizoguchi, H. Ikeno, and I. Tanaka, *Electronic Structure of Lithium Nickel Oxides by Electron Energy Loss Spectroscopy*, J. Phys. Chem. B **109**, 10749 (2005).

[204] S. Oswald and H. A. Gasteiger, *The Structural Stability Limit of Layered Lithium Transition Metal Oxides Due to Oxygen Release at High State of Charge and Its Dependence on the Nickel Content*, J. Electrochem. Soc. **170**, 030506 (2023).

[205] J. K. Papp, N. Li, L. A. Kaufman, A. J. Naylor, R. Younesi, W. Tong, and B. D. McCloskey, *A Comparison of High Voltage Outgassing of $LiCoO_2$, $LiNiO_2$, and Li_2MnO_3 Layered Li-Ion Cathode Materials*, Electrochimica Acta **368**, 137505 (2021).

[206] L. A. Kaufman, T.-Y. Huang, D. Lee, and B. D. McCloskey, *Particle Surface Cracking Is Correlated with Gas Evolution in High-Ni Li-Ion Cathode Materials*, ACS Appl. Mater. Interfaces **14**, 39959 (2022).

[207] C. R. Birkl, M. R. Roberts, E. McTurk, P. G. Bruce, and D. A. Howey, *Degradation Diagnostics for Lithium Ion Cells*, J. Power Sources **341**, 373 (2017).

[208] J. Kasnatscheew et al., *The Truth about the 1st Cycle Coulombic Efficiency of $LiNi_{1/3}Co_{1/3}Mn_{1/3}O_2$ (NCM) Cathodes*, Phys. Chem. Chem. Phys. **18**, 3956 (2016).

[209] H. Zhou, F. Xin, B. Pei, and M. S. Whittingham, *What Limits the Capacity of Layered Oxide Cathodes in Lithium Batteries?*, ACS Energy Lett. **4**, 1902 (2019).

[210] F. Riewald, P. Kurzhals, M. Bianchini, H. Sommer, J. Janek, and H. A. Gasteiger, *The $LiNiO_2$ Cathode Active Material: A Comprehensive Study of Calcination Conditions and Their Correlation with Physicochemical Properties Part II. Morphology*, J. Electrochem. Soc. **169**, 020529 (2022).

[211] P. Kurzhals, F. Riewald, M. Bianchini, H. Sommer, H. A. Gasteiger, and J. Janek, *The $LiNiO_2$ Cathode Active Material: A Comprehensive Study of Calcination Conditions and Their Correlation with Physicochemical Properties. Part I. Structural Chemistry*, J. Electrochem. Soc. **168**, 110518 (2021).

[212] C. Kalha et al., *Hard X-Ray Photoelectron Spectroscopy: A Snapshot of the State-of-the-Art in 2020*, J. Phys. Condens. Matter **33**, 233001 (2021).

[213] J. Woicik, editor , *Hard X-Ray Photoelectron Spectroscopy (HAXPES)*, Vol. 59 (Springer International Publishing, Cham, 2016).

[214] L. E. Strange, M. H. Engelhard, C. D. Easton, J. Kim, and D. R. Baer, *Surface Analysis Insight Note: X-ray Photoelectron Spectroscopy Analysis of Battery Electrodes—Challenges with Nickel–*

Manganese–Cobalt and Li Examples Using an Al Kα X-ray Source, Surf. Interface Anal. **55**, 715 (2023).

[215] O. Bondarchuk, A. P. LaGrow, A. Kvasha, T. Thieu, E. Ayerbe, and I. Urdampilleta, *On the X-Ray Photoelectron Spectroscopy Analysis of* $LiNi_xMn_yCo_zO_2$ *Material and Electrodes*, Appl. Surf. Sci. **535**, 147699 (2021).

[216] A. Laurita, Characterisation of the Surface Reactivity of Ni-Rich Positive Electrode Materials for Li-Ion Batteries, Nantes Université, 2022.

[217] S. Hufner, *Photoelectron Spectroscopy*, Third Edition (Springer, 2003).

[218] F. de Groot and A. Kotani, *Core Level Spectroscopy of Solids* (CRC Press, Boca Raton, 2008).

[219] M. W. Haverkort, M. Zwierzycki, and O. K. Andersen, *Multiplet Ligand-Field Theory Using Wannier Orbitals*, Phys. Rev. B **85**, 165113 (2012).

[220] V. I. Anisimov, J. Zaanen, and O. K. Andersen, *Band Theory and Mott Insulators: Hubbard* U *Instead of Stoner* I, Phys. Rev. B **44**, 943 (1991).

[221] V. I. Anisimov, F. Aryasetiawan, and A. I. Lichtenstein, *First-Principles Calculations of the Electronic Structure and Spectra of Strongly Correlated Systems: The* ***LDA*** + U *Method*, J. Phys. Condens. Matter **9**, 767 (1997).

[222] A. G. Petukhov, I. I. Mazin, L. Chioncel, and A. I. Lichtenstein, *Correlated Metals and the LDA + U Method*, Phys. Rev. B **67**, 153106 (2003).

[223] D. Ensling, A. Thissen, S. Laubach, P. C. Schmidt, and W. Jaegermann, *Electronic Structure of LiCoO 2 Thin Films: A Combined Photoemission Spectroscopy and Density Functional Theory Study*, Phys. Rev. B **82**, 195431 (2010).

[224] E. B. Isaacs, S. Patel, and C. Wolverton, *Prediction of Li Intercalation Voltages in Rechargeable Battery Cathode Materials: Effects of Exchange-Correlation Functional, van Der Waals Interactions, and Hubbard U*, Phys. Rev. Mater. **4**, 065405 (2020).

[225] M. Shishkin and H. Sato, *Self-Consistent Parametrization of DFT + U Framework Using Linear Response Approach: Application to Evaluation of Redox Potentials of Battery Cathodes*, Phys. Rev. B **93**, 085135 (2016).

[226] Y.-Y. Ting and P. M. Kowalski, *Refined DFT + U Method for Computation of Layered Oxide Cathode Materials*, Electrochimica Acta **443**, 141912 (2023).

[227] B. Kim, K. Kim, and S. Kim, *Quantification of Coulomb Interactions in Layered Lithium and Sodium Battery Cathode Materials*, Phys. Rev. Mater. **5**, 035404 (2021).

[228] E. B. Isaacs and C. A. Marianetti, *Compositional Phase Stability of Strongly Correlated Electron Materials within DFT+ U*, Phys. Rev. B **95**, 045141 (2017).

[229] A. Chakraborty, M. Dixit, D. Aurbach, and D. T. Major, *Predicting Accurate Cathode Properties of Layered Oxide Materials Using the SCAN Meta-GGA Density Functional*, Npj Comput. Mater. **4**, 60 (2018).

[230] C. Hébert, *Practical Aspects of Running the WIEN2k Code for Electron Spectroscopy*, Micron **38**, 12 (2007).

[231] W. F. Jr. Egelhoff, *Core-Level Binding-Energy Shifts at Surfaces and in Solids*, Surf. Sci. Rep. **6**, 253 (1987).

[232] M. V. Ganduglia-Pirovano, M. Scheffler, A. Baraldi, S. Lizzit, G. Comelli, G. Paolucci, and R. Rosei, *Oxygen-Induced Rh* $3d_{5/2}$ *Surface Core-Level Shifts on Rh(111)*, Phys. Rev. B **63**, 205415 (2001).

[233] T. Aizawa, S. Suehara, S. Hishita, S. Otani, and M. Arai, *Surface Core-Level Shift and Electronic Structure on Transition-Metal Diboride (0001) Surfaces*, Phys. Rev. B **71**, 165405 (2005).

[234] W. Olovsson, C. Göransson, L. V. Pourovskii, B. Johansson, and I. A. Abrikosov, *Core-Level Shifts in Fcc Random Alloys: A First-Principles Approach*, Phys. Rev. B **72**, 064203 (2005).

[235] Z. Zeng, X. Ma, W. Ding, and W. Li, *First-Principles Calculation of Core-Level Binding Energy Shift in Surface Chemical Processes*, Sci. China Chem. **53**, 402 (2010).

[236] C. J. Nelin, F. Uhl, V. Staemmler, P. S. Bagus, Y. Fujimori, M. Sterrer, H. Kuhlenbeck, and H.-J. Freund, *Surface Core-Level Binding Energy Shifts for MgO(100)*, Phys Chem Chem Phys **16**, 21953 (2014).

[237] Y. Fujimori, X. Zhao, X. Shao, S. V. Levchenko, N. Nilius, M. Sterrer, and H.-J. Freund, *Interaction of Water with the CaO(001) Surface*, J. Phys. Chem. C **120**, 5565 (2016).

[238] P. S. Bagus, C. J. Nelin, X. Zhao, S. V. Levchenko, E. Davis, X. Weng, F. Späth, C. Papp, H. Kuhlenbeck, and H.-J. Freund, *Revisiting Surface Core-Level Shifts for Ionic Compounds*, Phys. Rev. B **100**, 115419 (2019).

[239] M. Ebadi, A. Nasser, M. Carboni, R. Younesi, C. F. N. Marchiori, D. Brandell, and C. M. Araujo, *Insights into the Li-Metal/Organic Carbonate Interfacial Chemistry by Combined First-Principles Theory and X-Ray Photoelectron Spectroscopy*, J. Phys. Chem. C **123**, 347 (2019).

[240] F. Viñes, C. Sousa, and F. Illas, *On the Prediction of Core Level Binding Energies in Molecules, Surfaces and Solids*, Phys. Chem. Chem. Phys. **20**, 8403 (2018).

[241] T. Ozaki and C.-C. Lee, *Absolute Binding Energies of Core Levels in Solids from First Principles*, Phys. Rev. Lett. **118**, 026401 (2017).

[242] P. Blaha, K. Schwarz, F. Tran, R. Laskowski, G. K. H. Madsen, and L. D. Marks, *WIEN2k: An APW+lo Program for Calculating the Properties of Solids*, J. Chem. Phys. **152**, 074101 (2020).

[243] A. Fujimori, A. E. Bocquet, T. Saitoh, and T. Mizokawa, *Electronic Structure of 3d Transition Metal Compounds: Systematic Chemical Trends and Multiplet Effects*, J. Electron Spectrosc. Relat. Phenom. **62**, 141 (1993).

[244] T. Saitoh, A. E. Bocquet, T. Mizokawa, and A. Fujimori, *Systematic Variation of the Electronic Structure of 3*d *Transition-Metal Compounds*, Phys. Rev. B **52**, 7934 (1995).

[245] X. Li, Z. Su, and Y. Wang, *Electrochemical Properties of Monoclinic and Orthorhombic $LiMnO_2$ Synthesized by a One-Step Hydrothermal Method*, J. Alloys Compd. **735**, 2182 (2018).

[246] T. Uyama, K. Mukai, and I. Yamada, *High-Pressure Synthesis and Electrochemical Properties of Tetragonal $LiMnO_2$*, RSC Adv. **8**, 26325 (2018).

[247] X. Zhu et al., *$LiMnO_2$ Cathode Stabilized by Interfacial Orbital Ordering for Sustainable Lithium-Ion Batteries*, Nat. Sustain. **4**, 392 (2020).

[248] S. Siol, J. Mann, J. Newman, T. Miyayama, K. Watanabe, P. Schmutz, C. Cancellieri, and L. P. H. Jeurgens, *Concepts for Chemical State Analysis at Constant Probing Depth by Lab-based XPS/HAXPES Combining Soft and Hard X-ray Sources*, Surf. Interface Anal. **52**, 802 (2020).

[249] J. C. Dupin, D. Gonbeau, H. Benqlilou-Moudden, P. Vinatier, and A. Levasseur, *XPS Analysis of New Lithium Cobalt Oxide Thin-Films before and after Lithium Deintercalation*, Thin Solid Films **384**, 23 (2001).

[250] J. C. Dupin, D. Gonbeau, I. Martin-Litas, P. Vinatier, and A. Levasseur, *Lithium Intercalation/Deintercalation in Transition Metal Oxides Investigated by X-Ray Photoelectron Spectroscopy*, J. Electron Spectrosc. Relat. Phenom. **120**, 55 (2001).

[251] L. Dahéron, H. Martinez, R. Dedryvère, I. Baraille, M. Ménétrier, C. Denage, C. Delmas, and D. Gonbeau, *Surface Properties of $LiCoO_2$ Investigated by XPS Analyses and Theoretical Calculations*, J. Phys. Chem. C **113**, 5843 (2009).

[252] M. Gauthier, P. Karayaylali, L. Giordano, S. Feng, S. F. Lux, F. Maglia, P. Lamp, and Y. Shao-Horn, *Probing Surface Chemistry Changes Using $LiCoO_2$ -Only Electrodes in Li-Ion Batteries*, J. Electrochem. Soc. **165**, A1377 (2018).

[253] J. P. Kemp and P. A. Cox, *Electronic Structure of $LiCoO_2$ and Related Materials; Photoemission Studies*, J. Phys. Condens. Matter **2**, 9653 (1990).

[254] V. R. Galakhov, E. Z. Kurmaev, S. Uhlenbrock, M. Neumann, D. G. Kellerman, and V. S. Gorshkov, *Degree of Covalency of $LiCoO_2$: X-Ray Emission and Photoelectron Study*, Solid State Commun. **99**, 221 (1996).

[255] R. A. Quinlan, Y.-C. Lu, D. Kwabi, Y. Shao-Horn, and A. N. Mansour, *XPS Investigation of the Electrolyte Induced Stabilization of $LiCoO_2$ and "$AlPO_4$ "-Coated $LiCoO_2$ Composite Electrodes*, J. Electrochem. Soc. **163**, A300 (2016).

[256] H. Kiuchi, K. Hikima, K. Shimizu, R. Kanno, F. Toshiharu, and E. Matsubara, *Operando Hard X-Ray Photoelectron Spectroscopy of $LiCoO_2$ Thin Film in an All-Solid-State Lithium Ion Battery*, Electrochem. Commun. **118**, 106790 (2020).

[257] M. C. Biesinger, B. P. Payne, A. P. Grosvenor, L. W. M. Lau, A. R. Gerson, and R. St. C. Smart, *Resolving Surface Chemical States in XPS Analysis of First Row Transition Metals, Oxides and Hydroxides: Cr, Mn, Fe, Co and Ni*, Appl. Surf. Sci. **257**, 2717 (2011).

[258] D. Cabrera-German, G. Gomez-Sosa, and A. Herrera-Gomez, *Accurate Peak Fitting and Subsequent Quantitative Composition Analysis of the Spectrum of Co* 2p *Obtained with Al Kα Radiation: I: Cobalt Spinel: The Co* 2p *Photoemission Spectrum of Cobalt Spinel with Al Kα*, Surf. Interface Anal. **48**, 252 (2016).

[259] G. Greczynski and L. Hultman, *Compromising Science by Ignorant Instrument Calibration—Need to Revisit Half a Century of Published XPS Data*, Angew. Chem. Int. Ed. **59**, 5002 (2020).

[260] J. Maibach, F. Lindgren, H. Eriksson, K. Edström, and M. Hahlin, *Electric Potential Gradient at the Buried Interface between Lithium-Ion Battery Electrodes and the SEI Observed Using Photoelectron Spectroscopy*, J. Phys. Chem. Lett. **7**, 1775 (2016).

[261] M. Ménétrier, I. Saadoune, S. Levasseur, and C. Delmas, *The Insulator-Metal Transition upon Lithium Deintercalation from LiCoO2: Electronic Properties and ^7Li NMR Study*, J. Mater. Chem. **9**, 1135 (1999).

[262] S. Levasseur, *Evidence for Structural Defects in Non-Stoichiometric HT-$LiCoO_2$: Electrochemical, Electronic Properties and ^7Li NMR Studies*, Solid State Ion. **128**, 11 (2000).

[263] H. Idriss, *On the Wrong Assignment of the XPS O1s Signal at 531–532 eV Attributed to Oxygen Vacancies in Photo- and Electro-Catalysts for Water Splitting and Other Materials Applications*, Surf. Sci. **712**, 121894 (2021).

[264] B. Weng, F. Xu, C. Wang, W. Meng, C. R. Grice, and Y. Yan, *A Layered $Na_{1-x}Ni_yFe_{1-y}O_2$ Double Oxide Oxygen Evolution Reaction Electrocatalyst for Highly Efficient Water-Splitting*, Energy Environ. Sci. **10**, 121 (2017).

[265] A. W. Moses, H. G. G. Flores, J.-G. Kim, and M. A. Langell, *Surface Properties of $LiCoO_2$, $LiNiO_2$ and $LiNi_{1-x}Co_xO_2$*, Appl. Surf. Sci. **253**, 4782 (2007).

[266] L. Su, E. Jo, and A. Manthiram, *Protection of Cobalt-Free $LiNiO_2$ from Degradation with Localized Saturated Electrolytes in Lithium-Metal Batteries*, ACS Energy Lett. **7**, 2165 (2022).

[267] Z. Fu, J. Hu, W. Hu, S. Yang, and Y. Luo, *Quantitative Analysis of Ni^{2+}/Ni^{3+} in $Li[Ni_xMn_yCo_z]O_2$ Cathode Materials: Non-Linear Least-Squares Fitting of XPS Spectra*, Appl. Surf. Sci. **441**, 1048 (2018).

[268] E. Markevich, G. Salitra, Y. Talyosef, U.-H. Kim, H.-H. Ryu, Y.-K. Sun, and D. Aurbach, *High-Performance $LiNiO_2$ Cathodes with Practical Loading Cycled with Li Metal Anodes in Fluoroethylene Carbonate-Based Electrolyte Solution*, ACS Appl. Energy Mater. **1**, 2600 (2018).

[269] J. Xu, F. Lin, D. Nordlund, E. J. Crumlin, F. Wang, J. Bai, M. M. Doeff, and W. Tong, *Elucidation of the Surface Characteristics and Electrochemistry of High-Performance $LiNiO_2$*, Chem. Commun. **52**, 4239 (2016).

[270] I. de Meatza et al., *Influence of the Ambient Storage of* $LiNi_{0.8}Mn_{0.1}Co_{0.1}O_2$ *Powder and Electrodes on the Electrochemical Performance in Li-Ion Technology*, Batteries **8**, 79 (2022).

[271] G. Ding et al., *Molten Salt-Assisted Synthesis of Single-Crystalline Nonstoichiometric* $Li_{1+x}Ni_{1-x}O_2$ *with Improved Structural Stability*, Adv. Energy Mater. **13**, 2300407 (2023).

[272] R. Azmi, V. Trouillet, M. Strafela, S. Ulrich, H. Ehrenberg, and M. Bruns, *Surface Analytical Approaches to Reliably Characterize Lithium Ion Battery Electrodes*, Surf. Interface Anal. **50**, 43 (2018).

[273] R. Azmi, M. Masoumi, H. Ehrenberg, V. Trouillet, and M. Bruns, *Surface Analytical Characterization of* $LiNi_{0.8-y}Mn_yCo_{0.2}O_2$ *(*$0 \leq y \leq 0.4$*) Compounds for Lithium-Ion Battery Electrodes*, Surf. Interface Anal. **50**, 1132 (2018).

[274] W. Hua et al., *Lithium-Ion (de)Intercalation Mechanism in Core-Shell Layered* $Li(Ni,Co,Mn)O_2$ *Cathode Materials*, Nano Energy **78**, 105231 (2020).

[275] R. J. Green, H. Wadati, T. Z. Regier, A. J. Achkar, C. McMahon, J. P. Clancy, H. A. Dabkowska, B. D. Gaulin, G. A. Sawatzky, and D. G. Hawthorn, *Evidence for Bond-Disproportionation in* $LiNiO_2$ *from x-Ray Absorption Spectroscopy*, arXiv:2011.06441.

[276] Y. Fu et al., *Core-Level x-Ray Photoemission and Raman Spectroscopy Studies on Electronic Structures in Mott-Hubbard Type Nickelate Oxide* $NdNiO_2$, arXiv:1911.03177.

[277] K. Hikima, K. Shimizu, H. Kiuchi, Y. Hinuma, K. Suzuki, M. Hirayama, E. Matsubara, and R. Kanno, *Reaction Mechanism of* Li_2MnO_3 *Electrodes in an All-Solid-State Thin-Film Battery Analyzed by Operando Hard X-Ray Photoelectron Spectroscopy*, J. Am. Chem. Soc. **144**, 236 (2022).

[278] K. Hikima, Y. Hinuma, K. Shimizu, K. Suzuki, S. Taminato, M. Hirayama, T. Masuda, K. Tamura, and R. Kanno, *Reactions of the* Li_2MnO_3 *Cathode in an All-Solid-State Thin-Film Battery during Cycling*, ACS Appl. Mater. Interfaces **13**, 7650 (2021).

[279] K. Morita, M. Itoda, E. Hosono, D. Asakura, M. Okubo, Y. Takagi, A. Yasui, N. L. Saini, and T. Mizokawa, *Effect of Oxygen Hole in* Li_2MnO_3 *Revealed by Hard X-Ray Photoemission Spectroscopy and Band Structure Calculations*, J. Phys. Soc. Jpn. **92**, 014702 (2023).

[280] A. Quesne-Turin, D. Flahaut, G. Salvato Vallverdu, L. Croguennec, J. Allouche, F. Weill, M. Ménétrier, and I. Baraille, *Surface Reactivity of* Li_2MnO_3*: Structural and Morphological Impact*, Appl. Surf. Sci. **542**, 148514 (2021).

[281] E. S. Ilton, J. E. Post, P. J. Heaney, F. T. Ling, and S. N. Kerisit, *XPS Determination of Mn Oxidation States in Mn (Hydr)Oxides*, Appl. Surf. Sci. **366**, 475 (2016).

[282] F. Parmigiani and L. Sangaletti, *Fine Structures in the X-Ray Photoemission Spectra of MnO, FeO, CoO, and NiO Single Crystals*, J. Electron Spectrosc. Relat. Phenom. **98–99**, 287 (1999).

[283] M. Toupin, T. Brousse, and D. Bélanger, *Influence of Microstucture on the Charge Storage Properties of Chemically Synthesized Manganese Dioxide*, Chem. Mater. **14**, 3946 (2002).

[284] T. J. Chuang, C. R. Brundle, and K. Wandelt, *An X-Ray Photoelectron Spectroscopy Study of the Chemical Changes in Oxide and Hydroxide Surfaces Induced by Ar+ Ion Bombardment*, Thin Solid Films **53**, 19 (1978).

[285] R. Steinberger, J. Walter, T. Greunz, J. Duchoslav, M. Arndt, S. Molodtsov, D. C. Meyer, and D. Stifter, *XPS Study of the Effects of Long-Term Ar+ Ion and Ar Cluster Sputtering on the Chemical Degradation of Hydrozincite and Iron Oxide*, Corros. Sci. **99**, 66 (2015).

[286] R. Steinberger, J. Duchoslav, M. Arndt, and D. Stifter, *X-Ray Photoelectron Spectroscopy of the Effects of* Ar^+ *Ion Sputtering on the Nature of Some Standard Compounds of Zn, Cr, and Fe*, Corros. Sci. **82**, 154 (2014).

[287] M. Fondell, M. Gorgoi, M. Boman, and A. Lindblad, *Surface Modification of Iron Oxides by Ion Bombardment – Comparing Depth Profiling by HAXPES and Ar Ion Sputtering*, J. Electron Spectrosc. Relat. Phenom. **224**, 23 (2018).

[288] I. López, J. Morey, J. B. Ledeuil, L. Madec, and H. Martinez, *A Critical Discussion on the Analysis of Buried Interfaces in Li Solid-State Batteries.* Ex Situ *and* in Situ / Operando *Studies*, J. Mater. Chem. A **9**, 25341 (2021).

[289] G. Fey, P. Muralidharan, C. Lu, and Y. Cho, *Surface Modification of LiNiCoO with LaO for Lithium-Ion Batteries*, Solid State Ion. **176**, 2759 (2005).

[290] J. T. Lee, N. Nitta, J. Benson, A. Magasinski, T. F. Fuller, and G. Yushin, *Comparative Study of the Solid Electrolyte Interphase on Graphite in Full Li-Ion Battery Cells Using X-Ray Photoelectron Spectroscopy, Secondary Ion Mass Spectrometry, and Electron Microscopy*, Carbon **52**, 388 (2013).

[291] L. Yu, Y. Tian, X. Xiao, C. Hou, Y. Xing, Y. Si, H. Lu, and Y. Zhao, *Investigation on the Overlithiation Mechanism of $LiCoO_2$ Cathode for Lithium Ion Batteries*, J. Electrochem. Soc. **168**, 050516 (2021).

[292] B. Heidrich, M. Stamm, O. Fromm, J. Kauling, M. Börner, M. Winter, and P. Niehoff, *Determining the Origin of Lithium Inventory Loss in NMC622||Graphite Lithium Ion Cells Using an $LiPF_6$ -Based Electrolyte*, J. Electrochem. Soc. **170**, 010530 (2023).

[293] S. Altieri, L. H. Tjeng, A. Tanaka, and G. A. Sawatzky, *Core-Level x-Ray Photoemission on NiO in the Impurity Limit*, Phys. Rev. B **61**, 13403 (2000).

[294] N. Pauly, F. Yubero, F. J. García-García, and S. Tougaard, *Quantitative Analysis of Ni 2p Photoemission in NiO and Ni Diluted in a SiO_2 Matrix*, Surf. Sci. **644**, 46 (2016).

[295] A. Gupta, W. D. Chemelewski, C. Buddie Mullins, and J. B. Goodenough, *High-Rate Oxygen Evolution Reaction on Al-Doped $LiNiO_2$*, Adv. Mater. **27**, 6063 (2015).

[296] X. Zheng, X. Li, Z. Wang, H. Guo, Z. Huang, G. Yan, and D. Wang, *Investigation and Improvement on the Electrochemical Performance and Storage Characteristics of $LiNiO_2$-Based Materials for Lithium Ion Battery*, Electrochimica Acta **191**, 832 (2016).

[297] X. Ren et al., *Constructing an Adaptive Heterojunction as a Highly Active Catalyst for the Oxygen Evolution Reaction*, Adv. Mater. **32**, 2001292 (2020).

[298] K. Heo, J. Lee, Y.-W. Song, M.-Y. Kim, H. Jeong, A. DoCheon, K. Jaekook, and J. Lim, *Synthesis and Electrochemical Performance Analysis of $LiNiO_2$ Cathode Material Using Taylor-Couette Flow-Type Co-Precipitation Method*, J. Electrochem. Soc. **168**, 010521 (2021).

[299] T. Phan Nguyen, T. Thi Giang, and I. Tae Kim, *Restructuring NiO to $LiNiO_2$: Ultrastable and Reversible Anodes for Lithium-Ion Batteries*, Chem. Eng. J. **437**, 135292 (2022).

[300] T. Thi Bich Tran, E.-J. Park, H.-I. Kim, S.-H. Lee, H.-J. Jang, and J.-T. Son, *High Rate Performance of Lithium-Ion Batteries with Co-Free $LiNiO_2$ Cathode*, Mater. Lett. **316**, 131810 (2022).

[301] Z. Liu, J. Wu, J. Zeng, F. Li, C. Peng, D. Xue, M. Zhu, and J. Liu, *Co-Free Layered Oxide Cathode Material with Stable Anionic Redox Reaction for Sodium-Ion Batteries*, Adv. Energy Mater. 2301471 (2023).

[302] M. C. Biesinger, B. P. Payne, L. W. M. Lau, A. Gerson, and R. St. C. Smart, *X-Ray Photoelectron Spectroscopic Chemical State Quantification of Mixed Nickel Metal, Oxide and Hydroxide Systems*, Surf. Interface Anal. **41**, 324 (2009).

[303] A. P. Grosvenor, M. C. Biesinger, R. St. C. Smart, and N. S. McIntyre, *New Interpretations of XPS Spectra of Nickel Metal and Oxides*, Surf. Sci. **600**, 1771 (2006).

[304] R. P. Gupta and S. K. Sen, *Calculation of Multiplet Structure of Core p -Vacancy Levels. II*, Phys. Rev. B **12**, 15 (1975).

[305] P. Morin, Etude des propriétés d'électrolytes solides et d'interfaces dans les microbatteries tout solide: Cas du LiPON et des électrolytes soufrés, Université Grenoble Alpes, 2019.

[306] R. Dedryvère, H. Martinez, S. Leroy, D. Lemordant, F. Bonhomme, P. Biensan, and D. Gonbeau, *Surface Film Formation on Electrodes in a $LiCoO_2$/Graphite Cell: A Step by Step XPS Study*, J. Power Sources **174**, 462 (2007).

[307] M. Matsui, K. Dokko, and K. Kanamura, *Dynamic Behavior of Surface Film on $LiCoO_2$ Thin Film Electrode*, J. Power Sources **177**, 184 (2008).

[308] S. Lou, B. Shen, P. Zuo, G. Yin, L. Yang, Y. Ma, X. Cheng, C. Du, and Y. Gao, *Electrochemical Performance Degeneration Mechanism of $LiCoO_2$ with High State of Charge during Long-Term Charge/Discharge Cycling*, RSC Adv. **5**, 81235 (2015).

[309] R. Pan, E. Jo, Z. Cui, and A. Manthiram, *Degradation Pathways of Cobalt-Free $LiNiO_2$ Cathode in Lithium Batteries*, Adv. Funct. Mater. **33**, 2211461 (2023).

[310] E. Björklund, C. Xu, W. M. Dose, C. G. Sole, P. K. Thakur, T.-L. Lee, M. F. L. De Volder, C. P. Grey, and R. S. Weatherup, *Cycle-Induced Interfacial Degradation and Transition-Metal Cross-Over in $LiNi_{0.8}Mn_{0.1}Co_{0.1}O_2$ –Graphite Cells*, Chem. Mater. **34**, 2034 (2022).

[311] C. Guhl, J. Rohrer, P. Kehne, T. Ferber, L. Alff, K. Albe, W. Jaegermann, P. Komissinskiy, and R. Hausbrand, *The Role of Covalent Bonding and Anionic Redox for the Performance of Sodium Cobaltate Electrode Materials*, Energy Storage Mater. **37**, 190 (2021).

[312] A. Yano, M. Shikano, A. Ueda, H. Sakaebe, and Z. Ogumi, *$LiCoO_2$ Degradation Behavior in the High-Voltage Phase Transition Region and Improved Reversibility with Surface Coating*, J. Electrochem. Soc. **164**, A6116 (2017).

[313] C. Qin, Y. Jiang, P. Yan, and M. Sui, *Revealing the Minor Li-Ion Blocking Effect of $LiCoO_2$ Surface Phase Transition Layer*, J. Power Sources **460**, 228126 (2020).

[314] S. Sharifi-Asl et al., *Facet-Dependent Thermal Instability in $LiCoO_2$*, Nano Lett. **17**, 2165 (2017).

[315] J. Hou, R. Girod, N. Nianias, T.-H. Shen, J. Fan, and V. Tileli, *Lithium-Gold Reference Electrode for Potential Stability During In Situ Electron Microscopy Studies of Lithium-Ion Batteries*, J. Electrochem. Soc. **167**, 110515 (2020).

[316] A. Quesne-Turin, D. Flahaut, L. Croguennec, G. Vallverdu, J. Allouche, Y. Charles-Blin, J.-N. Chotard, M. Ménétrier, and I. Baraille, *Surface Reactivity of Li_2MnO_3 : First-Principles and Experimental Study*, ACS Appl. Mater. Interfaces **9**, 50 (2017).

[317] S. Laubach, S. Laubach, P. C. Schmidt, M. Gröting, K. Albe, W. Jaegermann, and W. Wolf, *Structure, Electronic Structure and Defect Formation Energies of $Li_xCo_{1-y}Ni_yO_2$ as a Function of x (0<x<1) and y (y = 0, 0.5, 1)*, Z. Für Phys. Chem. **223**, 10–11 (2009).

[318] R. Xiao, H. Li, and L. Chen, *Density Functional Investigation on Li_2MnO_3*, Chem. Mater. **24**, 21 (2012).

[319] R. C. G. Leckey, *Subshell Photoionization Cross Sections of the Elements for Al K α Radiation*, Phys. Rev. A **13**, 3 (1976).

[320] R. J. Green, M. W. Haverkort, and G. A. Sawatzky, *Bond Disproportionation and Dynamical Charge Fluctuations in the Perovskite Rare-Earth Nickelates*, Phys. Rev. B **94**, 19 (2016).

[321] T. Shang et al., *Real-Space Measurement of Orbital Electron Populations for $Li_{1-x}CoO_2$*, Nat. Commun. **13**, 1 (2022).

[322] M. Mellin, G. Cherkashinin, E. Mohseni, R. Phillips, W. Jaegermann, and J. P. Hofmann, *Voltage-Dependent Charge Compensation Mechanism and Cathode Electrolyte Interface Stability of the Lithium-Ion Battery Cathode Materials $LiCoO_2$ and $LiNi_{1/3}Mn_{1/3}Co_{1/3}O_2$ Studied by Photoelectron Spectroscopy*, J. Mater. Chem. A **Accepted**, (2024).

[323] M. Ghiasi, A. Hariki, M. Winder, J. Kuneš, A. Regoutz, T.-L. Lee, Y. Hu, J.-P. Rueff, and F. M. F. de Groot, *Charge-Transfer Effect in Hard x-Ray 1 s and 2 p Photoemission Spectra: LDA + DMFT and Cluster-Model Analysis*, Phys. Rev. B **100**, 7 (2019).

[324] L. S. R. Kumara, O. Sakata, A. Yang, R. Yamauchi, M. Taguchi, A. Matsuda, and M. Yoshimoto, *Hard X-Ray Photoelectron Spectroscopy of $Li_xNi_{1-x}O$ Epitaxial Thin Films with a High Lithium Content*, J. Chem. Phys. **141**, 4 (2014).

[325] S. Biermann and A. van Roekeghem, *Electronic Polarons, Cumulants and Doubly Dynamical Mean Field Theory: Theoretical Spectroscopy for Correlated and Less Correlated Materials*, J. Electron Spectrosc. Relat. Phenom. **208**, 17 (2016).

[326] M. van Veenendaal, *Competition between Screening Channels in Core-Level x-Ray Photoemission as a Probe of Changes in the Ground-State Properties of Transition-Metal Compounds*, Phys. Rev. B **74**, 8 (2006).

[327] M. A. van Veenendaal and G. A. Sawatzky, *Nonlocal Screening Effects in 2* p *x-Ray Photoemission Spectroscopy Core-Level Line Shapes of Transition Metal Compounds*, Phys. Rev. Lett. **70**, 16 (1993).

[328] M. Taguchi et al., *Revisiting the Valence-Band and Core-Level Photoemission Spectra of NiO*, Phys. Rev. Lett. **100**, 20 (2008).

[329] M. Taguchi et al., *Bulk Screening in Core-Level Photoemission from Mott-Hubbard and Charge-Transfer Systems*, Phys. Rev. B **71**, 15 (2005).

[330] A. Hariki, T. Uozumi, and J. Kuneš, *LDA+DMFT Approach to Core-Level Spectroscopy: Application to 3 d Transition Metal Compounds*, Phys. Rev. B **96**, 4 (2017).

[331] K. Higashi, M. Winder, J. Kuneš, and A. Hariki, *Core-Level X-Ray Spectroscopy of Infinite-Layer Nickelate: LDA+DMFT Study*, Phys. Rev. X **11**, 4 (2021).

[332] A. Hariki, A. Yamanaka, and T. Uozumi, *Theory of Spin-State Selective Nonlocal Screening in Co 2p X-Ray Photoemission Spectrum of $LaCoO_3$*, J. Phys. Soc. Jpn. **84**, 7 (2015).

[333] J. van Elp and A. Tanaka, *Threshold Electronic Structure at the Oxygen* K *Edge of 3d -Transition-Metal Oxides: A Configuration Interaction Approach*, Phys. Rev. B **60**, 8 (1999).

[334] S. Balandeh, R. J. Green, K. Foyevtsova, S. Chi, O. Foyevtsov, F. Li, and G. A. Sawatzky, *Experimental and Theoretical Study of the Electronic Structure of Single-Crystal BaBiO 3*, Phys. Rev. B **96**, 16 (2017).

[335] F. Lechermann, W. Körner, D. F. Urban, and C. Elsässer, *Interplay of Charge-Transfer and Mott-Hubbard Physics Approached by an Efficient Combination of Self-Interaction Correction and Dynamical Mean-Field Theory*, Phys. Rev. B **100**, 11 (2019).

[336] X. Xu, L. Pi, J.-J. Marie, G. J. Rees, C. Gong, S. Pu, R. A. House, A. W. Robertson, and P. G. Bruce, *Li_2NiO_2 F a New Oxyfluoride Disordered Rocksalt Cathode Material*, J. Electrochem. Soc. **168**, 080521 (2021).

[337] X. Hua et al., *Revisiting Metal Fluorides as Lithium-Ion Battery Cathodes*, Nat. Mater. **20**, 841 (2021).

[338] B. Li, G. Rousse, L. Zhang, M. Avdeev, M. Deschamps, A. M. Abakumov, and J.-M. Tarascon, *Constructing "Li-Rich Ni-Rich" Oxide Cathodes for High-Energy-Density Li-Ion Batteries*, Energy Environ. Sci. **16**, 3 (2023).

[339] Y. Li, J. Chen, P. Cai, and Z. Wen, *An Electrochemically Neutralized Energy-Assisted Low-Cost Acid-Alkaline Electrolyzer for Energy-Saving Electrolysis Hydrogen Generation*, J. Mater. Chem. A **6**, 4948 (2018).

[340] M. Chen, Y. Liu, Y. Zhang, G. Xing, and Y. Tang, *Lithium-Rich Sulfide/Selenide Cathodes for next-Generation Lithium-Ion Batteries: Challenges and Perspectives*, Chem. Commun. **58**, 3591 (2022).

[341] S. Saha et al., *Exploring the Bottlenecks of Anionic Redox in Li-Rich Layered Sulfides*, Nat. Energy **4**, 977 (2019).

[342] D. Goonetilleke, A. Mazilkin, D. Weber, Y. Ma, F. Fauth, J. Janek, T. Brezesinski, and M. Bianchini, *Single Step Synthesis of W-Modified $LiNiO_2$ Using an Ammonium Tungstate Flux*, J. Mater. Chem. A **10**, 7841 (2022).

[343] S. Tanuma, C. J. Powell, and D. R. Penn, *Calculations of Electron Inelastic Mean Free Paths. V. Data for 14 Organic Compounds over the 50-2000 eV Range*, Surf. Interface Anal. **21**, 165 (1994).

[344] S. Tanuma, C. J. Powell, and D. R. Penn, *Calculations of Electron Inelastic Mean Free Paths: VIII. Data for 15 Elemental Solids over the 50-2000 eV Range*, Surf. Interface Anal. **37**, 1 (2005).

[345] S. Tanuma, C. J. Powell, and D. R. Penn, *Calculations of Electron Inelastic Mean Free Paths. IX. Data for 41 Elemental Solids over the 50 eV to 30 keV Range*, Surf. Interface Anal. **43**, 3 (2011).

[346] M. Mirolo, D. Leanza, L. Höltschi, C. Jordy, V. Pelé, P. Novák, M. El Kazzi, and C. A. F. Vaz, Post Mortem *and* Operando *XPEEM: A Surface-Sensitive Tool for Studying Single Particles in Li-Ion Battery Composite Electrodes*, Anal. Chem. **92**, 3023 (2020).

[347] S. Marchesini et al., *Surface Analysis of Pristine and Cycled NMC/Graphite Lithium-Ion Battery Electrodes: Addressing the Measurement Challenges*, ACS Appl. Mater. Interfaces **14**, 52779 (2022).

[348] D. A. Shirley, *High-Resolution X-Ray Photoemission Spectrum of the Valence Bands of Gold*, Phys. Rev. B **5**, 4709 (1972).

[349] S. Tougaard, *Practical Algorithm for Background Subtraction*, Surf. Sci. **216**, 343 (1989).

[350] M. R. Linford et al., *Proliferation of Faulty Materials Data Analysis in the Literature*, Microsc. Microanal. **26**, 1 (2020).

[351] G. H. Major et al., *Assessment of the Frequency and Nature of Erroneous X-Ray Photoelectron Spectroscopy Analyses in the Scientific Literature*, J. Vac. Sci. Technol. A **38**, 061204 (2020).

[352] F. S. Gittleson and F. El Gabaly, *Non-Faradaic Li^+ Migration and Chemical Coordination across Solid-State Battery Interfaces*, Nano Lett. **17**, 6974 (2017).

[353] J. Hata, M. Hirayama, K. Suzuki, N. Dupré, D. Guyomard, and R. Kanno, *Effect of Surface Chemical Bonding States on Lithium Intercalation Properties of Surface-Modified Lithium Cobalt Oxide*, Batter. Supercaps **2**, 454 (2019).

[354] J. Li et al., *Construction of Inorganic-Rich Cathode Electrolyte Interphase on Co-Free Cathodes*, ACS Appl. Mater. Interfaces **15**, 26627 (2023).

[355] S. Asada and S. Sugano, *Satellites in X-Ray Photoelectron Spectra of Transition-Metal Compounds*, J. Phys. Soc. Jpn. **41**, 1291 (1976).

[356] A. Fujimori, F. Minami, and S. Sugano, *Multielectron Satellites and Spin Polarization in Photoemission from Ni Compounds*, Phys. Rev. B **29**, 5225 (1984).

[357] J. Zaanen, C. Westra, and G. A. Sawatzky, *Determination of the Electronic Structure of Transition-Metal Compounds:* 2p *x-Ray Photoemission Spectroscopy of the Nickel Dihalides*, Phys. Rev. B **33**, 8060 (1986).

[358] K. Okada and A. Kotani, *Interatomic and Intra-Atomic Configuration Interactions in Core-Level X-Ray Photoemission Spectra of Late Transition-Metal Compounds*, J. Phys. Soc. Jpn. **61**, 4619 (1992).

[359] F. C. Zhang and T. M. Rice, *Effective Hamiltonian for the Superconducting Cu Oxides*, Phys. Rev. B **37**, 3759 (1988).

[360] F. Giustino, *Materials Modelling Using Density Functional Theory* (Oxford University Press, 2014).

[361] P. Hohenberg and W. Kohn, *Inhomogeneous Electron Gas*, Phys. Rev. **136**, B864 (1964).

[362] W. Kohn and L. J. Sham, *Self-Consistent Equations Including Exchange and Correlation Effects*, Phys. Rev. **140**, A1133 (1965).

[363] M. Bagheri and P. Blaha, *DFT Calculations of Energy Dependent XPS Valence Band Spectra*, J. Electron Spectrosc. Relat. Phenom. **230**, 1 (2019).

[364] R. F. W. Bader, *Atoms and Molecules*, (https://www.chemistry.mcmaster.ca/bader/aim/).

[365] J. F. Janak, *Proof That $\partial E/\partial n_i = \varepsilon_i$ in density-functional theory*, Phys. Rev. B **18**, 7165 (1978).

[366] J. C. Slater, J. B. Mann, T. M. Wilson, and J. H. Wood, *Nonintegral Occupation Numbers in Transition Atoms in Crystals*, Phys. Rev. **184**, 672 (1969).

[367] A. R. Williams, R. A. deGroot, and C. B. Sommers, *Generalization of Slater's Transition State Concept*, J. Chem. Phys. **63**, 628 (1975).

[368] G. Pizzi et al., *Wannier90 as a Community Code: New Features and Applications*, J. Phys. Condens. Matter **32**, 165902 (2020).

[369] N. Marzari, A. A. Mostofi, J. R. Yates, I. Souza, and D. Vanderbilt, *Maximally Localized Wannier Functions: Theory and Applications*, Rev. Mod. Phys. **84**, 1419 (2012).

[370] J. Kuneš, R. Arita, P. Wissgott, A. Toschi, H. Ikeda, and K. Held, *Wien2wannier: From Linearized Augmented Plane Waves to Maximally Localized Wannier Functions*, Comput. Phys. Commun. **181**, 1888 (2010).

[371] E. Pavarini, E. Koch, D. Vollhardt, A. I. Lichtenstein, Institute for Advanced Simulation, German Research School for Simulation Sciences, and Deutsche Forschungsgemeinschaft, editors , *The LDA+DMFT Approach to Strongly Correlated Materials: Lecture Notes of the Autumn School 2011 Hands-on LDA+DMFT* (Forschungszentrum Jülich, Zentralbibliothek, 2011).

[372] L. Vaugier, Electronic Structure of Correlated Materials From First Principles: Hubbard Interaction and Hund's Exchange, Ecole Polytechnique Paris Tech, 2011.

[373] A. van Roekeghem, L. Vaugier, H. Jiang, and S. Biermann, *Hubbard Interactions in Iron-Based Pnictides and Chalcogenides: Slater Parametrization, Screening Channels, and Frequency Dependence*, Phys. Rev. B **94**, 12 (2016).

[374] H. Jiang and P. Blaha, *G W with Linearized Augmented Plane Waves Extended by High-Energy Local Orbitals*, Phys. Rev. B **93**, 115203 (2016).

[375] M. W. Haverkort, *Documentation - Quanty*, (2017).

[376] M. Karolak, G. Ulm, T. Wehling, V. Mazurenko, A. Poteryaev, and A. Lichtenstein, *Double Counting in LDA+DMFT—The Example of NiO*, J. Electron Spectrosc. Relat. Phenom. **181**, 11 (2010).

[377] A. Damascelli, *Probing the Electronic Structure of Complex Systems by ARPES*, Phys. Scr. **T109**, 61 (2004).

[378] G. Mahan, *Many-Particle Physics*, Third (Kluwer Academic, 2000).

[379] M. W. Haverkort, Quanty *for Core Level Spectroscopy - Excitons, Resonances and Band Excitations in Time and Frequency Domain*, J. Phys. Conf. Ser. **712**, 012001 (2016).

[380] M. Retegan, *Crispy: V0.7.4*, (2019).

[381] M. W. Haverkort, Spin and Orbital Degrees of Freedom in Transition Metal Oxides and Oxide Thin Films Studied by Soft X-Ray Absorption Spectroscopy, University of Cologne, 2005.

[382] M. Antaya, K. Cearns, J. S. Preston, J. N. Reimers, and J. R. Dahn, In Situ *Growth of Layered, Spinel, and Rock-salt $LiCoO_2$ by Laser Ablation Deposition*, J. Appl. Phys. **76**, 2799 (1994).

[383] L. Le Van-Jodin, D. Rouchon, V. Le, I. Chevalier, J. Brun, and C. Secouard, *Ex Situ and Operando Study of $LiCoO_2$ Thin Films by Raman Spectroscopy: Thermal and Electrochemical Properties*, J. Raman Spectrosc. **50**, 1594 (2019).

[384] J. Kieffer, V. Valls, N. Blanc, and C. Hennig, *New Tools for Calibrating Diffraction Setups*, J. Synchrotron Radiat. **27**, 558 (2020).

[385] J. Rodríguez-Carvajal, *Recent Advances in Magnetic Structure Determination by Neutron Powder Diffraction*, Phys. B Condens. Matter **192**, 55 (1993).

[386] L.-S. Chang, Y.-C. Lin, C.-Y. Su, H.-C. Wu, and J.-P. Pan, *Effect of C60 Ion Sputtering on the Compositional Depth Profiling in XPS for $Li(Ni,Co,Mn)O_2$ Electrodes*, Appl. Surf. Sci. **258**, 1279 (2011).

[387] Y. Takahashi, N. Kijima, K. Tokiwa, T. Watanabe, and J. Akimoto, *Single-Crystal Synthesis, Structure Refinement and Electrical Properties of $Li_{0.5}CoO_2$*, J. Phys. Condens. Matter **19**, 43 (2007).

[388] K. H. Razeg, M. F. AL-Hilli, A. A. Khalefa, and K. A. Aadim, *Structural and Optical Properties of ($Li_xNi_{2-x}O_2$) Thin Films Deposited by Pulsed Laser Deposited (PLD) Technique at Different Doping Ratio*, Int. J. Phys. **5**, 46 (2017).

[389] M. S. El-Bana, I. M. El Radaf, S. S. Fouad, and G. B. Sakr, *Structural and Optoelectrical Properties of Nanostructured $LiNiO_2$ Thin Films Grown by Spray Pyrolysis Technique*, J. Alloys Compd. **705**, 333 (2017).